UNIVERSITÉ DE LILLE

ECOLE DOCTORALE - 104 - SCIENCES DE LA MATIÈRE, DU RAYONNEMENT ET DE L'ENVIRONNEMENT

Development of time-stretch terahertz waveform recorders for high repetition rate accelerator-based light sources

(Développement d'enregistreurs de formes d'onde térahertz à étirement temporel pour les sources lumineuses basées sur des accélérateurs à taux de répétition élevé)

Thèse présentée par

Christelle HANOUN

pour l'obtention du grade de

***Docteur en* PHYSIQUE**

dans la spécialité

Milieux dilués et optique fondamentale

Soutenue le 20 décembre 2023 devant le jury composé de :

Pr. Ammar HIDEUR	CORIA - Université de Rouen	Rapporteur
Dr. Bernd STEFFEN	DESY, Hambourg	Examinateur
Dr. Eléonore ROUSSEL	Université de Lille	Co-encadrante de thèse
Pr. Géraud BOUWMANS	Université de Lille	Examinateur
Pr. Nicolas JOLY	Max Planck Institute – Erlangen	Président du Jury
Pr. Serge BIELAWSKI	Université de Lille	Directeur de thèse
Dr. Thibaut LEFEVRE	CERN	Rapporteur

UNIVERSITÉ DE LILLE

Abstract

Development of time-stretch terahertz waveform recorders for high repetition rate accelerator-based light sources

by Christelle HANOUN

THz science lacks of non-destructive waveform recorders for single-shot measurements of ultrafast signals with high repetition rates. This need is particularly crucial in accelerator-based light sources where electrons are accelerated to the speed of light, and holds substantial significance for researchers in the realm of time-domain THz spectroscopy, especially when investigating ultrafast irreversible phenomena. Existing detectors still present limitations in terms of recording window lengths, acquisition rates and sensitivity. This thesis aims to develop novel THz detectors that overcome existing limitations and capable of recording single-shot THz signals emitted by storage rings and free-electron lasers. In a first investigation, an experimental setup, based on single-shot electro-optic sampling combining photonic time-stretch and phase diversity techniques, is tested at the coherent diffraction radiation THz source at ELBE reaching up to 26 MHz acquisition rate with a sub-picosecond resolution. As this setup can provide systematically both the carrier and envelope of THz waveforms, we were able to measure for the first time ever the startup and turnoff of the free electron laser at ELBE in single-shot and offer valuable information on carrier-envelope phase. A second part of this work is dedicated to improve the performance of time-stretch electro-optic sampling, allowing to increase the stretch and consequently reduce the detection bandwidth. This study, conceived at the 1550 mm telecommunication laser wavelength, was performed at SOLEIL storage ring allowing to measure THz signals with 1 GHz oscilloscope, a milestone achievement in ultrafast studies. Notably, it enabled to measure unprecedentedly the complete coherent synchrotron radiation THz pulses in single-shot.

UNIVERSITÉ DE LILLE

Résumé

Développement d'enregistreurs de formes d'onde térahertz à étirement temporel pour les sources lumineuses basées sur des accélérateurs à taux de répétition élevé

by Christelle HANOUN

Le travail de Thèse concerne le développement de systèmes permettant l'enregistrement de signaux électriques, en single-shot, avec des bandes passantes allant jusqu'à plusieurs térahertz (THz). Ce travail est motivé par des besoins importants dans le développement et la recherche sur les sources de lumière basées sur des accélérateurs (les centres de rayonnement synchrotron et les lasers à électrons libres). Ce travail est également motivé par les besoins récents de spectroscopie THz avec des fréquences d'acquisition élevées. Cette thèse se focalise sur le développement de systèmes de mesure où les ondes THz à analyser sont sondées au moyen d'un laser femtoseconde. Plus spécifiquement, le travail porte sur le développement de la technique dite du *photonic time-stretch*, et vise à résoudre plusieurs problèmes ouverts. Jusqu'à récemment, les techniques de time-stretch souffraient d'une limite fondamentale qui limitait leurs durées d'enregistrement et/ou leurs résolutions temporelles à des valeurs incompatibles avec de nombreuses applications dans le domaine des accélérateurs. Dans une première partie, le travail a consisté à tenter de résoudre ce problème en développant, au laboratoire PhLAM, un système d'enregistrement THz monocoup associant la technique du photonic time-stretch et la technique dite du *Diversity Electro-Optic Sampling (DEOS)*. Le système d'enregistrement, basé sur un laser de sonde à 1030 nm a ensuite été testé lors de deux séries d'expériences sur les sources THz intense basées sur l'accélérateur ELBE, à Dresde. La première expérience s'est focalisée sur la source CDR (Coherent Diffraction Radiation) de ELBE – une source THz émettant des impulsions "single cycle". Le succès de cette expérience nous a ensuite mené à réaliser des mesures du rayonnement émis par le laser à électrons libres (FEL) Térahertz de FELBE. Ceci nous a permis de démontrer la possibilité d'enregistrer de signaux THz à une fréquence – record – de 13 MHz. De plus, d'un point de vue plus fondamental, l'étude expérimentale du démarrage du laser à électrons libres a permis – pour la première fois – de visualiser de façon directe le démarrage d'un laser impulsionnel, en enregistrant complètement les impulsions émises (c'est-à-dire leur amplitude et leur porteuse). Finalement, cette thèse s'est focalisée sur un problème ouvert différent, concernant le coût – extrêmement élevé – des systèmes de mesures THz de type time-stretch. En effet, ces systèmes de mesures requièrent des oscilloscopes avec des bandes passantes élevées (généralement au-delà de 10 ou 20 GHz). À partir d'une étude comparative détaillée, et de mesures effectuées à SOLEIL, nous avons démontré la supériorité d'une stratégie basée sur des lasers de sonde à 1550 nm, au lieu des lasers (essentiellement à 1030 nm) usuellement employés dans la littérature. En permettant l'utilisation d'oscilloscopes avec des bandes passantes relativement faibles (de l'ordre du GHz), ceci nous a permis de réduire les coûts de façon importante, permettant d'envisager une popularisation beaucoup plus importante de ces méthodes de time-stretch dans le domaine des accélérateurs et en spectroscopie.

Acknowledgements

Embarking on the intricate journey of my Ph.D. work has been an extraordinary experience, and I am profoundly grateful to all those who contributed to this remarkable and unforgettable adventure.

Foremost, I want to express sincere appreciation to the esteemed members of the defense jury — Bernd Steffen, Géraud Bouwmans, Nicolas Joly and especially the reporters Ammar Hideur and Thibault Lefevre. Your insightful remarks and invaluable advice were essential to the refinement of my work.

This PhD work would not have been possible without the guidance of my supervisor, Serge Bielawski, to whom I express my deepest gratitude. Your generous sharing of knowledge, support, guidance and insights throughout the research process were invaluable in shaping the direction of my thesis.

Special thanks extend to my co-supervisor, Eléonore Roussel, whose significant role both professionally and personally enriched my research journey. Your continuous support, counsel, and remarkable excellence were instrumental in guiding this PhD work.

I express gratitude to Christophe Szwaj for your expertise and advice, especially in experimental hacks that significantly optimized my work efficiency.

Working together in the same team has been a privilege, marked by shared amazing experiences during experimental shifts, trips, drinks and restaurants! You were source of inspiration. Your support and comprehension are invaluable, especially during the challenging times of the early days of the pandemic since my arrival in France.

I extend my gratitude to the CNRS and the Université de Lille for the financial support, enabling the successful completion of this research journey. This experience was enriched by participation in conferences contributing to my academic growth and enlarging my scientific community. A sincere thank you to every member of the PhLAM laboratory, from the esteemed director Cristian Focsa to individuals in administration, mechanical, and electronic shops. Being a part of this laboratory has been a pleasure. Special acknowledgment goes to Marc Le Parquier for his assistance in the development my THz detectors.

On the international front, gratitude extends to Pavel Evtushenko from ELBE, HZDR, for the warm welcome during our experimental shifts in Dresden. Working with you was a privilege, and I appreciate the insightful scientific discussions we shared. Special thanks also go to Michael Klopf, Sergey Kovalev and all the ELBE team members who generously shared their knowledge about the accelerator, making the wait for observing THz signals an exciting and enriching experience.

From SOLEIL Synchrotron, exceptional thanks go to Pascale Roy and Jean-Blaise Brubach for their welcome in AILES beamline and for their inspiring work and research.

I would like to express my gratitude to Nicolas Joly and Christelle Bruni for their continuous support and follow-up throughout my academic journey.

Appreciation extends to colleagues and friends for camaraderie and support during academic challenges. To Cecilia, Vikas, Shivang, Rabih, Alexandre, Maxime, Brahim, Georges, Eden, Jordan, Martin, Quentin, Loic, Joelle and Tony — who some of them became part of my family in Lille — thank you for sharing the highs and lows, drinks, outings, and countless memorable moments. Your friendship made the journey more enjoyable and memorable. I wish you continued success in your Ph.D. pursuits and I am sure that you will excel.

To my friends and family in France — Maha, Zeinab, Mikel, Nathalie and Sylvie — I am grateful for your unwavering support.

Profound and countless thanks for my Family in Lebanon for your continuous support and visits, adding a special dimension to this journey. The happy ending travel and seeing you so proud of me overwhelm my heart. Your love and support have been my pillars of strength.

Lastly, heartfelt and special thanks to Alexandre for giving my Ph.D., through which I met you, a unique flavor and offering support during my emotional moments. Here's to many more life challenges together!

In conclusion, I express my gratitude to all those who directly or indirectly contributed to the completion of this thesis. Your support has been instrumental, and I am truly appreciative.

Contents

List of Figures

List of Tables

List of Abbreviations

ADC	**A**nalog-to-**D**igital **C**onverter
AR	**A**nti-**R**eflection
BW	**B**and**W**idth
CDR	**C**oherent **D**iffraction **R**adiation
CEP	**C**arrier-**E**nvelope **P**hase
CSR	**C**oherent **S**ynchrotron **R**adiation
CTR	**C**oherent **T**ransition **R**adiation
cw	**c**ontinuous **w**ave
DCF	**D**ispersion **C**ompensation **F**iber
DCM	**D**ispersion **C**ompensation **M**odule
DEOS	**D**iversity **E**lectro **O**ptic **S**ampling
ELBE	**E**lectron **L**inac for beams with high **B**rilliance and low **E**mittance
EO	**E**lectro **O**ptic
EOS	**E**lectro **O**ptic **S**ampling
EOSD	**E**lectro **O**ptic **S**pectral **D**ecoding
EOSD-PTS	**E**lectro **O**ptic **S**ampling **D**ecoding - **P**hotonic **T**ime **S**tretch
FET	**F**ield **E**ffect **T**ransistor
FEL	**F**ree **E**lectron **L**aser
FELBE	**FEL** at **ELBE**
FT	**F**ourier **T**ransform
fs	**f**emto**s**econd
FWHM	**F**ull **W**idth at **H**alf **M**aximum
GaAs	**Ga**llium **As**enide
GaP	**Ga**llium **P**hosphide
GHz	**G**iga**H**er**z**
Hz	**H**er**z**
HWP	**H**alf **W**ave **P**late
IR	**I**nfra**R**ed
KALYPSO	**KA**rlsruhe **L**inear arra**Y** detector for MHz-re**P**etition rate **S**pectr**O**scopy
mA	**m**illi**A**mpere
MeV	**Mega-e**lectron **V**olt
MHz	**M**ega**H**er**z**
MRC	**M**aximal **R**atio **C**ombining
ms	**m**illi**s**econd
nm	**n**ano**m**eter
ps	**p**ico**s**econd
pC	**p**ico**C**oulomb
PC	**P**olarization **C**ontroller
PTS	**P**hotonic **T**ime **S**tretch
PBS	**P**olarizing **B**eam **S**plitter
QWP	**Q**uarter **W**ave **P**late
rad	**rad**ian

RF	**R**adio**F**requency
rms	**r**oot **m**ean **s**quare
SASE	**S**elf-**A**mplified **S**pontaneous **E**mission
SM	**S**ingle-**M**ode
SNR	**S**ignal-to-**N**oise **R**atio
SOLEIL	**S**ource **O**ptimisée de **L**umière d'**E**nergie **I**ntermédiaire du **L**URE
SR	**S**ynchrotron **R**adiation
SRF	**S**uperconducting **R**adio **F**requency
TDS	**T**ime-**D**omain **S**pectroscopy
TELBE	**T**Hz facility at **ELBE**
THz	**T**era**H**er**tz**
V	**V**olt
VFP	**V**lasov-**F**okker-**P**lanck
ZnTe	**Zn**c **Te**lluride

Physical Constants

Speed of Light	$c = 2.997\,924\,58 \times 10^{8}\,\mathrm{m\,s^{-1}}$
Elementary Charge	$e = 1.602\,176\,634 \times 10^{-19}\,\mathrm{C}$
Electron Mass	$m_e = 9.109\,383\,701\,5 \times 10^{-31}\,\mathrm{kg}$

List of Symbols

α	angle	rad
β_2	group velocity dispersion	s^2/m
C	chirp rate	rad/s^2
d	crystal thickness	m
D	dispersion parameter	s/m^2
$\Delta\lambda$	bandwidth	m
$\Delta\Phi$	phase shift	rad
E_e	electron energy	J (eV)
E_{THz}	THz electric field	V/m
ϵ	complex dielectric function	
f	frequency	Hz
$f(\tilde{\nu})$	bunch longitudinal form factor	
G	gain factor	dB
γ	relativistic Lorentz factor	
H	transfer function	
I	current	A
k	undulator parameter	
κ	extinction coefficient	
L	length	m
λ	wavelength	m
λ_u	undulator period	m
m	mass	kg
M	stretch factor	
n	refractive index	
n_f	refractive index along fast axis	
n_g	group refractive index	
n_s	refractive index along slow axis	
N_{eff}	number of effective points	
$N_{electrons}$	number of electrons	
$\tilde{\nu}$	wavenumber	m^{-1}
ω	angular frequency	rad/s
P	power	W ($J\,s^{-1}$)
ϕ	phase	rad
ψ	phase	rad
r_{41}	electro-optic coefficient	m/V
ρ	normalized longitudinal electron density	
t	time	s
T	duration	s
T_C	duration of chirped laser pulse	s
T_R	temporal resolution	s
θ	angle	rad
v	speed	m/s

v_g	optical group velocity	m/s
v_{ph}	phase velocity	m/s

To my family

Introduction

Accelerators-based light sources have emerged as powerful scientific tools employed to reveal the secrets of matter. These machines provide an intense radiation with unique properties over a wide of electromagnetic radiation in the infrared, ultraviolet and X-rays ranges, inaccessible by conventional sources. These wavelengths are of high interest in fields such as biological studies [1], chemical analyses [2] and material science.

Within accelerators, electrons are accelerated to relativistic speeds close to the velocity of light, serving as sources of synchrotron radiation. With the progress of accelerators, electrons have been generated with enhanced characteristics, including higher energies, shorter time scales from subnanoseconds to picoseconds, resulting in the generation of Terahertz (THz) radiation, both incoherently and coherently. This THz radiation has attracted researchers from diverse disciplines and started to find applications in various sectors such as in medicine, science, industry and technology [3, 4]. It has expanded rapidly after the development of THz time-domain spectroscopy since the early 1990 [5]. Diverse advancements have been consequently achieved to generate this THz radiation with various properties such as coherent synchrotron radiation, coherent transition radiation, coherent diffraction radiation, free-electron lasers, etc.

In accelerators, exploring the dynamics of electrons is crucial to get an understanding of their behavior and control their emission of radiation. This can be achieved either by characterizing electron bunch shapes by measuring the electric field inside the vacuum chamber or by measuring the THz emitted radiation that reflects the properties of electrons bunches within the accelerator. Consequently, measurements within these facilities are important to understand and control these machines. Measuring the shot-by-shot electrons behavior, allows to study the dynamic of the particles. Moreover, characterizing the coherent THz emitted radiation helps in getting information on the electron bunches. These observations serve as a validation and refinement tool to simulations models, helping with designing and optimizing accelerators. Additionally, the study of THz emitted radiation holds significant importance for THz spectroscopic applications, extending scientific exploration and provide ultrafast measurements tools.

Nevertheless, these ultrafast measurements are not straightforward and require advanced diagnostic tools with THz bandwidths. A popular technique for THz detection, called electro-optic sampling (EOS), consists in probing electric fields using a laser probe pulse. Based on this technique, many research studies have been conducted at various THz sources [6–8] and have been upgraded progressively to allow single-shot operation detection of high acquisition rates [9, 10]. Current available systems still exhibit certain limitations with challenges increasing continuously with the emergence of more sophisticated THz sources operating at high THz

frequencies and higher repetition rates (such as FELBE, PITZ, etc.).

The main objective of this PhD thesis is to go beyond existing limitations and to develop a novel real-time observation tool, based on optics and photonics, that encompasses all these needs into a single setup capable of performing single shot measurements at high repetition rates and a sufficient temporal resolution. This detector tool will be based on single shot EOS with photonic time stretch, enabling to reach high repetition rates. Additionally, a technique for numerical signal reconstruction will be employed to achieve the required temporal resolution. The second purpose consists in applying and using this diagnostic tool to study machines such as storage rings and free-electron lasers. Experiments will be conducted at three different THz sources, the coherent diffraction radiation at ELBE, the free-electron laser FELBE, and the coherent synchrotron radiation at SOLEIL storage ring. We will see how with combining photonic time stretch with single-shot EOS we will be able to measure repetition rates up to 13 MHz. A part of this work will be dedicated to work, using photonics, on reducing the cost of the diagnostic tool as existing techniques impose the use of expensive digitizers with high bandwidth, thus making these techniques more cost-effective and more accessible for scientists.

This thesis is organized as follows: Chapter 1 serves as an introduction to accelerator-based light sources, with a particular focus on those generating THz coherent radiation. It discusses the necessity of single-shot THz measurement in accelerators, existing detection methods and address briefly the associated challenges.

In Chapter 2, we will focus on the techniques involved for the development of the THz detectors that will be presented in the subsequent chapters. We will give a brief review on THz single-shot techniques, with a specific emphasis on spectral encoding electro-optic sampling using chirped laser pulses. We will introduce after the photonic time stretch technique that allows to reach repetition rates of the accelerators going up to the MHz range. The chapter also discusses the implementation of the phase diversity technique to overcome a known resolution limitation in THz single-shot detection. A substantial portion of this thesis is devoted to the development of a data analysis numerical algorithm for signal reconstruction with sufficient temporal resolution to retrieve accurately THz profiles from raw data.

Chapters 3 and 4 describe the experiments conducted at various THz sources to test our experimental setups using a 1030 nm Ytterbium laser, a common wavelength employed in accelerators, as used at DESY and KARA. These experiments provide practical insights into the performance and adaptability of the diagnostic tool for different THz sources. In Chapter 3, we describe the experimental setup we have developed with the first tests at the coherent THz diffraction source at ELBE with the measured signals and the data analysis protocols for signal reconstruction. Chapter 4 extends the exploration of our THz detection tool for the measurement of another THz source, which is the FEL THz source, emitting adjustable THz frequencies at a 13 MHz repetition rate.

In Chapter 5, a special purpose emerges, aiming to reduce the detector cost by exploring the capabilities of photonic time stretch at the 1550 nm telecommunication wavelength to further slow down signals, thereby reducing the detection bandwidth required. This approach offers the potential for cost reduction while

maintaining an efficient performance. This experimental setup is tested at SOLEIL storage ring to measure the complete coherent THz pulses in single-shot.

And to sum up, Chapter 6 offers reflections on the achieved outcomes throughout this thesis and their significance in advancing our understanding of THz radiation sources. It outlines potential avenues for future research work and development.

Chapter 1

Accelerators-based THz sources

This chapter gives a brief introduction about accelerators-driven light sources tracing their evolution with time followed by a description of several sources of THz radiation emitted by relativistic electron bunches. A second section is dedicated to electron beam diagnostics in accelerators, emphasizing on the need of single-shot measurements for signals with THz bandwidth and the challenges faced for these types of measurements.

1.1 Introduction on accelerators-based light sources

Particle accelerators are the biggest scientific tools and among the most expensive instruments for research. Their development improved on a rapid scale with different operation modes and configurations to produce an intense radiation uncommonly generated by conventional techniques, particularly in the X-ray and THz range.

The development of accelerators-based light sources started with the development of storage rings conceived to investigate nuclear and particle physics phenomena [11, 12]. As charged particles are accelerated, they emit an electromagnetic field, known as *synchrotron radiation (SR)*. At that time, this emitted radiation was considered as a limitation in accelerators [13], hampering high-energy experiments. Its utilization in research was limited [14, 15] because the machines were primarily optimized for other experiments rather than the production of SR.

After discovering synchrotron radiation, the potential uses of this radiation in research became apparent, leading to the emergence of a new generation of accelerators-based light sources in the early 1970s, storage rings designed and dedicated to produce SR, such as UVSOR [16] and SuperACO [17] using bending magnets. The high demand pushed researchers to expand existing facilities or construct new ones, such as Synchrotron SOLEIL [18], capable of generating more intense and higher energy X-rays with insertion devices such as wigglers and undulators to boost brightness.

An upgraded generation of accelerators-driven light sources is currently operational and features free-electron lasers (FEL)s where relativistic electrons are used to develop lasers, that provide an intense, coherent X-ray radiation like FELBE [19], FLASH [20], FERMI [21], etc.

On the ongoing advancement, a new light sources generation [22] is currently under development, based on laser wakefield acceleration towards ultra compact

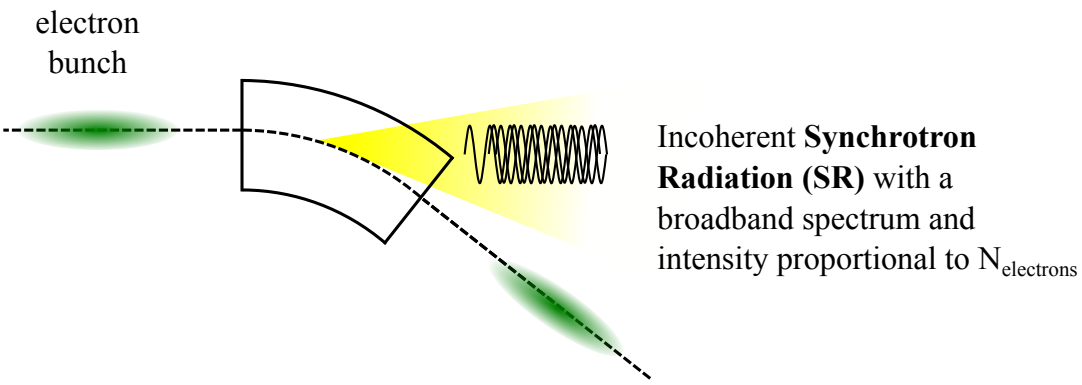

FIGURE 1.1: Emission of synchrotron radiation (SR) when an electron bunch passes through a bending magnet. As each electron forming the bunch emits at shorter wavelength than its length, the total synchrotron radiation results in an incoherent emission.

accelerators [22–25].

These light sources have become indispensable, performing milestone advancements in many research fields, medicine and technology. Their applications span across various disciplines, ranging from fundamental sciences such as physics, spectroscopy, and structural biology, to practical applications in medicine [26–29].

1.2 Relativistic electron bunches-based THz light sources

We will describe, in this section, the physical techniques on which are based accelerators-driven light sources that use relativistic electron bunches to generate THz radiation, and in particular on the THz sources that will be investigated in this thesis. Our work concerns the measurement of the coherent synchrotron radiation in a storage ring, the coherent diffraction radiation in a linear accelerator, on the THz emitted pulses by a free-electrons laser.

1.2.1 Synchrotron radiation

According to classical electrodynamics principles, an accelerated charge radiates energy in an electromagnetic pulse [30]. Based on this concept, a charged particle moving on a curved trajectory in the presence of a magnetic field emits an electromagnetic wave under the so-called *synchrotron radiation* (SR). Thereby, when an accelerated electron bunch traverse a magnetic field, it emits an incoherent synchrotron radiation with a broadband spectrum and an intensity proportional to the number of electrons N forming the bunch. A clear representation of this traditional phenomenon is schemed in Figure 1.1. This radiation was observed for the first time in 1947 [31, 32]. The intensity profile of this emitted SR represents the longitudinal bunch profile, serving as a tool for longitudinal beam diagnostics [33].

1.2.1.1 Undulators

An undulator consists of a pair of alternating magnets of the same length faced to each other, as seen in Figure 1.2. The electron bunch travels in the sinusoidal periodic magnetic field supplied by the undulator leading to periodic alternating oscillations

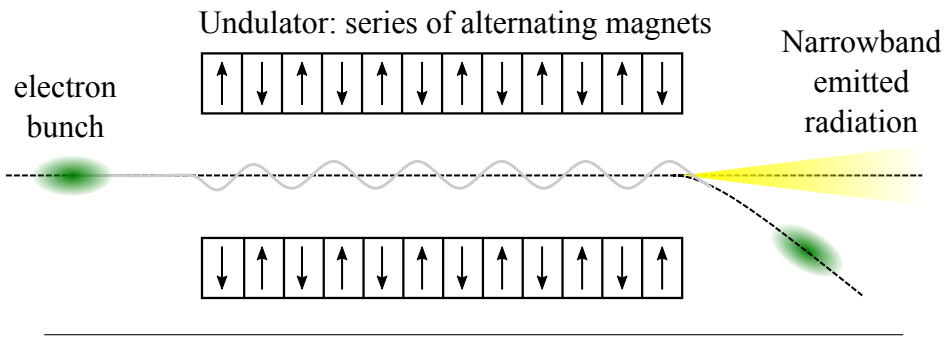

FIGURE 1.2: The electron bunch passes through an undulator, which consists of a pair series of alternating magnets faced to each other. Electrons undergo oscillations due to the periodic magnetic field of magnets and thus emit a narrowband radiation.

at the beam axis. Electrons radiate by spontaneous emission due to this periodic motion of particles and results in the emission of a narrowband radiation with high brilliance, improving the emitted beam quality and intensity with respect to bending magnets [34].
The emitted light wavelength λ depends on the electron energy $E_e = \gamma m_e c^2$ and the undulator parameter K, satisfying the following equation:

$$\lambda = \frac{\lambda_u}{2\gamma^2}(1 + \frac{K^2}{2} + \gamma^2\theta^2) \tag{1.1}$$

where

$$K = \frac{eB\lambda_u}{2\pi m_e c} \tag{1.2}$$

λ_u is the undulator period, B the magnetic field strength, θ the observation angle with respect to the electron beam (this angle is small in the undulator) and γ the relativistic Lorentz factor $\gamma = 1/\sqrt{1 - v^2/c^2}$. K-value is dependent on the magnetic field, and can be modified by adjusting the field strength applied on the undulator axis or by changing the electron beam energy.

1.2.2 Coherent Synchrotron Radiation (CSR)

The total emitted synchrotron radiation (SR), previously discussed, is given by [35]:

$$P(\bar{\nu}) = P_e(\bar{\nu})N_e + P_e N_e(N_e - 1)|f(\bar{\nu})|^2 \tag{1.3}$$

$$= P_{incoherent}(\bar{\nu}) + P_{coherent}(\bar{\nu}) \tag{1.4}$$

with $\bar{\nu}$ the radiation wavenumber, N_e the number of electron forming an electron bunch, P_e the power emitted by a single electron and f the bunch longitudinal form factor[1] expressed by:

$$f(\bar{\nu}) = \int_{-\infty}^{+\infty} e^{i2\pi\bar{\nu}z}\rho(z)\,dz \tag{1.5}$$

where $\rho(z)$ the normalized longitudinal density of the electron.

[1]The bunch form factor of electron bunches is given by the Fourier Transform of the electron beam distribution.

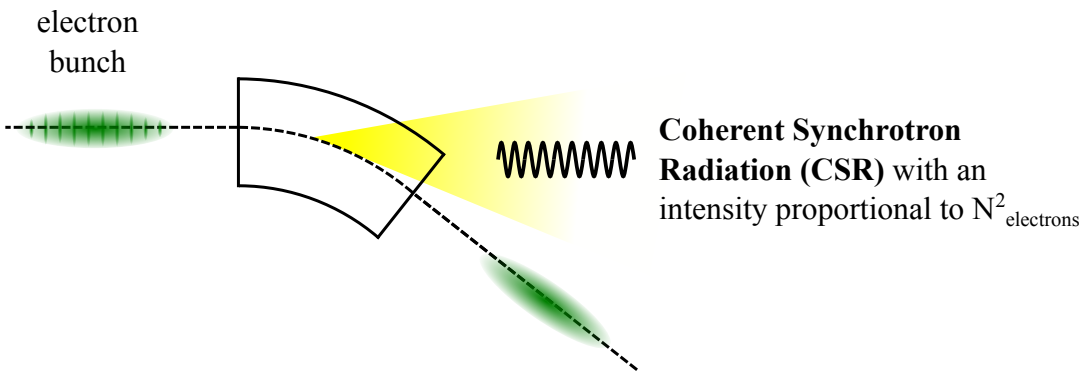

FIGURE 1.3: Emission of coherent synchrotron radiation (CSR) when an electron bunch with microstructures pass through a bending magnet. As electrons emit at longer wavelengths than the bunch length, the total radiation presents a coherent behavior.

The first term describes the incoherent emitted synchrotron radiation showing a linear evolution with the number of electrons, explained in paragraph 1.2.1. The second term corresponds to the *coherent synchrotron radiation (CSR)* with intensity proportional to N_e^2, the square of the number of electrons forming the bunch. This radiation exists only when $f(\bar{\nu}) > 0$. And as N_e is extremely large ($\sim 10^9$ - 10^{10}), this coherent part becomes clearly dominant on the incoherent radiation, even when a small spectral component appears along the longitudinal bunch profile.
The SR emission at long wavelengths (low $\bar{\nu}$ in Figure 1.4(a)) is not transmitted due the shielding of the vacuum chamber [35, 36]. To allow a coherent emission, spectral components should appear in the Fourier Transform at higher frequencies either by microbunching instability (will be detailed in next paragraph) as in Figure 1.4(b) when microstructures result in fast oscillations appearing along the electron bunch density or by using short electron bunches (below the shielding cutoff) [37, 38] as in Figure 1.4(c) where the spectral emission occurs over a large band of frequencies or even using laser bunch slicing [39]. This coherence enhances enormously the power of the emitted radiation.

CSR was first observed in 1989 [40] and in 1999 at NSLS VUV (National Synchrotron Light Source Vacuum Ultraviolet) [41, 42] and the investigation of CSR became experimentally possible in the 2000's where electron bunches were stored in storage rings. Thereafter, stable CSR was generated with the use of short bunches at BESSY [38] and at ANKA later [43]. Many experiments were performed after at different facilities, allowing to observe and measure CSR microbunching instability [44–53] with active investigations in many storage rings [42, 44, 46, 47, 50, 51, 54–57].

We will focus, in the next paragraph, on the CSR emitted by the microbunching instability as this will be a one of the THz sources where we will perform the experiment described in Chapter 5.

1.2.2.1 Microbunching instability: a source of CSR

Above a certain beam current, electrons interact with their own emitted radiation, causing "collective effects" [58]. This effect results in the formation of microstructures longitudinally along the bunch in the mm scale, as represented in Figure 1.3.

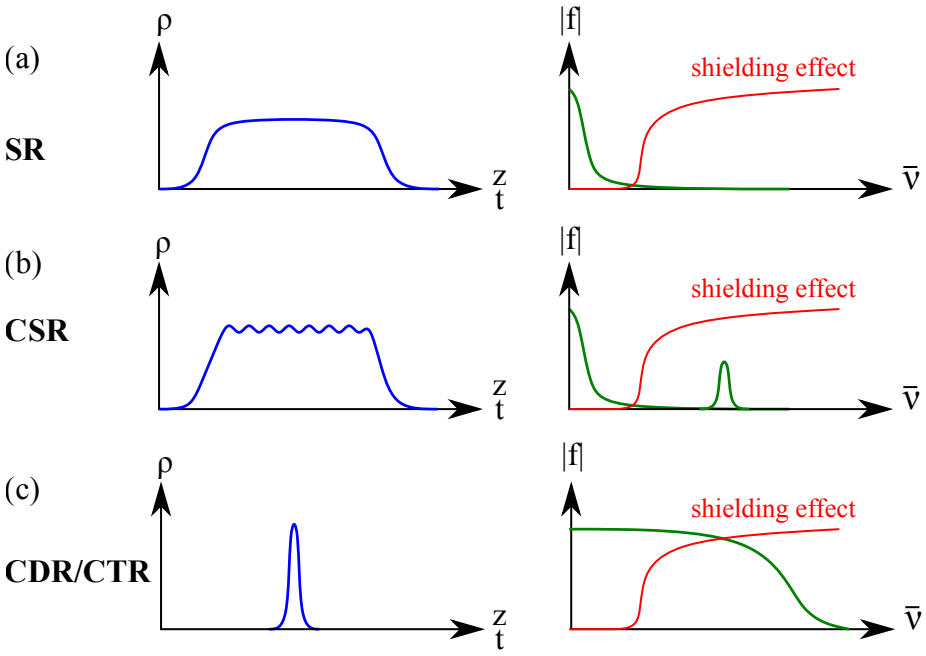

FIGURE 1.4: Spectral emission properties (in green) of synchrotron radiation emission for configurations of electron bunches distributions (in blue): (a) electron bunch distribution for an emission by a magnetic field resulting in a broadband spectrum at long wavelengths. This emission is suppressed by the shielding of the vacuum chamber. (b) Small modulations in the electron bunch distribution result in the emission of a transmittable frequency out of the chamber. (c) Short electron bunches with broadband spectrum at high frequencies engender high spectral components resulting in an emission of a coherent synchrotron radiation (CSR).

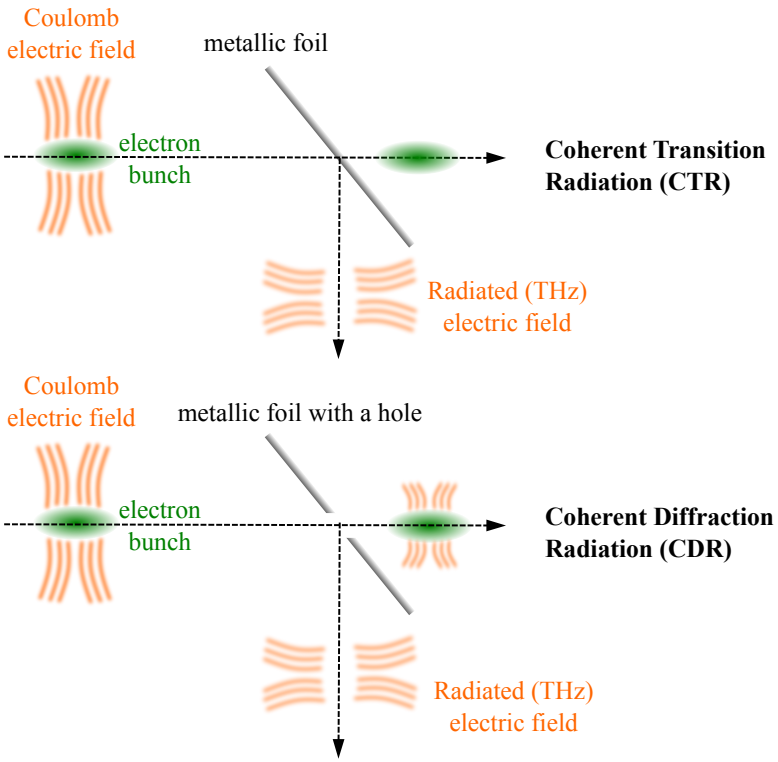

FIGURE 1.5: (a) Generation of Coherent Transition Radiation (CTR) by placing a metallic foil on the electron beam path resulting in the generation of a coherent radiation revealing the characteristics of the electron bunch profile.(b) Generation of Coherent Diffraction Radiation (CDR) operating similarly to CTR with the presence of a hole in the foil allowing the electron bunch to continue its path with a smaller perturbation with respect to the CTR.

As these microstructures are short, they emit radiation coherently with an intensity quadratically proportional to the number of electrons inside the bunch. This effect, known as *microbunching instability* [59, 60], can occur in storage rings, particularly in high-brightness electron storage rings and it is a source of coherent synchrotron radiation (CSR), as represented in Figure 1.3.

This phenomenon has been of particular scientific interest due to its dual nature, being both a limitation and serving a source of coherent THz radiation, typically $10^4 - 10^5$ times more intense than incoherent synchrotron radiation. Consequently, this duality has motivated researchers to delve into a thorough investigation of this phenomenon by conducting theoretical studies and simulations on the CSR or microbunching instability to simulate CSR formations and predict thresholds using the Vlasov-Fokker-Planck equation or the particle tracking approach [59–61] [62–65]. Many techniques such as feedback control system [66] and elimination of collective effect have been developed to eliminate this instability effect.

1.2.3 Coherent transition radiation and coherent diffraction radiation

When a charged particle passes by an inhomogeneity such as a medium, it encounters a change in the electromagnetic properties of its surroundings and the field carried by the particle induces alternating currents or polarizations in the medium,

giving arise to an emission of electromagnetic radiation [67].

Based on this concept, techniques such as transition radiation and diffraction radiation are used as sources of radiation.

In practical, the generation of transition radiation is done by placing a metallic foil on the electron bunch, as shown in Figure 1.5(a). The electron bunch sets up currents in the metallic foil which re-radiate the induced field reflecting the electron bunch properties. One can measure then the reflected emitted radiation.

Diffraction radiation operates similarly to transition radiation with the difference that the charged particle or the electron bunch travels through a slit or an aperture of a screen placed on its path as in Figure 1.5(b). The electric field is deflected in this case and the electrons continue their path without interception.

When the electron bunch length is shorter or comparable to the emitted radiation wavelength, electrons emit coherently, leading to a coherent transition radiation (CTR) as seen in Figure 1.5(a) or equivalently to a coherent diffraction radiation (CDR) as seen in Figure 1.5(b).

CTR and CDR provide a broadband source of THz and are commonly employed as a tool to monitor the transverse and longitudinal parameters of a charged beam. The spectral distribution of the emitted radiation represents the distribution of electrons within the bunch, providing valuable information for characterizing the bunch. The intensity of the emitted radiation is directly related to the current density of the bunch, allowing to deduce the information on the electron bunch longitudinal distribution profile.

CTR has been served, mostly in linacs, for analyzing the longitudinal bunch shape [68, 69]. Even though, this technique allows the generation of a coherent radiation, the interaction with the metallic foil has a destructive effect on the electron beam. Alternatively, CDR is a non-destructive technique offering a minimal perturbation and non-invasive nature [70], and is commonly used for longitudinal bunch profile measurements [71, 72].

1.2.4 Free-electron laser (FEL) operating principle

We have seen, in paragraph 1.2.1.1, that an electron bunch travelling in an undulator emits an electromagnetic radiation incoherently due to spontaneous emission. The configuration of an electron bunch travelling in an undulator can also operate as an amplifying medium for an external electromagnetic wave, as seen in Figure 1.6 where the light pulse propagates with the electron bunch all along the undulator. The electron bunch provides a gain and transfer a part of its energy for the electromagnetic wave that gets amplified. In this case, the electron bunch will emit not only due to the undulator field but also in the electromagnetic wave field due to stimulated emission.

This is the concept of a *free-electron laser* (FEL) which is a type of laser where high energy electrons traveling through an undulator are used as the amplification medium to generate a coherent monochromatic radiation at a wavelength defined by Eq. 1.1. The first operation of a FEL started in 1977 [73].

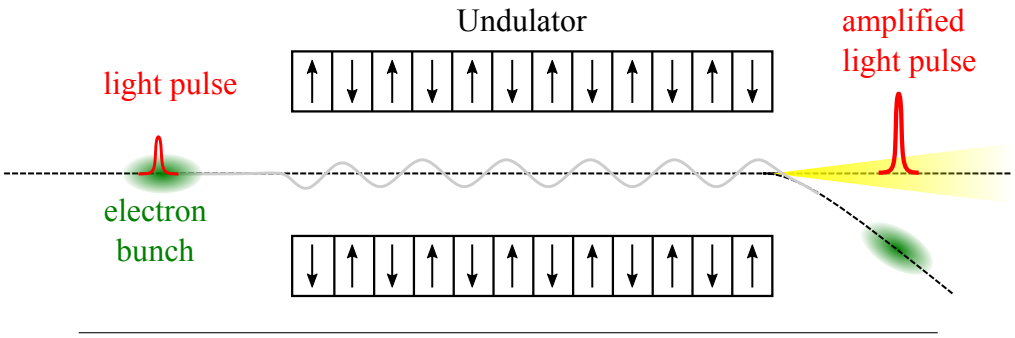

FIGURE 1.6: Electrons in Figure 1.2 emit due the magnetic field of the undulator. When a laser pulse is sent with the electron bunch, the electron beam not only due to the periodic magnet field but also due to the electromagnetic wave by stimulated emission and thus giving part of its energy to the laser pulse getting amplified.

The operation can be through a single passage of the electron bunch in a long undulator as in Figure 1.6 or an undulator within a resonant optical cavity, as in Figure 1.7.

An electron bunch travelling through a long undulator in a single pass can also operate as an amplifier for its own emitted radiation which is the case of a self-amplified spontaneous emission (SASE) FEL, where the spontaneous emitted radiation, travelling in a long undulator gets amplified and results in a coherent radiation.
Another type of FELs is the oscillator FEL based on a resonant optical cavity where the FEL generates its own radiation with the electron bunch wiggling in the undulator and trapped in its resonant cavity. The generated light interacts with the electron bunch and undergoes stimulated emission at each turn, resulting in the production of intense and coherent radiation.

In both operating modes, the emitted photons, in phase with the radiation field, are amplified by extracting energy from the electron bunch and results in an emission of a coherent radiation.

We will focus in this next paragraph on the oscillator FEL, which is the case of the FEL at ELBE where we will perform some THz measurements.

1.2.4.1 FEL with an optical resonator cavity: Oscillator FEL

The system described in Figure 1.6 is implemented into a laser system to store the electromagnetic wave in an optical resonant cavity. Electrons are then injected in a laser cavity formed of an undulator and an optical resonator as seen in Figure 1.7. In this way, the electron beam can give continuously its energy to the electromagnetic wave. The amplified photons are reflected back and forth in an optical resonator, made of a pair of mirrors. One of the mirrors of the cavity has an outcoupling hole to allow the bunch to exit the cavity. The mirror positions are adjusted so that the round-trip of the generated radiation coincides with the next electron bunch arriving at the entrance of the undulator. This synchronization is important to allow stimulated emission and amplify correctly the radiation to result in intense coherent light pulses.

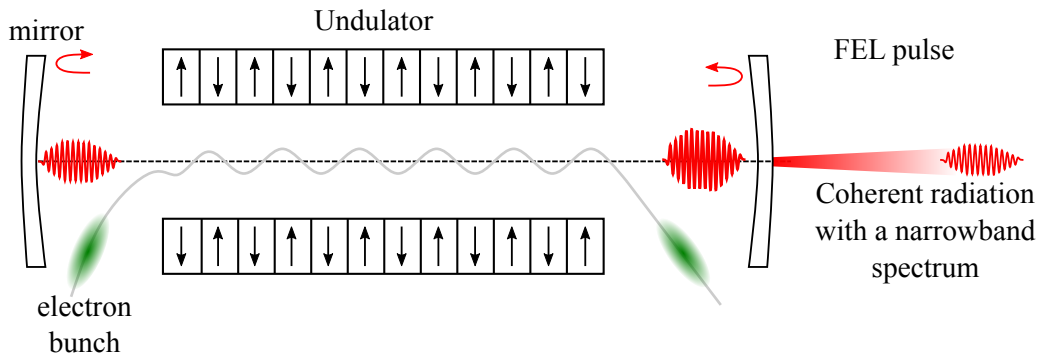

FIGURE 1.7: FEL operational principle: the previous system in Figure 1.6 is placed in a resonant cavity where the electron bunch gives it energy continuously to the light pulse trapped inside. This results in an emission of an intense coherent narrowband radiation.

1.3 Need for single-shot longitudinal beam diagnostics in accelerators

The operation of electron accelerators-based light sources requires advanced ultrafast longitudinal diagnostic tools to characterize electron bunches and measure their longitudinal bunch shapes. The time scales of these relativistic electron bunches with femtoseconds or picoseconds duration make their detection challenging, demanding diagnostics tools with THz bandwidths. Moreover, diagnostic tools are needed to characterize THz light sources such as CSR, CDR, CTR, FEL, etc.

In the last recent years, there have been many studies to measure the longitudinal bunch shapes and temporal profiles. A common used technique, called electro-optic sampling (EOS), consists in probing the electric field of electron bunches using a laser probe pulse (this method will be detailed in section 2.2).

A first approach of applying this technique can be done in the near field by placing an electro-optic crystal inside the tunnel in the vicinity of the electron beam and probe the Coulomb electric field of the electron bunch, as depicted in Figure 1.8(a).

A second strategy involves measuring, in the far-field, the THz radiation emitted by these relativistic electrons using THz detection systems, as illustrated in Figure 1.8(b) [69, 74]. THz sources such as CSR, CDR, CTR, etc. emitted radiation present viable diagnostics tools to provide information on the electron bunch profile.

EOS measurements started in 1982 for characterizing ultrafast electric transient signals in semiconductors [75, 76]. The first single-shot EO operation was done in 1998 to measure a THz pulse generated by a laser [77].
This EOS technique was applied for the first time in the realm of accelerators in the near-field at FELIX [78] to measure the electron bunch shapes. Many facilities introduced this technique to characterize electron bunches in the near-field and in the far field [7, 52, 79–82].

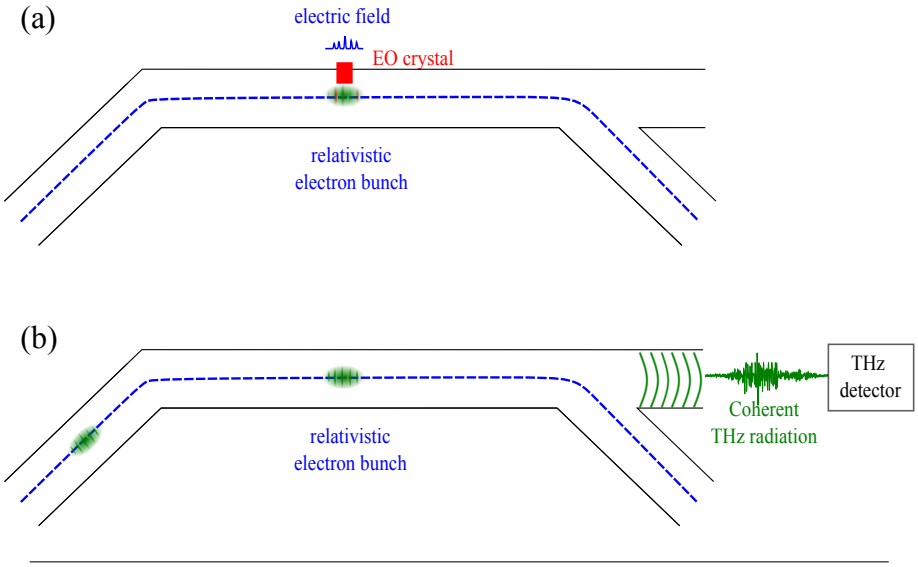

FIGURE 1.8: (a) Near-field diagnostic of electron bunches in accelerators. An electro-optic (EO) crystal is placed in the vicinity of electrons inside the vacuum chamber. By EO effect, this technique allows monitoring electron bunch shapes. (b) Far-field THz detection of relativistic electron bunches. This can be done by probing the radiation emitted by electrons reflecting the properties of electron bunches.

Then the question of single-shot measurements was opened, specially the need for nondestructive measurements. This is particularly necessary to allow an accurate capture and study shot by shot the electron beam dynamics.

Wilke *et al.* demonstrated the feasibility of near-field single-shot EOS for electron bunch measurements in the linear accelerator FELIX FEL facility [6]. The first far-field EOSD measurements were performed at SLS using laser bunch slicing [83] and for CSR measurements [8]. Single-shot measurements of near-field measurements were possible for the first time at the ANKA storage ring (KARA) by placing an EO crystal in vicinity of electron bunches [33].

The high repetition rates in accelerators-driven light sources has pushed researchers to upgrade single-shot EOS based diagnostic tools to achieve acquisition rates up to revolution frequencies in accelerators in the order of MHz (this challenge will be detailed in Chapter 2). The first demonstrations of MHz acquisition rate single-shot EOS have been performed independently by the KIT-DESY and PhLAM-SOLEIL collaborations, using different strategies [9, 10, 84].

Existing detectors still present limitations and encounter tradeoffs in terms of single-shot operation, acquisition rates, sufficient temporal resolution and sensitivity. The specificities and challenges of these measurements will be described gradually in Chapter 2.

The main work of this thesis is to develop a single-shot diagnostic tool based on electro-optic sampling that overcomes existing THz single-shot tradeoffs capable of reaching repetition rates in the order of MHz and provide non-destructive recordings of THz signals.

Chapter 2

Fundamental methodologies for THz detection

2.1 Introduction

This chapter gives an overview of the fundamental methodologies employed for the development of our single-shot THz-TDS (Terahertz Time-Domain Spectroscopy) based detector explaining their operating principles and limitations. We begin by introducing the most popular technique for THz detection, the so-called electro-optic sampling, and its single-shot versions. A special emphasis will be dedicated to the spectrally encoded electro-optic sampling on which is based our detector to enable a single-shot operation and allow real-time measurements. To reach high repetition rates and overcome speeds of commercial cameras, we integrate the so-called photonic time-stretch concept into the single-shot electro-optic sampling setup. Furthermore, we incorporate a balanced detection scheme, a commonly used noise reduction technique to improve sensitivity. Thereafter, we will discuss the limitation on temporal resolution by defining the transfer functions of the detection system and introduce the phase diversity strategy that will overcome constraints and lead to a sufficient sub-ps temporal resolution. Each method offers a specific property, the combination on which will lead to the development of a single-shot THz oscilloscope with a high acquisition rate.

2.2 Electro-optic sampling (EOS) and its single-shot versions

2.2.1 Classical (non single-shot) electro-optic sampling

Electro-optic sampling (EOS) is a popular detection technique capable of measuring temporal evolution of electric fields, up to THz signals. It is based on the electro-optic effect or Pockels effect, stipulating that when an electric field is applied to an isotropic electro-optic (EO) crystal, it modifies its optical properties by creating a birefringence equivalent to the electric field. More precisely, the electric field causes an anisotropy in the crystal, resulting in two different refractive indices along the slow and fast axes n_s and n_f respectively, both proportional to the applied electric field [1], as represented in Figure 2.1. This birefringence can be probed by sending a laser pulse simultaneously with the THz applied on the EO crystal, as in Figure 2.2. This will modify the laser polarization, usually initially linear, by creating an ellipticity. The phase shift $\Delta\phi_{in}$ between the ordinary and extraordinary components of the probe laser beam is proportional to the THz applied electric field E_{THz}. This phase shift is directly linked to the laser wavelength λ in vacuum, the EO crystal

[1] A full mathematically study can be found in [85].

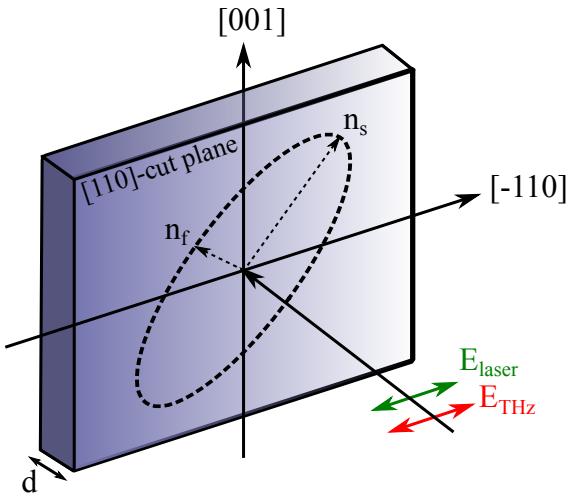

FIGURE 2.1: Electro-optic crystal with a [110]-cut plane and a thickness d on which the laser electric field and the THz electric field are sent parallel to each other and parallel to the [-110], perpendicularly to the (110)-plane. This induces a birefringence in the crystal inducing two indices of refraction n_s and n_f along the slow and the fast axis. Note that this representation is for the classic electro-optic configuration where the angle between the THz field and the [-110] crystal axis $\alpha = 0$.

thickness d and electro-optic coefficient r_{41} and to the untroubled refractive index n_0 by [7, 86]:

$$\Delta\phi_{in}(t) = \frac{2\pi d}{\lambda}\Delta n = \frac{2\pi d}{\lambda}|n_f - n_s| = \frac{\pi d}{\lambda} n_0^3 r_{41}\sqrt{1+3cos^2\alpha}E_{THz}(t) \quad (2.1)$$

$$= \beta E_{THz}(t) \quad (2.2)$$

where α is the orientation of the THz field with respect to the [-110] direction of the EO crystal.
The coefficient β depends on the relative orientations of the crystal axes and on the polarizations of the laser and THz field.

When no electric field is applied, $n_s = n_f = n_0$.
In the standard EOS configuration, the THz is sent parallel to the [-110] crystallographic axis, i.e. $\alpha = 0$ as in Figure 2.1, and β is equal to:

$$\beta = \frac{2\pi d}{\lambda} n_0^3 r_{41} \quad (2.3)$$

This induced ellipticity or polarization modulation is converted into an intensity modulation with the use of a quarter wave plate (QWP) and a polarizer so that it can be detected by a photodetector (see Figure 2.2).
This technique scans the time delay between the laser pulse and the studied THz signal and the acquisition is made in consecutive recordings enabling to cover each portion of the THz signal and thereby provide the full information on the THz electric field. The resolution of detection is limited by the duration of the laser probe pulse T_0 and the EO crystal properties. The EO crystal efficiency is limited by phonon resonances frequencies f_0, summarized for each crystal in Table 2.1, around

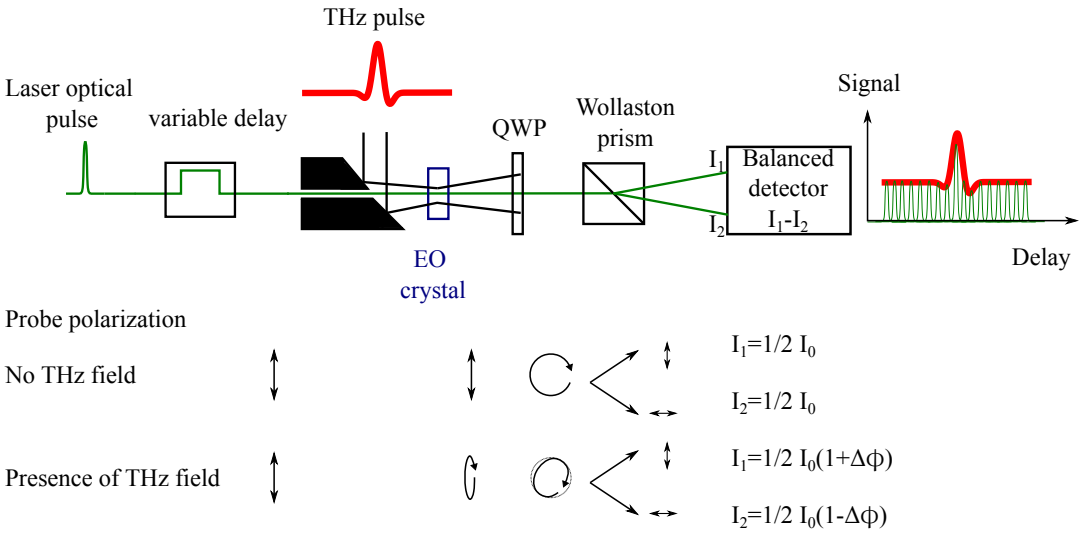

FIGURE 2.2: Classical electro-optic (EO) sampling operating scheme: the THz signal under interest is sent to an EO crystal. This electric field induces a birefringence in the crystal that will change the laser probe pulse polarization, initially linear, by creating an ellipticity that will be transformed to an intensity modulation with the use of a quarter wave plate (QWP) and a polarizer. This technique uses a mechanical delay stage to vary the time interval between the THz and the laser pulses and scan the complete electric field of the THz signal.

EO crystal	f_0 **(THz)**	**Detection wavelength (nm)**
ZnTe	5.3	800
GaP	10.98	1060
GaAs	8.025	1550

TABLE 2.1: Suitable EO crystals according to laser wavelengths with f_0 the frequency of phonon resonance in the THz range.

which strong absorptions are defined in the crystal lattice. Thereby, this technique enables the electric field to be measured completely with a sub-picosecond temporal resolution [78, 87, 88].

For an optimal EO effect with a maximal $\Delta\phi_{in}(t)$, α should be null, according to Eq. 2.2, which means that the THz signal and the laser probe pulse are aligned parallelly to the [-110] axis of the crystal, as in Figure 2.1. The selection of the appropriate EO crystal usually with a zinc blende symmetry such as Zinc telluride (ZnTe), Gallium arsenide (GaAs), Gallium phosphide (GaP), ... is critical to achieve a phase matching condition between the laser and the THz signals. This choice depends on factors such as the laser wavelength and the frequency of the THz signal being measured. This is of high-importance as it presents a trade-off between sensitivity and frequency response: thinner EO sensors provide a broader frequency response, reaching a wider range of THz frequencies, but results in a lower sensitivity due to the shorter interaction distance. On the other hand, thicker EO crystals offer higher sensitivity but at the expense of a reduced bandwidth due to the group velocity dispersion. A more detailed study of the selection of the EO crystal can be found in Appendix A and the appropriate EO crystal choices are summarized in Table 2.1

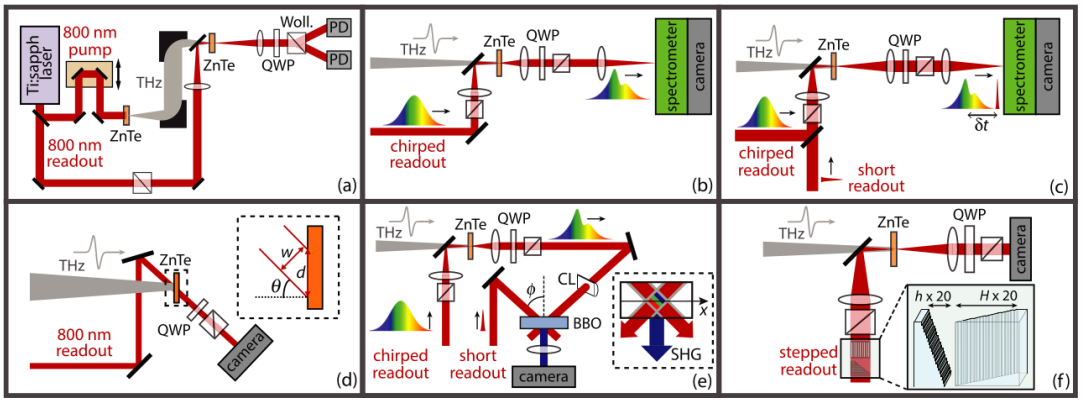

FIGURE 2.3: Single-shot electro-optic sampling (EOS) THz detection techniques: (a) Classical EOS. (b) Spectral encoding EOS using chirped laser pulses. (c) Amplitude encoding spectral interferometry using a chirped laser pulse and a short laser pulse having a time delay between each other. (d) Time-to-space encoding with non-collinear crossing or tilted geometry. (e) Time-to-space encoding with second harmonic generation cross correlation. (f) Time-to-angle mapping encoding with transmissive dual echelons. Figure taken from [93].

according to the most adapted laser wavelength detection.

The application of EOS initially focused on the measurement of ultrafast repetitive transient electric signals [76, 89], on THz characterization [87], and found applications in various fields such as spectroscopy [90], tomography [91] and imaging [92]. In the field of accelerators, this technique helped in measuring relativistic electron pulses at FELIX [78] and has been tested as well in storage ring using laser bunch slicing [52].

While classical EOS allows the measurement of ultrashort signals with picoseconds and femtosecond resolutions [78], it can be only applied to stable and repetitive THz signals. Moreover, this technique is time-consuming, limited by the varying speed of the delay and does not provide immediate access to the complete information on the electric field. This impracticality becomes evident when dealing with low-repetitive or non-repetitive events and physical irreversible phenomena in fast THz spectroscopy experiments. More particularly, it fails to meet the requirements of real-time measurements in storage rings and FELs to study electron beams dynamics, especially when there is a time jitter between electron bunches. Alternative approaches can be adopted such as parallel detection or multichannel acquisitions to overcome these problems but may be impractical.

We will see in next paragraph, how this technique was adapted in several ways to allow a single-shot operation.

2.2.2 Single-shot EOS methods

Many single-shot methodologies, based on EOS were developed for THz detection [93]. These techniques include three classes: time-to-frequency mapping, time-to-space mapping and time-to-angle mapping.

- time-to-frequency mapping consists in using chirped readout pulses, having a chirp of frequencies versus time. The temporal profile of the THz signal under interest is encoded in the frequency spectrum of the laser pulse. This category includes methods such as :
  - spectral encoding (see Figure 2.3(b)), explained in section 2.3.1
  - photonic time-stretch EOS, detailed in section 2.3.3
  - temporal cross-correlation using linear spectral interferometry [94]: this technique resolves the problem of resolution but requires a high resolution interferometer and a precise alignment for longer temporal window
  - amplitude encoding spectral interferometry (see Figure 2.3(c)): it is limited by the time window duration
- time-to-space mapping consists in using a titled optical readout and map the THz signal on it. It includes:
  - Non-collinear crossing (see Figure 2.3(d)): this technique consists in encoding transversely the information under interest, making it less sensitive compared to other methods. The acquisition rate is limited by the speed of commercial cameras
  - Non-collinear SHG cross correlation, with non-collinear geometry or collinear tilted optical readout intensity front, with time domain non-collinear second-harmonic cross-correlation (see Figure 2.3(e))

    Schemes of these techniques make it complicated to implement balanced detection configuration needed for a better SNR.
- time-to-angle mapping (see Figure 2.3(f)) consists in encoding with transmissive dual echelons [95]. It involves some requirements on the thickness and quality of optics.

Among all these techniques and others, methods in Figure 2.3(d)(e)(f), in addition to their limitations, present low acquisition rates due to camera speeds. Thereby, we opted for spectral encoding EOS using chirped laser pulses, as this technique can be implemented with photonic time-stretch to allow to reach the high repetition rates (MHz) involved in storage rings and FELs.

We will focus in the next paragraph on the frequency-to-time mapping spectral encoding EOS using photonic time-stretch to overcome speeds of cameras, keeping aside its temporal resolution limitation that will be discussed in section 2.5.1.

2.3 High repetition rate single-shot EOS based on chirped laser pulses

2.3.1 Basic principle of single-shot EOS based on chirped laser pulses

Electro-optic spectral encoding or decoding (EOSD)[77] is a single-shot technique for THz detection that involves the use of long chirped laser pulses to record the complete THz waveform.

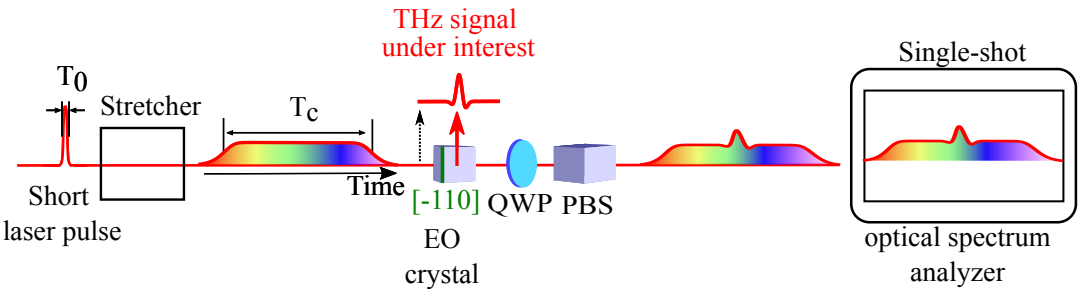

FIGURE 2.4: Schematic of the single-shot electro-optic sampling or spectral encoding electron-optic sampling technique: an upgraded version of classical EOS with a chirped laser pulse. An initial laser pulse is chirped spectrally, defining the acquisition window. The THz signal under interest is encoded on the spectrum of the chirped laser pulse resulting in a polarization modulation, through the Pockels effect. A set of wave plates and a polarizer is used to transform this ellipticity modulation into an intensity modulation. The modulated signal is measured using an optical spectrum analyzer.

By dispersing an ultrashort laser pulse with a certain bandwidth $\Delta\lambda$ in a dispersive medium such as a fiber, a crystal glass, a grating stretcher or a chirped fiber Bragg grating, the different wavelengths of this pulse travel at different velocities, resulting in a ramp of frequencies varying in time, ideally linearly. This results in a longer pulse duration defined by :

$$T_C = D\Delta\lambda \tag{2.4}$$

with D the total dispersion introduced.

When the chirped laser pulse co-propagate with the THz signal (see Figure 2.5), the THz waveform gets encoded onto the chirped spectrum, inducing a birefringence by some amount equivalent to the electric field of the THz signal under interest. A QWP and a polarizer are used to transform the polarization modulation into an intensity modulation. The spectrum of the modulated laser pulse is measured using a spectrum analyzer, as shown in Figure 2.4. The spectrum is measured with and without THz and are then subtracted to extract the information on THz signal electric field. To allow complete single shot measurements, the chirped pulse duration must be longer than the THz pulse duration of interest. More details can be found in [96].

The application of EOSD with chirped laser pulses started in the THz domain to measure transient electric signals with low repetition rates [77, 98] and has demonstrated its value in accelerators for the measurement of temporal profiles and lengths of electron bunches in single shot at FELIX [6] [99] and longitudinal bunch diagnostics at FLASH [7]. It has allowed to monitor the electron bunch length in single shot at SwissFEL [100] and found utility in storage rings for characterizing electron bunches in far field [101] and near-field [33] at KARA. Single-shot measurements of sliced electrons bunches were possible using this technique at Swiss Light Source [8] as well in a recent development, Steffen et al. used this latter technique to develop a very compact electro-optical detection system for single-shot longitudinal monitoring of electron bunch lengths down to 200 fs at accelerators [10].

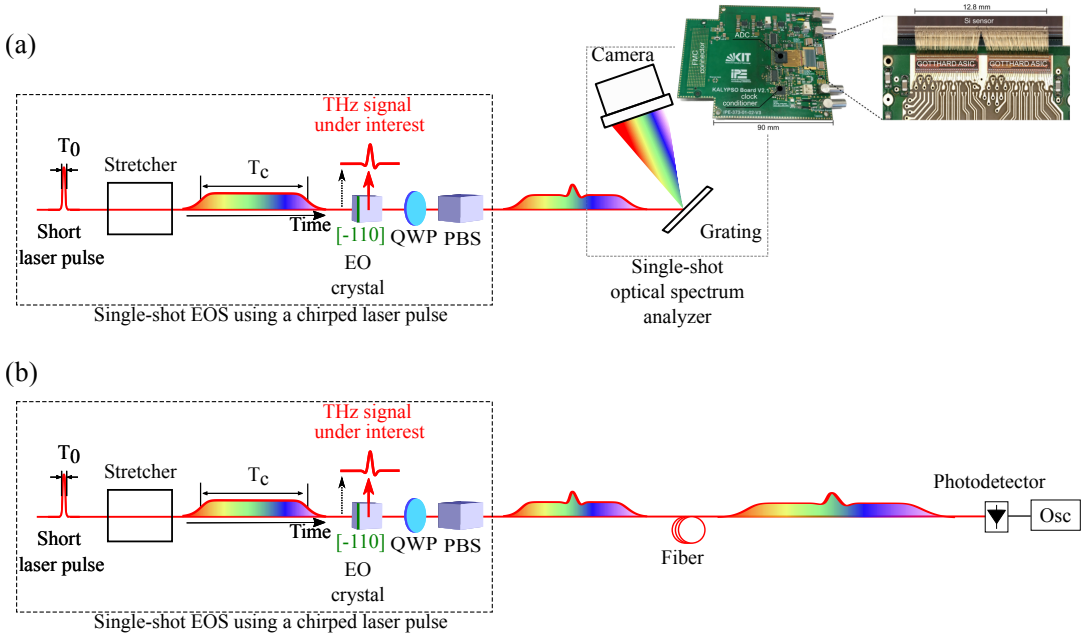

FIGURE 2.5: Schematic of the single-shot electro-optic sampling or spectral encoding electro-optic sampling technique for high acquisition rates: an upgraded version of classical EOS with a chirped laser pulse. An initial laser pulse is chirped spectrally to define the acquisition window, longer than the THz signal. The THz signal under interest is encoded on the spectrum of the chirped laser pulse resulting in a polarization modulation, through the Pockels effect. A set of wave plates and a polarizer is used to transform this ellipticity modulation into an intensity modulation. The output measured modulated spectrum can be analyzed using a grating and an ultrafast camera such as KALYPSO as in (a) or by slowing down the signal before recording it using photonic time-stretch as in (b). (KALYPSO camera photography taken from [97]).

Nevertheless, the use of EOSD imposes a tradeoff with respect to the temporal resolution [102] where a careful consideration on the amount of chirp introduced should be considered taking into account the time constraints imposed by the detector (more details in section 2.5.1).

EOSD-based techniques typically utilize a spectrometer or a diffraction grating along with a camera to analyze the modulated spectrum of the EO signal. However, the use of standard commercial cameras that can typically measure up to few hundreds of kHz restricts the range of EOS applications.
Reaching higher (MHz and above) repetition rates requires specific research on the readout strategies. Two main options have been envisaged. The first option overcome the problem electronically and the second one using photonics.

2.3.2 High repetition rate single-shot EOS: Spectral decoding with ultrafast cameras

To deal with low acquisition rates, a first option involves the development of ultrafast electronic cameras capable of reaching high repetition rates. This is the case of KALYPSO (KArlsruhe Linear arraY detector for MHz-rePetition rate SpectrOscopy), a linear array detector that has been developed at KARA [97, 103, 104] for high repetition rate with an excellent spatial resolution. This advanced detection system offers a 4 MHz frame rate (with a envisaged 12 MHz in the future) in continuous readout mode over long time periods with 512 pixels specifications. This camera meets demands of high-speed EOS applications and enables the capture of fast dynamics. By utilizing advanced cameras like KALYPSO, the utilization of the EO technique can be significantly enhanced, allowing for the measurement and analysis of fast phenomena with higher acquisition rates.

This camera KALYPSO has been installed along with a single-shot EOS scheme to allow measurements of longitudinal charge density profiles of electrons bunches in the near-field at storage ring KARA [105] and for longitudinal bunch studies [106] as well as an EOSD system using KALYPSO allowed to monitor electron bunch profiles in single-shot at the European X-ray Free Electron Laser (XFEL) [10] and FLASH [107].

2.3.3 High repetition rate single-shot EOS with photonic time-stretch

An alternative solution, called photonic time-stretch (PTS), based on photonics can overcome the speed of commercial cameras. This technique consists in manipulating time of ultrafast signals before recording them. This can be done by introducing some dispersion by real-time Fourier transformation, mostly known as Dispersive Fourier Transform [108] using dispersive mediums such as a dispersive fiber or a chirped fiber Bragg grating [109]. As a result, signals get slow down in time and can be recorded using a photodetector and an oscilloscope, as represented in Figure 2.5(b).

Associated with single-shot EOS as in Figure 2.6, photonic time-stretch is performed in several steps: femtosecond laser pulses are chirped in a dispersive medium with a dispersion D_1, here a fiber with length L_1 so that their durations

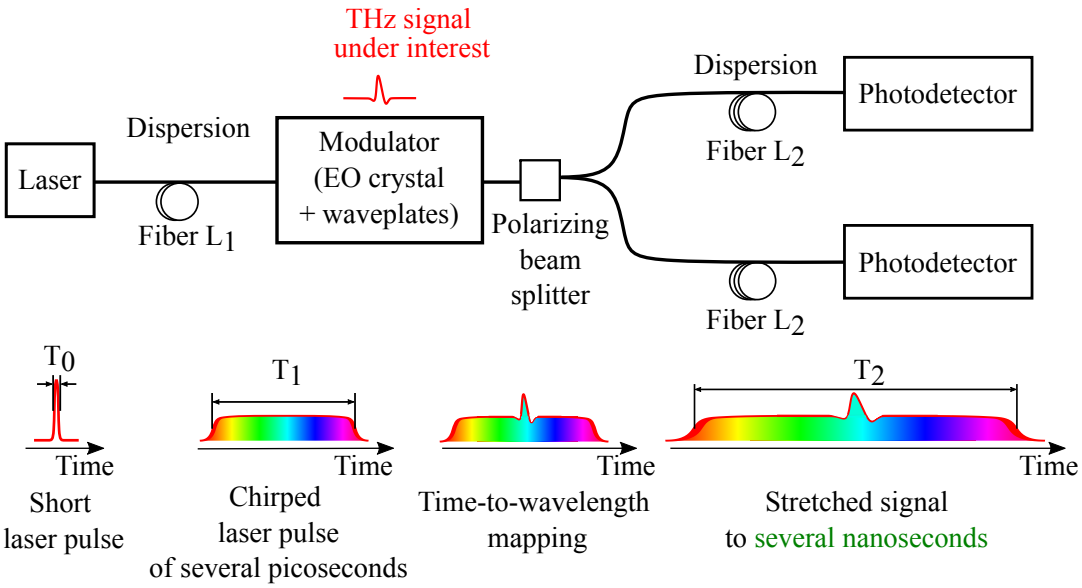

FIGURE 2.6: Concept of photonic time-stretch combined with electro-optic sampling: a pre-chirped laser pulse is spectrally modulated by the THz signal. A second dispersion is introduced by sending the modulated signal in a very long fiber so it gets slow down in time and can be recorded by a photodetector and an oscilloscope.

become in the order of picoseconds. The electric field of the THz signal under interest is encoded into the chirped laser pulse by EO effect. The modulated laser pulse is then sent in long fiber of length L_2 with some dispersion D_2. In this way, the pulse is stretched from picoseconds to several nanoseconds and can be recorded by a photodetector and an oscilloscope.
The detected output signal is a replica of the modulated input pulse, slowed down by a stretch factor or magnification factor M defined by [110]:

$$M = 1 + D_2/D_1 \tag{2.5}$$

with D_1 and D_2, the respective total dispersion before and after EOS. Both the chirped laser pulse and the THz signal are slow down in time.

For the case of fibers (such as dispersion-compensating fiber, etc.), the amount of dispersion introduced in a fiber results in a pulse stretched to a duration T_C defined by :

$$T_C = D_t \Delta\lambda = DL\Delta\lambda \tag{2.6}$$

where D is the dispersion of the fiber and L the length of the fiber and $\Delta\lambda$ the spectral width of the laser. The dispersive fiber decodes the spectrum of a pulse into a time domain waveform using chromatic dispersion, offering high dispersion with low losses.
Equivalently :

$$M = 1 + \frac{L_2}{L_1} = \frac{T_2}{T_1} = \frac{f_1}{f_2} \tag{2.7}$$

with L_1 and L_2 the total fiber before and after EOS, respectively. L_1 defines the recording window, and the fiber L_2 slows down the signal. In most cases for THz signals, $L_2 >> L_1$ and $D_2 >> D_1$.

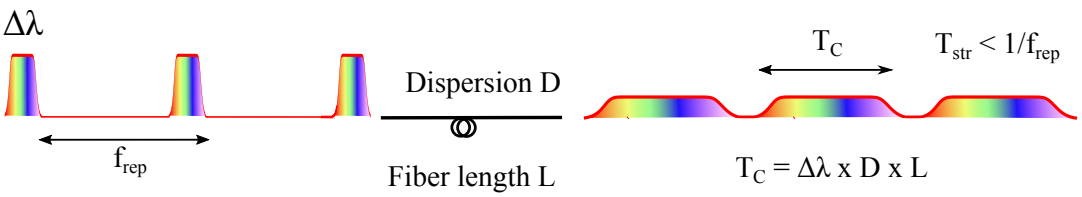

FIGURE 2.7: Schematic diagram representing the conditions on photonic time-stretch: It is crucial that the dispersion introduced by a fiber does not result in an overlap between successive laser pulses.

As an example, if $L_1 = 16$ m and $L_2 = 4$ km, then $M = 250$, which means that 4 GHz detected on the oscilloscope corresponds to 1 THz at the input.

The use of PTS allows replacing the diffraction grating and the camera in Figure 2.5(a) array by a fast photodetector and an oscilloscope, typically with multi-GHz bandwidth as in Figure 2.5(b) and overcome speed limitation of commercial existing detectors.

PTS was firstly concepted for increasing bandwidth of analog-to-digital converters for electronic signals in 1998 [111, 112] [110, 113]. It was introduced with single-shot EOS after for THz measurements in accelerators [9, 114, 115] and recently for table-top THz experiments [109, 116–118].

Important parameters need to be taken in consideration when using PTS such as the pulse bandwidth, the pulse duration, the repetition rate and the amount of introduced dispersion. In terms of stretch, one would like to stretch as much as possible to reach a higher sampling rate and to minimize the required bandwidth detection. However, many effects can be limiting as pulses overlapping and limiting the losses in fibers.

In Figure 2.7, f_{rep} refers to the laser repetition rate, T_c the chirped window duration and D the total temporal dispersion with $D = D_1 + D_2 \sim D_2$ ($D_2 >> D_1$). The pulse repetition rate f_{rep} should be smaller than the pulse duration to avoid overlapping between the stretched consecutive pulses:

$$f_{rep} < 1/T_c \tag{2.8}$$

By means that:

$$f_{rep} D \Delta\lambda < 1 \tag{2.9}$$

For a digitizer with N_{dig} sampling rate, the number of points N to be sampled becomes:

$$N = f_{dig} T_c = f_{dig} D \Delta\lambda \tag{2.10}$$

This defines a maximal number of sampled points by:

$$N < N_{max} = f_{dig}/f_{rep} \tag{2.11}$$

Thereby, when applying photonic time-stretch conditions $f_{rep} D \Delta\lambda < 1$ and $N < N_{max} = f_{dig}/f_{rep}$ should be verified to optimize its performance.

By associating single-shot EOS with PTS, this technique allows to reach high repetition rates and overcome the limitations imposed by commercial cameras and explore new applications and scientific investigations in the field of ultrafast measurements. Real time measurements are possible using acquisition tools such as oscilloscopes or FPGA allowing continuous processing. Nevertheless, this technique requires high bandwidth lasers, commercially limited by existing lasers.

To conclude, we can say that both KALYPSO and PTS allow high acquisition rate. PTS present the advantage to push the acquisition rate to the hundreds of MHz range by using commercial devices and off-the-shelf components. It can be also easily implemented with balanced detection to improve the signal-to-noise ratio. However, single-shot EOS has suffered from the temporal resolution limitation T_R (Eq. (2.12)), until recently [119] (more details in section 2.5.1).

2.4 Single-shot EOS time stretch with balanced detection

Another important property of time-stretch and spectral decoding is the sensitivity, i.e., the lowest electric field that can be measured. A classical way to optimize the sensitivity consists of using a balanced photodetector (see Figure 2.8(b) and (c)), instead of single photodetector as in Figure 2.8(a).

First, it is important to notice that each EO signal (P_1(t) and P_2(t)) are constituted of a small modulation (down to 2% in the case of the SOLEIL experiments in Chapter 5) on top of a laser pulse. The needed information is occupying few number of bins on the digitizer, as seen in Figure 2.8(a) reducing the dynamic range of detection and affecting the signal-to-noise ratio (SNR) of detection. Hence, a first advantage of balanced detection is to remove the unmodulated background P_0(t), so that the ADC bins get exclusively used for resolving the EO signal. A second advantage of the balanced detection is the possibility to cancel out a large part of the probe laser noise (in particular the laser excess noise, and of amplified emission noise when an amplifer is used at the output of the probe laser).

In BD, identical photodiodes or amplified photodetectors are used to detect the two optical signals. The resulting photocurrents generated by these photodiodes are then amplified differentially to produce an electrical signal of the difference between them.

Numerical balanced detection

BD can be performed numerically, as in Figure 2.8(a), by using two identical photodetectors to measure each EOS output corresponding to the two polarization states of the modulated signal. As seen, the recorded signal, amplified by the gain factor G of the detector, includes the full laser pulse with the noise and the THz polarization state. The signal under interest, i.e., the polarizations P_1 and P_2, occupy few number of bins. As the two outputs are recorded separately, the extraction of the important information can be done by a numerical processing to suppress the common laser shape and shot-to-shot fluctuations resulting in the difference between both polarizations or separate subtraction of modulated pulses from

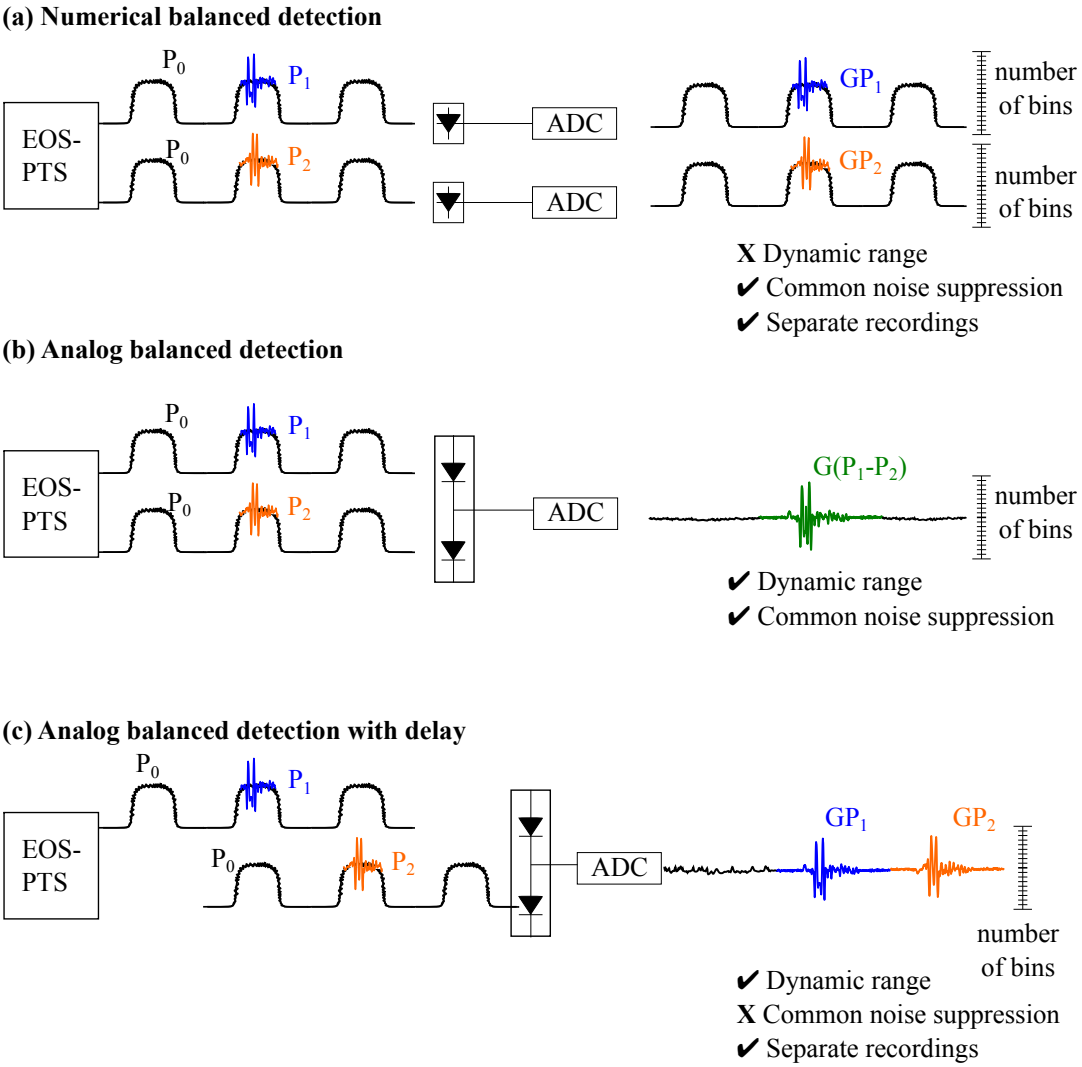

FIGURE 2.8: Balanced detection (BD) implementation methods. (a) Numerical BD performed using two identical photodetectors allowing separate recordings of THz polarization states or a common noise suppression at the expense of a low dynamic range. (b) Analog BD using a balanced detector allowing a common noise suppression with a high dynamic range. (c) Analog BD with adding a delay of one laser period to allow a separate recording of polarization states with a high dynamic range.

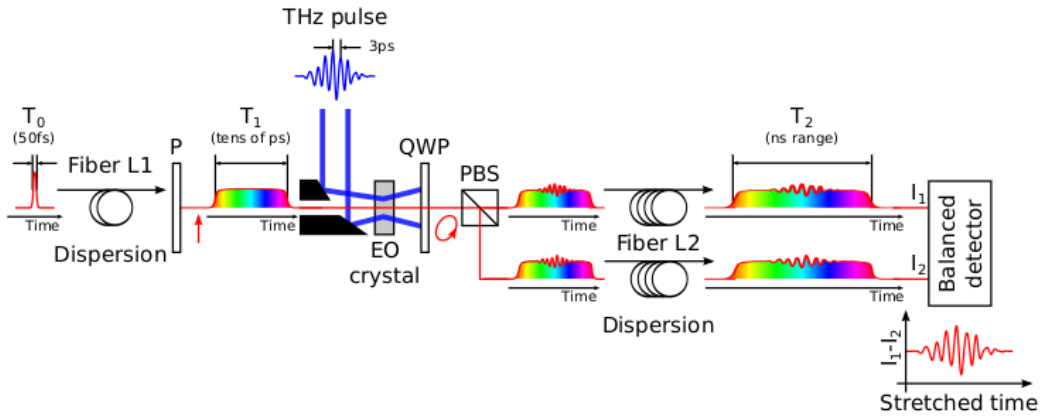

FIGURE 2.9: Concept of balanced detection implemented with single-shot time-stretch electro-optic sampling detection: The two polarization states of the modulated signal are separated using a polarizing beam splitter (PBS), stretched to several nanoseconds and measured with a balanced detector (or separate photodetectors), generating the difference between both inputs with a high dynamic range and a better sensitivity. Figure from [120] using the balanced detection configuration explained in Figure 2.8(b).

unmodulated pulses to eliminate the common laser shape to retrieve two separated information on each polarization state with a better sensitivity. This technique works well but requires a detector with a high resolution which is not the case of ultrafast detectors.

Analog balanced detection

Alternatively, BD can be performed analogically with the use of a balanced detector composed of two photodiodes, as in Figure 2.8(b). In this case, the two input signals are subtracted from each other and the resulting intensity is amplified and can be recorded by an oscilloscope at a higher dynamic range. In this way, the common noises and laser shape are directly suppressed between both arms and the resulted difference is amplified and recorded with a higher dynamic range. This technique allows increasing the SNR and optimizing the dynamic range. The bins ADC are exclusively used for the THz signal. This technique has found a particular interest in THz time-domain spectroscopy (THz-TDS) detection and has been widely adopted in various EOS measurements [9, 114, 121]. However, as simultaneous laser pulses are suppressed from each other, this will give the difference between both polarization states and will not allow to measure both polarizations separately.

Analog balanced detection with delay

As a separate recording of the two polarization states of the THz signal will be needed in our detector (this will be discussed in the next paragraph), the idea is to benefit from the dynamic range and increase the SNR while recording two polarization states separately. To do this, an innovative idea, implemeted in our experimental setup, consists of adding a delay of one laser period on one arm of detection, as schemed in Figure 2.8(c). This will delay the arrival of pulses of this

arm with respect to the other arm. Thereby, the subtraction will occur between different laser pulses. The advantage of this technique is that it allows to record each polarization separately but does not allow removing common laser fluctuations since the subtraction is not effectuated between same laser pulses on both arms.

To achieve optimal BD, it is necessary to have a symmetric wavelength-dependent transmission between both arms to guarantee a good cancelation of the noise. In addition, optical delay lines can be employed to carefully adjust the time delay between both arms and variable optical attenuators can be used to provide equal powers to ensure a better suppression of common signals. In most EO BD experiments, the probe laser pulse is split in two equal beams, with the use of a splitter or a coupler, one serves as a reference and the other carries the encoded information of interest.

Note that this technique can be implemented with photonic time-stretch to allow reaching high repetition rates at high sensitivity [122] but it cannot be implemented with spectrometer, i.e. with spectral encoding EOS.

Until now, we have seen that the combination of single-shot EOS with the photonic time-stretch technique has resolved two main problems: measuring in single-shot and achieving high repetition rates. But this has not mitigated the limitation of temporal resolution. Achieving higher resolutions in single-shot measurements remains a significant challenge for researchers in the field due to the limitations imposed by bandwidth. The bandwidth limitations of electronic components and measurement devices can restrict the ability to accurately capture and analyze ultrafast signals in real-time. In the next section, we will focus on the temporal resolution limitation and discuss the solution to overcome it.

2.5 Numerical reconstruction algorithm using phase diversity (DEOS) for a better temporal resolution

2.5.1 Temporal resolution / bandwidth limitation

While EOSD enables single-shot measurements, the use of a chirped pulse results in a limitation on the temporal resolution compared to conventional EOS. To tackle the question on temporal resolution, let us see how does this property affect measured signals by checking if the output waveform measured by the spectrometer or photodetector corresponds exactly to the input signal (Figure 2.11).

To answer this question, simulations were performed [119] by considering several THz pulse durations and simulating the output spectrum measured by a spectrometer after background subtraction and normalization, as seen in Figure 2.10. It has been approved that for long pulse durations, of 2 ps for example, the output measured signal is accurate and corresponds to the input signal. However, for shorter pulses, some distortions begin to appear in the output spectrum to some point that for ultrashort pulses (250 fs for example), this technique loses totally its reliability to provide the exact THz information.

It turns out that this technique is valuable to a certain limit whereas, above a certain bandwidth or chirp duration, the measured does not correspond to the encoded signal due to distortions appearing as seen in Figure 2.10.

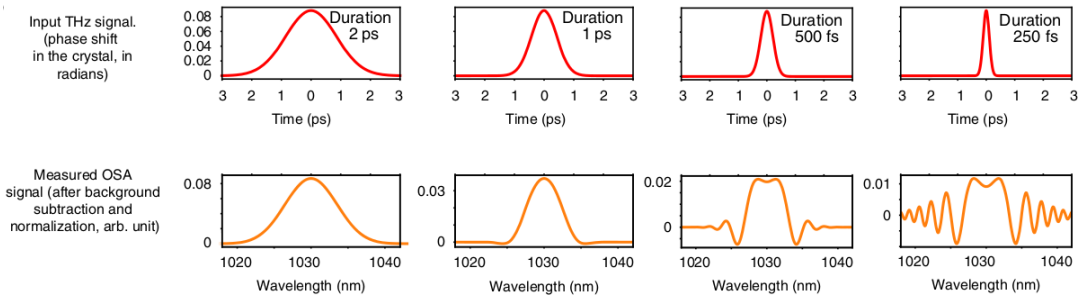

FIGURE 2.10: Simulation of THz measured signals measured by a spectrometer for several THz pulses durations. Output signals are identical for THz pulse duration of 2 ps whereas for short durations, distortions appear in the measured spectrum due to low temporal resolution. Figure taken from [119].

This matter is a problem of temporal resolution known since 1998 [98] that limits the measurement of signals below a certain duration T_R defined by:

$$T_R \approx \sqrt{T_0 T_C} \tag{2.12}$$

where T_0 is the probe laser pulse duration (unchirped pulse duration) and T_C the chirped pulse duration. T_R represents the minimal duration that can be recorded without significant distortion.
As an example, a 100 fs input laser pulse duration, chirped to 10 ps brings about a temporal resolution of 1 ps, which is above the duration of the input pulse. This resolution limitation, commonly faced, has hampered the application range of single-shot EOS.

To solve this obstacle, we will study in the next paragraph the origin of the problem by considering the notion of the transfer function of the system, defined in Figure 2.11, to see what is happening from the input to the output of the detection system, passing by the crystal and waveplates.

2.5.2 Transfer functions of the system

A transfer function defines the relation between the input signal $X(\Omega)$, here the THz signal under investigation, and the output signal $Y(\Omega)$ measured by the detection system, as represented in Figure 2.11, according to the relation applicable in Fourier space, defined by:

$$Y(\Omega) = H(\Omega)X(\Omega) \tag{2.13}$$

where Ω is the frequency in the Fourier space.

To determine this function H, we will consider the classical spectrally encoded EOS, represented in Figure 2.12 and follow step by step the physical phenomena of encoding and recording with a spectrometer. Note that all calculations figuring in this section are summarized and can be found in [119].

Let us consider a linearly chirped laser pulse of the form:

$$E_0(t) = A(t)e^{-i\frac{C}{2}t^2} \tag{2.14}$$

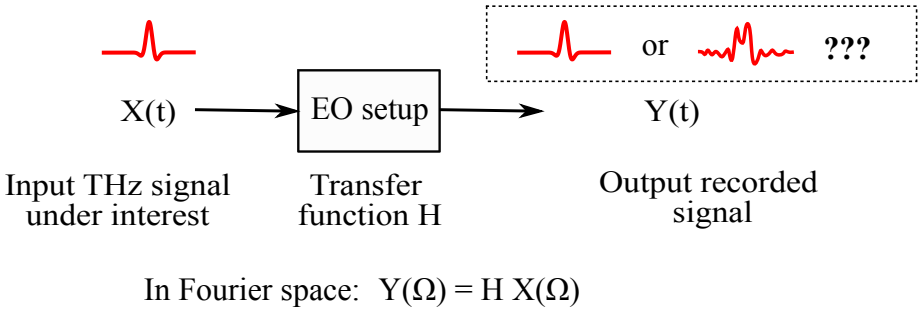

FIGURE 2.11: Transfer function notion defining the relation between the input signal to the output measured signal in Fourier space.

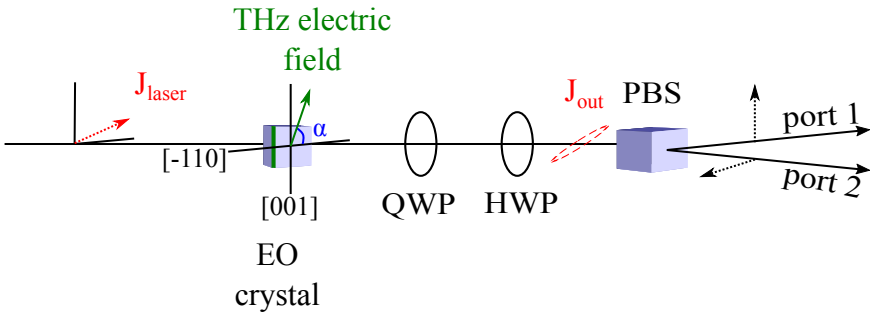

FIGURE 2.12: Classic electro-optic setup arrangement for Jones matrix calculations with two polarizations outputs.

where $A(t)$ is the slowly varying envelope passing over the carrier frequency and $C = \partial\omega/\partial t$ the chirp rate of the laser.

When measured by the spectrometer without any modulation, the observed laser spectrum is defined by the Fourier transform:

$$\tilde{E}_0(\omega) = \int_{-\infty}^{+\infty} A(t) e^{-i\frac{C}{2}t^2} e^{-i\omega t} dt \tag{2.15}$$

where the sign $\sim$ refers to the Fourier transform,
and the resulting detected spectrum is equal to:

$$|\tilde{E}_0(\omega)|^2 = \frac{2\pi}{C} |A(-\frac{\omega}{C})|^2 \tag{2.16}$$

with an established equivalence between the input time t and the output frequency ω defined by:

$$t \equiv -\frac{\omega}{C} \tag{2.17}$$

A detailed demonstration of calculations can be found in the Supplementary Material of [119].

The THz input signal under interest is chosen to be monochromatic, defined by:

$$X_{in}(t) = a\cos(\Omega t + \phi) \tag{2.18}$$

In spectral encoding EOS, the spectrum of the laser pulse is temporally modulated by the applied electric field $X_{in}(t)$ under interest. This induces an amplitude and a phase modulation of the laser pulse, resulting in:

$$E(t) = T(t)E_0(t) \tag{2.19}$$

where $T(t) = T_0[1 + m_a X_{in}(t)]e^{im_\phi X_{in}(t)}$ the transmission function with T_0 generally complex and m_a and m_ϕ the amplitude and phase modulations.
For small modulation, the transmission function can be simplified in the form:

$$T(t) = T_0[1 + me^{i\Psi} X_{in}(t)] \tag{2.20}$$

with $m_a = m\cos\Psi$ and $m_\phi = m\sin\Psi$ with Ψ dependent on the ratio of the EO effect. The modulated laser pulse spectrum is given by:

$$\tilde{E}(\omega) = T_0\tilde{E_0}(\omega) + \int_{-\infty}^{+\infty} T_0 m e^{i\Psi} X_{in}(t)E_0(t)e^{-i\omega t}dt \tag{2.21}$$

and can be simplified by:

$$\tilde{E}(\omega) = T_0\tilde{E_0}(\omega)[1 + me^{i\Psi}e^{i\frac{\Omega^2}{2C}} X_{in}(-\frac{\omega}{C})]. \tag{2.22}$$

The recorded optical spectrum on the spectrometer is $|\tilde{E}(\omega)|^2$. As we are interested in small signal response, the optical spectrum becomes:

$$|\tilde{E}(\omega)|^2 = |T\tilde{E_0}(\omega)|^2[1 + 2m\cos(\Psi + \frac{\Omega^2}{2C})X_{in}(-\frac{\omega}{C})] + O(m^2). \tag{2.23}$$

The output signal, i.e., the measured electro-optic signal, after subtraction and normalization is given by

$$Y(t) \equiv \frac{|\tilde{E}(\omega)|^2 - |T_0\tilde{E_0}(\omega)|^2}{|T_0\tilde{E_0}(\omega)|^2} \tag{2.24}$$

For small input signal $X_{in}(t)$, the output signal becomes:

$$Y(t) \approx 2m\cos(\Psi + \frac{\Omega^2}{2C})X_{in}(t). \tag{2.25}$$

The analogy with Eq. (2.13) implies that the transfer function $H(\Omega)$ is of the form:

$$H(\Omega) = 2m\cos(\Psi + \frac{\Omega^2}{2C}). \tag{2.26}$$

2.5.2.1 Transfer functions in the case of classical EOS configuration

In this paragraph, we derive the transfer functions $H_1(\Omega)$ and $H_2(\Omega)$ in the case of the standard EOS arrangement displayed in Figure 2.13 where:

- The THz field is sent parallel to the [-110] crystallographic, i.e., $\alpha = 0$ with the [-110] axis assumed to be in the horizontal plane for the calculation.
- The birefringence axes of the crystal are at 45° with respect to the horizontal direction ($\psi = 45°$).

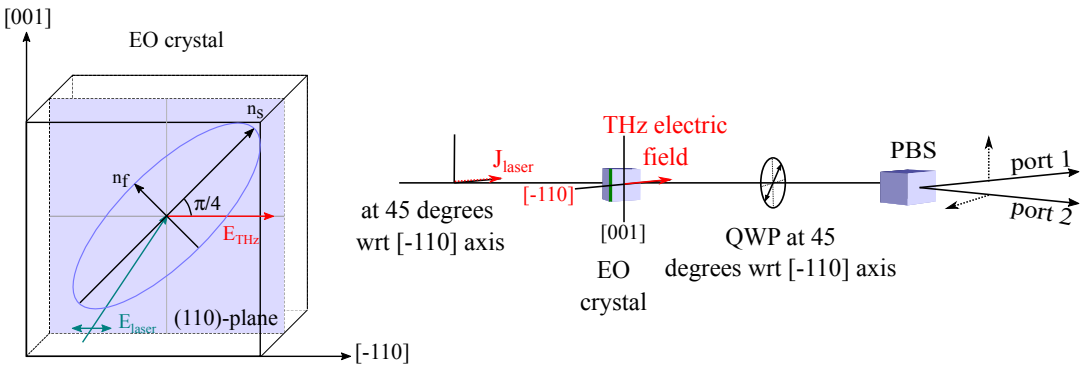

FIGURE 2.13: Optical components orientations for the standard EO sampling: both the laser and the THz electric field polarizations are parallel to the [-110] crystal axis.

- The quarter wave plate axes are at 45° with respect to horizontal, having the same orientation as the crystal birefringence axes.
- The laser polarization is horizontal or vertical.
- The half-wave plate is not needed and can be removed.

For this configuration where $\alpha = 0$, the induced phase shift $\Delta\phi$ is proportional to the THz electric field by Eq. (2.2):

$$\Delta\phi = \Delta\phi^{std} = \frac{2\pi d}{\lambda} n_0^3 r_{41} E_{THz}(t) \tag{2.27}$$

(^{std} stands for the standard EOS configuration).
The Jones matrix of the whole system, skipping the HWP, as in Figure 2.13 can be written:

$$M = M^{std} = R^{-1}(\frac{\pi}{4}) M_{QWP} M_{Xtal} R(\frac{\pi}{4}), \tag{2.28}$$

where M_{QWP} and M_{Xtal} are the Jones matrices of a QWP and of the crystal, respectively and $R()$ the rotational matrix by an angle .
Considering a horizontal laser polarization, the Jones vector of the input laser is:

$$J_{laser}^{std} = E_0(t) \begin{pmatrix} 1 \\ 0 \end{pmatrix} \tag{2.29}$$

where $E_0(t)$ is the complex electric field of the laser.

This results in an output Jones vector J_{out}^{std} that can be written as:

$$\begin{aligned} J_{out}^{std} &= M^{std} J_{laser} = \begin{pmatrix} E_1^{std}(t) \\ E_2^{std}(t) \end{pmatrix} \\ &= \frac{E_0(t)}{\sqrt{2}} \cdot \begin{pmatrix} \cos(\frac{\Delta\phi^{std}(t)}{2}) + \sin(\frac{\Delta\phi^{std}(t)}{2}) \\ i[\cos(\frac{\Delta\phi^{std}(t)}{2}) - \sin(\frac{\Delta\phi^{std}(t)}{2})] \end{pmatrix} \end{aligned} \tag{2.30}$$

Each component of this Jones vector correspond to the complex field of a polarization state that will be recorded by the optical spectrum analyzer.

For a small phase modulation, $\Delta\phi^{std}(t) \ll 1$:

$$\begin{pmatrix} E_1^{std}(t) \\ E_2^{std}(t) \end{pmatrix} \approx \frac{E_0(t)}{\sqrt{2}} \cdot \begin{pmatrix} 1 + \frac{\Delta\phi^{std}(t)}{2} \\ i[1 - \frac{\Delta\phi^{std}(t)}{2}] \end{pmatrix}. \tag{2.31}$$

Corresponding with section 2.5.2, Eq. (2.19) can be written in the form:

$$\begin{pmatrix} E_1^{std}(t) \\ E_2^{std}(t) \end{pmatrix} = E_0(t) \cdot \begin{pmatrix} T_1^{std}(t) \\ T_2^{std}(t) \end{pmatrix} \tag{2.32}$$

defining the two transmission functions, as in Eq. (2.20), by:

$$T_1^{std}(t) = T_{01}[1 + m_1 e^{i\psi_1}\Delta\phi^{std}(t) \tag{2.33}$$

$$T_2^{std}(t) = T_{02}[1 + m_2 e^{i\psi_2}\Delta\phi^{std}(t) \tag{2.34}$$

with $T_{01} = 1/\sqrt{2}$, $T_{02} = i/\sqrt{2}$, $m_1 = 1/2$, $m_2 = -1/2$ and $\psi_{1,2} = 0$.

The two measured optical polarizations are defined, according to Eq. (2.24) by:

$$Y_1(t) \equiv \frac{|\tilde{E_1}^{std}(\omega)|^2 - |T_0\tilde{E_{01}}(\omega)|^2}{|T_{01}\tilde{E_{01}}(\omega)|^2} \tag{2.35}$$

$$Y_2(t) \equiv \frac{|\tilde{E_2}^{std}(\omega)|^2 - |T_0\tilde{E_{02}}(\omega)|^2}{|T_{02}\tilde{E_{02}}(\omega)|^2} \tag{2.36}$$

As the input signal, equivalent to the phase shift $\Delta\phi^{std}(t)$ is linked to the output measured signals by the transfer functions in the Fourier space:

$$\tilde{Y_1}(\Omega) = H_1^{std}(\Omega)\Delta\tilde{\phi}^{std}(\Omega) \tag{2.37}$$

$$\tilde{Y_2}(\Omega) = H_2^{std}(\Omega)\Delta\tilde{\phi}^{std}(\Omega) \tag{2.38}$$

with $\tilde{Y}_{1,2}(\Omega)$ and $\Delta\tilde{\phi}^{std}(\Omega)$ the Fourier transforms of $Y_{1,2}(t)$ and $\Delta\phi^{std}(t)$ respectively.

By corresponding Eq. (2.20) and Eq. (2.26), the transfer functions for the standard EOS can be written:

$$H_1^{std}(\Omega) = \cos(\frac{\Omega^2}{2C}) \tag{2.39}$$

$$H_2^{std}(\Omega) = -\cos(\frac{\Omega^2}{2C}) \tag{2.40}$$

We can see that the transfer functions of the system have the same module and present some zeros at some frequencies as in Figure 2.14. This shows that some information is missing at certain frequencies, leading to the appearance of distortions in the recorded waveforms of output signals. As to retrieve the phase shift $\Delta\phi_{in}(\Omega)(\Delta\phi_{in}(t))$ or equivalently the input signal $E(\Omega)(E(t))$, one needs to divide the output recorded data using a single channel $Y_1(t)$ or $Y_2(t)$ by the transfer functions H_1 and H_2 (division by zero) (Eq. 2.13), it is impossible to retrieve the full information on the THz. These nulls correspond to the dispersion penalty phenomenon, which is observed in the photonic time-stretch digitizer [123].
It limits the bandwidth of the system to the position of the first zero in the transfer

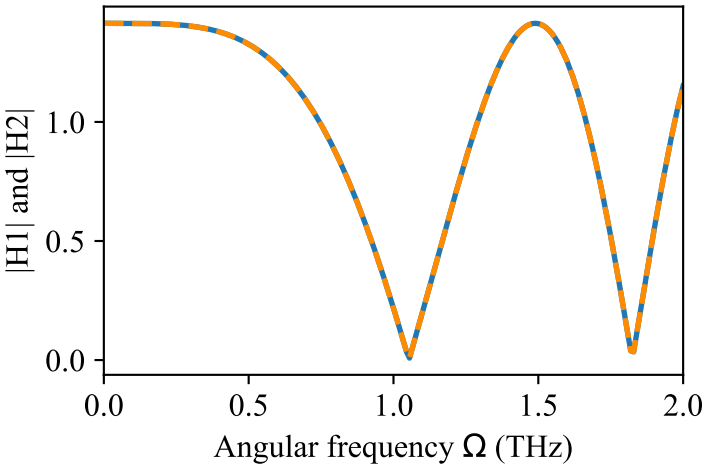

FIGURE 2.14: Norms of the transfer functions $|H_1|$ and $|H_2|$ of the two EO arms in the standard EO configuration ($|H_1^{std}(\Omega)|$ and $|H_2^{std}(\Omega)|$). Both transfer functions are identical and reveal the presence of zeros at some frequencies.

function which is defined according to [110, 124]:

$$|H(f_{THz})|^2 = cos^2(2\pi^2\beta_2 L_1 f_{THz}^2) \tag{2.41}$$

with β_2 the group velocity dispersion of the fiber. It is linked to the dispersion parameter by $D = -2\pi c\beta_2/\lambda^2$. The first zero of the transfer function, and thereby the bandwidth of the detection system is limited to :

$$f_0 = \sqrt{\frac{1}{4\pi\beta_2 L_1}} = \sqrt{\frac{c\Delta\lambda}{2\lambda^2 T_1}} \tag{2.42}$$

The position of this first zero is inversely proportional to the fiber length L_1 before EOS, implying that for longer acquisition windows (chirped pulse duration T_1), the first zero position will shift to shorter frequencies, and thereby reduce the detection bandwidth of the system.

As the input signal cannot be reconstructed by deconvolution, the limitation in temporal resolution persists, reducing single-shot EOS application range.

An alternative technique appeared to resolve the problem, which is the phase diversity. It consists in using diverse information from two measured output signals corresponding to the polarization states of the modulated signal, to have interleaved zeros and allow a deconvolution operation.

2.5.3 Transfer functions in a special EOS configuration: Diversity EOS (DEOS)

As classical EOS does not allow deconvolution, diverse information on the phase is expected to overcome this limitation. This has been previously done in the case of a

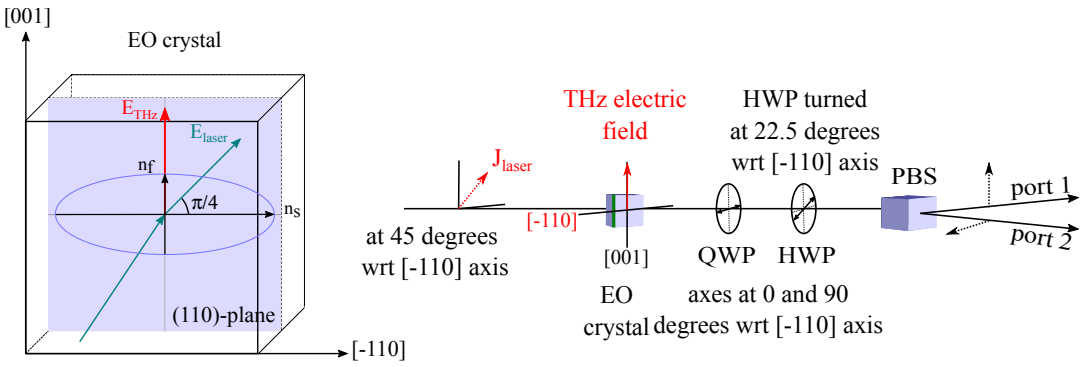

FIGURE 2.15: Optical components orientations for the phase diversity EO sampling: the THz electric field polarization is perpendicular to the [-110] crystal axis and the laser polarization is at 45° with respect to the [-110] crystal axis.

Mach-Zehnder modulator with photonic time-stretch, providing diversity information and allowing to reach high bandwidth detection [123]. Based on this previous work, we consider in this section a special configuration, the diversity electro-optic sampling (DEOS) where the angle $\alpha \neq 0$, i.e. the THz field is not parallel to the [-110] axis of the EO crystal. The value of α, providing a diverse phase, is not unique, but we will limit the study to $\alpha = \pi/2$, where the THz field is perpendicular to the [-110] crystallographic axis. The [-110] is assumed to be horizontal for calculations.
The DEOS scheme is represented in Figure 2.15. A similar reasoning is done as section 2.5.2.1 but for $\alpha = \pi/2$:

- $\psi = 0$, by means that the birefringence axes of the crystal are horizontal and vertical.
- The phase modulations $\phi_1 \neq 0$ and $\phi_2 = 0$.
- The laser polarization is taken at 45° with respect to horizontal, i.e., at 45° from the crystal optical axes.
- The quarter wave plate axes have the same crystal orientations, horizontal and vertical.
- as the detection directions should be at 45° with respect to the input laser polarization, the half-wave is fixed at 22.5° with respect to the horizontal.

The birefringence $\Delta\phi^{phd}$ induced by the electric field in Eq.(2.2) in the case of phase diversity becomes:

$$\Delta\phi^{phd}(t) = \phi_1(t) = \frac{\pi d}{\lambda_0} \cdot n_0^3 r_{41} E_{THz}(t) \tag{2.43}$$

and it is reduced by half compared to the classic EOS configuration where $\alpha = 0$.
The total Jones matrix of the system, represented in Figure 2.15, is :

$$M = M^{phd} = M_{HWP}(\pi/8) M_{QWP} M_{Xtal} \tag{2.44}$$

with :

$$M_{Xtal}^{phd} = M_{\phi}^{phd} = \begin{pmatrix} e^{i\phi_1} & 0 \\ 0 & 1 \end{pmatrix} \tag{2.45}$$

The Jones vector of the input laser is:

$$\mathbf{J}_{laser}^{phd} = E_0(t) \begin{pmatrix} 1/\sqrt{2} \\ 1/\sqrt{2} \end{pmatrix}, \tag{2.46}$$

with $E_0(t)$ the complex electric field of the laser.
The output Jones vector is:

$$\mathbf{J}_{out}^{phd} = \mathbf{M}^{phd}\mathbf{J}_{laser}^{phd} = \begin{pmatrix} E_1^{phd}(t) \\ E_2^{phd}(t) \end{pmatrix} = \frac{E_0(t)}{2\sqrt{2}} \cdot \begin{pmatrix} (1+i)\left(e^{i\Delta\phi^{phd}(t)} - i\right) \\ -(1+i)\left(e^{i\Delta\phi^{phd}(t)} + i\right) \end{pmatrix} \tag{2.47}$$

For small phase modulation $\Delta\phi^{phd}(t) \ll 1$, the two polarization components can be approximated by

$$\begin{pmatrix} E_1^{phd}(t) \\ E_2^{phd}(t) \end{pmatrix} \approx \frac{E_0(t)}{\sqrt{2}} \cdot \begin{pmatrix} 1 + (-1+i)\frac{\Delta\phi^{phd}(t)}{2} \\ -i(1 + (1+i)\frac{\Delta\phi^{phd}(t)}{2}) \end{pmatrix} \tag{2.48}$$

According to Eq. (2.19) and Eq. (2.48) can be written in the form:

$$\begin{pmatrix} E_1^{phd}(t) \\ E_2^{phd}(t) \end{pmatrix} = E_0(t) \cdot \begin{pmatrix} T_1^{phd}(t) \\ T_2^{phd}(t) \end{pmatrix}, \tag{2.49}$$

with the two transmission functions:

$$T_1^{phd}(t) = T_{01}\left[1 + m_1 e^{i\psi_1}\Delta\phi^{phd}(t)\right] \tag{2.50}$$

$$T_2^{phd}(t) = T_{02}\left[1 + m_2 e^{i\psi_2}\Delta\phi^{phd}(t)\right] \tag{2.51}$$

with $T_{01} = 1/\sqrt{2}$, $T_{02} = -i/\sqrt{2}$, $m_1 = \sqrt{2}/2$, $m_2 = \sqrt{2}/2$, $\psi_1 = 3\pi/4$ and $\psi_2 = \pi/4$.

In this case, using Eq (2.20) and Eq. (2.26), the transfer functions of the setup become:

$$H_1^{phd}(\Omega) = -\sqrt{2}\cos\left(\frac{\Omega^2}{2C} - \frac{\pi}{4}\right) \tag{2.52}$$

$$H_2^{phd}(\Omega) = \sqrt{2}\cos\left(\frac{\Omega^2}{2C} + \frac{\pi}{4}\right) \tag{2.53}$$

These transfer functions, represented in Figure 2.16, show interleaved zeros at different frequencies, implying missing information but at different frequencies. By this way, the diverse information on both transfer functions is complementary. It is necessary to take notice that the relative positions of the zeros depend on the crystal orientations [119]. Many methods can be used to retrieve the unexplored input electric field. One can benefit from the first transfer function H_1 at a certain frequency when the other transfer function H_2 is null and inversely use the second H_2 when the first is null and thereby retrieve the input signal $E(t)$ (or $\Delta\phi_{in}$) using both recorded outputs $Y_1(t)$ and $Y_2(t)$.

Alternatively, we will use the so-called Maximal Ratio Combining (MRC) technique that will be described in the next paragraph.

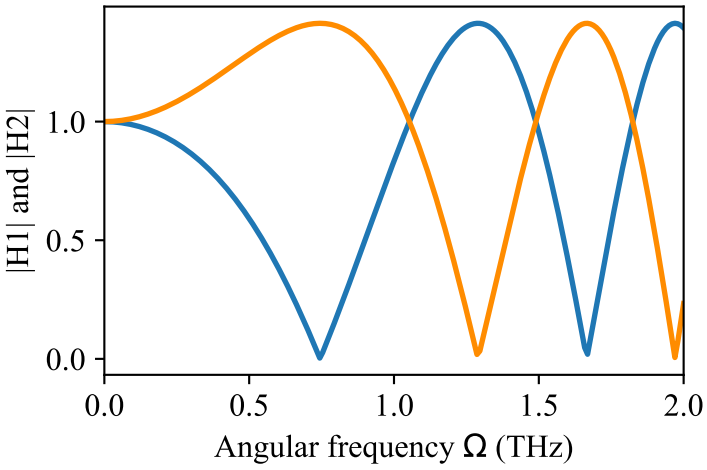

FIGURE 2.16: Norms of the transfer functions $|H_1|$ and $|H_2|$ of both EO arms for the diverse EO special configuration. $|H_1|$ and $|H_2|$ expose interleaved zeros at different frequencies.

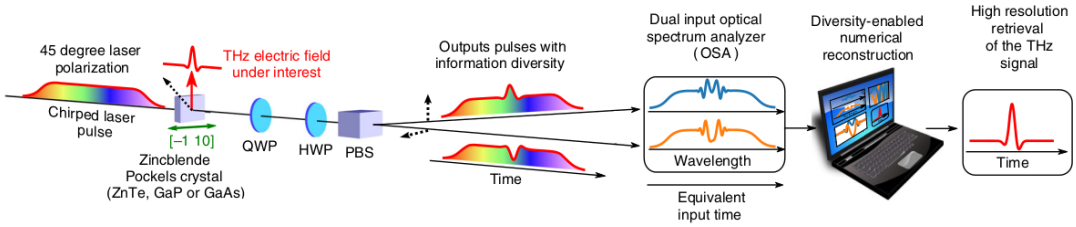

FIGURE 2.17: Schematic of the phase diversity EO sampling concept: as the measured spectra present some distortions, this DEOS technique uses two different outputs information, corresponding to the polarizations states of the modulated signal, to retrieve the THz input signal with a reconstruction numerical algorithm. Figure from [119].

2.5.4 Phase diversity with MRC reconstruction algorithm

In order to benefit from phase diversity previously elaborated and solve the temporal resolution problem, we will make use of an advanced technique called maximal ratio combining (MRC) technique [125]. This technique finds a large utility in telecommunication, specially in wireless communication to improve the performance of receivers and avoid fading effects due to interferences [126, 127]. It was implemented with photonic time stretch ADC in order to reach high bandwidth RF signals [123]. Thereafter, this technique was combined with spectral encoding for single-shot measurements of THz signals with sufficient resolution [119].

We will review the problem from the beginning to show how with phase diversity we will be able to determine the THz signal using MRC algorithm by considering the system represented in Figure 2.17.

The input signal under interest is the THz electric field $E(t)$. This electric field induces by the Pockels effect a proportional phase-shift $\Delta\phi_{in}(t)$ inside the

crystal linked by a constant β :

$$\Delta\phi_{in}(t) = \beta E(t) \tag{2.54}$$

with

$$\beta = \frac{\pi d}{\lambda} n_0^3 r_{41} \tag{2.55}$$

where n_0 is the refractive index when no electric field is applied, d the crystal thickness, λ the laser wavelength in vacuum and r_{41} the electro-optic coefficient of the crystal. The coefficient β depends on the relative orientations of the crystal axes and on the polarizations of the laser and terahertz field.

The measured output signals $Y_{1,2}(t)$ are coupled to the input field $E(t)$ by transfer functions $H_{1,2}$ in Fourier space. An approximation can be considered for a small electric field:

$$\tilde{Y}_1(\Omega) \approx H_1(\Omega)\Delta\tilde{\phi}_{in}(\Omega) \tag{2.56}$$

$$\tilde{Y}_2(\Omega) \approx H_2(\Omega)\Delta\tilde{\phi}_{in}(\Omega) \tag{2.57}$$

with Ω is the terahertz frequency at the input.

The transfer functions $H_{1,2}(\Omega)$ depend on the orientations of the waveplates, the crystal as well as on the polarizations of the laser and the THz. As we consider the case of phase diversity, the transfer functions of the system can be expressed by[2]:

$$H_1(\Omega) = H_1^{phd}(\Omega) = \sqrt{2}cos(B\Omega^2 + \phi) \tag{2.58}$$

$$H_2(\Omega) = H_2^{phd}(\Omega) = -\sqrt{2}cos(B\Omega^2 - \phi) \tag{2.59}$$

as previously demonstrated, where $B = \frac{1}{2C}$ depends on the chirp rate and

$$t = -\frac{\partial w_{opt}}{\partial t} = -\frac{w_{opt} - w_{opt}^{center}}{C} \tag{2.60}$$

To retrieve $\Delta\phi_{in}(\Omega)$, instead of dividing $Y_1(\Omega)$ or $Y_2(\Omega)$ by H_1 or H_2 respectively (Eq. (2.56) and Eq. (2.57)), MRC uses a combination of both to minimize the error and can be applied as:

$$\Delta\tilde{\phi}_{in}^{retr}(\Omega) = \frac{H_1(\Omega)\tilde{Y}_1(\Omega) + H_2(\Omega)\tilde{Y}_2(\Omega)}{H_1^2(\Omega) + H_2^2(\Omega)} \tag{2.61}$$

However, the parameter B in Eq.(2.58) and Eq.(2.59) is unknown experimentally, causing a problem for determining the transfer functions. To bypass this issue, we have developed an algorithm which recover the parameter B from experimental measured spectrum $\tilde{Y}_1(\Omega)$ and $\tilde{Y}_2(\Omega)$ to retrieve the induced phase shift.
First, we consider a set of values for B and calculate for each the transfer functions H_1^{retr} and H_2^{retr}, using Eq. (2.58) and (2.59).
Using the retrieved transfer functions, we calculate, for every single value of B, the value of $\Delta\tilde{\phi}_{in}^{retr}(\Omega)$ defined by:

$$\Delta\tilde{\phi}_{in}^{retr}(\Omega) = \frac{H_1^{retr}(\Omega)\tilde{Y}_1(\Omega) + H_2^{retr}(\Omega)\tilde{Y}_2(\Omega)}{H_1^{retr2}(\Omega) + H_2^{retr2}(\Omega)} \tag{2.62}$$

[2]See Appendix D for demonstration.

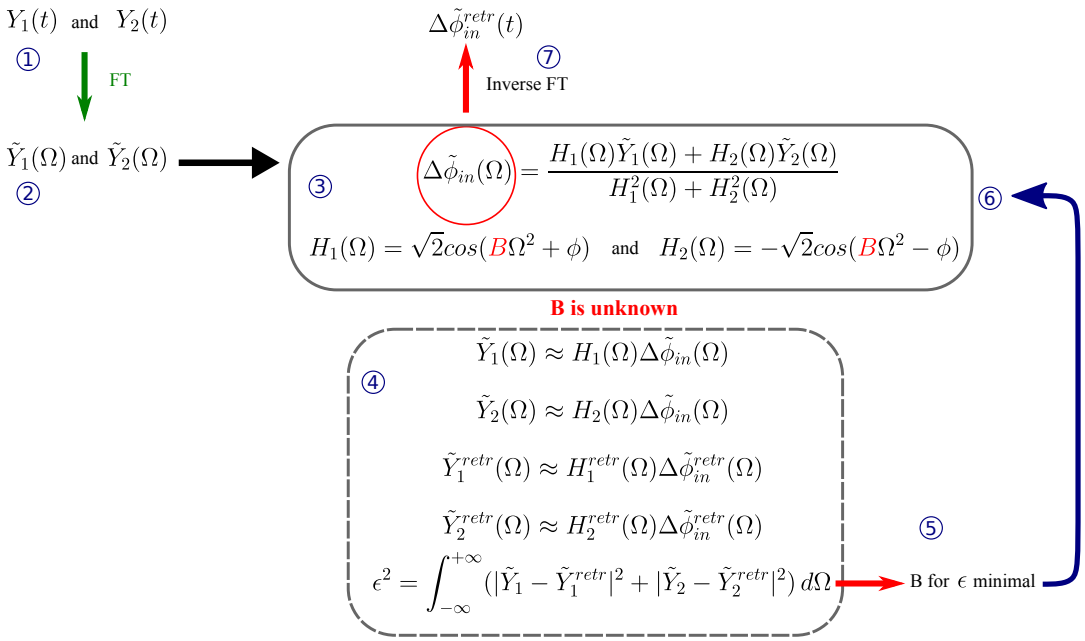

FIGURE 2.18: Representative diagram summarizing MRC reconstruction algorithm adopted for retrieving the phase shift induced birefringence $\Delta\phi_{in}^{retr}$ from two recorded outputs $Y_1(t)$ and $Y_2(t)$ by going through transfer functions in Fourier space. As a parameter B is unknown, a square fit is done revealing an optimal B parameter corresponding to a minimal error and thus, allowing the reconstruction of the THz signal under investigation.

and pretend the spectra of both polarizations signals $\tilde{Y}_1^{retr}(\Omega)$ and $\tilde{Y}_2^{retr}(\Omega)$ using the following equations:

$$\tilde{Y}_1^{retr}(\Omega) \approx H_1^{retr}(\Omega)\Delta\tilde{\phi}_{in}^{retr}(\Omega) \tag{2.63}$$

$$\tilde{Y}_2^{retr}(\Omega) \approx H_2^{retr}(\Omega)\Delta\tilde{\phi}_{in}^{retr}(\Omega) \tag{2.64}$$

We perform a classical least-square fit to find the reconstruction error ϵ:

$$\epsilon^2 = \int_{-\infty}^{+\infty} (|\tilde{Y}_1 - \tilde{Y}_1^{retr}|^2 + |\tilde{Y}_2 - \tilde{Y}_2^{retr}|^2)\, d\Omega \tag{2.65}$$

that minimizes the error between retrieved signals and experimentally measured signals. This leads to an optimal value of B and ϕ for which the error is minimal. Once the value of B and ϕ are known, the correct functions $H_1(\Omega)$ and $H_2(\Omega)$ can be found allowing to retrieve the phase shift induced $\Delta\tilde{\phi}_{in}^{retr}(\Omega)$ without distortions according to:

$$\Delta\tilde{\phi}_{in}^{retr}(\Omega) = \frac{H_1(\Omega)\tilde{Y}_1(\Omega) + H_2(\Omega)\tilde{Y}_2(\Omega)}{H_1^2(\Omega) + H_2^2(\Omega)} \tag{2.66}$$

By simply applying the inverse FT, one can obtain $\Delta\tilde{\phi}_{in}^{retr}(t)$

$$\Delta\tilde{\phi}_{in}^{retr} = H_{MRC}(\Omega)\Delta\tilde{\phi}_{in} \tag{2.67}$$

$$H_{MRC}(\Omega) = 1 \tag{2.68}$$

with

$$\Delta\phi_{in}^{retr}(t) = \Delta\phi_{in}(t) \tag{2.69}$$

and thereby deduce the THz electric field $E_{in}^{retr}(t)$:

$$\tilde{E}_{in}^{retr}(\Omega) = \frac{1}{\beta}\Delta\tilde{\phi}_{in}^{retr}(\Omega) \tag{2.70}$$

This algorithm is summarized in Figure 2.18.

By doing so, one can benefit from diverse phase information to reconstruct the THz input signal without any limit on the temporal resolution for any long duration of chirped pulses or analysis windows. This phase diversity technique has been demonstrated efficient with single-shot EOS to measure THz signals and have been tested in context of particle accelerator by measuring the shape of a 200 fs RMS electron bunch at European X-FEL [119]. Recently, it has been efficient to measure the CTR THz spectra in single-shot at the TeraFERMI [128].

This chapter reviewed optical, photonic and numerical techniques, each offering a distinct measurement property. As previously mentioned, single-shot EOS has been previously combined with photonic time stretch allowing to perform THz single-shot measurements at high acquisition rates. Balanced detection integrated with EOS have been confirmed to reach high dynamic range with a better SNR. Single-shot EOS has been demonstrated efficient when combined with diversity EOS as well to reach sufficient temporal resolution in single shot measurements. Nevertheless, combining all these techniques together is not straightforward and is challenging in single shot THz detection.

Chapter 3

Photonic time-stretch electro-optic sampling associated with phase diversity at ELBE

3.1 Introduction

As outlined in Chapter 2, several techniques exist to perform single shot THz measurements enabling to overcome limitations, such as repetition rate, temporal resolution and sensibility. In 2015, Roussel *et al.* demonstrated the effectiveness of combining the single-shot electro-optic sampling (EOS) with photonic time-stretch [9] by performing single shot measurements of CSR THz signals with a 850 kHz repetition rate at Synchrotron SOLEIL. In 2021, Roussel *et al.* presented a novel method, based on the so-called diversity concept [119], that increases considerably the time resolution of EO systems using chirped laser probes. Nevertheless, achieving both high acquisition rate and high resolution simultaneously when long duration or/and a broadband signals are involved, remained an open challenge as the only demonstrations have been done using EO systems with a camera readout (see section 2.3.2).

The aim of this chapter is to design and develop an experimental scheme that combines single-shot EOS with photonic time-stretch and phase diversity techniques. In this chapter, we present our experimental setup that combines the three techniques together for the first time and conducted tests at the coherent diffraction radiator (CDR) THz source at ELBE, known as TELBE, in order to measure the THz signals in single-shot configuration with a sufficient sub-ps resolution.

The chapter is divided into three main parts. The first part presents the ELBE THz source to be measured and provides a detailed description of the experimental setup design, including its specifications, and highlighting on the challenges faced during its construction. We emphasize, in a second part, on the importance of implementing the phase diversity technique and present the experimental measurements obtained. We show how the maximum ratio combining (MRC) reconstruction algorithm enabled to obtain the CDR THz signal with a sufficient temporal resolution. In the last part, we investigate the ELBE machine, using the experimental EOS scheme, by performing sets of measurements versus some machine parameters.

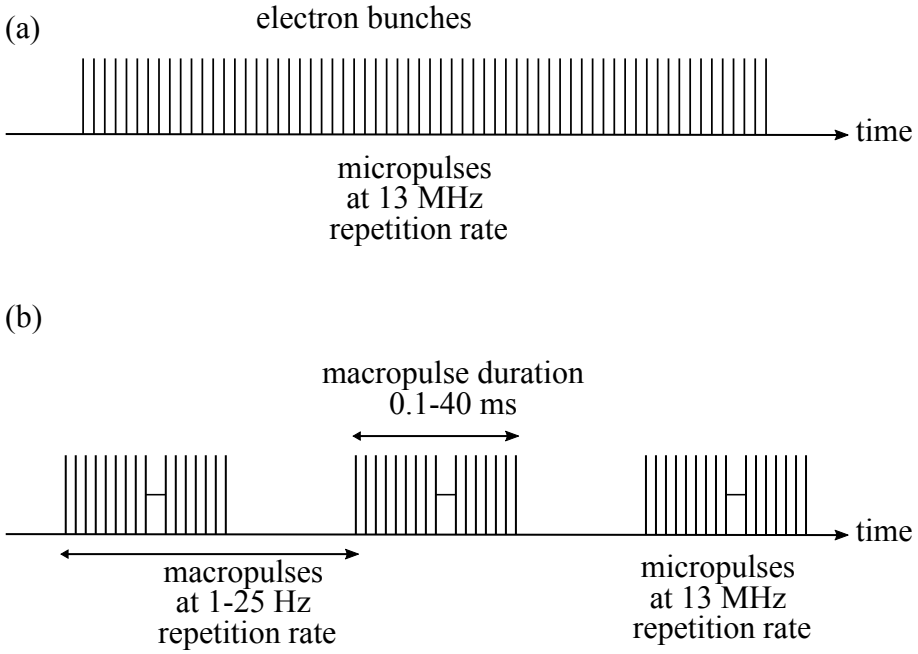

FIGURE 3.1: Emission of electron bunches at ELBE at different regimes: in quasi-continuous wave and macropulses. (a) Electron bunches can be emitted continuously up to 13 MHz repetition rate (b) or in macropulses of ms durations at adjustable repetition rates.

3.2 ELBE facility

ELBE is an **E**lectron **L**inac for **B**eams with high **B**rilliance and low **E**mittance center located at Forschungszentrum Dresden-Rossendorf, Germany, user operational since 2002 providing high power radiation sources. It is a superconducting compact linear accelerator that can operate in high average power mode and delivers short electron bunches with a 40 MeV energy.
The cryogenic technology of this accelerator allows continuous wave (cw) operation (as in Figure 3.1(a)) between 26 MHz and 101.6 kHz, as well as macropulse mode (as in Figure 3.1(b)), according to user requirements. ELBE parameters can be found in Table 3.1.

The electron linac at ELBE is designed to guide the accelerated electrons towards several experimental areas. It serves as a primary electron driver for generating various types of secondary radiation sources and particle beams, as seen in Figure 3.2, such as 2 FELs (FELBE), Bremsstrahlung, electrons, neutrons (nELBE), positrons (pELBE), hard-X-ray radiation and a superradiant THz facility, having diverse applications across different scientific fields.

We will focus in this thesis on the investigation of two THz sources at ELBE: the CDR source within the THz facility at ELBE in this chapter and on the study of one of the two FELs housed in FELBE in Chapter 4, highlighted by circles in Figure 3.2.

3.2.1 THz facility at ELBE

One of secondary radiation delivered by the accelerator is the superradiant THz source known as TELBE. The THz facility includes two THz sources: a broadband

Parameter	
Electron beam energy / MeV	5 - 40
Max. bunch charge /pC	<200 pC
Max. average beam current /mA	1.6
Normalized transverse emittance /mm mrad (rms)	<20
Normalized longitudinal emittance /keV ps (rms)	<100
Micropulse duration /ps	1 ... 5 (>150 fs)
Micropulse repetition rate /MHz	<= 26 or Single pulse
Macropulse duration /ms	0.1 - 40 or cw
Macropulse repetition rate /Hz	1–25

TABLE 3.1: ELBE linac parameters. Data from hzdr.de.

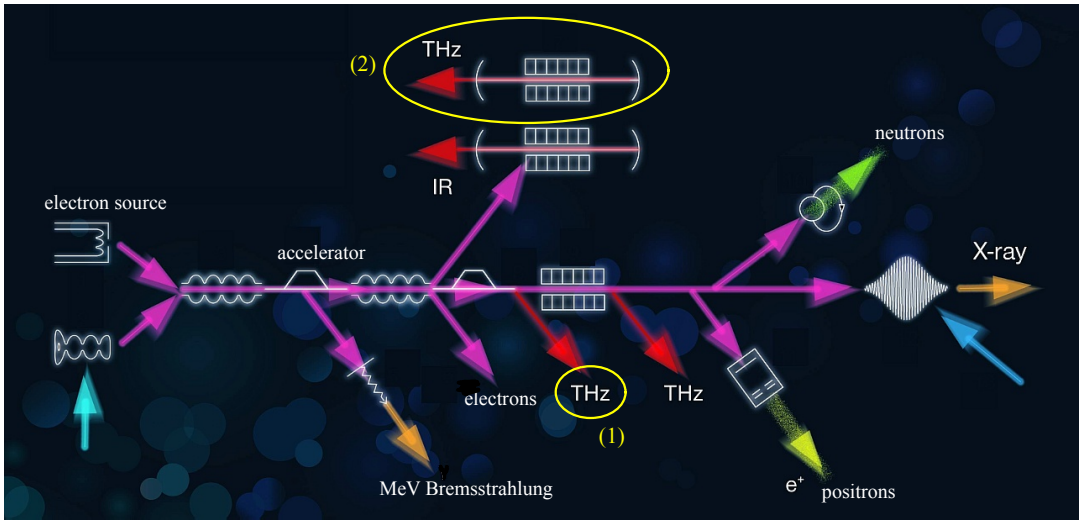

FIGURE 3.2: Architecture of the ELBE linear accelerator delivering relativistic electrons for several kind of radiations stations, including high-energy gamma rays, infrared and THz radiation, neutron, positron, and electron beams. Experiments studied in this thesis are performed at THz stations: (1) the CDR THz source and (2) the U100-FEL. Figure modified from hzdr.de.

coherent diffraction radiator (CDR) and a narrowband undulator. These sources operate in two different modes of operation: a high field mode and a high repetition rate mode. This facility provides stable high-field THz pulses with adjustable repetition rates from tens of Hz to 13 MHz. It covers the lower THz range between 0.1 and 3 THz with pulse energies up to the μJ range.

We will limit our study to the measurement of the THz radiation emitted by the CDR source.

3.3 EOS-TS phase diversity experiment for coherent diffraction radiation (CDR) THz detection

3.3.1 CDR THz generation and transport

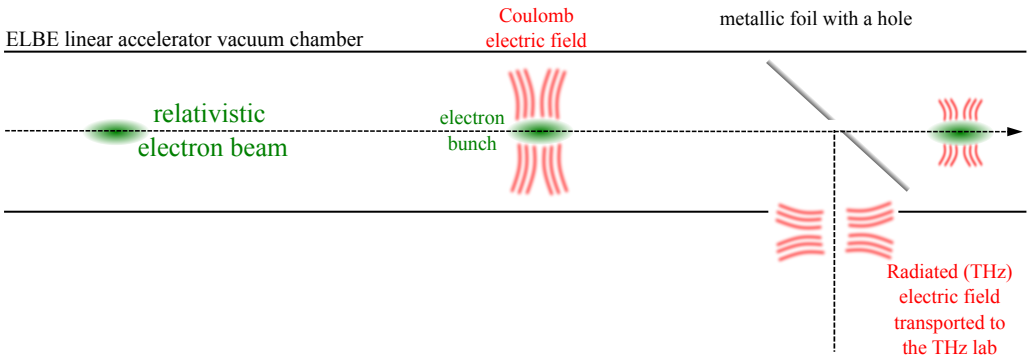

FIGURE 3.3: Illustration of THz generation using the coherent diffraction radiation (CDR) at ELBE. CDR occurs when the electron bunch travels through the hole of a metallic foil.

The THz signal under investigation here emanates from the coherent diffraction radiation (CDR) emitted when a metallic foil with a hole is placed on the electron beam path exiting from the linear accelerator ELBE (see Figure 3.3). In this experiment, the accelerator is operating at a 50 kHz repetition rate with a 45 mW optical power emanating from the CDR and generating a radially polarized THz signal . In the THz laboratory, it is transported to the EO crystal using parabolic mirrors. Three THz polarizers are used, as seen in Figure 3.4 to change the THz polarization into a linear vertical polarization with two polarizers fixed and an adjustable middle one in between used as an attenuator to control the THz power, and redirected by a mirror to the 2" diameter parabolic mirror placed on the EO board (more details in section 3.3.2). According to Malus law, the resulting THz output power delivered to the EOS board and to be measured by EOS is :

$$P_{measured} = P_{THz} cos^4 \Theta \tag{3.1}$$

where P_{THz} is the THz power emitted by the CDR source and Θ is the angle of the second THz polarizer.

3.3.2 Experimental setup

The experimental setup, represented in Figure 3.4, is formed of three main units that are connected by optical fibers: a first unit for EOS detection in which the CDR THz

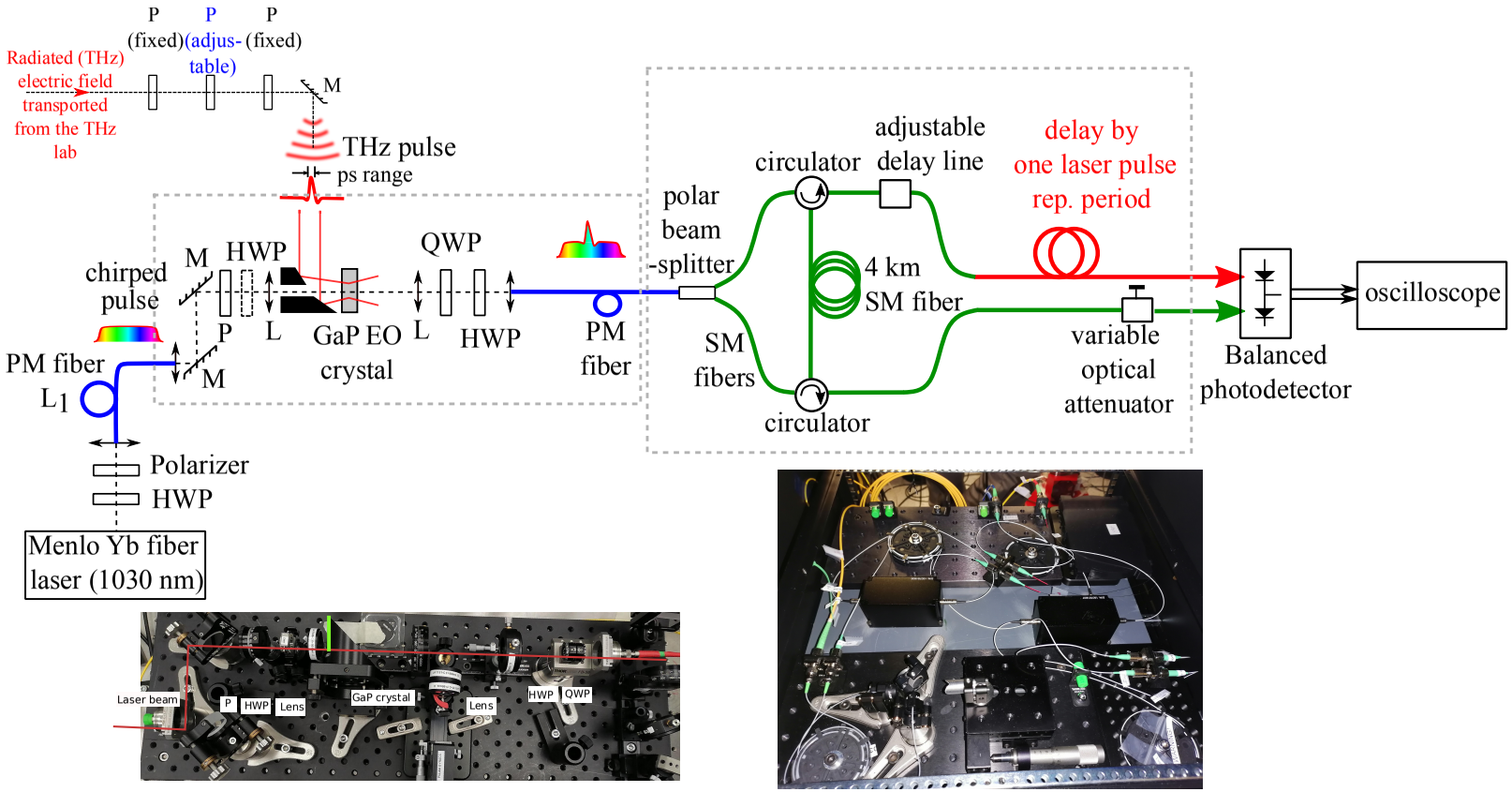

FIGURE 3.4: Experimental setup for single-shot electro-optic sampling combining photonic time-stretch with the phase diversity techniques. An ytterbium (Yb) chirped laser pulse is focused simultaneously with the CDR THz signal on a Gallium Phosphide (GaP) EO crystal, modulating the laser spectrum. A fibered PBS splits the modulated signal into separate polarization states, redirected by circulators to 4 km HI1060 fiber for slowing them down in time. An additional fiber delays pulses on one arm by a period of repetition rate before applying a balanced detection between both arms and recording each polarization separately with an oscilloscope. PM: polarization maintaining fiber (blue fiber), SM fiber: single mode fiber (in green), HWP: Half wave plate, QWP: Quarter wave plate, M: mirror, L: lens.

signal is imprinted on a chirped laser pulse, a second unit for photonic time stretch where the modulated signal is slowed down in time and a last one for detecting and recording the signals separately.
The probe pulse consists of a Menlo Orange Ytterbium laser with a 1040 nm central wavelength, a 4.927 ps pulse duration specified and a 35 nm spectral width, operating at a 78 MHz repetition rate with 180 mW output power. The laser output is free-space with a horizontal polarization. A set of half-wave plate (HWP) and a polarizer, from Thorlabs, is placed at the output of the laser to attenuate the laser power. The laser is then injected, using a PAF2A-A10B collimator, into a first PM980 fiber with a length L_1, towards the electro-optic (EO) sampling setup. This fiber pre-chirps the laser pulse and its length defines the recording window length on which the THz signal will be imprinted.

The EO part is placed on a 60 cm$\times$ 20 cm breadboard where the laser beam is collimated in a 11 mm focal length collimator (PAF X-11C from Thorlabs) followed by two mirrors for easier coupling. A thin film Glan-Thompson polarizer, from Thorlabs, is used to provide a clean linear polarization. An achromatic HWP (FBRF-AH2 from Thorlabs) is used to adjust the laser polarization, according to the phase diversity configuration chosen here (see section 2.5 for which the laser polarization should be at 45° with respect to the THz polarization[1]. The THz signal, emanating from the CDR source, with a $\phi = 500$ μm FWHM beam diameter, is focused simultaneously with the laser pulse on a 5 mm Gallium Phosphide (GaP) crystal AR coated, from MolTech GmbH, using a protected gold off-axis parabolic mirror with a 2" diameter, a 2" focal length and a 3 mm hole diameter, from Thorlabs, through which the laser travels through the hole. The electric field of the THz signal induces a birefringence in the crystal, that will be temporally imprinted on the spectrum of the chirped laser pulse. The laser beam is focused on the EO crystal using a set of two plano-convex lenses with $f = 100mm$ focal lens before and after the EO crystal for an optimal focusing. A set of a quarter wave plate (QWP) and a HWP, from Thorlabs, is used to transform the ellipticity modulation into an intensity modulation and choose the polarization of the modulated signal before being focused in a PAF-X-11-B and injected in a $\sim$20 m PM980 fiber. For the phase diversity configuration, a special arrangement of the wave plates should be considered. The first HWP in the EO head is fixed at 22.5° with respect to the vertical, as well as the second one fixed at 22.5°. The QWP is fixed at 0° and the GaP crystal is oriented in a way that its [-110] axis is at 45° with respect to the laser and at 90° with the THz.
In the following, $P_{EO} = 25$ mW is defined as the laser power just before the second collimator of the EO setup before injection in the PM fiber.

The second part includes the photonic time-stretch technique and consists in slowing down the modulated signal by introducing dispersion by the Dispersive Fourier Transform. A fibered polarizing beam splitter (PBS) separates the two polarization states of the modulated signal and redirect them to two identical circulators (with less than 1 dB loss), so they travel in the same 4 km HI1060 fiber, from Corning, providing a dispersion of -38 ps/nm/km and a maximum attenuation of 1.5 dB/km @ 1060 nm and get dispersed exactly by the same amount. A homemade delay line, adjustable over 166 ps, is added on one arm output to adjust the delay

[1]For classic balanced detection configuration, the THz polarization should be parallel to the THz polarization and to the [-110] axis of the EO crystal.

between pulses of both arms resulting from the differences between fiber lengths as well as a variable optical attenuator used to adjust the optical power differences between both arms.

The particularity of this setup is to allow separate recordings of both polarization states of the modulated signal. This was possible by adding on the path of one polarization state, an extra fiber with a length equivalent to the time travel of one period of laser pulse for a 78 MHz repetition rate. A clear explanation of this disposition is shown in Figure 3.5.

The last part of the experimental scheme is the detection part where a balanced detection is applied between both arms using a DSC-R412 balanced optical receiver from Discovery Semiconductors, offering a bandwidth to 20 GHz, a gain between 30 and 2800 V/W and a 40 pW/$\sqrt{\text{Hz}}$ optical noise equivalent power. The output signals are recorded by a SDA820Zi-B20 WaveMaster 8 Zi-B oscilloscope with a 20 GHz bandwidth with 80 GS/s, from Teledyne Lecroy, and an 8 bits 8 GHz DSA90804A Agilent oscilloscope with a maximum sampling rate of 40 GS/s. The oscilloscope is synchronized to the 50 kHz repetition rate of the accelerator.

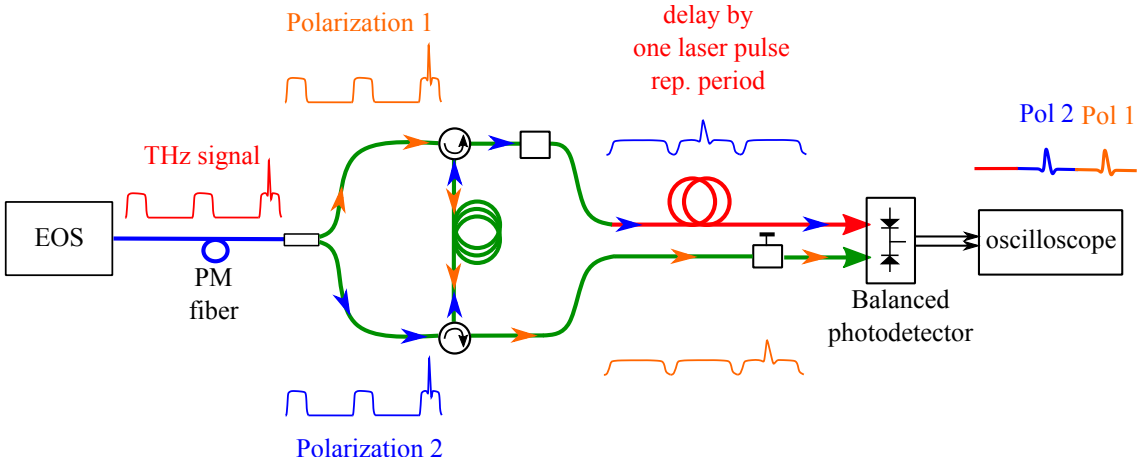

FIGURE 3.5: Diagram explaining the special configuration for phase diversity. An additional fiber is inserted on one arm delaying the modulated laser pulse by a period of repetition rate of the laser. Each polarization state is recorded separately with an implementation of the analog balanced detection applied between both outputs, suppressing the common laser shape.

3.3.3 Laser - THz beam alignment

The THz is aligned transversely with the laser on the crystal using a pyroelectric camera, after the parabolic mirror. The delay between the THz and laser pulses has been adjusted using a FET (Field Effect Transistor) THz detector, and a 5 GHz InGaAs high-speed photodetector (DET08CFC) from Thorlabs. The timing between THz and laser was adjusted by delaying the RF reference sent to the laser repetition rate synchronization system using a mechanical RF delay line (ARRA 2448A) in such a way that the full THz signal is centered on the laser pulse.

3.3.4 EO measurements

We performed EO measurements in phase diversity configuration, where each polarization is recorded separately. The first fiber, noted L_1, defines the acquisition recording window. The CDR THz pulse is expected to have a duration of few picoseconds. At first, we considered a 3 m fiber length L_1 that, according to calculation, should result in a pre-chirped laser pulse of 9 ps. The laser pulse stretched in the 4 km HI1060 fiber resulted in a stretch laser pulse duration of 6 ns. Signals are subsequently recorded with a 20 GHz bandwidth WaveMaster 8 Zi-B oscilloscope and are then interpolated and cut to the laser repetition rate. Pulses are categorized between those modulated with the THz signal and others without THz. Pulses without THz, resulting from the response of optical components and common noise sources, are used as residue that is suppressed from raw signals to extract the THz polarizations[2]. The repetition rate of the laser is 78 MHz whereas the repetition rate of the THz source is 50 kHz by means that among each 1560 pulses, only one laser pulse is modulated by the THz radiation. We performed some measurements using different recording modes of the oscilloscopes: in continuous recording mode and others in sequence mode. Up to 16000 THz pulses could be recorded.

3.3.4.1 Preliminary measurements with $L_1 = 3m$

Figure 3.6(a) displays the two polarization states of the modulated signal recorded separately of one single shot, along with their corresponding single-shot Fourier Transform in Figure 3.6(b). However, it appears that the laser pulse duration is insufficient, resulting in truncated signal edges.

3.3.4.2 Measurement with $L_1 = 13m$

Therefore, to ensure the entire recording of THz polarizations, we opted to increase the length of the acquisition window so that the complete signal, including the oscillations on the sides, gets encoded on the chirped laser pulse. An extra 10 m PM980 fiber was added before the first 3 m PM fiber, resulting in a total length L_1 of 13 m and a stretched pulse of 24 ps as seen in Figure 3.6(c) in green. The laser pulse duration was sufficient for recording condition for the use of the DEOS method as observed in Figure 3.6(c). The single shot FT are shown in Figure 3.6(d).

For the rest of the experiment, the fiber with a length 13 m is kept unchanged, with a recording window of 24 ps.

The recorded signals in Figure 3.6(a) and (c) and their Fourier spectra in Figure 3.6(b) and (d) do not correspond to what is expected for a CDR THz signal due to insufficient temporal resolution. Additionally, the spectra of these polarizations reveal the presence of zeros at certain frequencies, indicating that some information is missing about the THz at these frequencies. Their positions correspond to the same frequencies presenting zeros in the transfer functions of the system, which are dependent on the fiber length L_1, shown in Figure 3.7(a) and 3.7(b) for $L_1 = 3m$ and $L_1 = 13m$, respectively. The position of the first zero moves to lower frequencies (to the left) for longer fiber L_1.

Hence, we can see the necessity of implementing the phase diversity that makes

[2]See Appendix B.

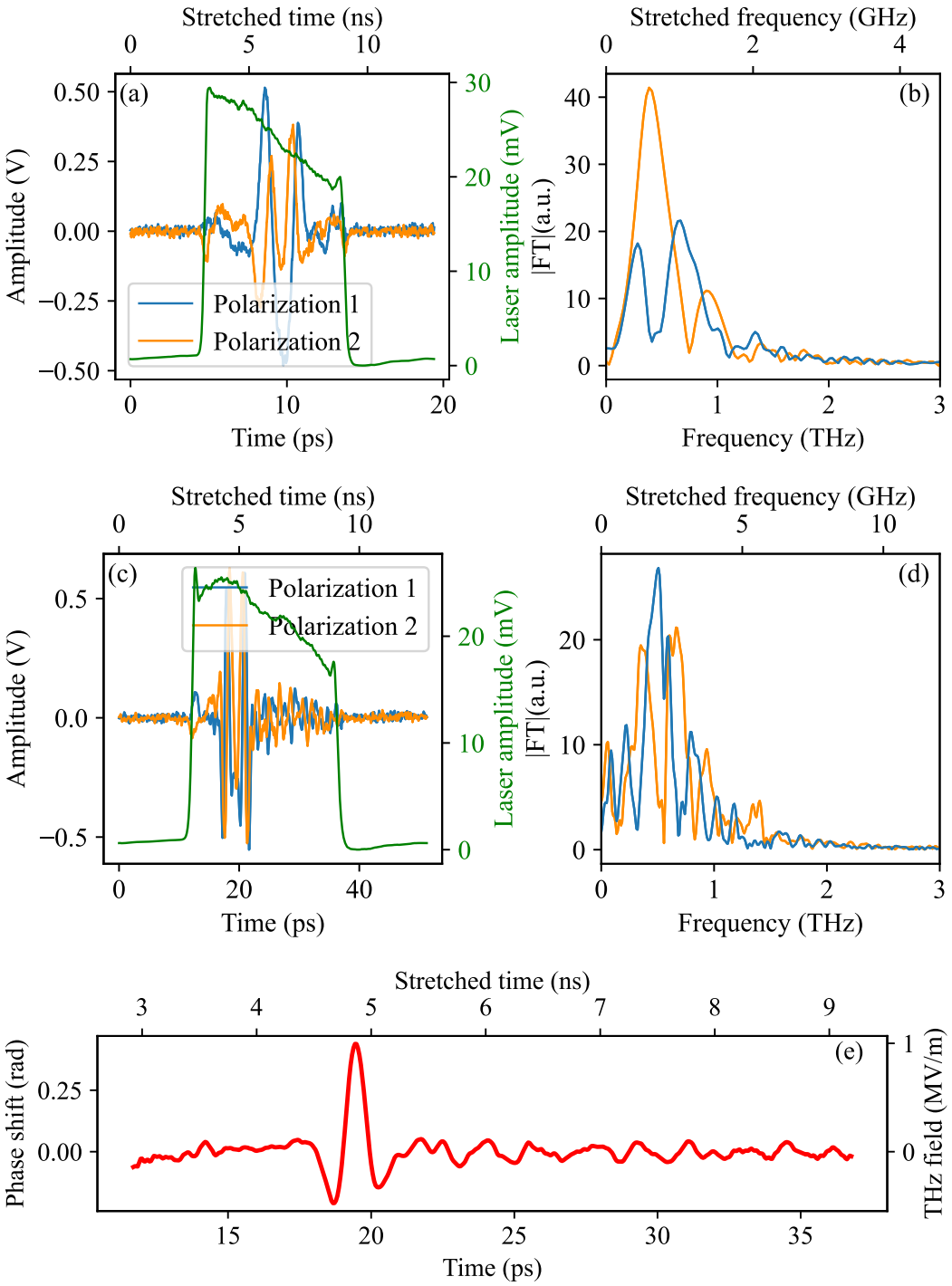

FIGURE 3.6: (a) and (c) Single-shot THz polarization states recorded separately in phase diversity configuration with their respective single shot spectrum (color code respected) in (b) and (c) using different fiber lengths: (a) a recording window defined by a 3 m fiber L_1 resulting in signal cut-offs on the edges by the short laser pulse of 9 ps, and (b) with a recording window of L_1 =13 m defining a longer acquisition window of 24 ps. (e) Real THz single shot signal after reconstruction using both polarizations states using L_1 =13 m.

use of both polarization states, as previously discussed in section 2.5, in order to reconstruct the input THz signal. We will see in next section, how the real CDR THz signal in single-shot with its exact shape represented in 3.6(e) was reconstructed using MRC reconstruction algorithm.

3.4 Phase diversity with MRC numerical reconstruction of CDR THz signal

The orientation of the wave plates in the EO head is crucial in adjusting the transfer function zeros, so that the zeros of both polarizations get interleaved and do not coincide on the same frequencies. This allows to benefit from the information of the second polarization when the first is providing zero information.

With the MRC reconstruction algorithm detailed in section 2.5.4, we were able to determine the optimal values of coefficients B and phi of the transfer function (Eq. 2.58), corresponding to the minimal error as visualized in Figure 3.8.

These values are used to reconstruct accurately the Fourier transform spectra of both polarizations, showing a good agreement with the measured spectra as presented in Figure 3.9 for both acquisition windows. With this information, we were able to retrieve the single shot THz input signal after normalization, as demonstrated in Figure 3.10(a) for L_1 = 3 m and in Figure 3.11(a) L_1= 13 m, with their respective optical spectra in Figure 3.10(b)(c) and in Figure 3.11(b)(c). These reconstructed signals correspond to the phase shifts induced by the CDR THz signals by EO effect on the pre-chirped laser pulses. This reconstruction process was repeated for each shot, allowing to create a colormap of successive THz signals in single shot showing electron bunches arrival time as well as their single shot spectra, as illustrated in Figure 3.12(a) and (b) respectively. We can see that even though a high jitter appears, the THz spectra are still the same, showing a spectral stability of the THz exiting the CDR.
This can give an idea about the relative time jitter between the electron bunch and the laser which is of $\sim$ 3 ps as seen in Figure 3.12(a). This value is not the same for all recorded data, but shows the arrival time for only 80 shots. However, a higher jitter about 7 ps is observed for longer recordings, as in Figure 3.13(b) over more than 14000 consecutive shots recorded in sequence mode (see Figure 3.13(a)).

Additional measurements were taken with an 8 GHz oscilloscope available at ELBE. Measurements, shown in Appendix C, and data analysis are similar to the one presented in this section and allow a satisfying reconstruction of the THz waveform in single-shot, confirming the efficiency of both acquisition tools for recording THz signals, under the specified conditions. A more detailed discussion about both oscilloscopes noises will be discussed in section 3.5.2.1.

3.5 Characterization of the experimental setup

3.5.1 Precise determination of the stretch factor

The time-stretch method requires knowing the stretch factor. It is straightforward to have an estimate from the length of fibers used in the setup. However, obtaining a

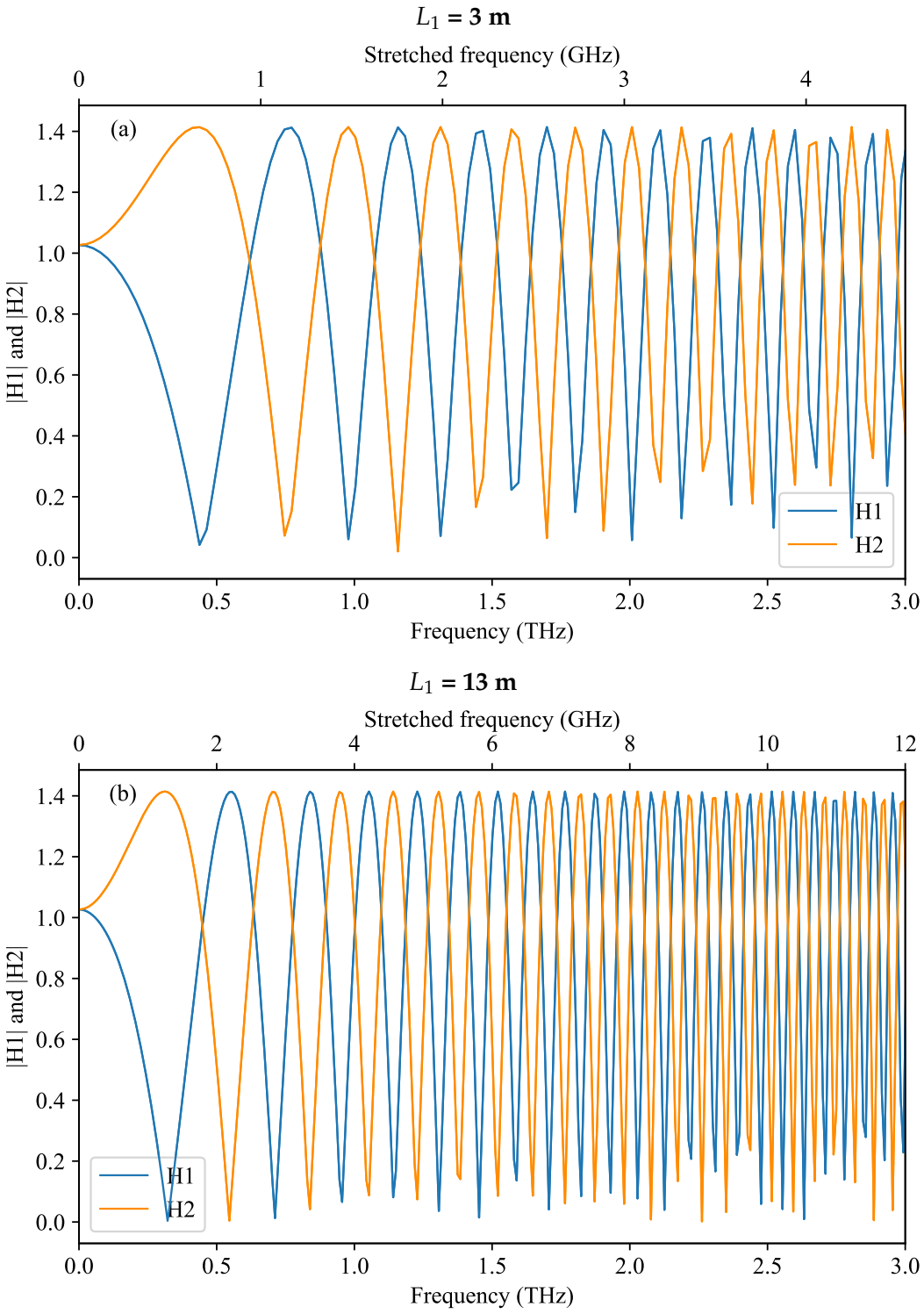

FIGURE 3.7: Transfer functions of the system for recording windows of L_1=3 m in (a) and L_1=13 m in (b) showing zeros at some frequencies. The position of the first zeros shifts to lower frequencies when L_1 increases. Zeros in the transfer functions correspond to the same zeros in the Fourier transforms of recorded signals represented in Figure 3.6(b) and (d).

precise value for M - and thus a precise time calibration - requires a specific work.

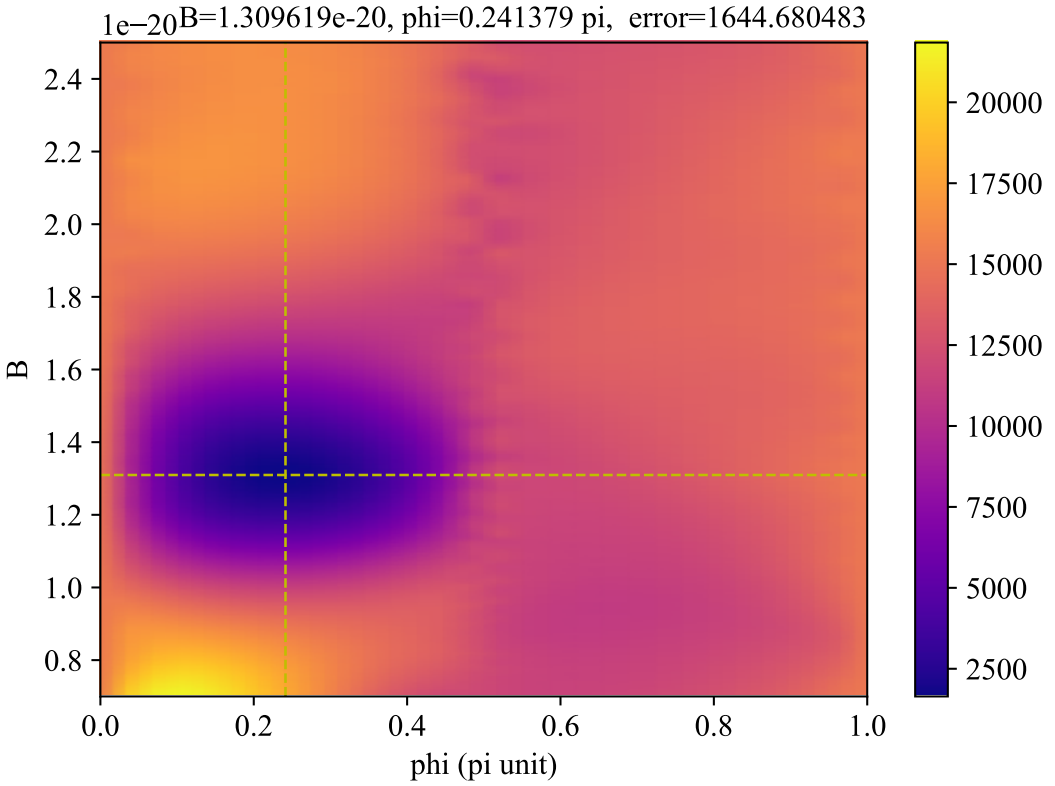

FIGURE 3.8: Color map of the relative error of the MRC reconstruction over a range of phis and factor B as defined in equation 2.58. A minimum of error is observed at specific values of B and phi.

In all previous figures, two time scales are represented on the x axis: a "stretched time" corresponding to the recording time observed on the oscilloscope and a second one "time" that corresponds to the time theoretically calculated from the stretch factor value M detailed in this paragraph. This time is associated to the real time of the THz radiation emitted by the electron bunch before being stretched.

A classic technique to determine this stretch factor consists in scanning the delay between the laser pulse and the THz signal and deduce the equivalent time calibration. However, this technique is reliable only for stable signals which is not the case for this THz source showing a high time jitter as in Figure 3.12(a).

3.5.1.1 Approximate determination of the stretch factor

The stretch factor is directly related to the fibers lengths before and after EO sampling and is defined by:

$$M = 1 + \frac{L_2}{L_{f1}} = 1 + \frac{L_2}{L_0 + L_1} \tag{3.2}$$

where L_2 is the total length after EOS and L_{f1} is the total fiber lengths before the EO sampling in the laser that includes the unknown fiber lengths in the laser denoted as L_0 and the chosen fiber L_1.

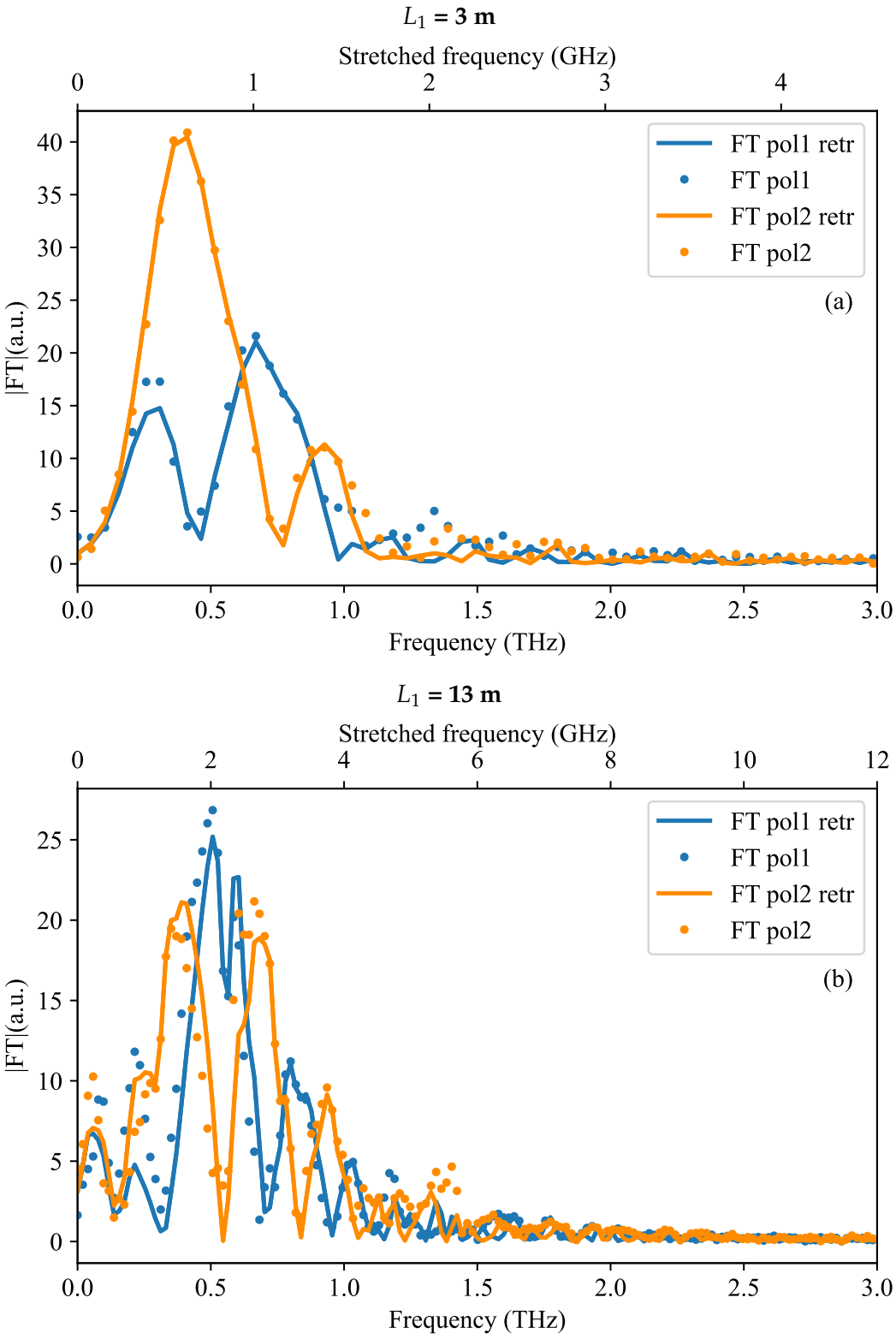

FIGURE 3.9: Single shot Fourier spectra reconstructed by MRC algorithm for one shot using signals from Figure 3.6, respecting the color code. A good fit is observed between retrieved spectra (in solid line) and measured spectra (in dots) for both polarizations for $L_1 = 3m$ (a) and for $L_1 = 13m$ (b).

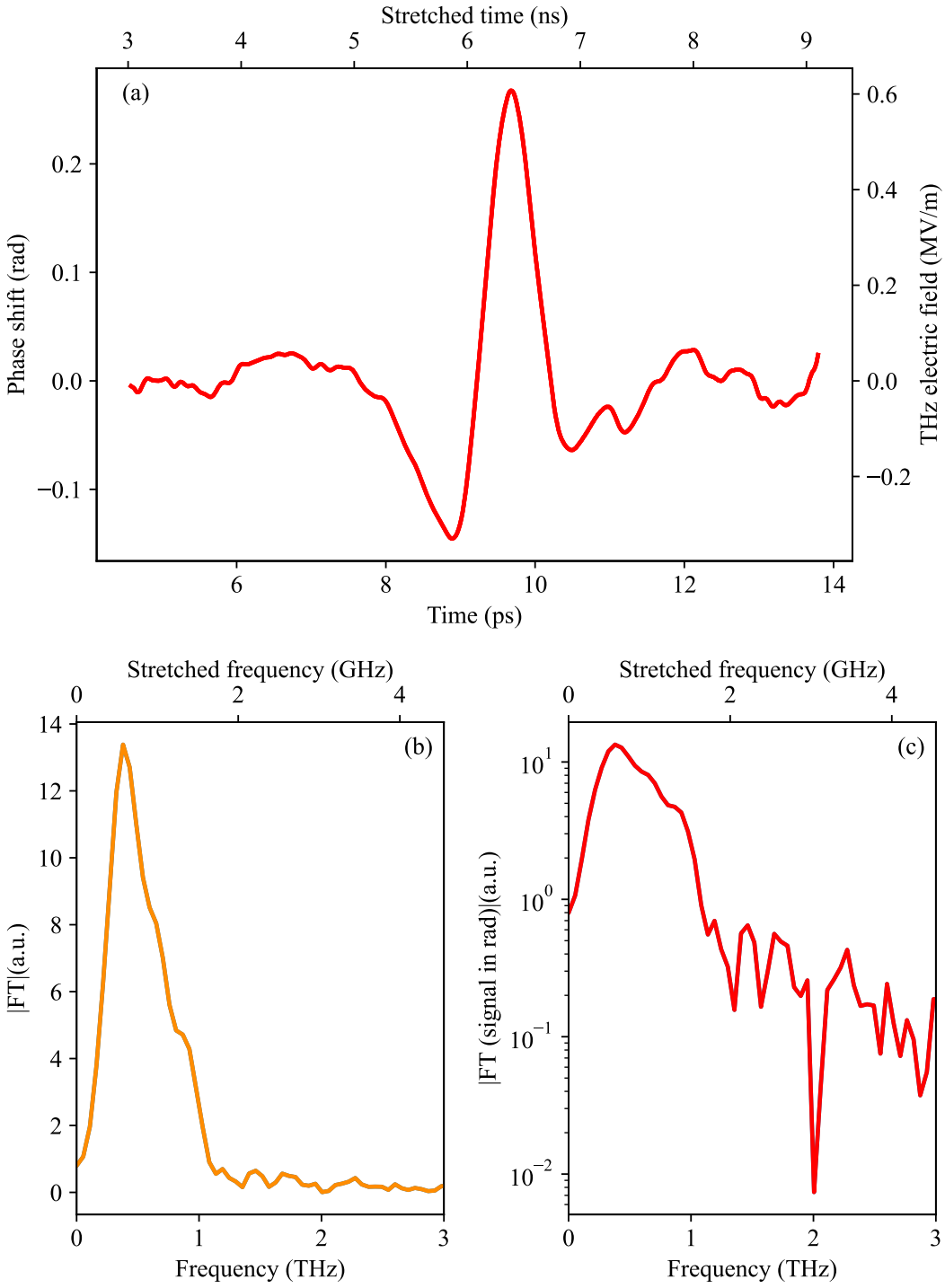

FIGURE 3.10: (a) Single-shot CDR THz signal of a THz signal recorded with the acquisition window corresponding to $L_1 = 3$ m and reconstructed by MRC algorithm representing the phase shift induced by the THz in the EO crystal with its associated THz single shot spectrum in (b) and in logarithmic scale in (c).

An estimate of the fiber length inside the laser can be deduced using the equation $T = \Delta\lambda DL$ where $\Delta\lambda$ is the spectral width of the laser (35 nm in this case) and D the dispersion of the fiber (D∼-44 ps/nm/km for PM980) and L the fiber length. For the

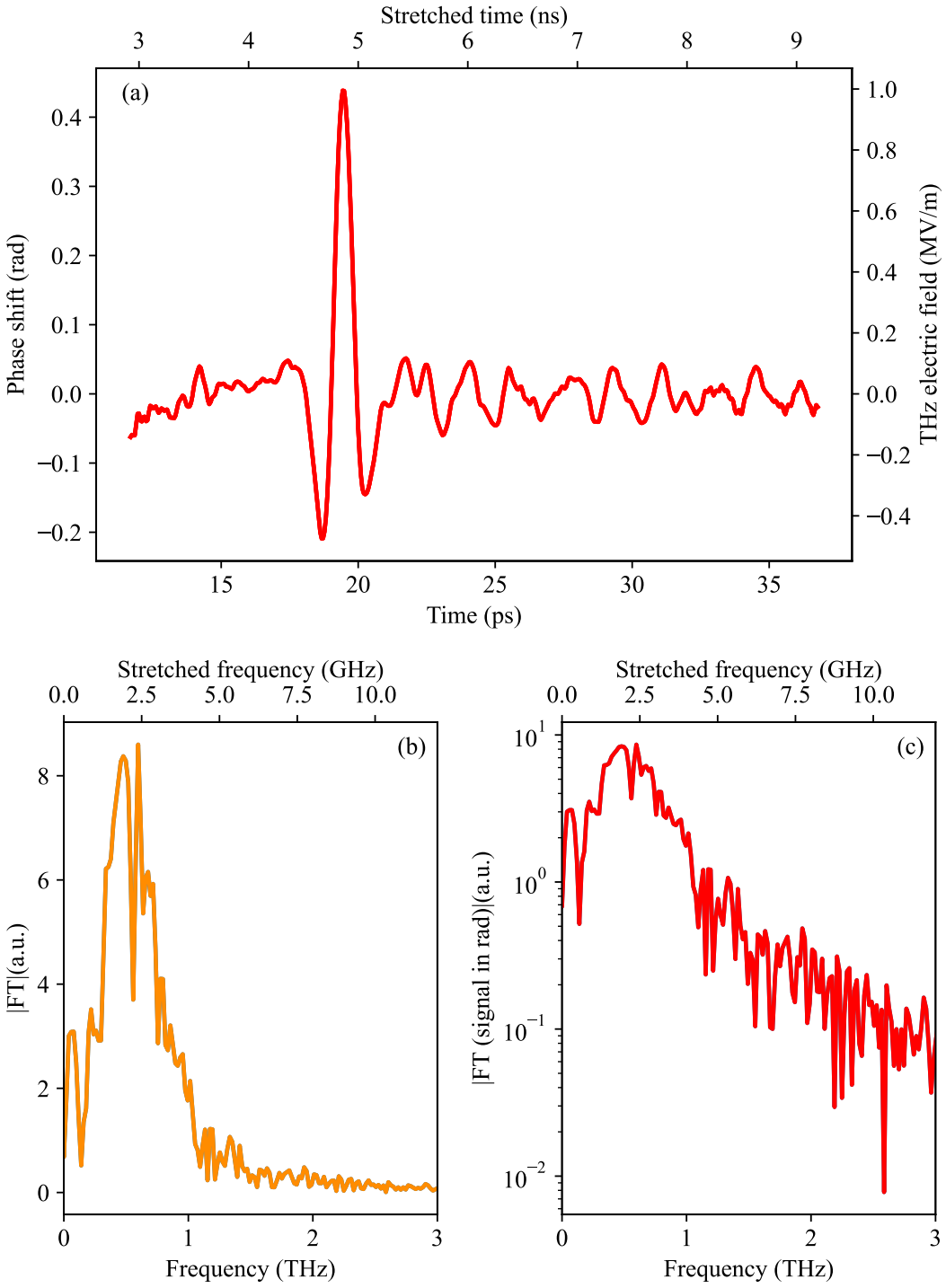

FIGURE 3.11: (a) Single-shot CDR THz signal of a THz signal recorded with the acquisition window corresponding to L_1 = 13 m and reconstructed by MRC algorithm representing the phase shift induced by the THz in the EO crystal with its associated THz single shot spectrum in (b) and in logarithmic scale in (c).

case where $T_0 = 4.927$ ps and $\Delta\lambda = 35nm$, L_0 can be estimated to be equal to 3.19 m. This results in an estimated stretch factor of 248 for $L_2 = 4km$, $L_0 = 3.19m$ and $L_1 = 13m$. However, this value is just an estimate and is not accurate. Two methods

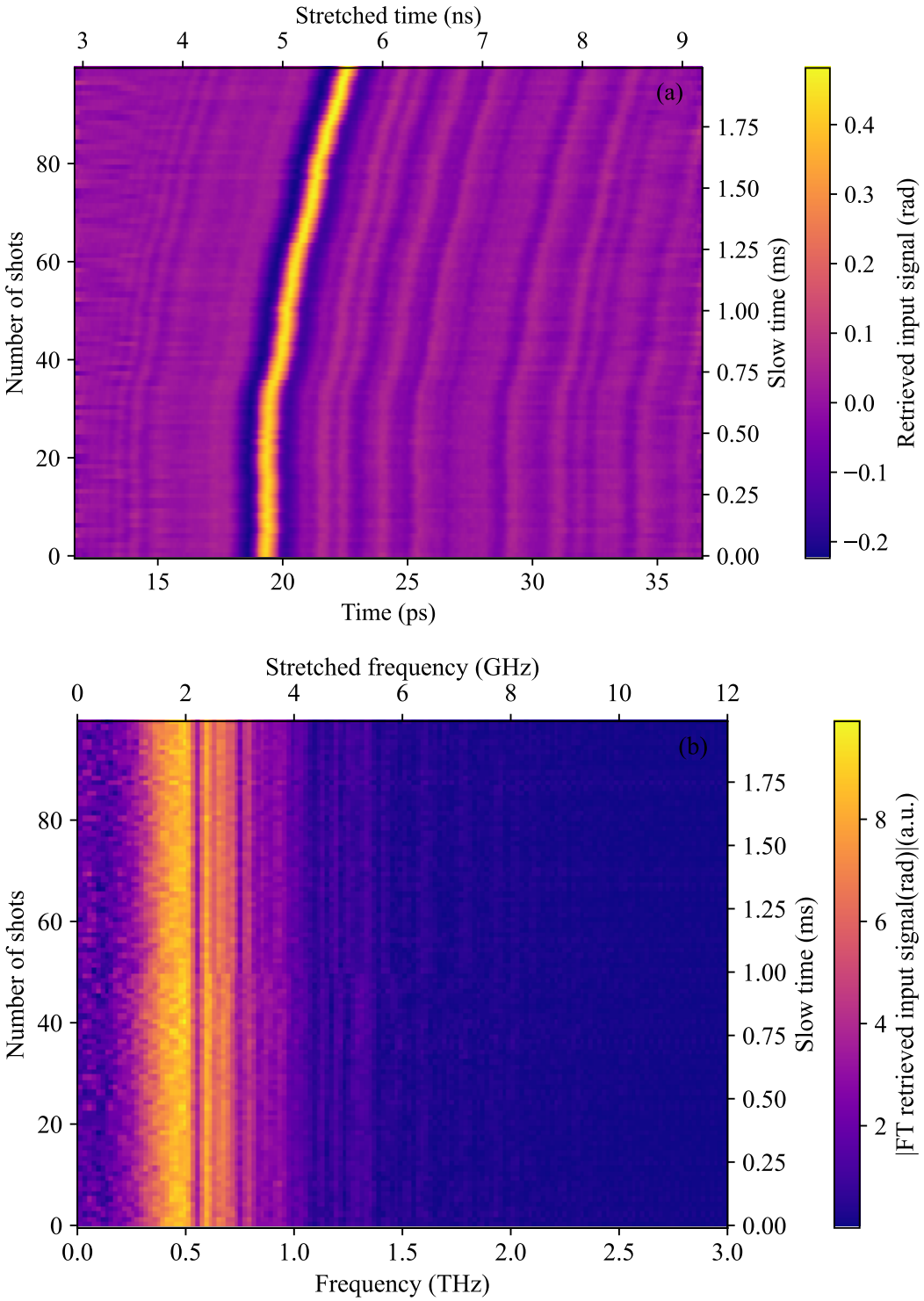

FIGURE 3.12: (a) Color map showing the CDR THz signal reconstructed showing the evolution over many shots as well as (b) their single shot spectra, recorded with the 20 GHz oscilloscope.

were employed here to determine the stretch factor M value: THz optical filters and water absorption lines.

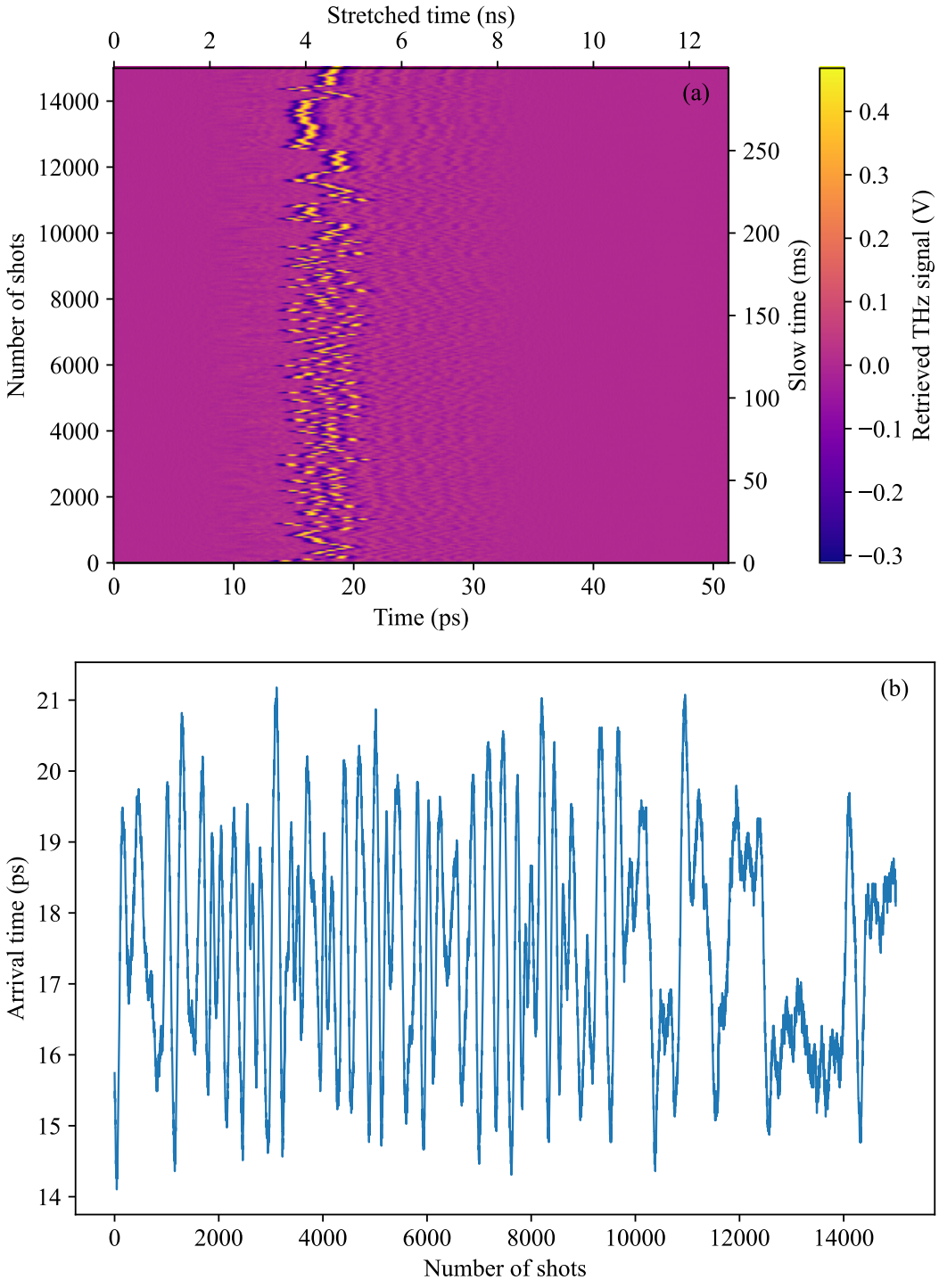

FIGURE 3.13: (a) Colormap showing the reconstructed EO signal in Volts for a set of data recorded in sequence mode capturing more than 14000 electrons bunches recorded with the 20 GHz oscilloscope, exhibiting a high jitter. (b) Representation of the bunch arrival time to the CDR source showing a high jitter ranging from 14 ps to 21 ps with an average arrival time at 17.49 ps with a relative standard deviation of 1.5 ps.

3.5.1.2 First calibration using THz filters

In order to determine the magnification factor resulting from the photonic time-stretch, we used optical filters at THz frequencies. With their specified frequencies, these filters serve as good calibration tools for this kind of experiments, as one can correspond the measured main frequency peak detected in the THz optical spectrum on the oscilloscope with the actual filter frequency. At ELBE, we placed a filter after the mirror that reflects the THz to the EO setup at maximum THz input power. We used two band pass filters, with 400 GHz and 750 GHz , from Swiss Terahertz.

For the case where L_1 = 13 m:

- Using the 400 GHz filter, we find a stretch factor equal to 251 as seen in Figure 3.14(a).
- with the 750 GHz filter, the stretch factor is approximately equal to 248. With this filter, there is no a "main" peak for which we can determine the exact stretch factor as shown in Figure 3.14(c) due to an absorption line at 751 GHz verifying the value of the stretch factor.

Note that the stretch factor is determined using the average of all shots of $|FT|$ of the THz signal in radians.

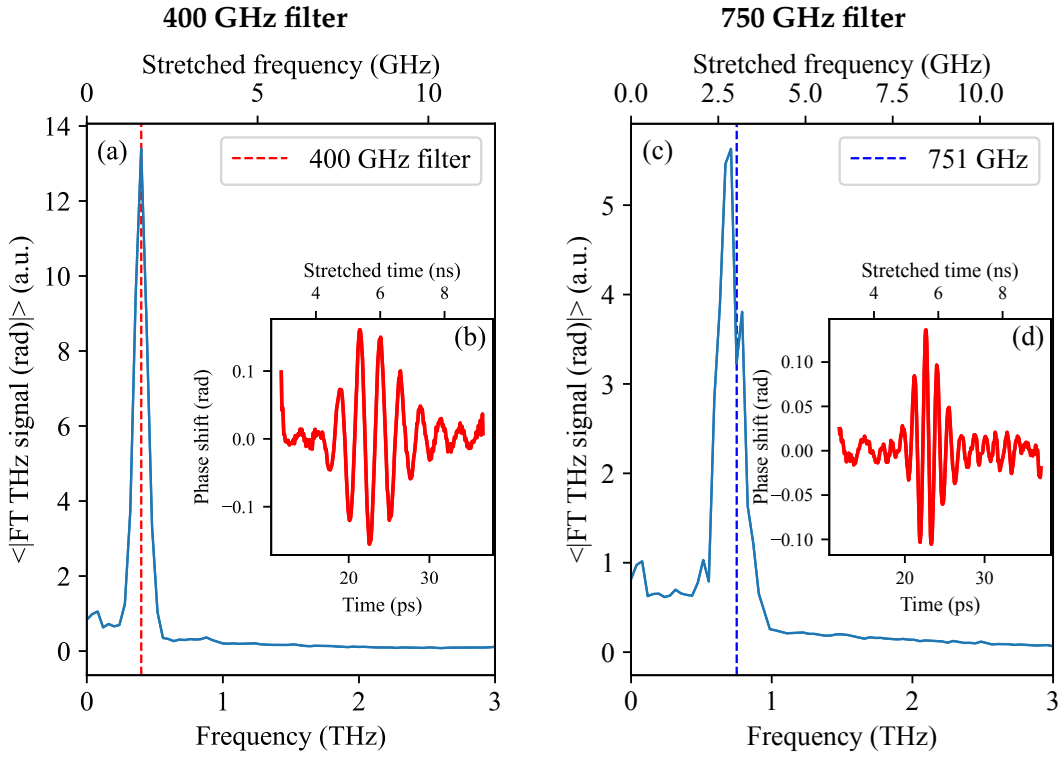

FIGURE 3.14: Average FT spectra recorded with EOS with insertion of THz optical filters of 400 GHz in (a) and 750 GHz filter in (c) for determining stretch factor values when L_1 = 13 m with their respective inset temporal profiles in (b) and (d).

The filters responses gave the range of the stretch factor, which is similar to the

estimated value.

We will see in the next paragraph how to determine more accurately these values using the water absorption rays in the THz spectrum.

3.5.1.3 Precise calibration using water absorption lines

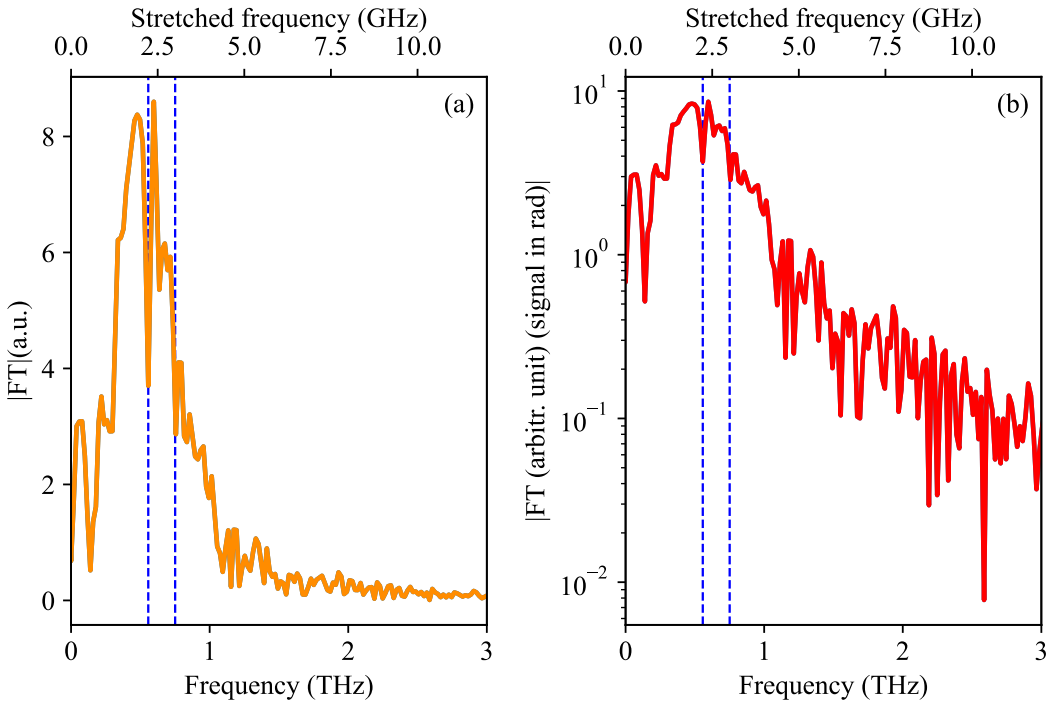

FIGURE 3.15: (a) Single-shot CDR THz with the acquisition window corresponding to L_1 = 13 m reconstructed by MRC algorithm representing spectrum in (a) and in logarithmic scale in (b) showing water absorption lines at 0.557 THz and 0.751 THz.

The THz radiation emitted by the CDR experiences absorption by water molecules as it gets in the ambient atmosphere. This effect is clearly seen in the THz spectrum, measured by EOS as in Figure 3.11(b) and (c), Figure 3.12(b) and Figure 3.15, resulting in the appearance of absorption lines at some frequencies. These water absorption lines, known in THz spectroscopy experiments [129, 130], can be utilized to determine the stretch factor by associating the measured frequencies with the water absorption frequencies in the THz range. They can be identified according to the range of the stretch factor determined using the optical filters in the previous section and deduce accurately the stretch factor value. Figure 3.15(a) and (b) display the water absorption lines in the THz recorded spectrum, which are associated with frequencies of 557 GHz and 751 GHz, resulting in stretch factors of 250 for $L_1 = 13m$.

Note that, in addition to providing the two stretch factors, these measurements also give L_0, i.e., the pulse dispersion at the laser output expressed in length of PM980 fiber. This value L_0 = 3 m will also be useful for designing next experiments as we will see in Chapter 4.

Thereby, water absorption lines appearing in the spectra, helped to determine the precise stretch factor $M = 250$ for $L_1 = 13$ m.
This allows the characterization of the electron bunch arrival time, and the CDR THz duration, which is typically around 0.88 ps, with the laser pulse duration stretched from 24 ps to 6 ns. As a result, a frequency of 1.2 GHz on the oscilloscope corresponds to a 0.3 THz input frequency.

3.5.2 Noise floor and saturation of the detector

3.5.2.1 Noise floor

Sensitivity, or noise floor of a system, indicates the minimal detectable signal that the system can resolve. This characteristic corresponds to the ratio of the detector noise without THz signal with respect to the input laser power or, equivalently, noise equivalent phase shift in radians or in V/m. This property depends directly on the input laser power, with sensitivity increasing as the input power increases.

We considered different laser powers P_{EO} of 10 mW, 15 mW, 25 mW, 35 mW and 45 mW, and calculated the noise floor as shown in Figure 3.16(b). Results confirm that higher laser powers lead to reduced fluctuations and improve the sensitivity of the detector. So ideally, choosing the highest laser input power ($P_{EO} = 45$ mW), will provide the best detection sensibility.
The noise floor of our setup is found to be 0.025 radian for an input laser power $P_{EO} = 10$ mW, and ∼0.015 rad and for an input power of $P_{EO} = 25$ mW at which the remaining measurements are done.

3.5.2.2 Linearity of the time-stretch detector

As previously discussed, the level of sensitivity can be regulated by adjusting the laser power. However, it is important to note that a tradeoff is linking the chosen sensitivity and the dynamic range of the EO system.

In this experiment, the THz signal is encoded onto the probe laser pulse and an amplified photodetector is employed to suppress the common laser shape between the two arms. More precisely, any balanced photoreceiver will saturate when the differential signal (composed by the EO signal and asymetry imperfections here) exceeds a given value. However, it is also important to note that this saturation value depends on the laser power level used in the experiment. Hence, a compromise should be taken in account to optimize the sensitivity while having the highest THz detected field with the highest laser input power.
Therefore, we investigated the linearity of the EO system versus laser power P_{EO} and THz power.

According to Malus' law, the THz power should vary proportionally to $cos^4\theta$ with θ the polarizer's angle (see Figure 3.4). As we represent, in Figure 3.17, the maximal detection phase shift max (ϕ_{THz}), the variation should be linear with $cos^2\theta$. We can see in Figure 3.17 a satisfying linearity throughout the available THz power range for $P_{EO} = 10mW$ and $P_{EO} = 15mW$. Moreover, for higher laser powers $P_{EO} = 25mW$, $P_{EO} = 35mW$ and $P_{EO} = 45mW$, this linearity is observed only for low THz powers (lower angles).

Therefore, when implementing balanced detection, it is important to keep in mind this trade-off between laser power and THz power to ensure that the linearity

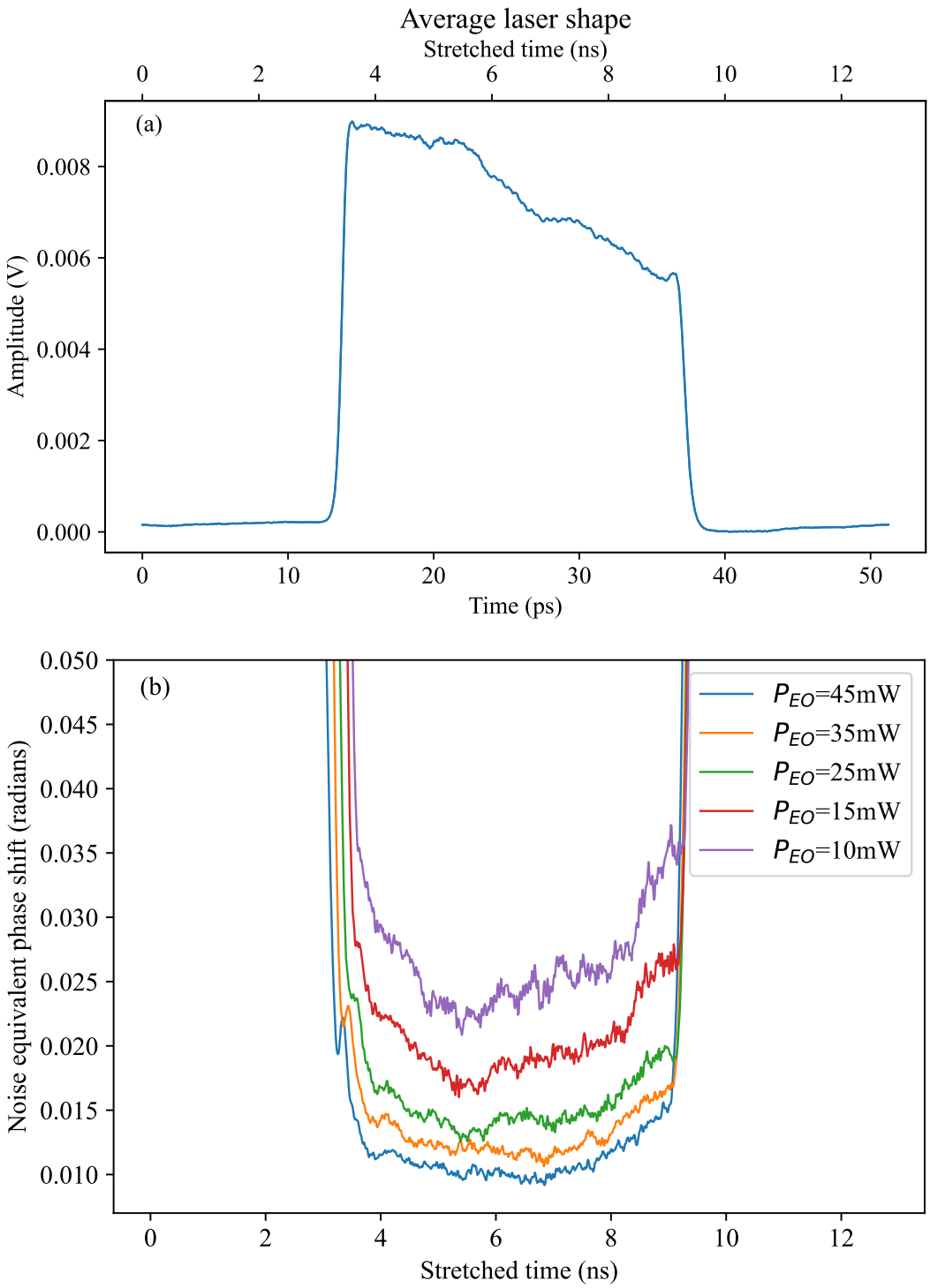

FIGURE 3.16: (a) Laser shape stretched up to $\sim$ 6 ns recorded by the oscilloscope. (b) Noise equivalent phase shift or fluctuations of the experimental setup for different laser input powers.

and the sensitivity are adequate to measure the maximum THz power accurately without saturation and avoid THz waveform deformation.

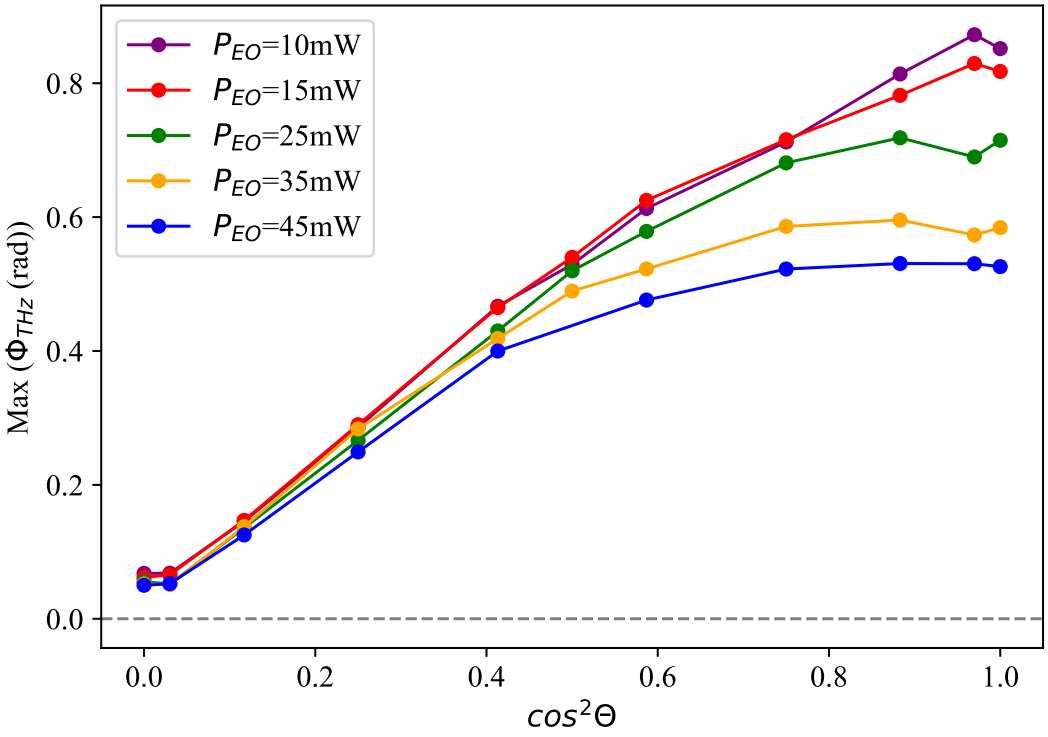

FIGURE 3.17: Dependence of the maximal phase shift measured by EOS versus THz polarizer angle for several laser input powers. A linear response is observed at low laser powers ($P_{EO} = 10mW$ and $P_{EO} = 15mW$) while a non-proportionality response is observed at higher input powers ($P_{EO} = 25mW$, $P_{EO} = 35mW$ and $P_{EO} = 45mW$). P_{EO} is the laser power just before the second collimator of the EO head.

3.6 Machine study at ELBE

The development of such a diagnostic tool opens up new horizons for two main research fields. First, for time domain spectroscopy, the single-shot operation is not sensitive to time jitter, in contrast with classical (scanned) TDS. Secondly, the access to the reach CDR THz pulse can be potentially used as a diagnostic tool for the accelerator.

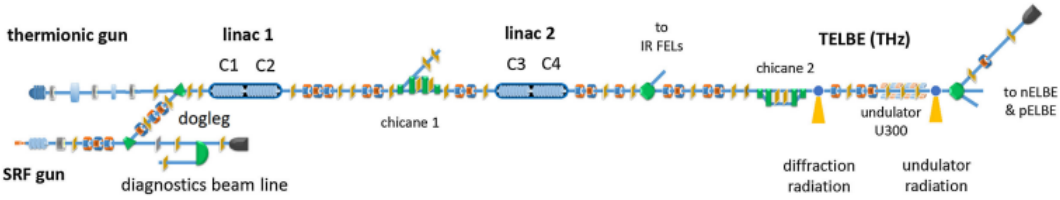

FIGURE 3.18: Diagram of THz beamline at ELBE illustrating four RF accelerating cavities and THz radiation production. Figure from [131].

Therefore, testing our detection scheme at TELBE, we naturally studied the EO signal, while varying several machine parameters. Our study involved two main

investigations. Firstly, we deduced from EO measured signals the detected THz signal versus the bunch charge. Secondly, we recorded the THz CDR pulses for different compression conditions of the electron bunch. Technically, this has been performed by varying the phase of one of the accelerating cavities (see Figure 3.18). It was conducted in parallel with a classic Martin Puplett THz spectrometer.

3.6.1 Study versus bunch charge

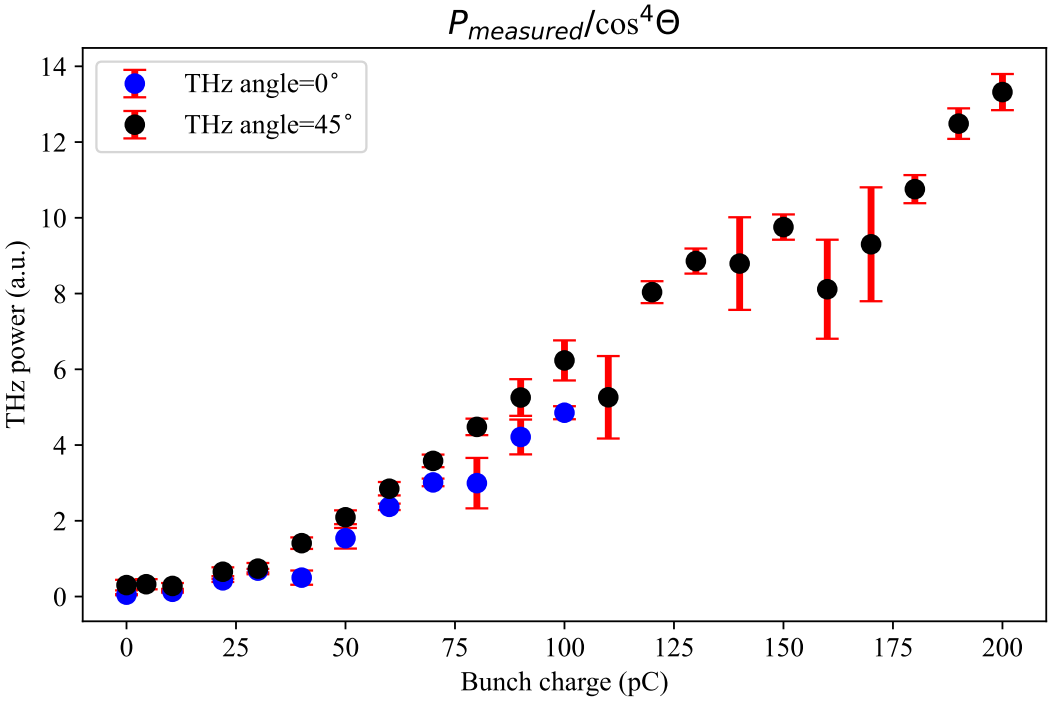

FIGURE 3.19: Study of the CDR THz power measured by EOS as function of the bunch charge in the accelerator for two fixed THz input power.

The ELBE machine utilizes a magnesium (Mg) photocathode driven by a 258 nm laser system to extract electrons forming the initial beam. The drive laser system is followed by a quarter wave plate and a polarizer in order to attenuate and control the laser power sent to the photocathode. The laser power determines the bunch charge in the accelerator by extracting electrons from the cathode. The higher the laser power is, the more electrons will be extracted.

The present investigation explores the impact of varying the laser input power sent to the photocathode on the electron beam quality by measuring the THz emitted radiation.
To achieve this, we varied the bunch charge by modifying the photocathode laser power for the injector, noted P_{laser}, which was controlled from the control room by changing the polarizer angle of the laser power. Data were collected for each bunch charge to evaluate the THz emitted power.

The EO laser optical power was fixed at $P_{EO} = 25mW$ throughout the study and the THz power was set on the monitor screen to $P_{monitorTHz} = 22mW$. The THz polarizer was initially fixed at 0° to obtain higher signals, but as the bunch

charge increased, we observed saturation in the THz emitted power and therefore attenuated the THz signal by setting the THz polarizer at 45°.

Results presented in Figure 3.19 show a quadratic increase in THz power with bunch charge up to approximately ∼150 pC. As far as the bunch charge increases, this quadratic behavior is not observed anymore, where we can see more like a linear evolution. This can be due to collective effects leading to important changes of the bunch shape at high bunch charges. In this experiment, the chicane parameters were fixed during the experiment to maintain transverse beam parameters.
According to theory, the radiation spectral angular distribution of the electron bunch is defined by an incoherent and a coherent component:

$$\frac{d^2I}{d\omega d\Omega} = N\{1 + (N-1)F(\omega)\}\frac{d^2I_{se}}{d\omega d\Omega} \tag{3.3}$$

with $F(\omega)$ the bunch longitudinal form factor of the normalized charge distribution $\rho(z)$, N the electron number constituting the electron bunch and w denoting the angular frequency of the radiation with

$$F(\omega) = |\int \rho(z) e^{\frac{-i\omega z}{c}} dz|^2 \tag{3.4}$$

The coherent part exhibits a quadratic increase only if the form factor $F(\omega)$ of the charge distribution remains unchanged.

This behavior is consistent with previous work, detailed in [131], which demonstrated a similar dependence of the electron bunch charge on undulator radiation power measured with a powermeter, limited to coherent emission up to 150 pC. However, our measurements have the advantage of capturing the shape of the emitted CDR THz signal of each electron bunch.

3.6.2 Study versus the RF phase of cavity number 4

The ELBE acceleration mechanism involves the use of four radiofrequency (RF) cavities, as illustrated in Figure 3.18 to achieve electrons acceleration. The fourth cavity was recently installed, allowing for energies up to 40 MeV [19]. Researchers involved in machine development were interested in evaluating the performance of the latest. This prompted conducting EOS measurements of the THz signals emitted by CDR at different RF phases and analyzing the variation of THz detected power as function of the phase as well as their single-shot spectra. These results were compared with those detected by a commercial THz powermeter. We can see in Figure 3.20 a similitude between EOS detected power and THz powermeter measurements. The detected THz power shows approximately a Gaussian distribution as function of the RF phase, with an optimum at $\sim 47^\circ$ phase. This behavior can be attributed to the maximum compression of electrons achieved at the optimal phase, which allows for higher emitted CDR power. The phase of the electric field generated by the RF determines the acceleration of electrons entering the cavity, with electrons arriving at a maximum of field acquiring more energy and are being accelerated more rapidly than those arriving at a minimum. Consequently, in order to ensure an optimal effect in acceleration, the RF cavity should be adjusted at a specific phase angle so that the electrons acquire the maximal field and get compressed to the maximum.

In Figure 3.21, we represented the THz reconstructed signals in the first row with their FT spectra in the second row in single shot by our EOS system at various phases. The third and fourth rows show, respectively, the phase shift of one THz signal and its FT spectrum giving an idea about the bunch length.

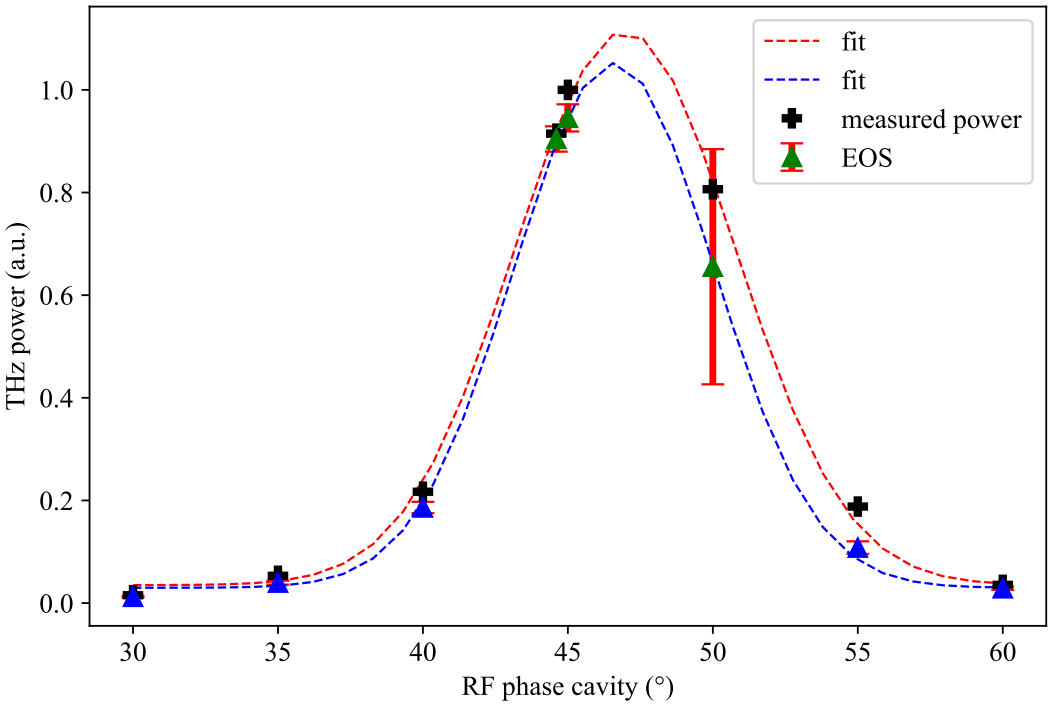

FIGURE 3.20: Variation of THz power for different RF phases of the cavity measured by EOS versus THz power detected by a commercial THz powermeter.

3.7 Conclusion and perspective

In this chapter, we have presented a novel experimental setup that combines the photonic time stretch approach with the diversity electro-optic sampling, marking the first time that these techniques have been used together. This was demonstrated by measuring the ultrafast THz signals emitted by the ELBE CDR source at a high repetition rate and a sub-picosecond resolution in single-shot mode. The CDR THz radiation is measured in single shot with a broadband spectrum, ranging from 0.1 THz to above 1 THz. Notably, the measured pulses demonstrate stable behavior.
Measurements shot after shot, allowed to observe the electron bunch arrival time revealing the time jitter. Additionally, our diagnostic tool validates the study of machine parameters of the linear accelerator ELBE, including the bunch charge and the RF cavity phase.
Our setup is autonomous (once adapted) and capable of continuous measurements over long periods of time. During a single night of operation, the system recorded automatically 301 sets of data in sequence mode, indicating that the system is robust and reliable. The only limitation was the oscilloscope memory. If needed, continuous (real time) operation should nevertheless be possible by an ADC board instead of an oscilloscope.

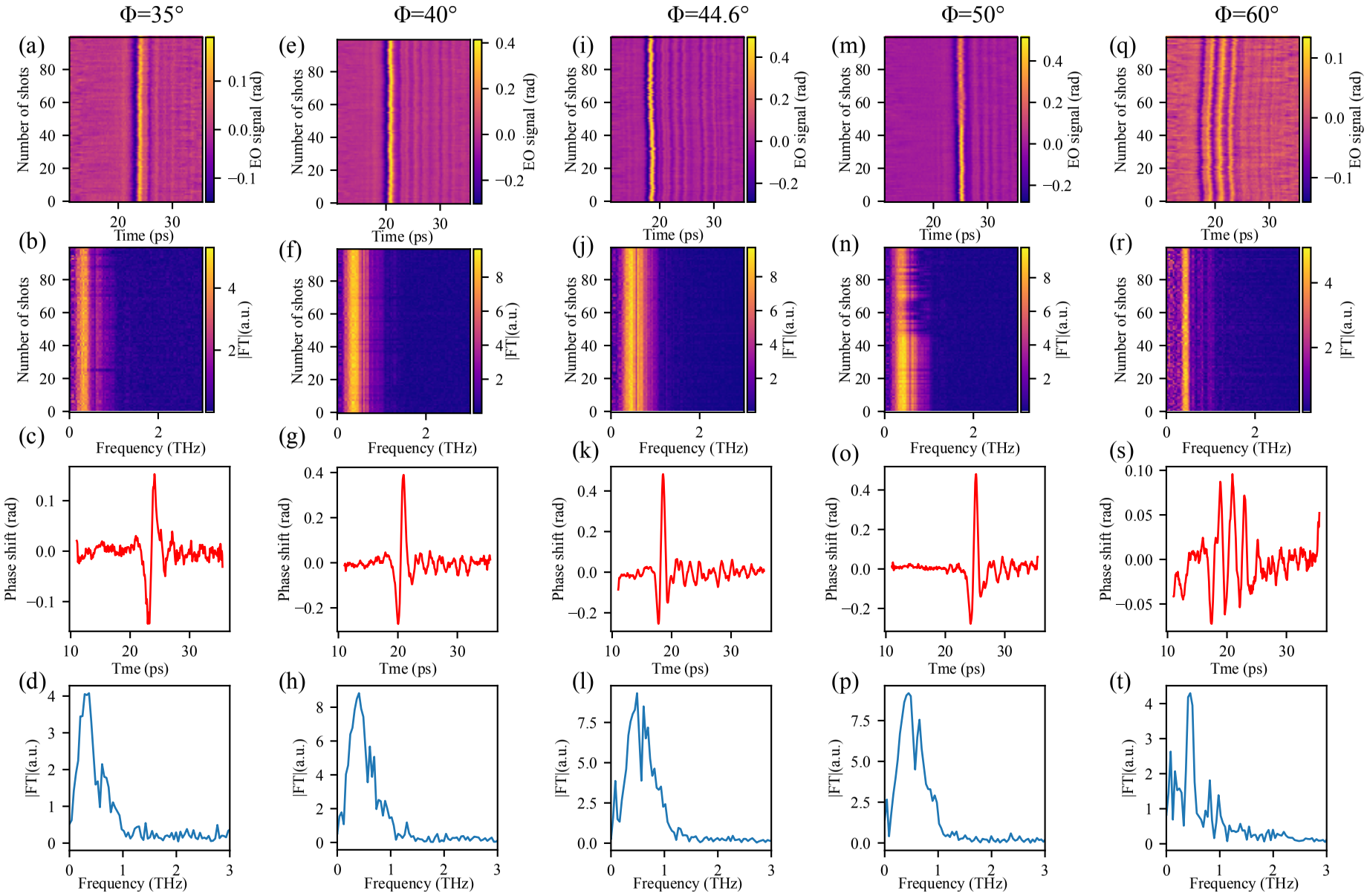

FIGURE 3.21: Series of EOS measurements performed for different RF phases. Each column correspond to RF phases successively of 35°, 40°, 44.6°, 50° and 60°. The first row shows the THz reconstructed phase shift of the THz signal shot-to-shot, followed by their respective FT spectra in the second row. The third and fourth rows show, respectively, the temporal profile and spectrum of one selected THz shot, corresponding to one electron bunch.

This optical photonic-based setup is compact and ready to be installed at ELBE, allowing real-time measurements in single-shot and enabling the monitoring of accelerator functionality. Additionally, the setup can be easily adapted to fit different recording windows, within certain limits, by changing the fiber length L_1.

This contribution represents a significant advancement in ultrafast measurement systems and expands the range of applications such as THz spectroscopy measurements, for table-top experiments, irreversible phenomena and improving synchrotrons and particle accelerators functionality. Our monitoring setup has a 26 MHz acquisition rate[3], which is significantly higher than the 50 kHz repetition rate of the THz source, indicating the potential for even higher repetition rates.

In the next chapter, we will explore how, with few modifications, this innovative setup can be adapted to measure in real-time the full FEL pulses at ELBE in single-shot.

[3]The laser repetition rate is 78 MHz. For data processing, three pulses are needed, one for each polarization and one used as a reference without THz signal, leading to a 26 MHz acquisition rate.

Chapter 4

First single-shot measurements of the FEL pulses: experiment at ELBE

4.1 Introduction: Investigating the free-electron laser (FEL) at ELBE with the previous constructed detector

Referring to previous chapter, a significant advancement has been made in the development of THz detectors, combining photonic time-stretch with diversity electro-optic sampling allowing to measure up to 26 MHz repetition. With this detector, we were able to measure in single shot, with a sub-ps temporal resolution, the single-cycle THz coherent diffraction radiation emitted by the electron bunches at the linear accelerator ELBE, at a 50 kHz repetition rate with a broadband THz spectrum around 0.3 THz.

Building upon this success, we looked after investigating, with our "THz oscilloscope", more challenging THz sources such as the THz free-electron laser (FEL). One possibility was the FEL at ELBE emitting monochromatic radiation with adjustable frequencies, from 1.2 THz to $\sim$16 THz at a 13 MHz repetition rate. This THz source emits multi-cycles THz pulses, requiring a long acquisition window and presents a high repetition rate of 13 MHz. Though, a full characterization of the THz pulses emitted by the FEL in single-shot is demanding. These measurements are needed to study the dynamics of the FEL as well as to characterize the emitted radiation. In addition, these THz sources lack of carrier envelope phase (CEP) stability, required for THz spectroscopic applications. Previous techniques have been developed to get information on the CEP in single-shot [132] but do not provide the temporal profile in single-shot.

As our experimental detection tool has technically the ability to record the complete electric field of THz signals, we aimed in this chapter to measure in single shot the temporal profile, carrier and envelope, of the THz pulses emitted by the FEL at ELBE, marking the first-ever single-shot measurement of a FEL pulse or even a mode locked laser. This piece of information will give access to the CEP and observe the dynamics of the FEL in single-shot mode.

We will describe in this chapter the experiment conducted at the THz FEL at ELBE to capture and characterize the THz pulses emitted in single-shot. We will start by reviewing the FEL characteristics and evaluate through calculations the necessary modifications to the experimental setup to reach and measure successfully the chosen FEL frequency. These measurements will allow to observe the turnon

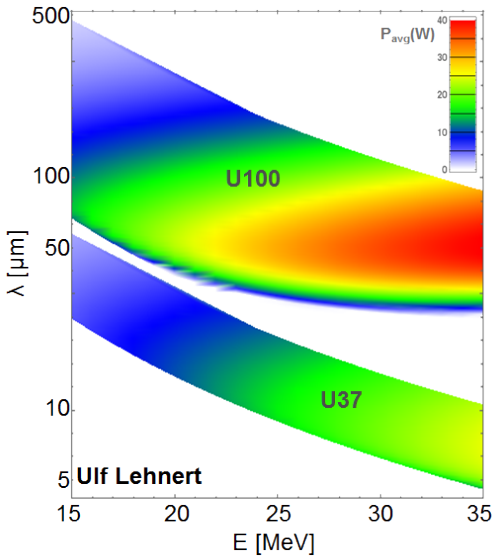

FIGURE 4.1: Energy and wavelength range provided by undulators U37 and U100. Credits to Ulf Lehnert.

and the turnoff of the FEL pulses shot-by-shot. By characterizing the temporal profile, envelope and carrier of the FEL pulses, we seek to address the challenge of CEP instability and provide insights for optimizing FEL performance. We will explore in a second part the impact of detuning the FEL by varying the mirror position to find the optimal configuration for generating CEP-stable pulses.

4.2 FELBE: FEL at ELBE

	U37	U100
Undulator period λ_U	37 mm	100 mm
Number of periods N_U	54	38
Undulator parameter K_U	0.4-1.35	0.5-2.8

TABLE 4.1: Parameters of the undulators of the FELs at ELBE.

Wavelength range	5 - 40 μm	Undulator U37
	18 - 250 μm	Undulator U100
Pulse energy	0.01 - 2 μJ	depending on wavelength
Pulse length	1 - 25 ps	depending on wavelength
Repetition rate	13 MHz	3 modes: - continuous wave - macropulse >100 μs, <25 Hz - single-pulse switched at kHz/Hz

TABLE 4.2: Parameters of the FEL radiation at ELBE.

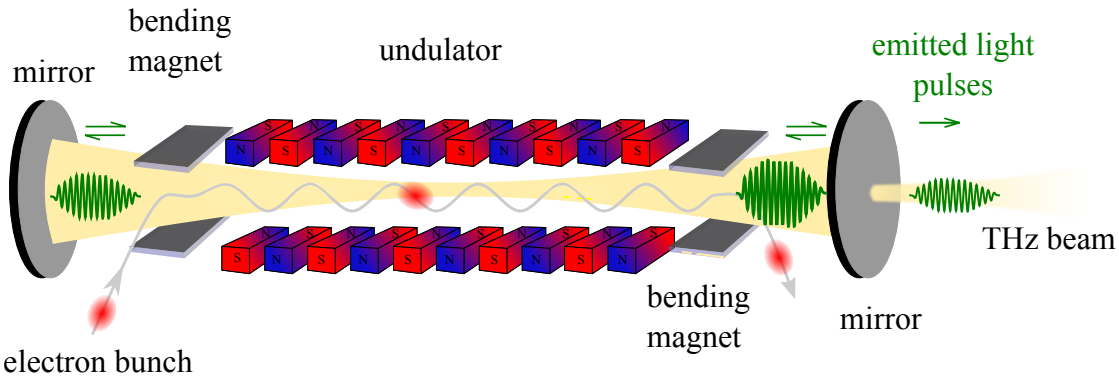

FIGURE 4.2: Operating principle of an oscillator FEL, consisting of a pair of mirrors forming the resonant cavity for the electron accelerated beam emerging from the accelerator and wiggling in the undulator.

ELBE is equipped with two FEL systems using two different undulators: U37-FEL and U100-FEL with a 37 mm period and a 100 mm undulator period respectively. The undulators properties outlined in Table 4.1. They produce an intense, coherent electromagnetic radiation that can be tuned from the mid to the far infrared covering wavelengths from 5 μm-250 μm emitting pulses with durations ranging from 1 to 25 ps, and pulse energies varying from 0.01 to 2 μJ, depending on the wavelength, as seen in Figure 4.1. Among the wide range of wavelengths covered by both operational FELs at ELBE, we are interested in measuring FEL pulses with relatively low frequencies and long wavelengths and decided to conduct the experiment at the U100-FEL for THz radiation.

The undulator U100 is installed to cover the far infrared range with wavelengths from 18 μm to 250 μm with energies from 20 to 35 MeV with a first lasing in 2006 [133]. This U100-FEL uses an undulator, composed of 38 magnet periods with 100 mm long each with adjustable gaps. The undulator gap parameter K can be varied from 0.5 to 2.7 as shown in Figure 4.1 to vary the emitted radiation wavelength according to Eq. 1.1. This FEL is optical resonator as described in paragraph 1.2.4.1 based on an optical cavity, as seen in Figure 4.2. It is equipped with a parallel-plate waveguide to allow small undulator gaps [134]. The FEL emitted radiation properties are summarized in Table 4.2.

FELBE is an oscillator FEL based on a resonant cavity consisting of two mirrors and an undulator U100, enabling the generation of coherent radiation up to approximately 250 μm, as represented in Figure 4.2. Electrons travel in the resonant cavity passing by the undulator composed by a series of alternating magnets, inducing a transverse wiggling motion of the electron beam orthogonal to the magnetic field, as seen in Figure 4.2. The optical resonant cavity consists of two parallel mirrors focussing the electron beam with respect to the undulator axis and separated by a resonant length equivalent to the distance ensuring that the produced circulating light pulse coincides with the subsequent electron beam at the entrance of the undulator. The extraction ratio from the resonant cavity over the entire wavelength range is done using mirrors with different outcoupling hole sizes to control the amount of extracted radiation.

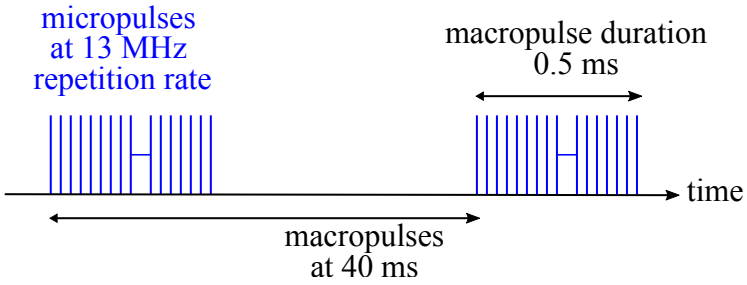

FIGURE 4.3: Temporal structure of THz emission in micropulses at 13 MHz repetition rate in macropulses of 0.5 ms at a period of 40 ms chosen for FELBE experiment.

4.3 THz source properties and setup modifications

4.3.1 FEL time structure

The FEL at ELBE can be emitted in 3 different modes (as described in Table 4.2): in continuous wave at a 13 MHz repetition rate, in macropulses, or single-pulse switched mode. For this experiment, we chose an emission at 13 MHz in macropulse mode or burst mode as represented in Figure 4.3. This choice was made for two main reasons: to work at moderated powers and decrease the average power around 20 mW and secondly, to allow observing the turnon and turnoff of the FEL. The macropulse period is of 40 ms and the macropulse duration is around 0.5 ms.

4.3.2 THz FELBE operation

To conduct our experiment and due to short shifts, we performed the experiment at a fixed wavelength of 75 μm, generating a THz signal with a 4 THz central frequency in macropulse mode with a 13 MHz micropulse repetition rate. The choice behind this chosen frequency was made according to calculations on the efficiency of the FEL. A tradeoff was taken between the THz frequency and the power of the FEL. When the frequency increases, the power increases. However, to reach higher frequencies, thinner crystals are needed resulting in a low SNR. Thereby, few THz was expected to be suitable frequency at which the FEL is efficient and that can be detected by our detector.

4.3.3 Experimental setup at FELBE: setup modifications

We used the same experimental setup described in Chapter 3. Our experimental setup is configured in phase diversity configuration, allowing to record the two polarization outputs of the EO system. The setup enables signal acquisition at up to 26 MHz repetition rates with a sensitivity less than 15 mrad (0.034 MV/m noise equivalent phase shift see Chapter 3). The advantage of our setup is the flexibility to change the fiber length L_1 and thereby the recording window.

As the signal has a different time duration, it was necessary to change the acquisition window. The U100-FEL undulator consists of 38 periods, excepting FEL pulses with 38 cycles.

Frequency f_1 before stretch	**Fiber length L_1**	**Stretch factor M**	**Pulse width T_1**	**Stretched frequency f_2**	**Number of cycles**
4 THz	3 m	666	9 ps	6 GHz	36
	5 m	500	12 ps	8 GHz	48
	10 m	307	19.5ps	13 GHz	78
	20 m	173	34.5ps	23 GHz	138

TABLE 4.3: Table summarizing the number of cycles achieved and the needed bandwidth detection f_2 as function of the first fiber L_1. The choice is made to reach the FEL frequency while optimizing the detection range and allowing a long recording window.

When choosing the acquisition window length, many factors must be taken into consideration such as the number of periods to be recorded, the THz frequency and the detection bandwidth. All these parameters are resumed in Table 4.3 where we considered the 4 THz frequency and calculated the number of cycles that can be measured as well as the bandwidth needed for recording. First estimate, the number of periods to be recorded, 38 periods for the U100-FEL, should fit within the chirped laser pulse length, taking into account a margin of double the known period number. The recording length duration denoted T_1, determined by the first fiber length L_1 should be the longest to fit all the THz signal periods. Nevertheless, for a fixed recorded duration T_2 dependent of the second fiber L_2, the magnification of the signal resulting from photonic time-stretch decreases for longer T_1, necessitating a higher detection bandwidth. The stretch factor defined by $M=1+\frac{L_2}{L_1}=\frac{T_2}{T_1}=\frac{f_1}{f_2}$ is inversely proportional to the recording window defined by L_1. Hence, L_1 should be as long as possible to capture all periods while ensuring that f_1 is small enough to fall within the detection range of the detector. We can see that a longer prechirped window allows to reach more cycles but requires a higher detection bandwidth. It is worth noting that the balanced detector receiver has a limitation of 20 GHz in terms of bandwidth so f_2 should remain within the capabilities of our balanced detector receiver.

Based on these calculations, summarized in Table 4.3, we chose a fiber length of $L_1 = 10$ m as it should be sufficient and convenient to measure the desired parameters at a frequency of 4 THz. As we previously calibrated the system in Chapter 3 and determined the laser internal equivalent fiber length with $L_0 = 3$ m, the stretch factor is estimated to be equal to 307, resulting in a pulse duration T_1 =19.5 ps and a corresponding stretched THz frequency of 13 GHz.

Based on this reasoning and calculations, we modified our experimental setup to reach and characterize the FEL frequency.

The setup in this study is similar to the previous one with few modifications. The main differences concern the fiber length L_1 and some technical modifications in the components of the EO head. The new setup is represented in Figure 4.4. We used the same Menlo Orange Ytterbium laser at 78 MHz with a 35 nm bandwidth and a 130 mW output power. A HWP and a cube polarizing beam splitter are added to attenuate the laser power, followed by two mirrors for easier coupling. The laser beam is injected using a collimator PAF2A-A10B into a first fiber L_1, chosen to be a 10 m PM980 fiber.
Regarding the EO head, new types of collimators were introduced to replace the

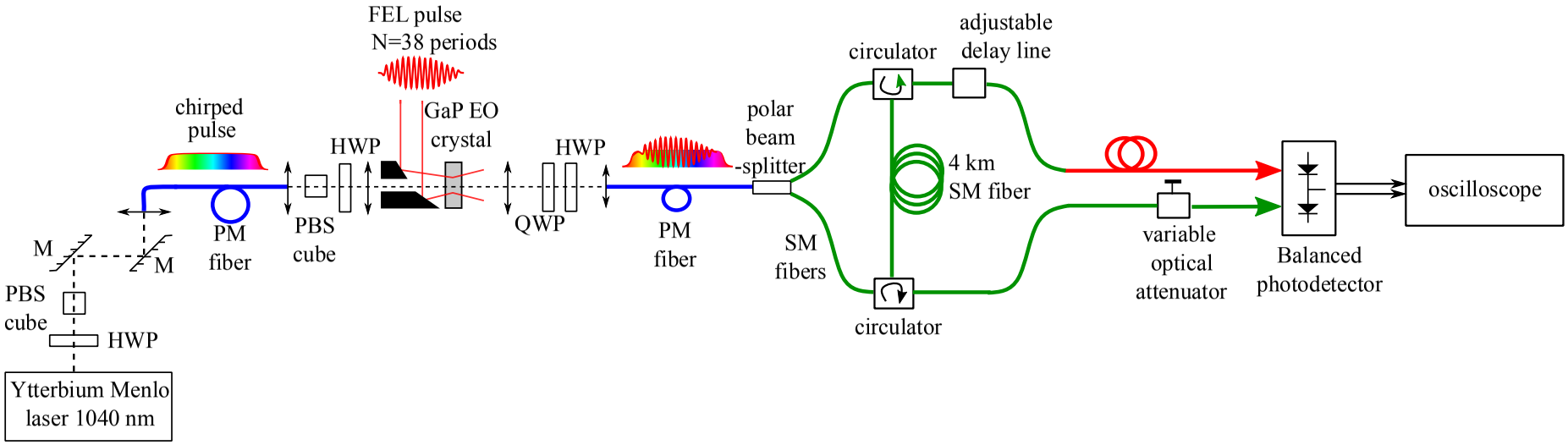

FIGURE 4.4: Experimental setup for FEL pulses detection at FELBE, similar to the one described in Chapter 3 with few modifications such as the prechirp fiber length, some components on the EO head and the EO crystal thickness.

previous ones used with mirrors. We used two collimators with a 12 mm focal length (12APC1064, from Thorlabs) that offer easier manipulation and coupling[1]. The polarizer was replaced by a 5 mm PBS cube (PBS1053, from Thorlabs) to clean the laser polarization.
For signal acquisition, a 33 GHz bandwidth oscilloscope with 128 GSamples/s KEYS-IGHT UXR0334A Infiniium UXR-Series with 10-bit resolution was used. The oscilloscope was double triggered to the macropulse signal at first (the slow signal) and to the micropulse repetition rate 13 MHz signal.

The setup is configured in DEOS. The laser polarization is horizontal. The first HWP is fixed at 22.5°. The second HWP is also set at 22.5° (adjusted in a way that all power on 1 arm without the QWP) and the QWP is fixed at 0°. The THz polarization is horizontal. The crystal is oriented in such a way that the [-110] axis is perpendicular to the THz field.

4.3.4 THz transport and alignement

To align the THz beam transversely with the laser beam, we used a 532 nm visible green laser previously aligned with the THz to do the gross adjustment. For a precise transverse alignment, we superposed the 1030 nm IR laser and the visible laser by replacing the crystal with a pinhole. The temporal timing was similar to previous experiment (see Chapter 3) using a Field Effect Transistor (FET) for the THz [135] and a 5 GHz Thorlabs photodiode for the laser beam.

4.4 EO measurements

As the system is configured in phase diversity, the FEL THz signal was encoded on the chirped laser pulse with its two polarization states recorded separately with the same design described in Chapter 3.
To analyze the data, we used the same data analysis software Since the THz frequency is narrowband, we filtered the data to extract signals around 4 THz slowed down in time to 13 GHz with a 307 stretch factor around 10 GHz and 20 GHz, for a better SNR. Note that the stretch factor $M = 307$ is calculated based on the calibration done for the previous detector. The laser repetition rate is 6 times the THz repetition rate.

Figure 4.5(a) and (b) show the two outputs polarization states in radians for one single THz emitted pulse with their respective measured single shot spectrum in Figure 4.6(a) and (c). We can see that both polarization waveforms are not identical and are much longer than expected. This is spectrally explained by the presence of zeros in their corresponding Fourier transform (FT) spectra. These zeros can be attributed to the zero of the transfer function which are causing the broadening of the temporal waveform. The spectra present a narrowband response with a 4 THz peak frequency clearly defined. In Figure 4.6(b) and (c) are represented the average FT. Figure 4.7 shows the shot-to-shot THz spectra of each polarization recorded individually. Figure 4.8 displays the colormap of the shot-to-shot FEL pulses of one polarization in particular polarization 2, where no zero is observed in the THz spectrum in Figure 4.6(b). Figure 4.8 displays a global view of a full recording, including the startup and turn-off of the FEL. It is important to note that -at this

[1]The used components are the same as the ones described in the previous chapter

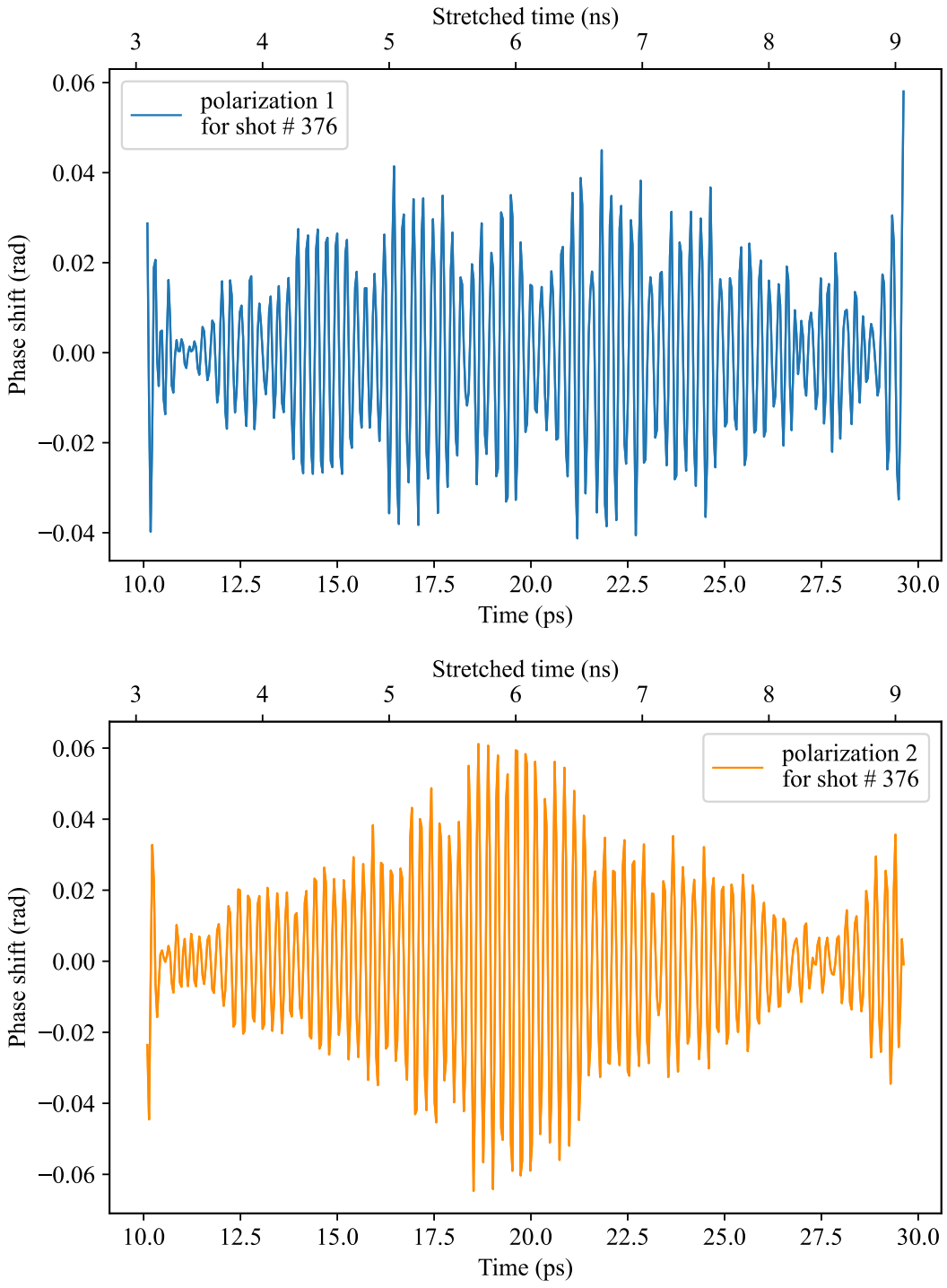

FIGURE 4.5: Single shot temporal profiles of two measured polarizations corresponding to the phase shift induced by the FEL THz signal of one typical single shot signal. Note that this shot corresponds to pulse number 376 in Figure 4.8.

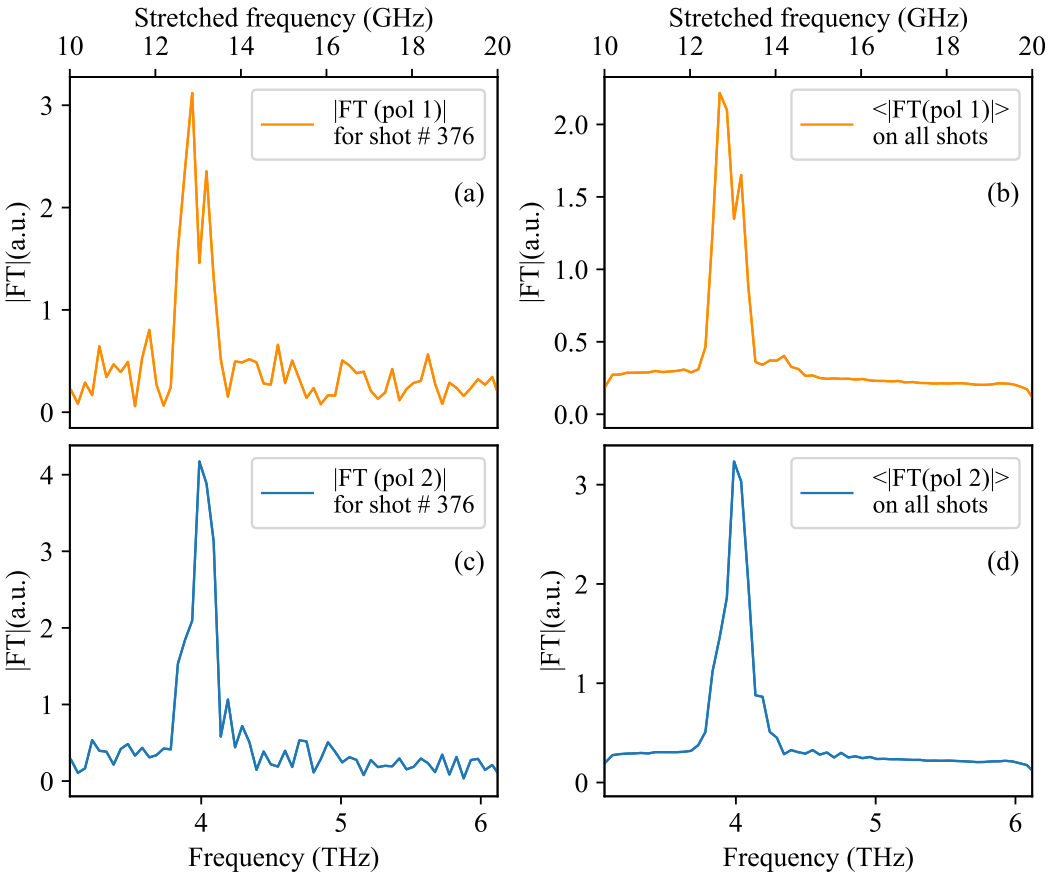

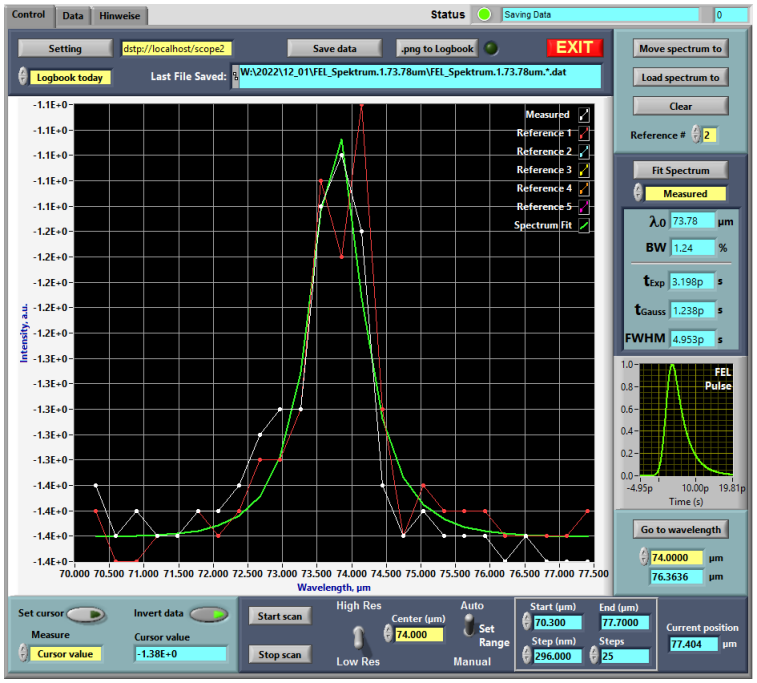

FIGURE 4.6: THz spectra represented by the Fourier transform of the EO measured THz signal emitted by the FEL. (a) and (c) show the single shot spectrum of the measured polarization represented in Figure 4.5 (a) and (c) respectively. In (b) and (d) are shown the average spectra of both polarization over the number of pulses in one macropulse. (e) THz spectrum recorded at ELBE using an interferometer for $L = 8.3380$ mm at 73.78 μm.

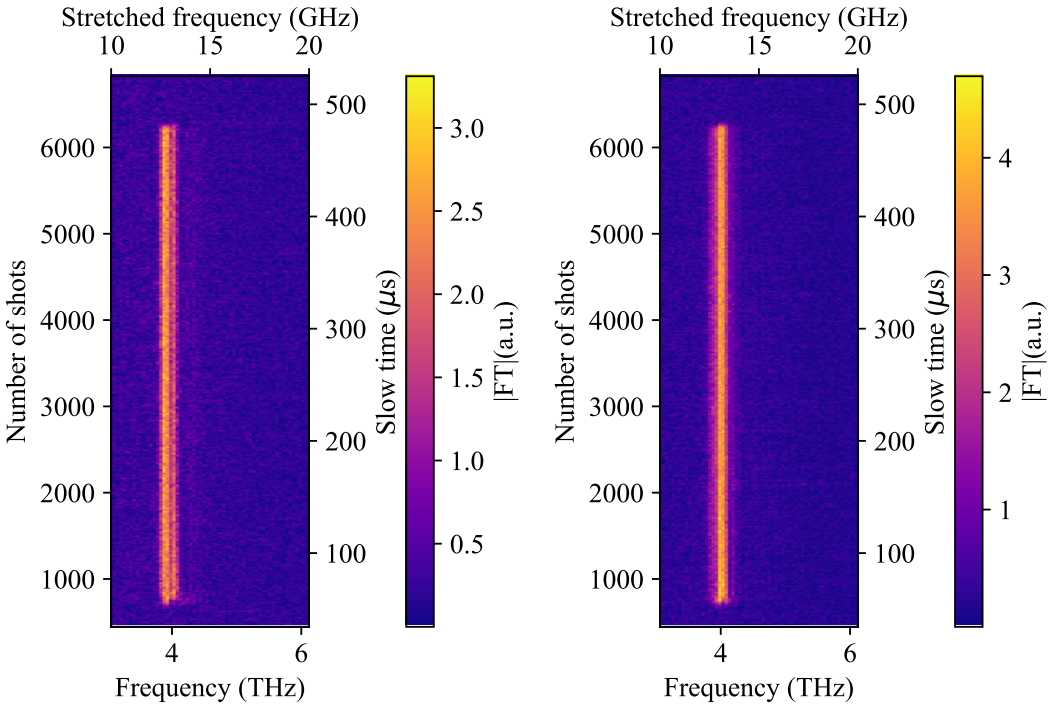

FIGURE 4.7: Colormaps of the measured THz spectra of polarization 1 in (a) and polarization 2 in (b) showing a narrow band spectrum around 4 THz.

scale- the optical carrier is not visible, due to aliasing effect in the display. The optical carrier is visible in the zoom shown in Figure 4.9. The energy evaluation (deduced from the EO measurements) is displayed in Figure 4.10. The horizontal axis of the colormaps represents the time that resolves the THz pulse shape recorded by the oscilloscope. The vertical axis corresponds to the number of THz shots of the FEL.

In parallel, some THz spectrum measurements were taken to verify the THz spectra to compare it with the EOS. The THz measured spectrum in Figure 4.6(e) shows the same spectral properties as EOS measurements.

As the first experimental results of FEL pulses, we settle for showing the two outputs of the EO system. As expected, few deformations appear in the measured temporal profiles. Applying MRC here requires a supplementary effort (that will be done in the near future) as the THz signal is narrowband and the zeros of the transfer functions are very close to each other.

4.5 Study of the CEP versus detuning at FELBE

In a FEL, it is important to have a good synchronization between the electron bunch arrival time and the round-trip time of the FEL pulse. This condition, defined by detuning, affects the efficiency of the FEL. It can be easily modified by changing the distance between the mirrors of the resonant cavity, i.e. the position of one of the

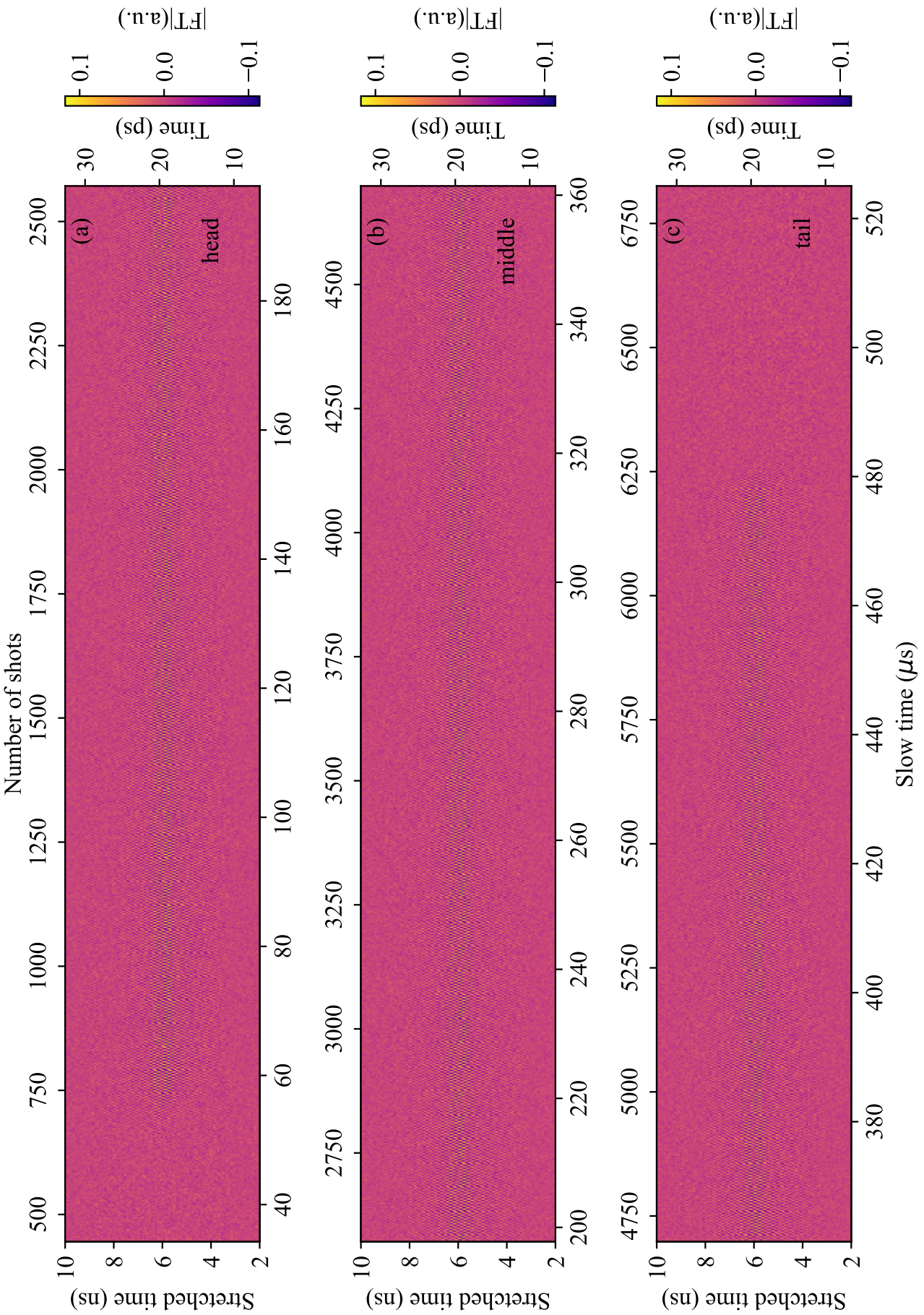

FIGURE 4.8: Three subplots colormaps of one macropulse FEL pulse showing the head of the macropulse in (a), its middle in (b) and the macropulse trail pulse in (c) showing the turn-on and turn-off of the FEL in single-shot. A zoom of the figure is represented in Figure 4.8 for a clear visualization. The CEP is not clearly observable due to aliasing effect.

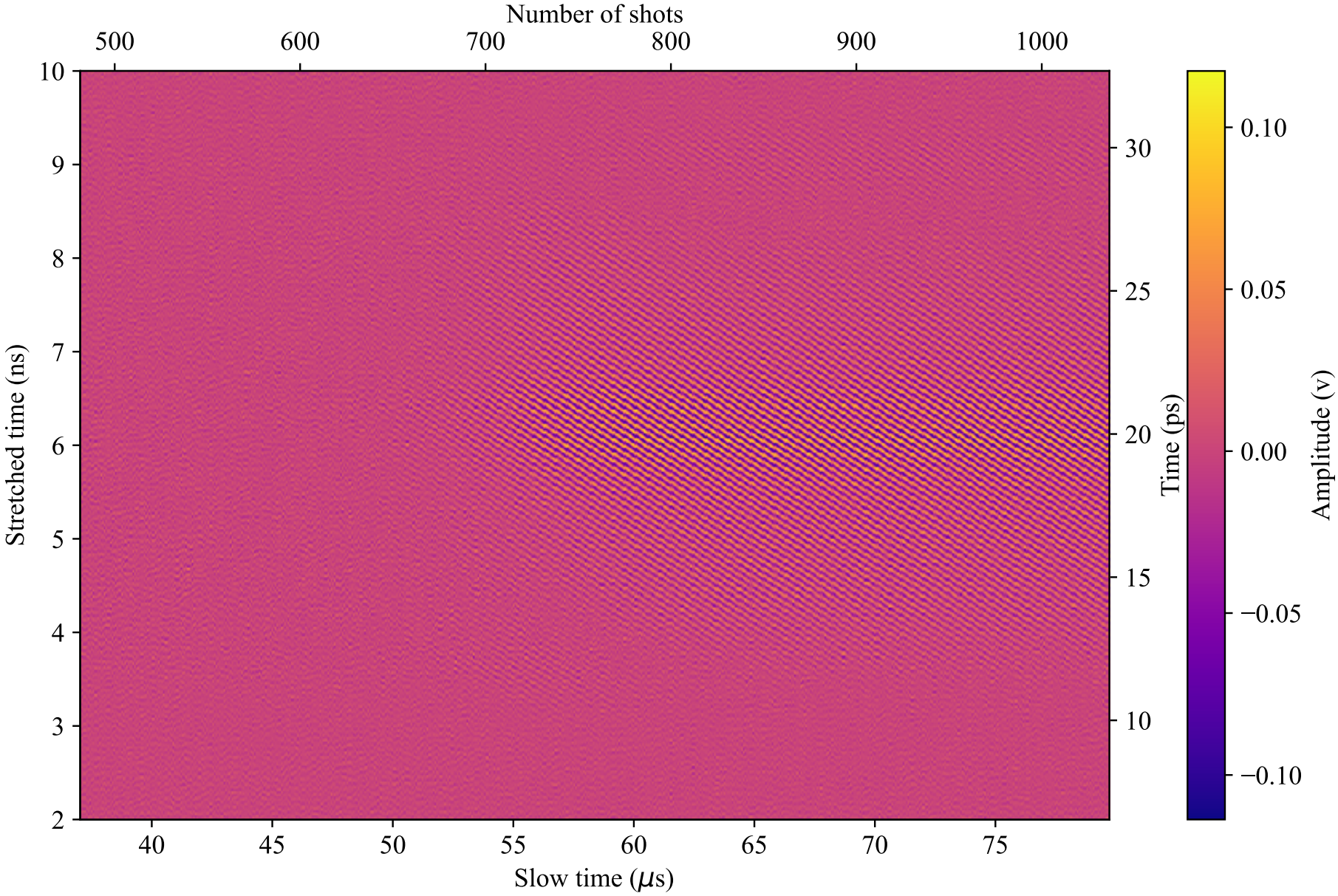

FIGURE 4.9: Zoom of Figure 4.8(a) showing clearly the optical carrier. Note how the phase of the carrier drifts with respect to the envelope, at each shot of the FEL (i.e., the CEP drift phenomenon).

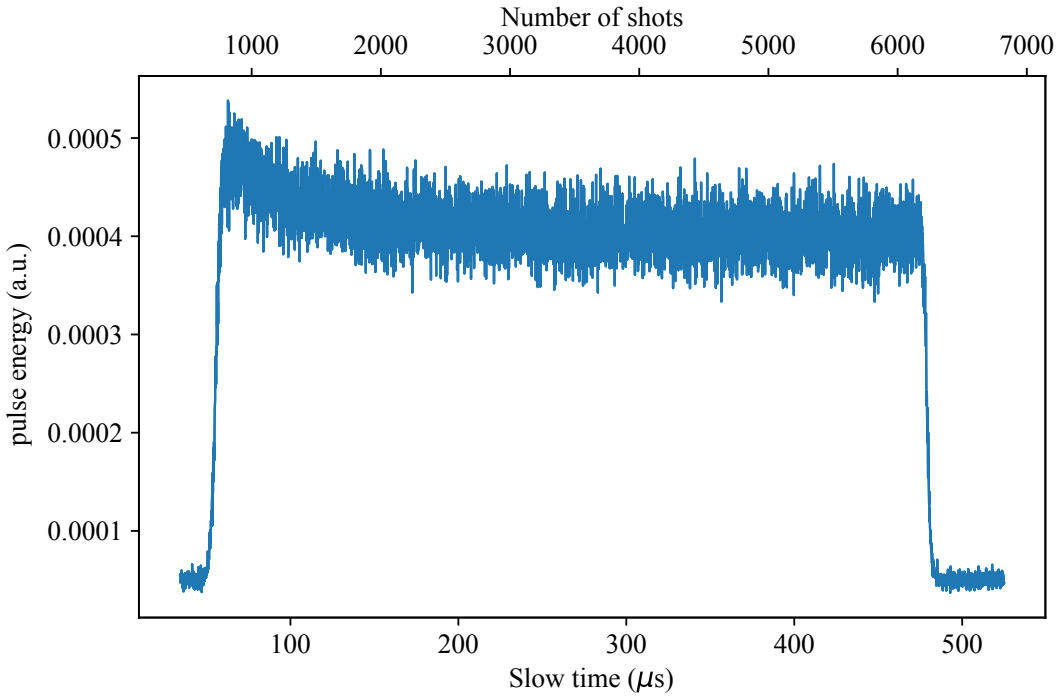

FIGURE 4.10: Energy evolution (in arbitrary unit) of one macropulse calculated from EOS measured polarization 2 showing the turnon and the turnoff of the FEL.

mirrors.

We conducted a study versus the detuning to evaluate the emission of THz for different mirror positions. To do this, we varied the position of one of the two mirrors, scanning from 8.335 mm to 8.494 mm by steps of 6 μm (see Figure 4.11). The FEL was observed to be ON at 8.344 mm and OFF at 8.496 mm. The FEL emitted power measured using a THz powermeter is represented in Figure 4.11 as function of the mirror position. This detuning curve shows a dependency of the FEL emitted power as function of the cavity length, where an optimal efficiency at the left of the curve.

This cavity detuning also affects the carrier-envelope phase (CEP) drift of the FEL. This is defined by the difference between the round-trip time of the THz signal envelope τ_g with respect to the duration of the carrier τ_ϕ in the renonant cavity, as represented in Figure 4.12. This difference is due to the velocity mismatch between the group velocity and the phase velocity when they interact in the amplifying medium, i.e., the electron bunch. This effect is clearly seen in the measured polarization in Figure 4.9 where the CEP is varying from a shot to another and drifting along the pulses.

To study systematically this effect, we represented the two-dimensional Fourier transform $\tilde{E}_{EO}$ of the single-shot EO measured signals over n round-trips $E_{EOn}(t)$ (as the ones shown in Figure 4.8 and Figure 4.9) according to :

$$E_{EO_n}(t) \rightleftharpoons \tilde{E}_{EO}(\nu_{drift}, \nu_{THz}) \tag{4.1}$$

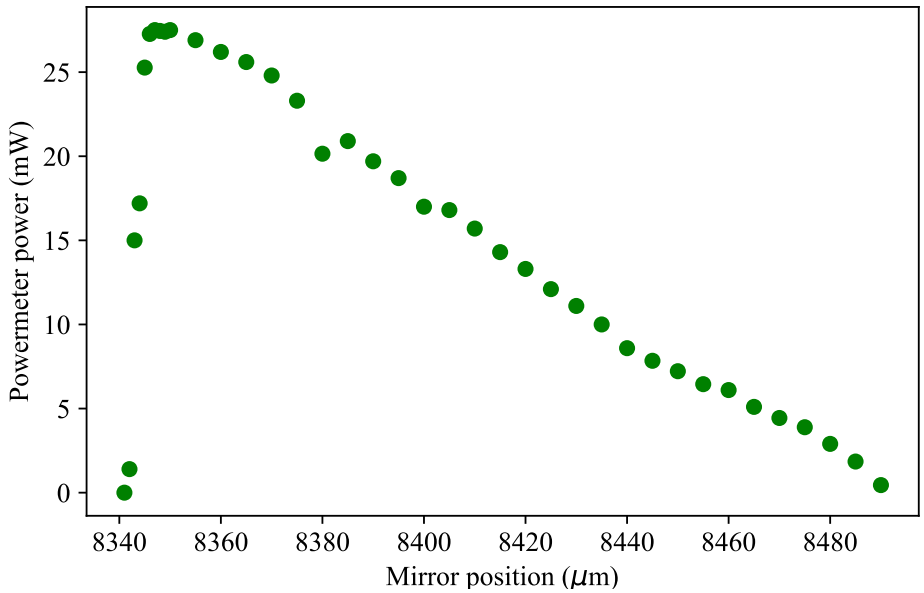

FIGURE 4.11: FEL detuning curve showing the optical power by a THz powermeter.

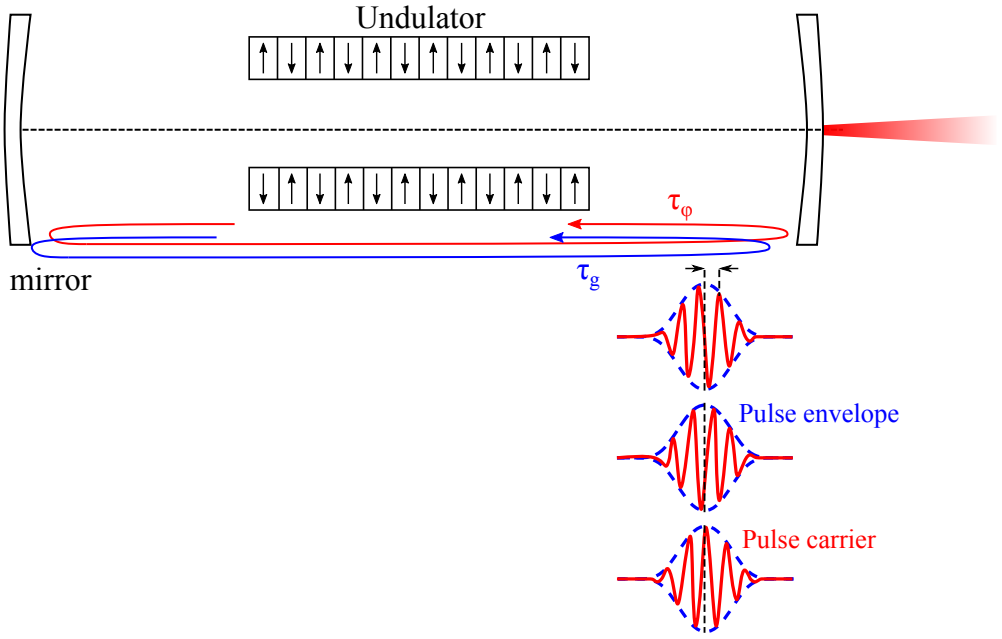

FIGURE 4.12: Carrier-Envelope Phase (CEP) concept showing drift from a pulse to another.

with ν_{THz} the frequency associated to the time t and ν_{drift} the frequency associated to $n\tau_R$, the time over round-trips n or the THz repetition rate. The latest corresponds to the frequency at which the FEL pulses are drifting from a pulse to another, describing the CEP drift speed.

These Fourier transforms are represented in Figure 4.13 for several mirror positions. A spot at the 4 THz frequency of the THz FEL signal, is observed in Figure 4.13(a) with $\nu_{drift} \approx 0$, indicating an almost constant CEP phase over all measured shots at a mirror position of 8.350 mm. As the mirror position is increased or decreased, a drift in frequency appears, gradually shifting to higher frequencies, as depicted in Figure 4.13(b), (c), and (d). Further increase of the mirror position presents a repetitive behavior in terms of CEP drift speed, as clearly demonstrated in Figure 4.14 where more shift in the THz behavior is observed in Figure 4.13(e),(f),(g) and (h). We can see in Figure 4.14 that the drift passes from one side to the other, by passing a zero position confirming the possibility to stabilize the FEL emission, using a feedback system for example. As expected, this repetitive behavior happening at a period of $\sim 36\mu m$ is equivalent to half the period of the THz frequency.

Figure 4.15 provides a clear shot-by-shot visual comparison between an almost CEP stable position at 8.350 mm and a position where the CEP drift is large. The EO signals in single shot at the specific mirror position 8.350 mm shows almost no shifts, whereas other mirror positions exhibit noticeable drifts.

4.6 Conclusion

In this chapter, we have successfully conducted the first single-shot measurements of the THz pulses emitted by the FEL at ELBE, showing the startup and turnoff behavior of the FEL shot by shot. These results demonstrate the capability of our experimental setup to measure high THz frequencies, specifically at 4 THz with a repetition rate of 13 MHz. The recording of temporal profile of THz FEL signals, envelope and carrier, as observed in this study, has conquered the challenge of measuring complete signals with multi-cycle oscillations of mode-locked lasers. The measured temporal profiles include the envelope and carrier of an FEL pulse for the first time. By varying the mirror position, we have observed the variation of the CEP drift at different mirror positions. This achievement of capturing the CEP of FEL pulses in single-shot is particular and holds a significant importance for future FEL experiments where phase information is crucial, particularly for pump-probe experiments.

While we have made substantial progress in the measurement and characterization of FEL pulses, there is still work to be done. One important area of focus is to improve the temporal resolution, by applying MRC reconstruction algorithm as the results presented are preliminary confirming the possibility of performing single-shot measurements of the FEL pulses. Further research can concentrate on developing detection techniques that can extend the capture of the full range of FEL emission, up to 16 THz and thinking of alternative solutions for the EO crystal and the parabolic mirror. This comprehensive detection capability will enable a deeper understanding of FEL behavior and facilitate a wider range of experimental applications.

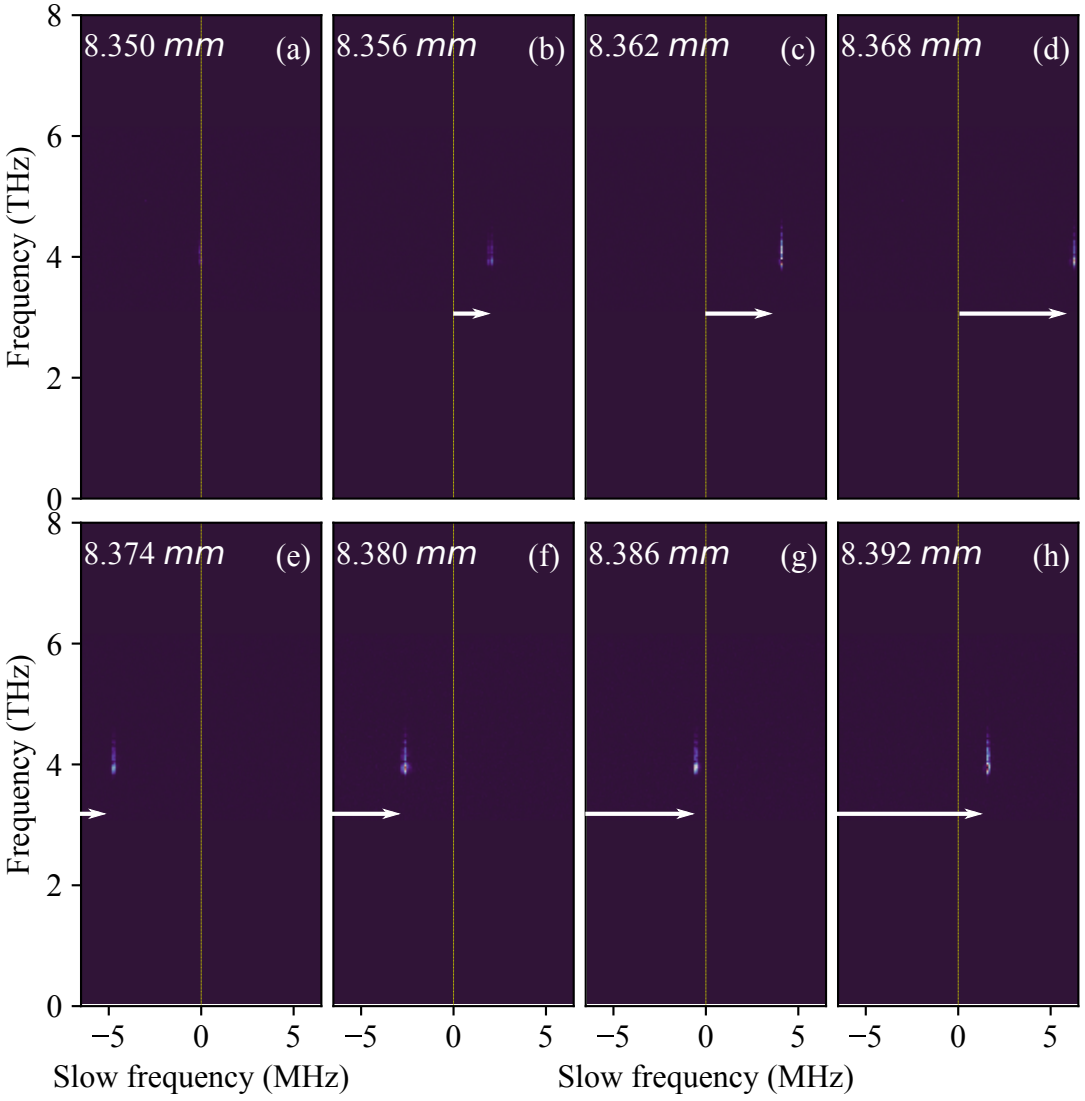

FIGURE 4.13: Module of the two-dimensional Fourier transform of the EO measured signals (as the one in Figure 4.9 for example) of the CEP frequency for several mirror positions. A zero drift frequency is observed at 8.350 *mm*. This frequency increases as mirrors gets far from each other but according to a repetitive behavior repassing by zero.

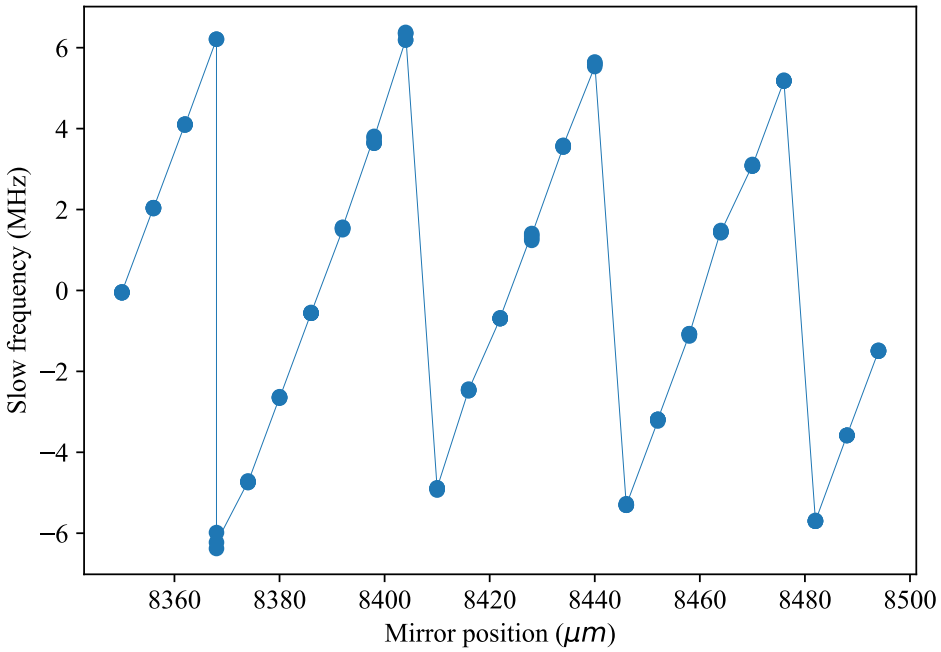

FIGURE 4.14: Variation of the CEP frequency as function of the mirror position. A periodic behavior is observed at the frequency of the THz signal.

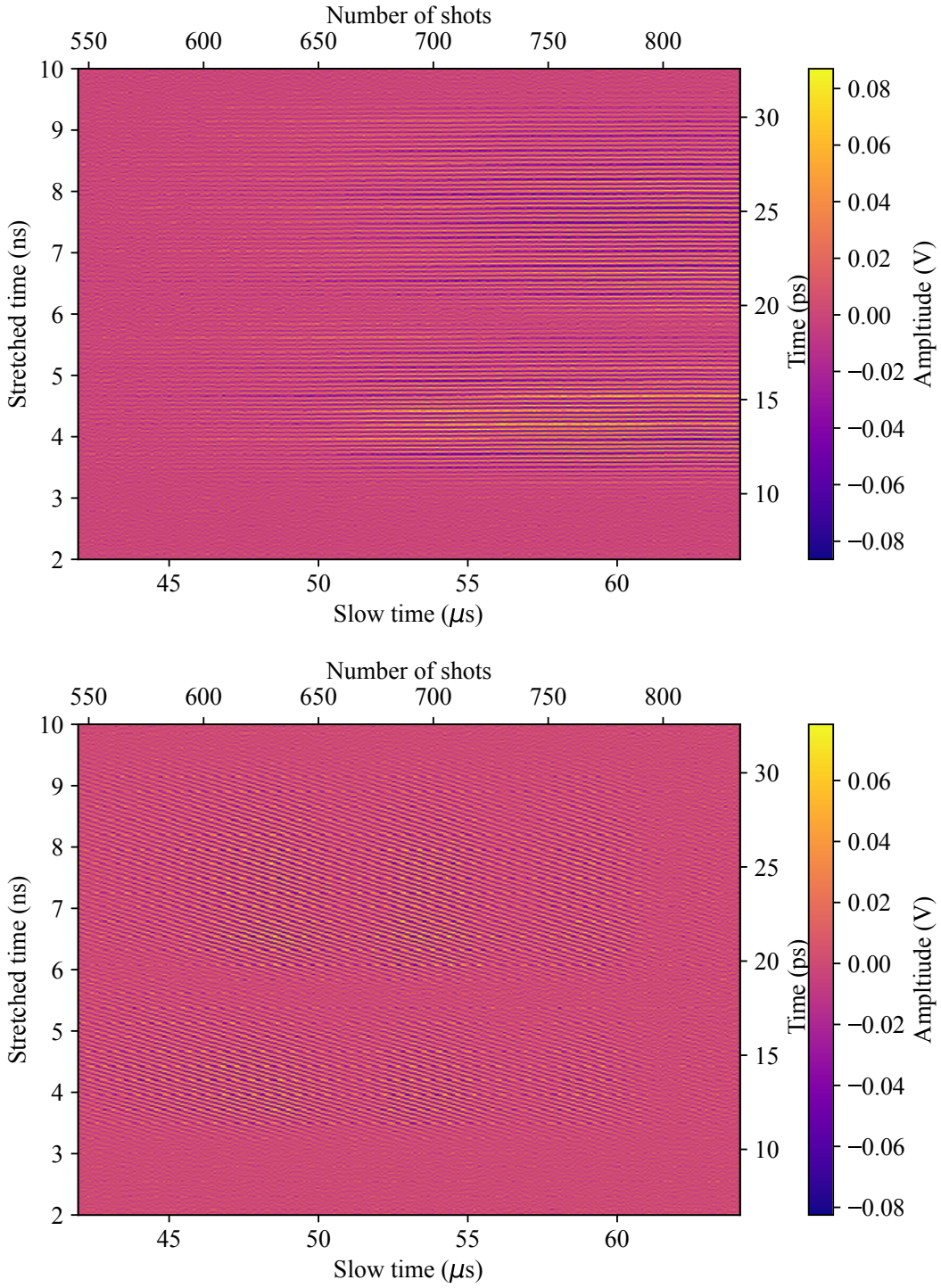

FIGURE 4.15: Colormap showing temporal profile of polarization 2 for two different mirror positions (a) 8.350 mm and (b) 8.356 mm. The difference of CEP drift is clearly seen that no shifts are shown whereas by looking at other mirror position, a clear drift is visible affecting the stability of the FEL.

Chapter 5

Photonic time-stretch electro-optic sampling at 1550 nm

5.1 Introduction

As demonstrated in Chapter 3 and Chapter 4, the development of an ultrafast detector operating at 1030 nm has been accomplished by combining electro-optic sampling photonic time stretch and phase diversity techniques, enabling the reconstruction of the THz input signal, in a non-destructive way, with a sufficient temporal resolution. Despite being able to attain high acquisition rates with photonic time stretch, mainly up to 26 MHz, and reaching a maximal stretch of $\sim$ 6 ns, the required bandwidth of the oscilloscope, which is typically 20 GHz, results in a cost around 100,000 euros, which is prohibitively expensive. The high cost of such components has limited and discouraged the utilization of photonic time-stretch, despite its potential and usefulness. Nevertheless, motivations of this technique still stand for two particular environments, mainly science of optics and particle accelerators, where manipulating ultrafast signals is critical.

In the field of optics, several researchers conducting table-top experiments are striving to achieve high values of stretch [116, 136, 137]. This has the potential to reduce investments in big-budget oscilloscopes and expand research possibilities.

On the other hand, this technique has a significant role in the field of particle accelerators and free-electron lasers where the challenge lies in measuring ultrafast high repetition rate THz emitted signals in single shot. In this context, photonic time-stretch can facilitate measurements of these signals and contribute to advancements in this field and for machine development.

In light of these motivations, we explore in this chapter the feasibility of the photonic time-stretch at the special 1550 nm wavelength with the goal of exploring the stretch limit by introducing more dispersion and thereby reduce the required detection bandwidth and cost of the needed oscilloscope. By achieving these objectives, photonic time-stretch may become more operational at reasonable costs and accessible for more applications.

This study marks the first demonstration of photonic time-stretch electro-optic sampling at the 1550 nm wavelength for investigating the CSR pulses emitted by the microbunching instability at SOLEIL storage ring.

These THz pulses were recorded for the first time in single-shot at high repetition rates using photonic time-stretch at a 1030 nm wavelength in 2015 at SOLEIL storage ring [9, 138](see Figure 5.1). This allowed to stretch the laser pulse up to approximately 4.5 ns, corresponding to a recording window of 24 ps, and requiring a high-end oscilloscope with an 8-20 GHz bandwidth. This acquisition window

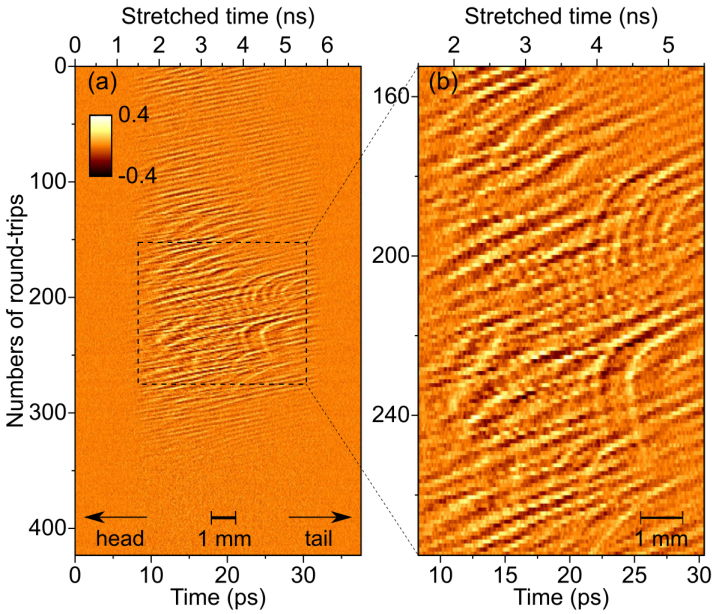

FIGURE 5.1: (a) Single-shot CSR pulses recorded at SOLEIL in 2015 with an electro-optic sampling setup associated with the photonic time-stretch at 1030 nm. Showing a rectangular shape, CSR pulses are like to be cut by the stretched laser acquisition window limited to ∼4.5 ns, equivalent to ∼24 ps real bunch time, which is shorter than the THz pulse duration. (b) is a zoom of (a). Figure from [9].

was smaller than the CSR pulse duration, allowing only a small portion of the THz to be imprinted on the laser chirped probe pulse, delimited by a rectangle in Figure 5.1(a). Increasing the stretch can indeed result in significant longer recording windows and slower signals to be recorded, by some order of magnitude, and thus reduce the effective detection bandwidth. However, this comes at a cost of higher dispersion, leading to more insertion loss and less detected power. As a result, the signal-to-noise ratio can be reduced, making it difficult to reach low signals and limiting the range of applications. In 2017, an amelioration of the setup allowed to increase the signal-to-noise ratio by a factor of 6.7 by introducing Brewster plates and enhancing the sensitivity [114]. However, this did not change the stretch limit.

The chapter begins by discussing the rationale behind the selection of the 1550 nm wavelength and its advantages, followed by a detailed description of the experimental setup at SOLEIL storage ring. Results of the first single-shot EO measurements of the complete CSR THz pulses will then be presented and compared to previous recorded signals. In a further study, we will investigate the versatility of the experimental setup by observing the formation of the microbunching instability at different beam currents and measuring the resulting THz CSR pulses in single shot. Finally, an attempt of combining phase diversity with the photonic time-stretch at 1550 nm will show promising insights towards a better temporal resolution.

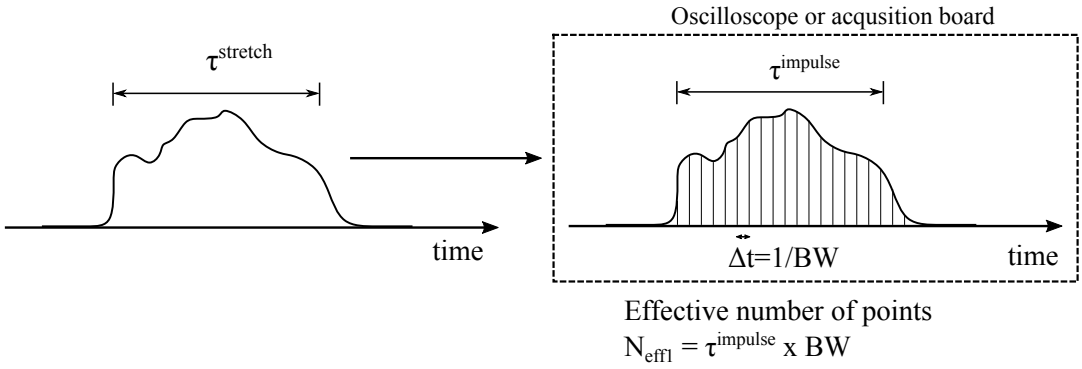

FIGURE 5.2: Effective number of points recorded with a detector of a certain bandwidth BW defined as function of the signal duration T.

5.2 Exploring photonic time-stretch at 1550 nm

The time duration resulting from stretching a laser pulse of a wavelength λ and a spectral width $\Delta\lambda$ in a fiber length L with a dispersion D is defined by:

$$\Delta t = \Delta\lambda \times D \times L \tag{5.1}$$

For a higher temporal stretch Δt, it is possible either to choose a laser with a higher spectral width $\Delta\lambda$ or to use a longer fiber L and/or with a higher dispersion D. Concerning the laser, the choice is limited by commercially available lasers that is also chosen depending on the possibility of obtaining high EO effect in existing EO crystals. The selected wavelength affects in parallel the corresponding fibers options. In order to stretch more, our choice got selected on the 1550 nm wavelength, which is widely used in telecommunications for long-distance information transport. This wavelength exhibits low attenuation in optical fibers with the ability to maintain a high signal-to-noise ratio over large distances. This wavelength offers less absorption and less scattering in glass optical fibers compared to 1030 nm. We chose an 80 km Dispersion Compensation Module, a small commercial electronic device from FS company, for stretching the modulated laser pulse. This device is based on anomalous dispersion, allowing to compensate normal dispersion and providing a high pulse spread out. The anomalous dispersion allows short wavelengths to travel faster than long wavelengths, contrarily to normal dispersion used at 1030 nm. Erbium lasers are the corresponding lasers that emit, in the infrared region of the electromagnetic spectrum, the 1550 nm wavelength. Fibers associated with this wavelength offer a range of options and a diverse choice for various components at cheaper price, compared to other wavelengths.

To compare fairly between the performance of photonic time-stretch at different wavelengths, it is important to take into consideration the effective number of points N_{eff} sampling the recorded signal, influenced by the duration of signal and its bandwidth. Another parameter is the amount of dispersion introduced with respect to the losses in power that may decrease the signal-to-noise ratio.

Let us define the effective number of samples to be recorded N_{eff} as an intuitive parameter that stays unchanged when choosing different lengths L_1, i.e., different input analysis time-window or bandwidth with:

$$N_{eff} = \frac{\tau^{stretch}}{\tau^{impulse}} \tag{5.2}$$

where $\tau^{stretch}$ is the probe laser duration at the photodetector, and $\tau^{impulse}$ defines the "time resolution" of the electronics (from photodetector to analog to digital converter (ADC) or oscilloscope). As in any low-pass electronics, the impulse response duration $\tau^{impulse}$ is inversely proportional to the bandwidth, i.e.:

$$\tau^{impulse} = \frac{1}{C} \times BW^{-1} \tag{5.3}$$

with C a parameter that depends on the definition of the bandwidth, rise/fall times (e.g., FWMH or 10-90 %), etc. The effective number of recorded samples can be therefore directly expressed as a time-bandwidth product at the readout electronics:

$$N_{eff} = CN_{eff1} \tag{5.4}$$

with

$$N_{eff1} = \tau^{impulse} \times BW \tag{5.5}$$

We propose to use the time-bandwidth product N_{eff1} as a figure-of-merit of a given THz time-stretch recorder design. This has the advantage to separate the tasks of comparing different time-stretch ADCs (by comparing their respective time-bandwidth products N_{eff1}) and the task of defining a effective number of points N_{eff} when relevant (i.e., agreeing on a value of the parameter C). To summarize, N_{eff1} can be used to compare the effective number of points of two designs (i.e., the larger, the better). However we should keep in mind that the effective number of samples N_{eff} will be usually larger than N_{eff1}, by a factor C that depends on the bandwidth and impulse response time definitions that are relevant to the application.

It is important to note that, for THz time-stretch systems, the stretch factor M is typically large. As a consequence, for a given electronics bandwidth, the effective number of samples defined above (N_{eff1}) is determined only by the dispersion of the second dispersion device D_2 (expressed here in ps/nm bandwidth), and the laser bandwidth $\Delta\lambda_{laser}$:

$$N_{eff1} = BWD_2\Delta\lambda_{laser} \tag{5.6}$$

Hence, in principle, the effective number of samples N_{eff1} can be increased arbitrarily by increasing the second dispersion of the time-stretch system. However, in practice, this amount of dispersion will be limited by the allowable losses that are compatible with a precise application.

A comparison in Table 5.1 shows the difference between the possible stretched pulse duration achievable at the 1030 nm wavelength, implemented in the previous detector (Chapters 3 and 4), and the one at 1550 nm investigated in this chapter, as well as the effective number of points recorded. We can see that for the same 6 dB optical loss, it is possible to stretch more than 10 times and reach up to 108 ns at the 1550 nm wavelength compared to 6 ns at 1030 nm with much more effective points recorded with the same oscilloscope, considering 2 different oscilloscope bandwidths (6 points compared to 108 points with a 1 GHz bandwidth oscilloscope, for example). This will resolve the need of an expensive oscilloscope with a 8-20 GHz

[1]DCM 80 km from FS with -1360 $\pm$ 3% ps/nm dispersion @ 1545 nm and an insertion loss $\leq$5.8dB

Wavelength (nm)	Spectral width $\Delta\lambda$ (nm)	Fiber	For 6 dB loss: Fiber length L	For 6 dB loss: Final stretch for a typical laser	For 6 dB loss: Effective "nb. of points" N_{eff1} recorded with bandwidth	
					1 GHz	20 GHz
1030	35	HI1060	4 km	6 ns	6	120
1550	68.2	SMF28	33 km	48 ns	48	960
		DCM[1]	Equivalent to 80 km of SMF28	108.8 ns	108	2160

TABLE 5.1: Stretched pulse duration and effective number of recorded points in the new 1550 nm setup, compared to typical 1030 nm situations. In each case, we limit the stretch to the maximal value leading to 6 dB loss. Note that the effective number of points N_{eff} is actually proportional to N_{eff1} by a factor (of few units) that depends on the recording electronics- see text.

bandwidth by a more cost-effective solution, a 1 GHz bandwidth oscilloscope or few GHz digitizer board ($\sim$ 10,000-15,000 euros). On the other side, this is supposed to increase the recording window length and hence imprint on it for the complete CSR THz pulse while maintaining a good signal-to-noise ratio with an acceptable dynamic range.

5.3 Experimental studies of the microbunching instability at SOLEIL storage ring

The ULTRASYNC project, funded by the Agence Nationale de la Recherche aims to observe, understand and control the microbunching instability by developing a novel detection tool for ultrafast signals in the THz range. Based on this project, funds will be used to install a detection station at SOLEIL at the AILES beamline and efforts are being made to build an ultrafast THz oscilloscope with high acquisition rate at a reasonable cost. As part of this project, tests are done at SOLEIL to evaluate the efficiency of the photonic time-stretch EOS at 1550 nm at SOLEIL storage ring. We review in this section the SOLEIL Synchrotron facility and expose the THz source to be investigated.

SOLEIL is a high-energy third-generation accelerator-based light source located in Paris, France (see Figure 5.3). It stands for “Source Optimisée de Lumière d’Energie Intermédiaire du LURE[2]" or “Optimized Light Source of Intermediate Energy to LURE". This particle accelerator, operating since 2006, produces a powerful synchrotron radiation from infrared to X-rays radiation. It is designed to produce a continuous spectrum of radiation across a wide range of wavelengths, having 29 beamlines covering the full electromagnetic spectrum range each with a specialized laboratory.

[2]Laboratoire d’Utilisation du Rayonnement Électromagnétique

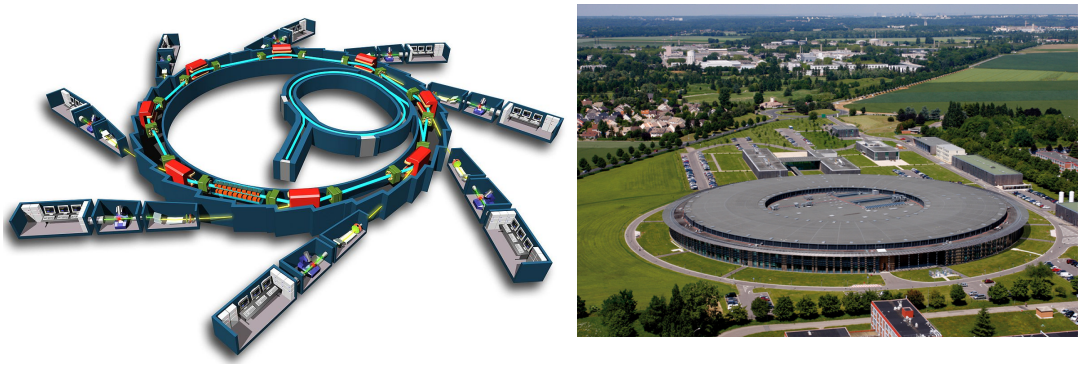

FIGURE 5.3: (a) Design of the interior architecture and (b) Photo of SOLEIL Synchrotron facility with a 354 meters circumference located at Plateau de Saclay, Saint-Aubin, France. Figures from [139].

First, the electrons ejected from an electron gun are injected into a linear accelerator called linac that pre-accelerates the particles to a high energy, as schemed in Figure 5.4. After exiting the linac, the particles are injected into a booster ring to further accelerate them to higher energies. The accelerated particles are then injected into the main circular storage ring. The storage ring contains a series of powerful bending magnets and focusing elements, that serve to bend the path of the particles using strong magnetic fields, keeping them in a circular orbit with insertion devices such as wigglers and undulators. These devices consist of an arrangement of periodic magnets that create alternating magnetic fields, causing the particles to oscillate transversely, emitting more intense and coherent radiation. As the particles move along the curved path, they emit electromagnetic radiation, including X-rays, due to their acceleration. High frequency accelerating sections are used to compensate the energy dissipated when the circulating electrons radiate. The emitted radiation is extracted from the storage ring using beamlines, that guide and shape the emitted radiation to experimental stations, where scientists can use it for various applications such as imaging, spectroscopy, or diffraction.

SOLEIL can operate in different modes, providing several beam characteristics such as multibunch pattern (4 trains of 100 bunches uniformly filled), hybrid mode (a single bunch with a high charge), an 8 bunch mode and a single bunch mode [140]. SOLEIL storage ring parameters and operational modes are summarized in Table 5.2.

Above a certain beam current, interactions between electrons lead to an instability and to the formation of microstructures along the electron bunch. This phenomenon, known by microbunching instability, results in the emission of a coherent synchrotron radiation (CSR), 10000 more intense than the normal synchrotron radiation. We investigate in this work these CSR THz pulses above the beam current threshold by trying to measure them in single-shot.

5.4 First experimental trial at SOLEIL storage ring

As a first trial, we designed an SM fiber-based setup without introducing the phase diversity technique to study the feasibility of the photonic time-stretch electro-optic

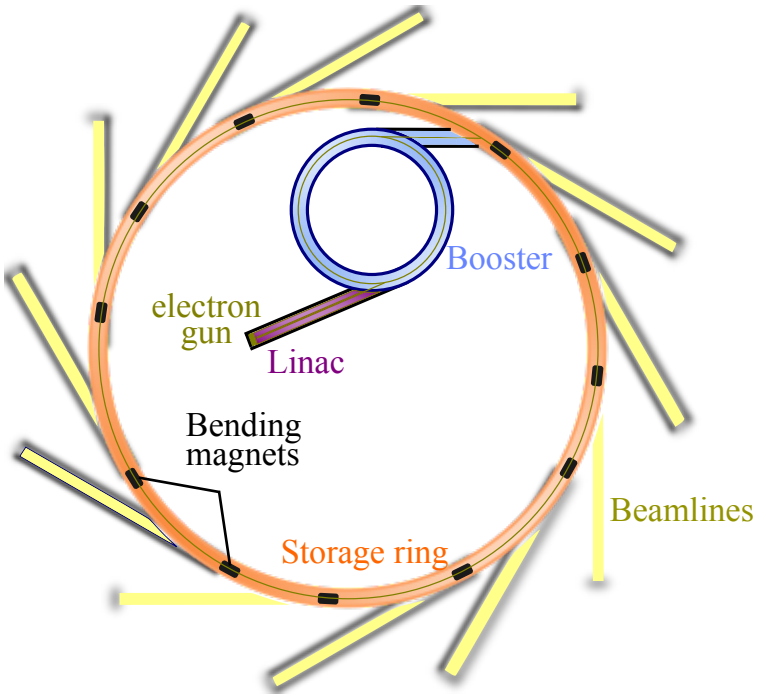

FIGURE 5.4: Schematic design of a storage ring: electrons ejected from an electron gun are pre-accelerated in a linac and after in a booster to reach higher energies before being stored in a storage ring. Magnets are used to control and guide electrons trajectory. Insertion devices such as undulators or wigglers are used to generate synchrotron radiation directed to beamlines.

SOLEIL storage ring parameters		
Energy (GeV)		2.75
Circumference (m)		354
Revolution period (μs)		1.1814
Revolution frequency (kHz)		846.64
Filling modes	Uniform	500
Maximum stored current (mA)	Hybrid	450
	8 bunches	110
	1 bunch	20

TABLE 5.2: Main parameters of SOLEIL storage ring.

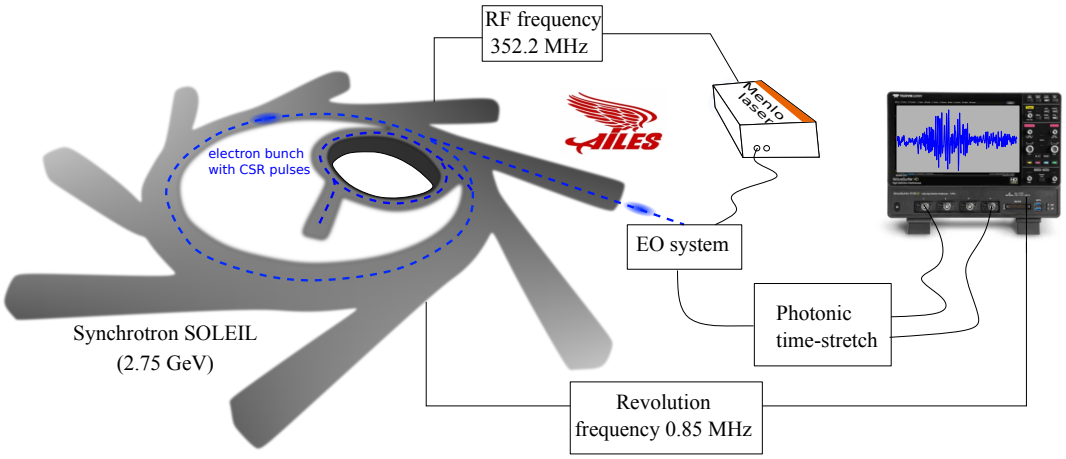

FIGURE 5.5: SOLEIL storage ring in which a single electron bunch is circulating at 850 kHz revolution frequency with CSR microstructures formed along. THz radiation emitted by the latest is encoded, by EO effect, on probe laser pulses and slowed down in time using photonic time-stretch to be recorded by a photodetector and an oscilloscope. The oscilloscope is synchronized to the revolution frequency of the storage ring.

(EO-PTS) detection at the 1550 nm laser wavelength. The setup is similar to the one developed at 1030 nm with the adapted components suitable for 1550 nm and mainly with the use, of an amplifier and a pulse picker. This section provides a detailed description of the experimental setup at SOLEIL.

5.4.1 THz beam transportation

For this experiment, SOLEIL storage ring is operating in single bunch normal alpha mode in which a single bunch of electrons is circulating in the storage ring at a repetition rate of 850 kHz (see Figure 5.5). The experiment was operated at the AILES beamline, one of the two infrared beamlines at SOLEIL [141]. The THz beam delivered at the beamline is collimated and focused on the EO crystal using two off-axis parabolic mirrors (respectively with 4″ and 2″ focal lengths and a 2″ diameter). The THz is vertically polarized.

5.4.2 Optical scheme

The experimental setup consists of a Menlo C-Fiber femtosecond Erbium laser with a central wavelength of 1550 nm, a 1.8 ps specified pulse width, a 68.2 nm[3] spectral width and a 60 mW output power from Menlo Systems[4]. The repetition rate of the laser is 88.05 MHz and it is synchronized to the RF frequency of the accelerator of 352.2 MHz using a RRE-SYNCRO by Menlo Systems. Laser pulses are chirped in a first fiber L_1 that defines the recording analysis window, here a 40 m SM dispersion compensating fiber (DCF) with a -140 ps/nm/km dispersion . A polarization controller (PC) (FPC560, from Thorlabs) is used to regulate the laser polarization state prior to its entry into a PM pulse picker, manufactured by Gooch&Housego. The pulse picker parameters are set such as the division number, N_{PP} defining the output frequency of the pulse picker 88.05 MHz/N_{PP} is set to 13, the pulse width is

[3]test report specified value
[4]The laser is transported from PhLAM to SOLEIL for the experiment.

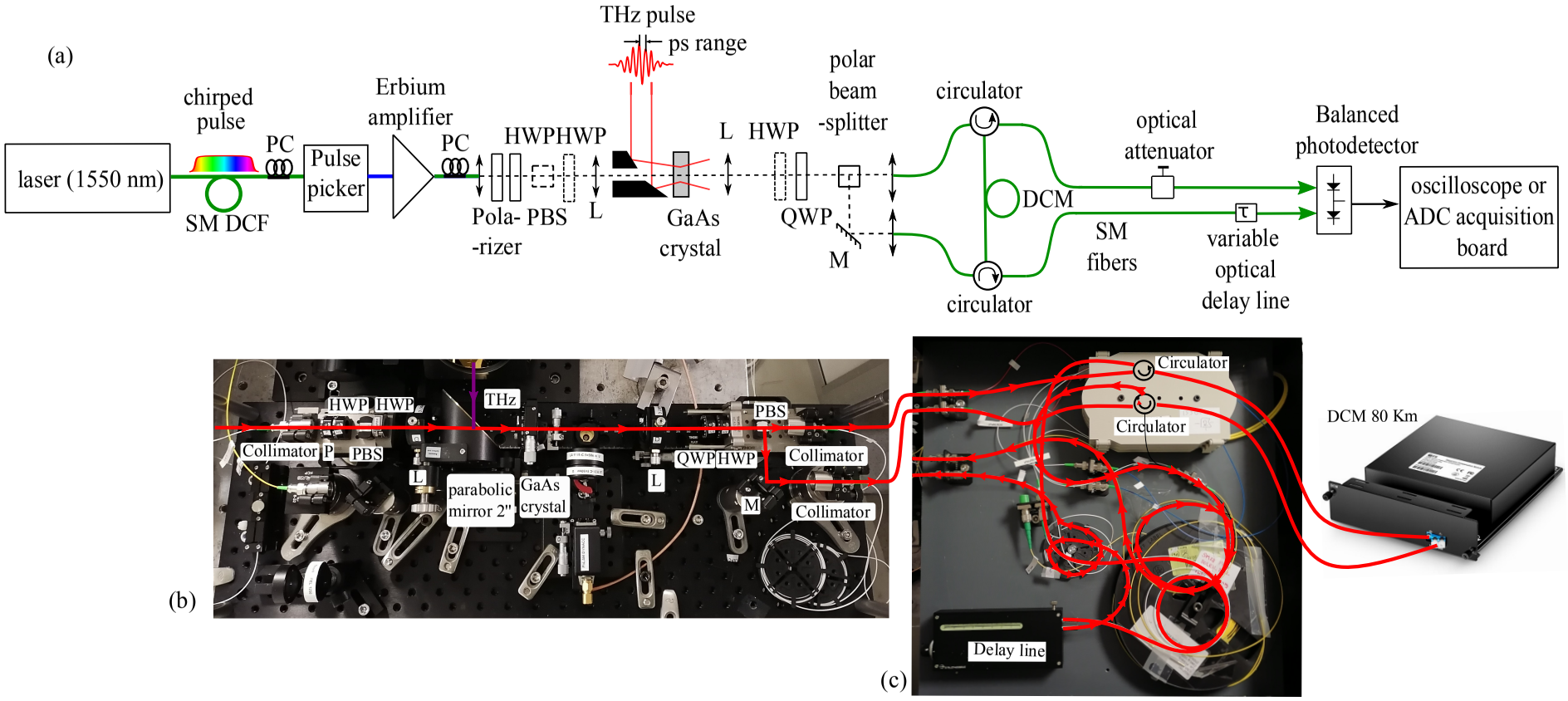

FIGURE 5.6: Experimental setup combining electro-optic sampling with photonic time-stretch at SOLEIL. A laser pulse emitted by a 1550 nm Erbium fibered laser is pre-chirped in 40 m single mode (SM) dispersion compensating fiber (DCF). When the CSR THz signal and the laser pulse co-propagate in a Gallium Arsenide (GaAs) crystal, the THz signal modulates the laser pulse through the electro-optic effect resulting in a polarization modulation. The latest is transformed into an intensity modulation with a set of wave plates and a polarizer. Each polarization state of the modulated signal is stretched in a 80 km dispersion compensation module (DCM). A balanced detection is performed between both arms. Recordings are made using either a 1 GHz oscilloscope or a 3 GHz analog-to-digital converter (ADC) acquisition board. PC: polarization controller, HWP: Half wave plate, QWP: Quarter wave plate.

set to 12 ns in order to reduce the laser repetition rate before amplifying to increase the energy per pulse for a better sensitivity as well as to prevent overlap when stretching. A 5 m PM fiber links the pulse picker output to a homemade Erbium SM fibered amplifier. A second polarization controller is placed between the Erbium amplifier and the EO head.

The EO head is placed on a 20 cm $\times$ 60 cm breadboard (see Figure 5.6(b)), with a 6.18 mm focal length collimator (TC06 APC-1550, from Thorlabs). A linear polarizer is used to ensure a clean linear polarized state output. An achromatic half wave plate (HWP) FBR-AH3 for 1100-2000 nm from Thorlabs is used to rotate the laser polarization so that it is aligned with the direction of the THz and with the [-110] axis of the GaAs crystal. This configuration corresponds to the classic EOS with standard balanced detection. A 5 mm polarizing beam splitter (PBS) cube PBS054 followed by a second HWP were previewed for another experiment but has no effect here. A 10 cm focal length N-BK7 C coated plano convex lens LA1207-C is inserted to focus the laser beam on the EO crystal. The THz is transported to the EO board with a 2" (50.8 mm) focal length off-axis parabolic mirror with a 2" diameter, from Thorlabs, focusing both THz and laser beams onto the crystal with the laser beam passing through the hole of the parabolic mirror to reach the EO crystal. A $10\times10\times3$ mm 110-cut Gallium Arsenide (GaAs) crystal with AR coating at 1550 nm, from Del mar Photonics, is used. When the THz and the laser co-propagate together in the crystal, the electric field of the THz modulates the laser polarization due to the electro-optic effect. This results in encoding the THz signal onto the laser. A second 100 mm focal length LA1207-C lens is used, followed by an achromatic quarter wave plate (QWP) (FBR-AH3, from Thorlabs) rotated at 45° with respect to the [-110] crystal axis and a HWP is added for the phase diversity configuration (but has no effect in the configuration described here), rotated at 0°. A 5 mm PBS cube separates the modulated signal polarization state into two components along both axes, which are then focused using two collimators and a mirror PF05-03-P01. All components used after the collimators are SM-fiber based. The two EO head optical output are connected to two identical circulators, with losses$<$0.88 dB from ANYLINK that redirect the modulated laser pulses of both polarizations in the same 80 km dispersion compensation fiber (DCF)-based Passive Dispersion Compensation Module (DCM) from FS. This DCM offers a dispersion of -1360 ps/nm @1545 nm with a 5.8 dB insertion loss leading to stretch up to 35 ns (see Figure 5.14(a)). This symmetrical design allows providing the same stretch and delay for both polarizations. A variable optical delay line, operating over an optical range of 0-500 ps from AFR, is used on one arm to adjust the small delay between both polarizations arising from differences in fibers lengths. A variable optical attenuator is added on the second arm to balance the laser powers of both polarizations. Providing equal powers on both arms with same arrival time with equal fiber length, a classic balanced detection is performed using an InGaAs balanced amplified photodetector PDB780/AC operating at bandwidth of 1 MHz to 2.5 GHz. This photoreceiver, from Thorlabs, has a 2125 V/W @1310 nm RF OUTPUT Conversion Gain of, 15 pW/$\sqrt{\text{Hz}}$ Noise Equivalent Power. In the absence of THz imprinted on the laser pulse, the balanced detection signal should be null, with a residual signal coming from the imperfections of optical components. Data are recorded using a 1 GHz Teledyne LECROY WaveSurfer 4104HD oscilloscope and an 3 GHz analog-to-digital conversion (ADC) ADQ7DC acquisition board from TELEDYNE SP Devices.

5.4.3 Timing between THz and laser

The timing between the THz signal and the laser probing pulse was adjusted using the near-IR part of the synchrotron radiation. A mirror (not shown here), just after the GaAs crystal, collected both the synchrotron radiation and the probe laser pulses. Both pulses were focused on a 5 GHz InGasAs photodetector (DET08CFC-5 GHz from Thorlabs) connected to the ADC board.

5.5 Experimental results

5.5.1 EO measurements with a 1 GHz bandwidth oscilloscope

The current setup is configured in classic balanced detection where the same laser is subtracted between both arms. This configuration gives the difference between both polarization states and enhances the detection dynamic range, by removing the common laser shape and cancelling the noise fluctuations of the laser, as detailed in section 2.4.

With the photonic time stretch in the DCM-80km, the resulting stretched laser pulse has a duration of approximately 35 ns (see Figure 5.14(a)) which is within the measurement capability of a 1 GHz oscilloscope or more. The detection bandwidth is limited by the bandwidth of the balanced detector bandwidth which is 2.5 GHz.

The acquisition frequency of the resulting experimental setup is around 6.7 MHz, while the THz repetition rate is 850 kHz. The resulting acquisition rate is 8 times the repetition rate of the revolution frequency by means that out of every 8 laser pulses, only one pulse is modulated by THz radiation. Data are interpolated and cut at the repetition rate of the laser and separated between pulses with THz and without THz. The unmodulated pulses being used to evaluate the residual response of the detection system, which is then subtracted from the modulated signals. For each EO measurement, an unmodulated reference laser pulse is recorded to normalize the obtained signal.

At first, we used a Teledyne LECROY WaveSurfer 4104HD oscilloscope with a bandwidth of 1 GHz and a sampling rate of 5 GigaSamples/s to develop, test and calibrate our experimental setup. This was practical, easily manipulative and interactive, allowing to observe the signal on the scope.

We can observe in Figure 5.7(a) the first complete CSR pulses measured in single shot with the 1 GHz scope for three successive THz signals. These single-shot EO signals in Volts, accorded to three consecutive round-trips of the electron bunch in the storage ring, are obtained after subtraction of the residual noise. They show the temporal profile, envelope and carrier, of the CSR pulses emitted by the electron microstructures due to microbunching instability. The THz pulse is observed completely with a $\sim$ 90 ps pulse duration with a stretch factor of 270[5]. Figure 5.7(b) displays the color map of EO signals recorded by the 1 GHz oscilloscope in single shot, showing the evolution of CSR pulses formation of one burst round after round in the storage ring. With this oscilloscope, we were able to measure the CSR pulses in single shot over 5 ms and their spectra in single-shot as well (Figure 5.7(c)). The

[5]This value is determined in section 5.5.4

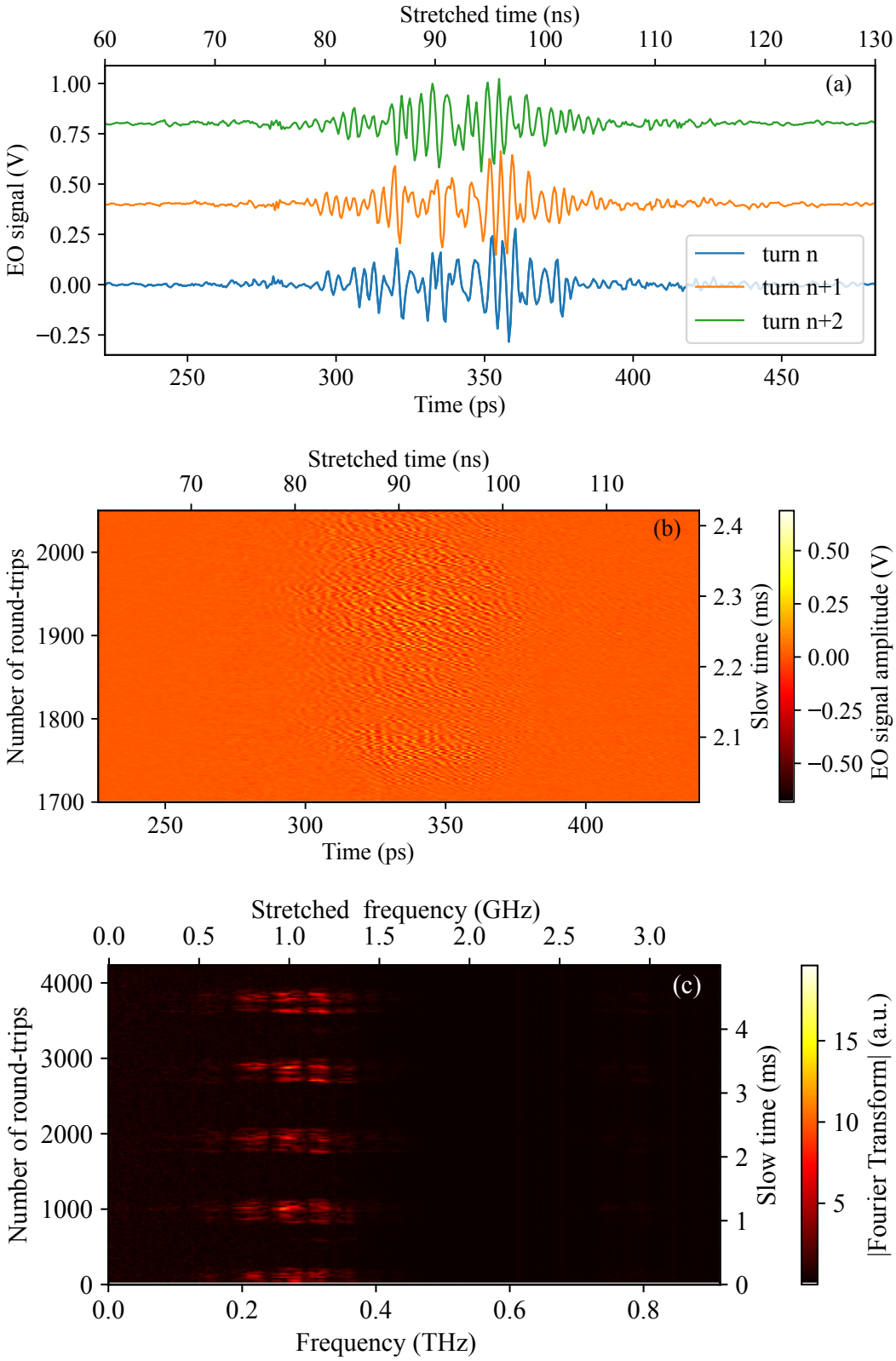

FIGURE 5.7: (a) Three successive single-shot CSR THz pulses of consecutive round-trips of the electron bunch recorded by the 1 GHz oscilloscope. For a better visualization, signals were shifted by 0.4 V. (b) and (c) Respective color maps of the CSR THz signals and their FT spectra measured in single-shot with the 1 GHz oscilloscope versus the number of round-trips traveled by the electron bunch in the storage ring.

Property	WaveSurfer 4104 HD oscilloscope	ADQ7DC acquisition board
3 dB Bandwidth	1 GHz	3 GHz
Vertical resolution	12-bit	14-bit
Max. sampling rate	5 GSa/s (2 channels)	10 GSa/s in single-channel
Memory depth	25 Mpts/2 channels	2 Gpts
User interface	Touchscreen & buttons	Software

TABLE 5.3: Comparison between specifications of the Teledyne LeCroy WaveSurfer 4104 oscilloscope with a 1 GHz bandwidth and the ADQ7DC acquisition board with a 3 GHz bandwidth from Teledyne SP devices.

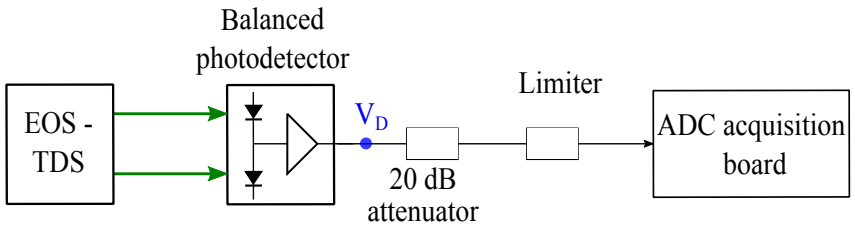

FIGURE 5.8: Physical scheme of attenuation before the ADC board showing the voltage measured in EO measurements results at the output of the detector V_D.

single spectra shown in Figure 5.7(c) over ∼4000 shots are formed in bursts, showing a burst emission mode of the CSR THz signals at high beam current (16 mA). It should be noted that figures 5.7 (a) and (b) present two time axes, the stretched time which is the time visualized on the oscilloscope (or acquisition board later) and the time axis representing the real time of the THz signal calculated according to the stretch factor, which is detailed further in section 5.5.4.

5.5.2 Measurements with a 3 GHz ADC board

Although using an oscilloscope is particularly efficient for development purposes, ADC acquisition boards turn out to be more advantageous for systematic recordings allowing long-term recording of single-shot CSR pulses, which is crucial in understanding the evolution of microstructures in the storage ring. Once our system was calibrated and operational, we aimed to test a different acquisition system, the ADQ7DC high resolution ADC board from TELEDYNE SP Devices. ADQ7DC features 14-bit resolution, a 10 GSamples/s sampling rate in dual-channel mode, a 3 GHz bandwidth, and a large memory size of 4 GBytes (2 bytes per sample). This card with a 3 GHz bandwidth enables to record 3 times more effective number of points for each shot compared to the 1 GHz oscilloscope and has a larger memory size enabling to record over longer time, being thereby more convenient for studying the behavior of electron bunches inside the storage ring. Key features of both instruments are compared in Table 5.3.

To adjust the balanced detector signal level to the ADC requirements, we placed two 10 dB attenuators (VAT-10+ from Mini-circuits) (equivalent to 20 dB) and a +13 dBm limiter (VLM-33W-2W-S+ from Mini-circuits) at the input of the ADC, as schemed in Figure 5.8. In all represented results, signals are shown

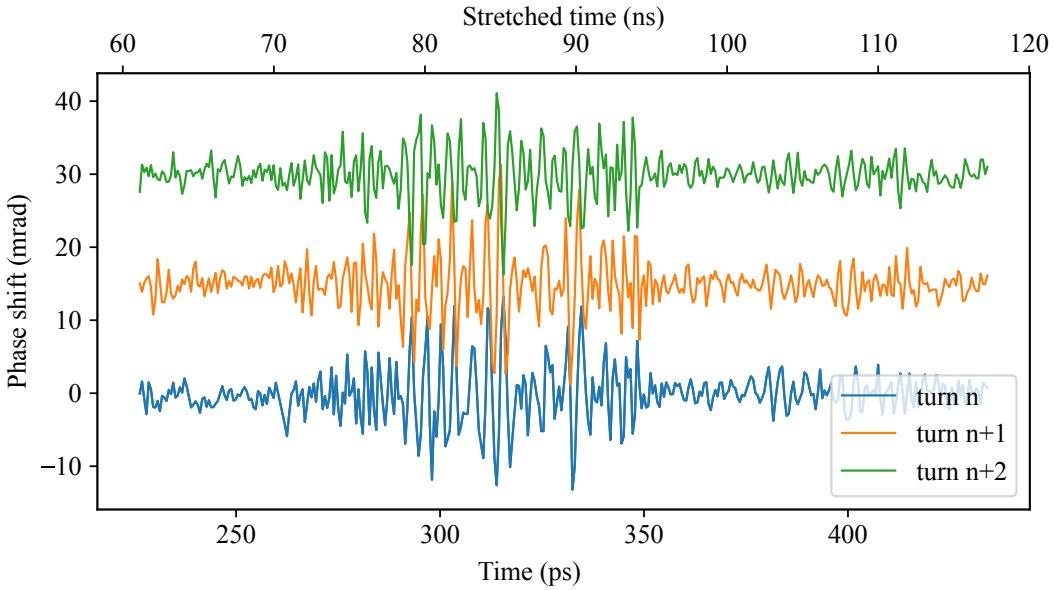

FIGURE 5.9: Three successive single-shot CSR THz pulses recorded by the 3 GHz ADC board. For a better visualization, signals were shifted by 15 mrad.

in their original voltage V_D at the output of the photodetector, i.e. before attenuation.

Figure 5.9 displays three single shot CSR THz signals for consecutive round-trips recorded by the acquisition board, after subtraction and normalization. These signals show finer details than the ones measured with the oscilloscope due to the higher bandwidth of the ADC board. With the present stretch factor of 270[6], the total measured THz duration is around 130 ps, and it is possible to observe, for each shot, the complete CSR pulse, measuring approximately 92 ps, and its replica just after which is its reflection inside the EO crystal over $\sim$ 60 ps.

The main achievement of performing photonic time-stretch at 1550 nm is to considerably increase the effective number of points that is recorded at each shot. This has also allowed to record the whole CSR pulses with few GHz digitizer, contrarily to the small portion of $\sim$ 24 ps captured previously in 2015 using a 36 GHz bandwidth oscilloscope [9], see Figure 5.10.

[6]This value is determined in section 5.5.4

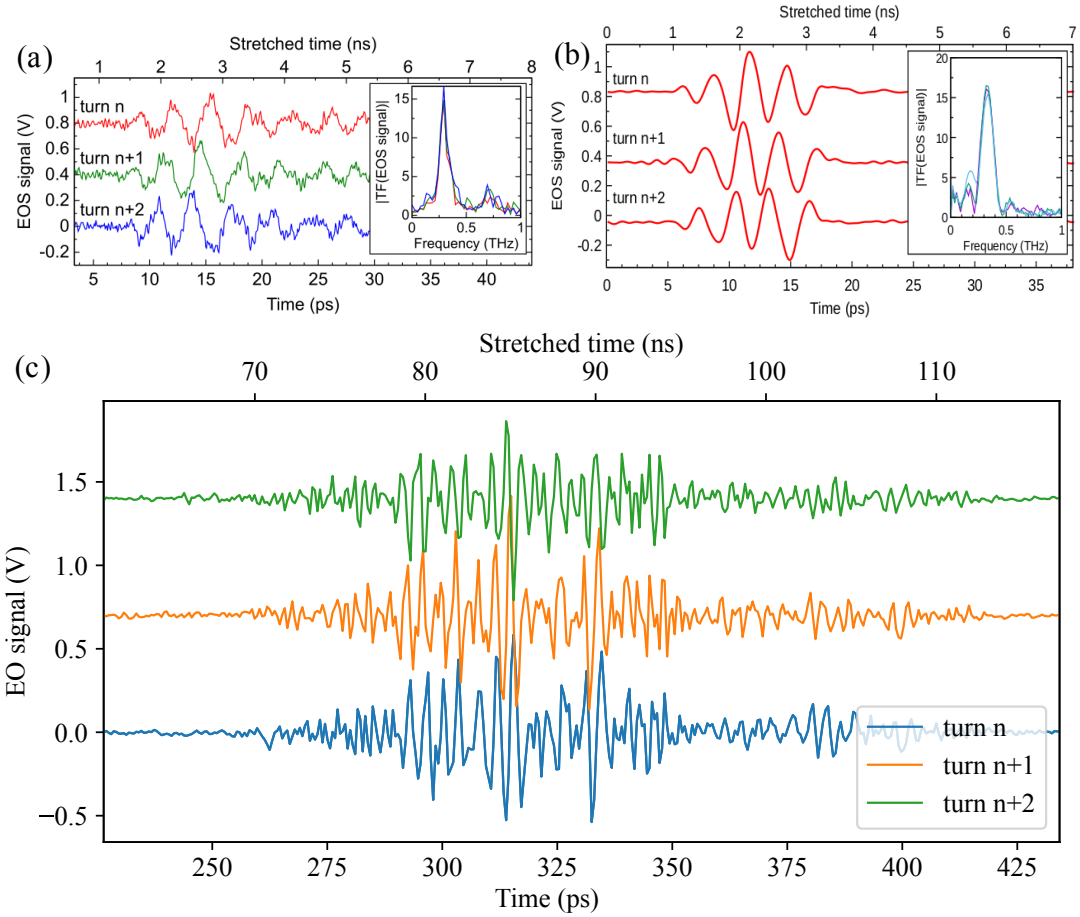

FIGURE 5.10: (a) Three successive single-shot measurements recorded in 2015 with a 1030 nm laser. Figure from [9]. (b) Three successive shots measured also with a 1030 nm with the introduction of Brewster plates for a better sensitivity, experiment in 2017. Figure from [115]. (c) Three successive single-shot measurements recorded with the experimental setup presented in this chapter with a 1550 nm laser wavelength. Signals are shifted by 0.7 V for clarity.

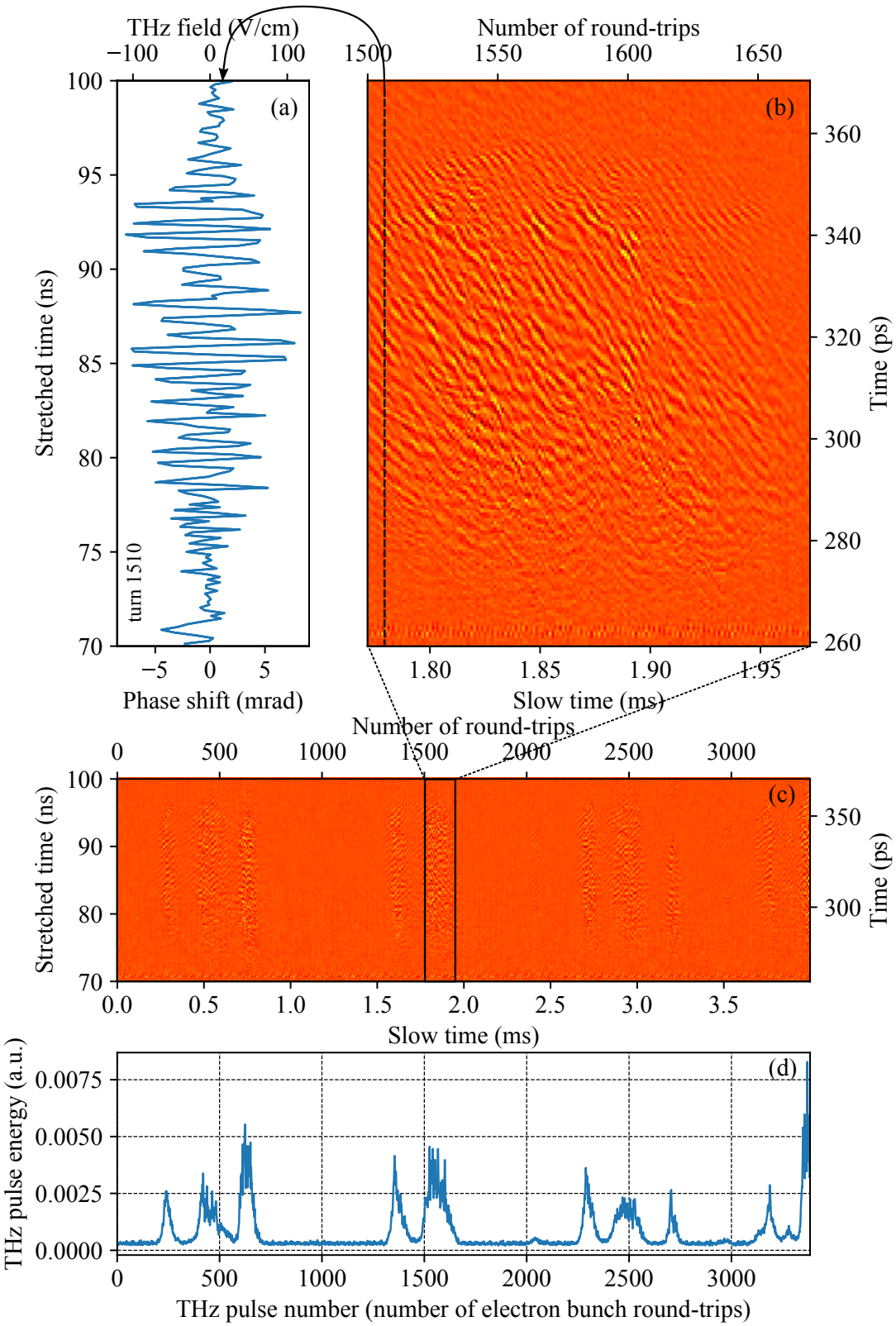
THz field (V/cm)
−100
0
100
1500
Number of round-trips
1550
1600
1650
(a)
(b)
(c)
(d)
Stretched time (ns)
Time (ps)
turn 1510
Phase shift (mrad)
Slow time (ms)
Number of round-trips
THz pulse energy (a.u.)
THz pulse number (number of electron bunch round-trips)

FIGURE 5.11: Series of coherent THz pulses recorded in real-time, at SOLEIL, during a study of the so-called microbunching instability at I=15 mA. (a) Electro-optic signal of a single THz pulse. (b) Series of successive THz pulses displaying characteristic details of the dynamics during a THz burst (including carrier-envelope phase-drift and spatio-temporal dislocations). (c) Same data plotted over a longer time period, displaying the characteristic bursting behavior of the THz emission. (d) Corresponding THz pulse energy versus pulse number. The electro-optic signal is expressed as the THz-induced phase-shift in the electro-optic crystal in radian. Note that one record contains aproximately 150000 THz pulses (only part of the data has been displayed for clarity).

Figure 5.11(a) shows the EO measured signal for one single CSR THz pulse after subtraction and normalization, defined by the phase shift induced in the EO crystal. Grouping consecutive THz signals in a colormap show a representation of the CSR emission dynamics as in Figure 5.11(b) of one burst and for larger series in Figure 5.11(c) showing a train of 4 bursts with more than 3000 successive CSR shots. We can see in Figure 5.11(c) how the THz CSR signals are emitted in burst mode. Figure 5.11(d) shows the THz pulse energy of CSR pulses measured versus the THz pulse number.

In Figure 5.12(a) are represented the single shot CSR THz spectra given by the Fourier transform of the normalized EO signals for more than 3000 round-trips recorded by the ADC board, with one single spectrum around 0.3 THz represented in Figure 5.12(b) and the average over all measured round-trips in figure 5.12(c). All measured spectra reveal a broadband spectrum centered at 0.3 THz. The presence of zeros at some frequencies is expected, corresponding to the same frequencies in the transfer functions described in section 2.5.2 presenting zeros.

5.5.3 Detection noise level

Figure 5.13 and Figure 5.14(b) show the noise in radians of the setup with the oscilloscope and acquisition board, respectively, determined by the ratio between the residual noise in the absence of THz and the input laser shape.
The noise equivalent phase shift in radians of the setup as measured by the oscilloscope, represented in Figure 5.13 without THz signal shows that the fluctuations of the setup are 3.10^{-4} rad for a 2.4 mW input average power at the balanced detector corresponding to $\sim$ 5 V/cm in the present 3 mm GaAs crystal with r_{41} =$1.5.10^{-12}$ m/V [142].
The noise level of the experimental setup measured by the acquisition board is $4.5.10^{-4}$ rad, experimentally equivalent to 6.5 V/cm as seen in green in Figure 5.14(b). The noise level measured with the oscilloscope is slightly lower than that measured with the ADC board. This difference is normal and can be explained by the higher bandwidth of the ADQ7DC (3 GHz) compared to the bandwidth of the oscilloscope (1 GHz). Figure 5.14(b) displays the sensitivity (i.e. the noise-equivalent phase shift versus time, together with the noise contribution of the balanced detector and oscilloscope.

Finally, it is worth noting that both oscilloscope and acquisition board are suitable for recording EOS signals in this experiment, and that it is important to consider factors such as bandwidth, number of samples and price.

5.5.4 Determination of the stretch factor

As previously mentioned, the stretch factor in photonic time-stretch depends on the length of the first fiber noted L_1. This fiber length includes the equivalent effective fiber length before the EOS and encompasses the unknown fiber lengths inside the laser, the pulse picker and the amplifier making it challenging to determine its value accurately. Nevertheless, it is important to calibrate the system, in a way or other, to get the exact stretch factor enabling the characterization of the signal being measured. In this experiment, two ways, described below, were used to determine the magnification factor.

5.5.4.1 Calibration using delay

In order to calibrate the system, we varied the delay between the THz and the laser using the synchronization system, that locks the laser repetition rate to the revolution frequency of the storage ring with the THz radiation. Even though it is complicated to locate the maximal position of the CSR THz signal, the sum of the squared EO signal over all shots was calculated for each delay. A cross-correlation is done between the relative timings, and the arrival time of the optimal correlated signal is identified and studied as function of the measured stretched time on the acquisition board as depicted in Figure 5.15.

The color map, in Figure 5.15, demonstrates a linear relationship between the stretched time and the delay, as expected. Note that the Menlo synchronization system displays the delay as a phase shift between the second harmonic of the storage ring RF frequency (2×352.2 MHz) and the 8th harmonic of the laser repetition rate. This correspondence can be easily related to the real time of recording. The proportionality results a stretch factor M equal to 274 with:

$$stretched\ time = M \times real\ time = M \times delay[^\circ] \times 3.94[ps/^\circ] \tag{5.7}$$

This stretch factor is an important piece of information useful to calibrate the system and define the properties of the signals under investigation.

5.5.4.2 Reflection inside the EO crystal

Having a sufficiently long recording window, we benefited from the reflection of the THz signal inside the crystal to determine the stretch factor. Note that the choice of the EO crystal is critical to meet requirements such as: a long crystal for a higher sensitivity as well as to prevent overlap between the original signal and its reflection, small enough to ensure a good phase matching at the required frequency and AR coated in order to limit the reflection of the laser inside the crystal. A fair tradeoff is considered between all these needs to avoid constraints that may degrade the single-shot EO effect. We have chosen an AR coated GaAs crystal with a 3 mm thickness.

We can see, in Figure 5.16, that the THz reflection is happening after 19.5 ns which, according to theory, should corresponds to the round-trip time inside the crystal defined by :

$$t = \frac{2ne}{c} \tag{5.8}$$

where e is the crystal thickness, n the refractive index of the THz in the crystal and c the light velocity. In our case, n = 3.662 and $e = 3$ mm implying a 73 ps round-trip time, separating the initial signal away from its reflection. This replication implies a stretch factor equal to 267.

From both methods used in this experiment, two stretch factors were identified to be 274 and 267. As the difference between these values is negligible, we can consider a stretch factor of 270 (the mean value). This result confirms the reliability and consistency of the methods used in determining the stretch factor for this experiment. As an example, with a stretch factor of 270, 1.1 GHz recorded by the acquisition board is equivalent to 0.3 THz as an input frequency.

5.6 Study of the CSR evolution as function of the beam current

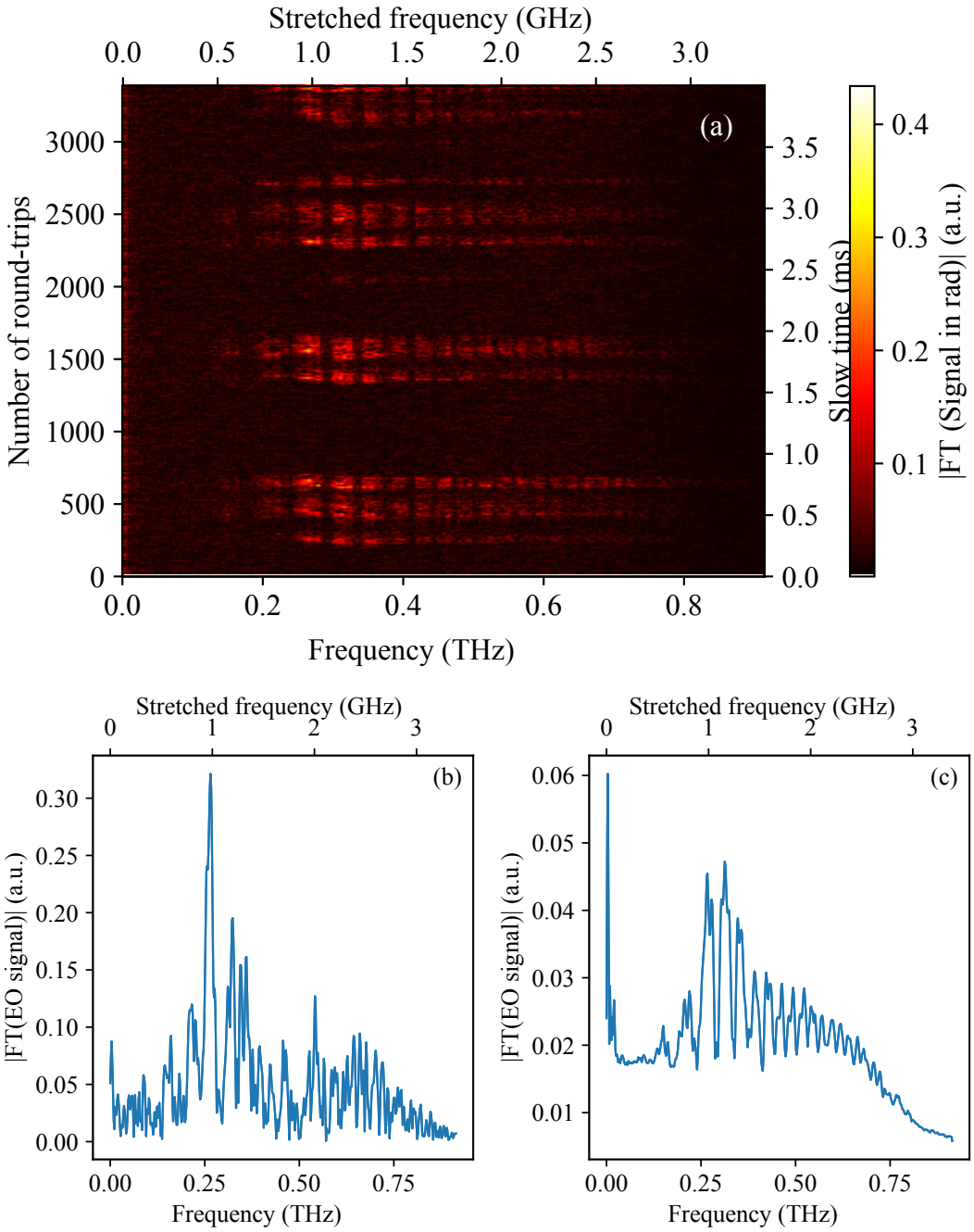

FIGURE 5.12: (a) Single-shot Fourier transform of CSR pulses of EO recorded signals in radian recorded with the 3 GHz ADC board. The higher detection bandwidth of the acquisition board results in more frequencies appearing after $\sim$ 1.4 GHz compared to Figure 5.7(c). However, the bandwidth of the balanced detector of 2.5 GHz limits the visibility of the signal beyond this frequency on the ADC board, despite its 3 GHz bandwidth. The upper axes labeled 'Stretched frequency' represent the recording frequency of the detectors after stretch. The lower axes represent the real frequencies corresponding to the CSR THz pulses. (b) One single shot spectrum. (c) Average spectra over all shots, revealing clearly the presence of zeros. These zeros in the spectra represents zeros of the transfer functions of the system, see section 2.5.2.

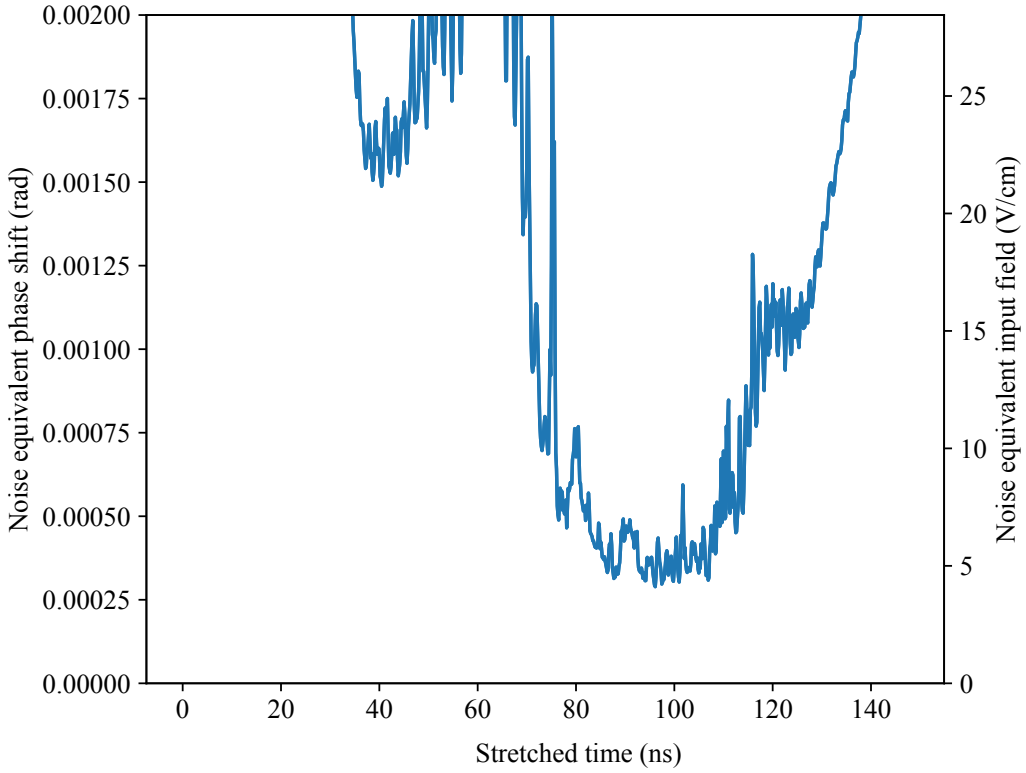

FIGURE 5.13: Noise equivalent phase shift of the experimental setup recorded with the 1 GHz oscilloscope. Fluctuations are lower than the ones recorded with the 3 GHz ADC board shown in Figure 5.14.

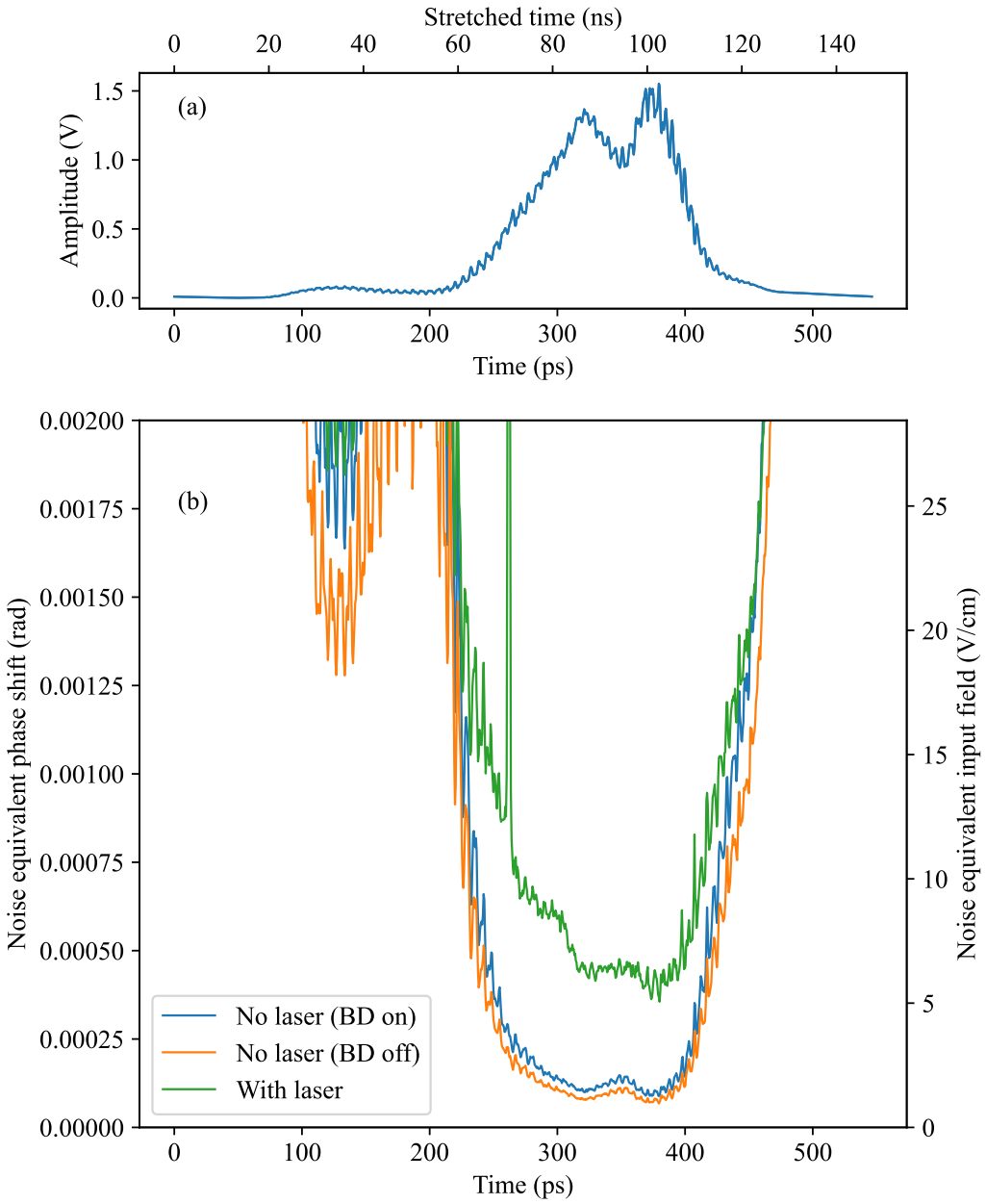

FIGURE 5.14: Sensitivity and detail of noise contributions in the absence of THz signal. (a) Laser pulse shape measured on one single input of the balanced detector. (b) green: sensitivity of the EO system, defined as the THz electric field (and phase-shift in the EO crystal), that is equivalent to the measured noise. Blue and orange: measured contributions of the balanced detector and of the ADC board respectively.

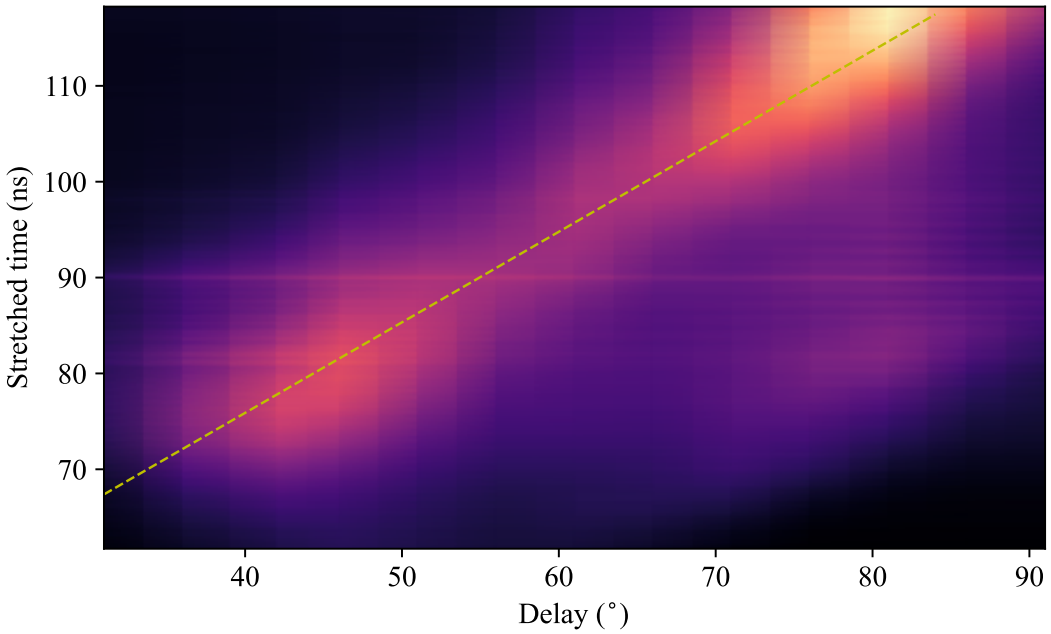

FIGURE 5.15: Calibration done with varying the delay between the THz signal and the laser pulse. This shows a linear response between stretched time, the time measured by the oscilloscope or the ADC board, and real time in correspondence with the delay.

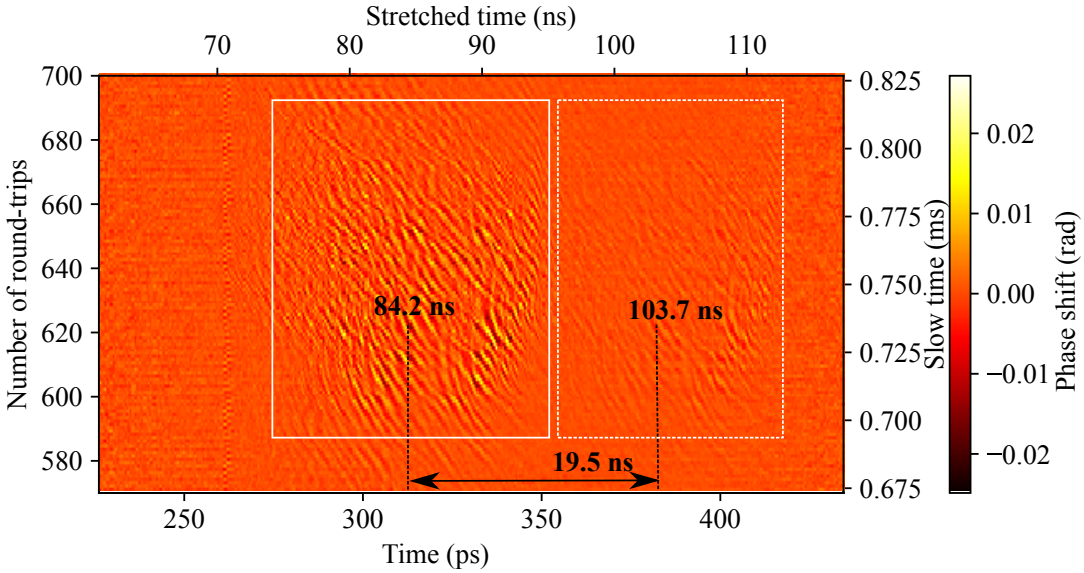

FIGURE 5.16: A color map of the CSR THz signals measured in single-shot showing the original THz signal and its reflection inside the GaAs crystal. The round-trip time helps in calibrating the system and determining the stretch factor.

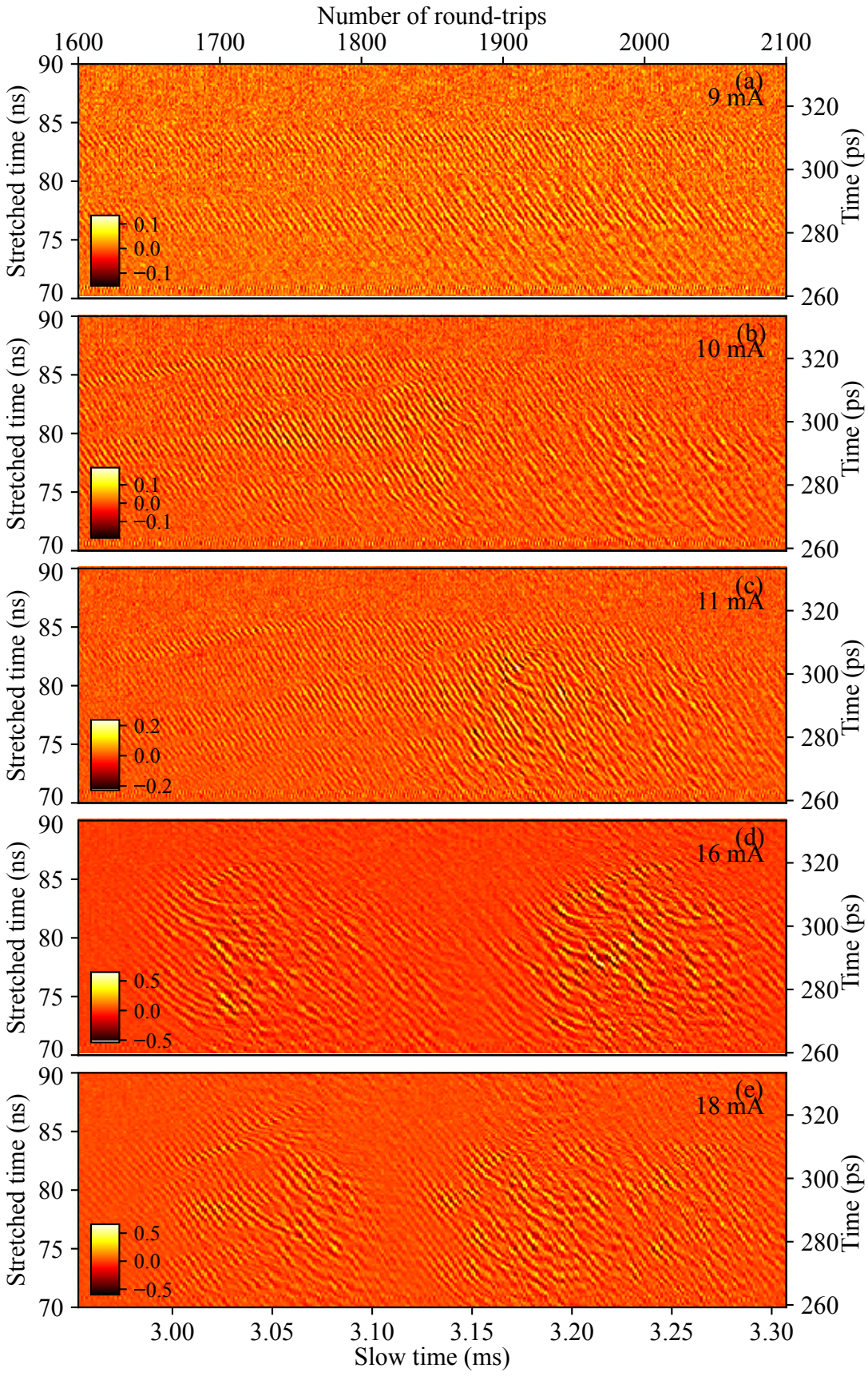
Number of round-trips
1600
1700
1800
1900
2000
2100
(a)
9 mA
(b)
10 mA
(c)
11 mA
(d)
16 mA
(e)
18 mA
Stretched time (ns)
90
85
80
75
70
Time (ps)
320
300
280
260
0.1
0.0
−0.1
0.2
−0.2
0.5
−0.5
3.00
3.05
3.10
3.15
3.20
3.25
3.30
Slow time (ms)

FIGURE 5.17: Colormaps showing EO signals measured in single shot, using the ADQ7DC acquisition board of the CSR THz pulses at increasing beam currents in the accelerator. These colormaps provide a visual representation of the changes in the EO signal along the electron bunch as the beam current is increased, giving insights on the behavior of the CSR emitted pulses and how they are impacted by variations in the beam current. Note that signals are cut for a better visualization and the colorbar represents of the scale of the EO signal in Volts.

As we have now a functional ultrafast detection tool for monitoring CSR, it is interesting to observe how these microstructures are formed and understand their behavior at different beam currents. We performed measurements as function of the beam current in the storage ring, in balanced detection configuration, with the ADQ7DC board around and above threshold. The system was calibrated first with a high beam current of I = 14.992 mA. Subsequently, a scan was performed over a range of intensities going from the threshold around 8.52 mA to the highest current 18.1 mA.

Single-shot recorded EO signals in Figure 5.17 with their spectra in Figure 5.18 provide a good visual representation of the behavior of these microstructures at different beam currents. When the beam current is below a certain threshold (result now shown here), the microstructures are either not formed yet or their field strength is so weak that they are not visible or have negligible effect on the electron bunch. As the beam current increases around threshold (around 8.5 mA), the microstructures begin to form in more regular patterns with a remarkable amplitude, as seen in Figure 5.17(a) at 9 mA. They present parallel shapes appearing and drifting longitudinally inside the electron bunches in a continuous way. As the beam current further increases above threshold, these microstructures acquire more field, become more conspicuous and start losing their parallel movement (Figure 5.17 (b) and (c)). They start to bunch together in bursts, at higher intensities, and rotate inside and along the electron bunches as seen in Figure 5.17(d) and (e). This effect can be clearly observed in Figure 5.19 showing the evolution of THz pulses energy with the increase of the beam current, where around threshold in Figure 5.19(a), the THz energy is quasi constant. This emission is revealed in burst mode for high beam currents and behaves in more and more irregular patterns. In addition, the CSR electric fields become more significant with higher amplitudes at higher intensities, i.e. at 18 mA in Figure 5.19(d, e).

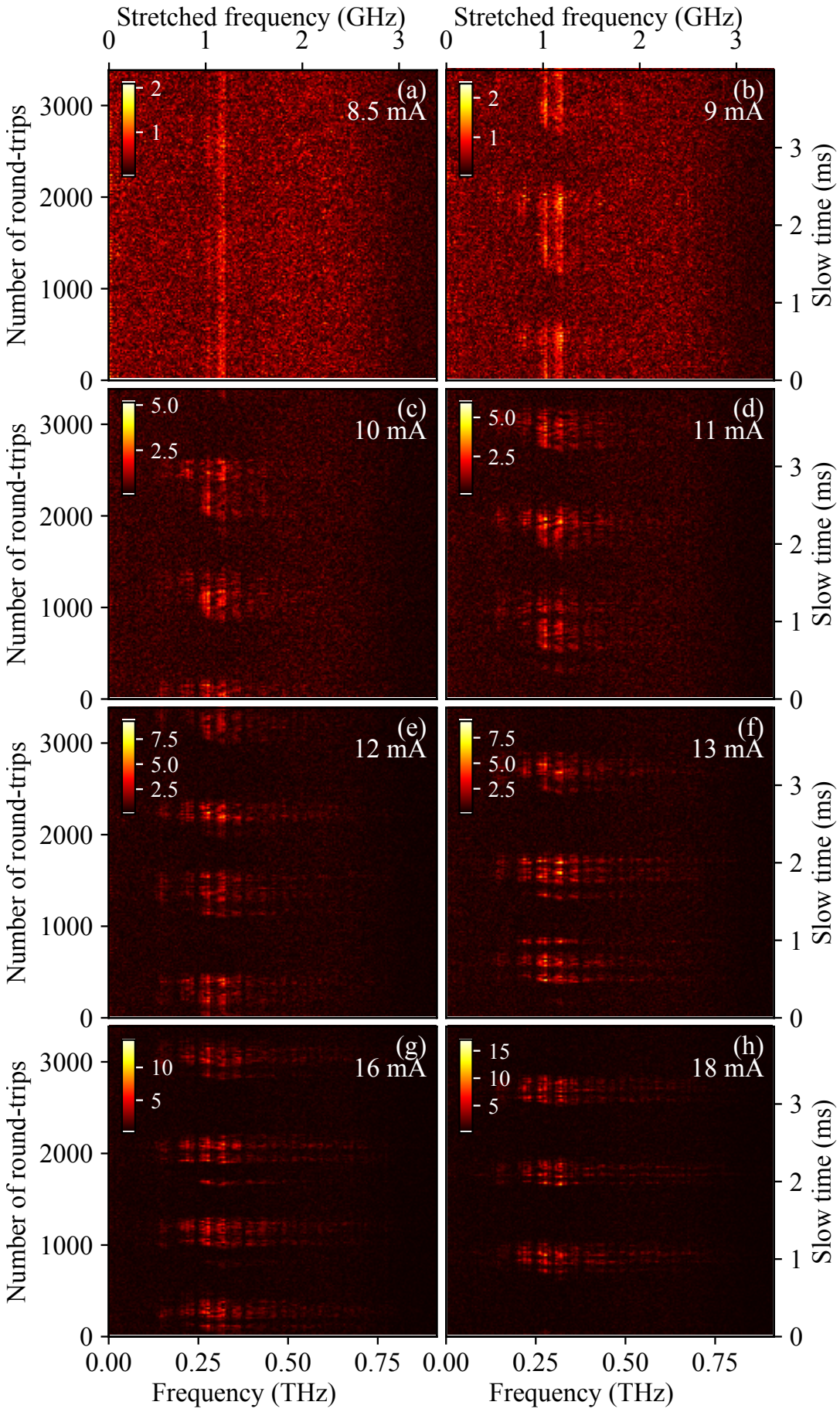
Stretched frequency (GHz)
Stretched frequency (GHz)
(a) 8.5 mA
(b) 9 mA
(c) 10 mA
(d) 11 mA
(e) 12 mA
(f) 13 mA
(g) 16 mA
(h) 18 mA
Number of round-trips
Slow time (ms)
Frequency (THz)
Frequency (THz)

FIGURE 5.18: Colormaps showing the spectra of EO signals measured in single shot, using the ADQ7DC acquisition board, of the CSR THz pulses at increasing beam currents in the accelerator. These colormaps provide a visual representation of the changes in the spectra as the beam current is increased. A single frequency is observed at the threshold current (around 8.52 mA) and additional frequencies begin to appear at higher beam currents. The colorbars indicate the scale of the spectra modules of EO signals measured in Volts.

The Fourier Transform of the recorded EO signals reveal the presence of a relatively narrow spectrum at a dominant frequency peak around 0.3 THz in Figure 5.18(a) when the beam current is at the threshold intensity of 8.5 mA. A second threshold is determined above which the CSR are emitted in bursting mode as in Figure 5.18(b, c,d,e,f,g and h). In addition, additional peaks emerge at more frequencies and the spectra become broader as the beam current increases. With further increases in beam currents (Figures 5.18(d, e, f, g and h)), the peaks become more visible and pronounced, their spectra become wider and the bursting mode becomes clearer. Note that the vertical dark lines appearing in the measured spectra are due to limitations of the setup, related to the transfer functions.

To sum up, these observations showed the presence of microstructures at all intensities above threshold, and the high dynamic range of our detector allowed accurate measurements even near the threshold current. These results provide insights into the behavior of these particular structures and allow a better understanding of the underlying physical processes involved in CSR production. We can visualize how these CSR pulses are affected by beam currents in the accelerator, helping in optimizing the machine parameters for providing THz pulses with the desired properties. The dynamics of these experimental observations can be helpful to compare with developed simulations and predicted models. For example, the obtained results reveal a similar behavior as the numerical simulations [120] previously performed at SOLEIL using the Vlasov-Fokker-Planck (VFP) integration and the macro particles tracking shown in Figure 5.20 at a 15 mA.

Further investigations can be done at different parameters of the accelerator and other machine modes to gain a deeper understanding of this phenomenon and possibly discover new insights.

5.7 First attempt to achieve phase diversity with time-stretch at 1550 nm

5.7.1 Results of the first attempt

The objective of this experiment was mainly to test the limit of photonic time-stretch at 1550 nm. And as expected, Figure 5.7(c), Figure 5.12 and Figure 5.18 reveal the presence of zeros in the measured spectra of the CSR THz signals, which are caused by dispersion penalty phenomenon, limiting the temporal resolution of detection, previously discussed in section 2.5.1.

An attempt was made to implement the phase diversity technique with the experimental setup described in this chapter. We adapted the setup with a similar

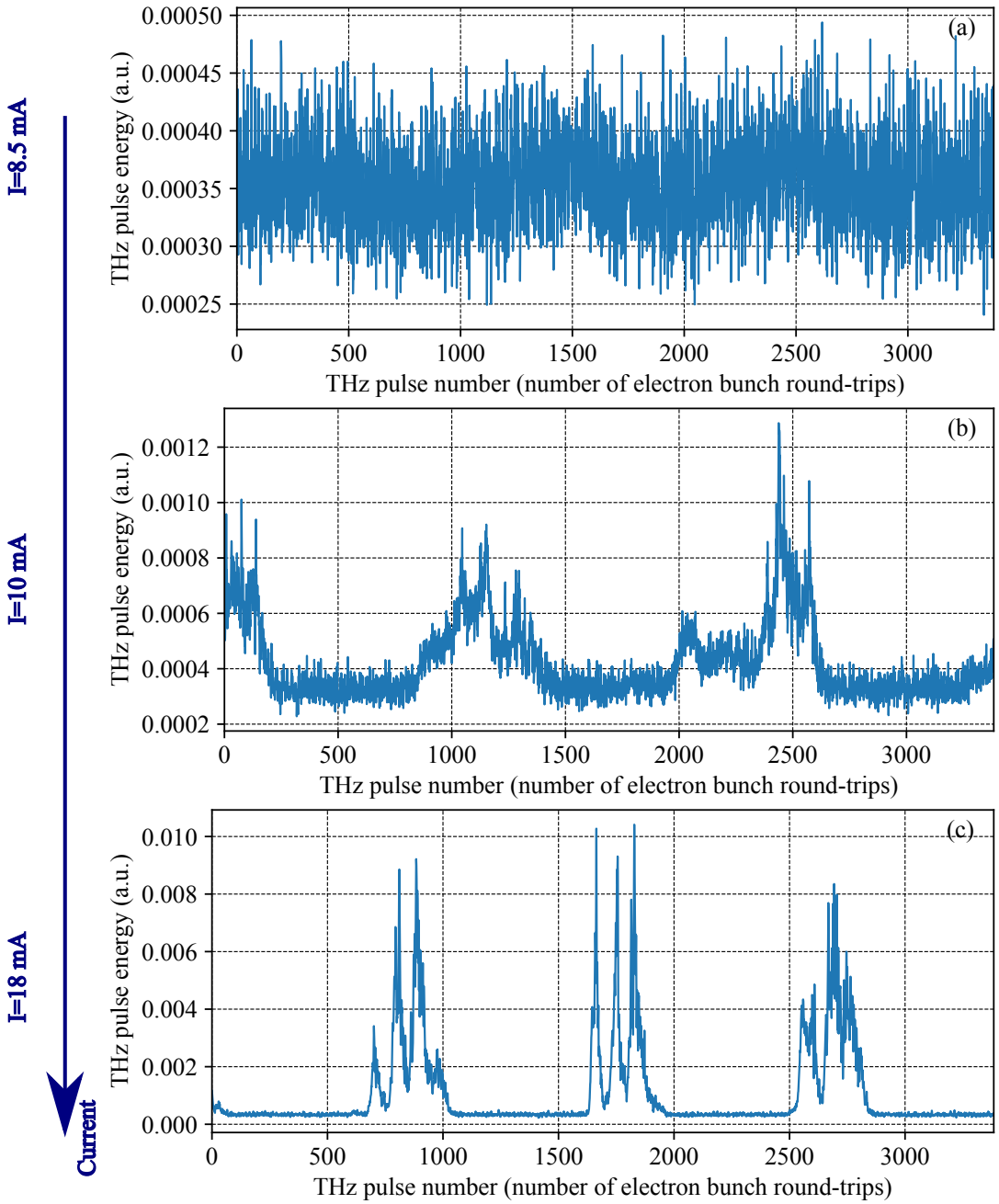

FIGURE 5.19: Measurements of THz pulses energies over more than 3000 electron bunch round-trips with the increase of the beam current in the storage ring with I = 8.5 mA in (a), I = 10 mA in (b) and I = 18 mA in (c).

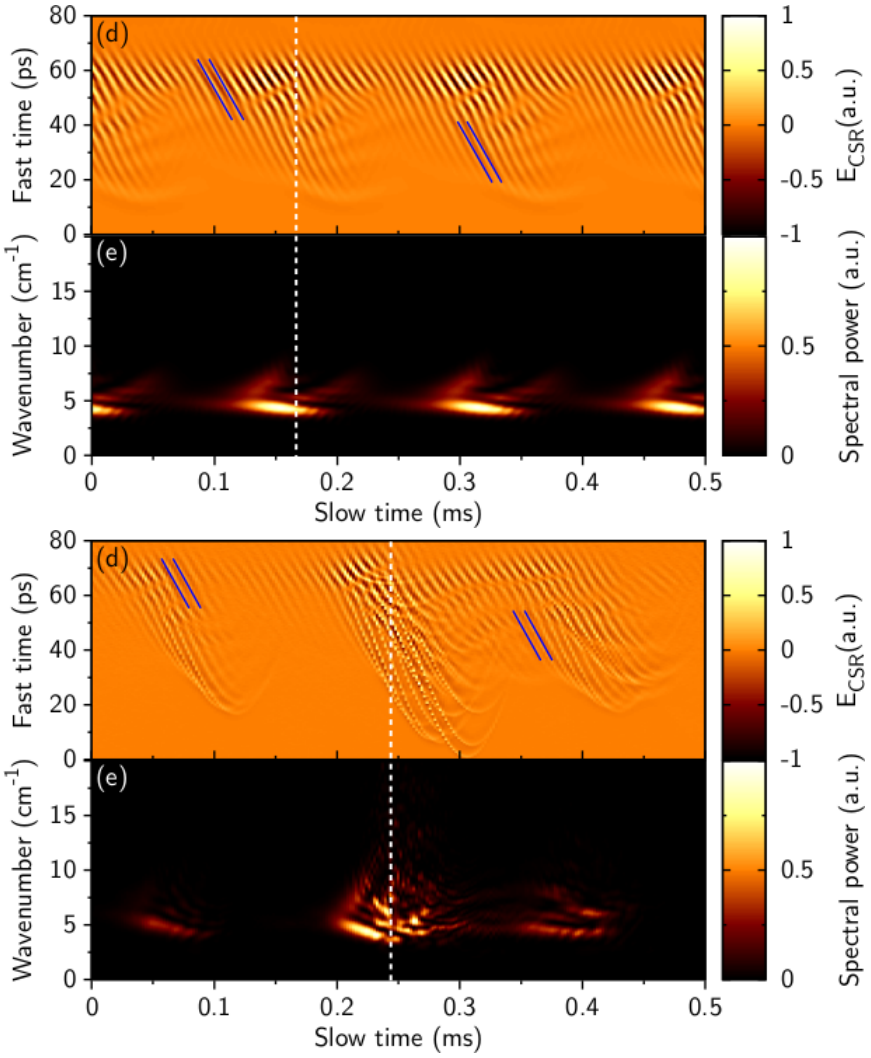

FIGURE 5.20: Numerical simulations showing the microbunching instability for a beam current of 15 mA using the VFP integration in (a) and the macro particles tracking based simulation in (b). Figures from [120].

configuration to the experimental setup presented in Chapter 3 by adding one fiber of length ∼29.5 m, corresponding to the time travel of light of one repetition rate of the laser pulse in the fiber and the same configuration for the wave plates orientations. This allowed to record each polarization alone simultaneously (see Figure 5.21). We can see in Figure 5.22 the average Fourier transform of the measured signals showing interleaved zeros.

However, the SNR is insufficient for applying the MRC algorithm. Experimentally, the noise level of the setup in the phase diversity configuration is 10 times higher than the balanced detection configuration as seen in Figure 5.23, as in the phase diversity configuration, different pulses are subtracted between each other, and thus the common laser fluctuations are not suppressed, as described in Figure 2.8(c).

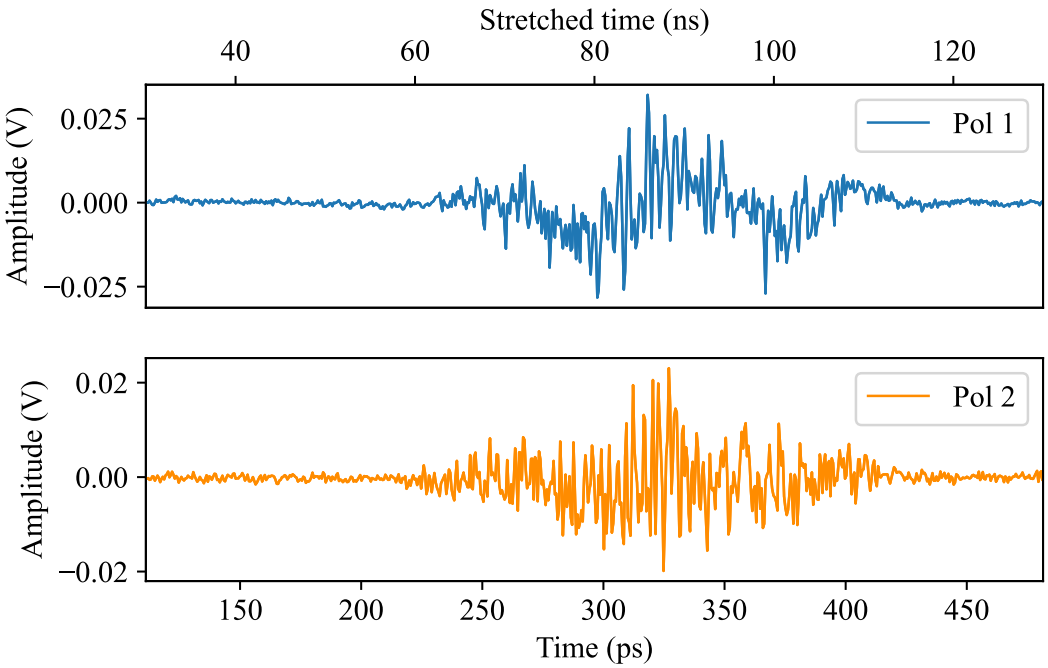

FIGURE 5.21: Single shot temporal profile of THz polarizations states recorded separately in the phase diversity configuration.

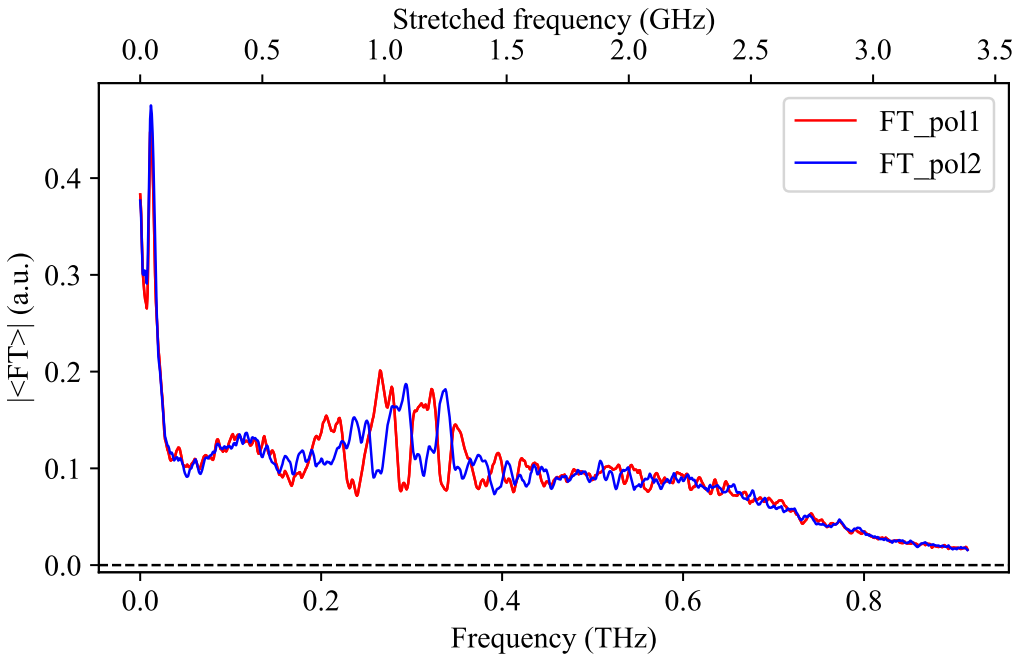

FIGURE 5.22: Average Fourier Transform of polarization 1 and polarization 2 recorded by the acquisition board showing interleaved zeros.

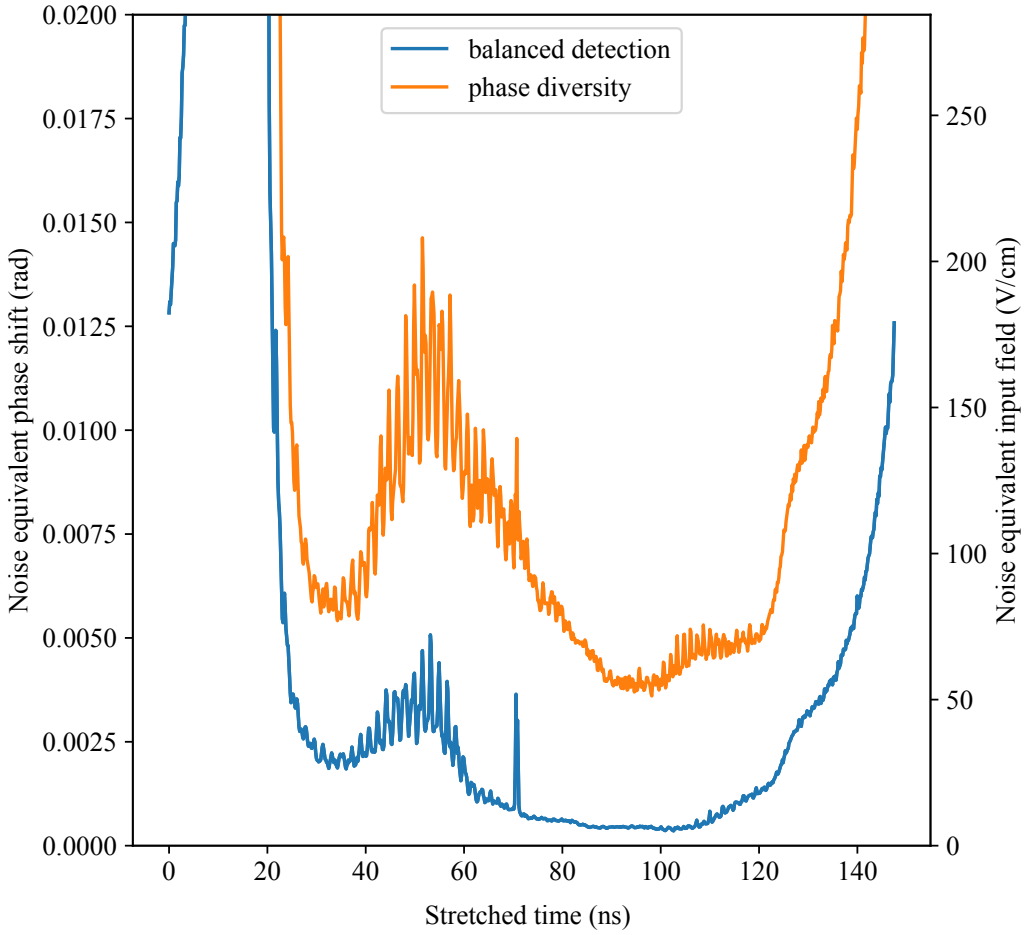

FIGURE 5.23: Noise equivalent phase shift of the setup without any THz modulation in phase diversity configuration versus in balanced detection configuration for recording with the ADC board.

5.7.2 Foreseen upgrades

Though, a next step could to be to design a new experimental scheme allowing to suppress common noises and thus improve the SNR of the system in the phase diversity configuration. One possibility for reducing the noise can be the optimization of the amplifier used in the detection system. In the current experiment, a home-made amplifier was used. But due to the limited time before the shift and to the complication of getting a shift, we had to settle for this option. A future amelioration would be the use of an amplifier with a lower amplified spontaneous emission (ASE), which is expected to increase the SNR of the detector or to apply a numerical BD with two different photodetectors.

5.8 Conclusion

To conclude, we have demonstrated in this chapter the functionality of photonic time-stretch electro-optic sampling at the 1550 nm wavelength for the first time. At this wavelength, we exploded the limit of stretch reaching 35 ns, the highest to our knowledge. And being able to measure THz signals with a 1 GHz oscilloscope, with a relatively high effective number of points is a significant improvement compared to previous detection schemes. Now we have a functional THz detector similar to the one presented at 1030 nm in Chapters 3 and 4 but with a 10 times cheaper digitizer where the most expensive component is the laser. Our detector can measure, in real-time, single-shot THz signals with rates up to 3.3 MHz in balanced detection configuration with 1.35 TSamples/s and a recording window of 130 ps. This acquisition rate can be increased according to the laser repetition rate, to the pulse picker division and to the desired recording window. A longer recording window is and can be easily adjusted according to needs. The sensibility of the detector is 0.45 mrad or equivalently 6.5 V/cm (with the acquisition board) in balanced detection configuration. Additionally, the use of an acquisition board as presented in this chapter, helps in direct custom processing data easier than the scope and for longer time acquisition.

This THz detector allowed as well to measure the whole CSR THz pulses in single shot, a first in CSR single-shot measurements, compared to previous recordings where only a small part of the signals was measured. The use of the acquisition board made it possible to record over long duration the formation of the CSR pulses in bursts in the storage ring. Our results are in accordance with simulations and will help to optimize and adapt existing models to real experimental observations, giving better understanding on the behavior of these special microstructures. Our detector can also serve for several applications, including single shot measurements related to THz spectroscopy and table-top experiments.

Our experimental setup is compact and ready to be installed in accelerators-based light sources, with the possibility to adapt it easily to the coherent synchrotron emitted radiation characteristics and to THz signals under investigation. The operational device, presented in this chapter, will be installed soon permanently at the AILES beamline at SOLEIL to monitor microbunching instability.

However, in terms of limitations and optimization, one important aspect to work on is the noise level of the detector in phase diversity configuration. A further possibility can be to enhance the sensitivity of detection by adding Brewster plates that

can increase the sensitivity by a factor 6.7 [114]. Another potential solution can be the application of the backpropagation technique that will enable the reconstruction of the THz input signal without limitation on the resolution [143, 144].

Chapter 6

Conclusion and future directions

We have exposed in this thesis the THz detectors we have developed to measure ultrafast signals in a free electron laser (FEL), a storage ring and a CDR THz source. These detectors are based on single shot electro-optic sampling (EOS) and are associated with photonic time-stretch to reach high acquisition rates.

In a first experimental setup built upon single-shot EOS at 1030 nm, detailed in Chapter 3, we combined for the first time photonic time-stretch, phase diversity and balanced detection all together in a single setup to allow single-shot measurements, and repress limitations over temporal resolution and acquisition rate. The first prototype experimental setup was tested at the CDR THz source at the linear accelerator ELBE. The experiment was successful as we were able to measure in single-shot the THz pulses around 0.3 THz at a 26 MHz acquisition rate with a sufficient sub-ps temporal resolution. This allowed to follow the arrival time of the electron bunch and get information on the time jitter. This monitoring tool shows promising insights for diagnostics in accelerators-driven light sources and for machine development.

In Chapter 4, we showed how the same experimental setup, with slight modifications, allowed to measure the evolution of the THz pulses emitted by a FEL in single shot at FELBE. This study marks the first measurement of FEL pulses in single-shot and of a mode locked laser in general, permitting to observe the dynamic of the FEL. We were able to measure the FEL radiation characterized by a 4 THz central frequency and a 13 MHz repetition rate and observe the startup and the turnoff of the FEL in single shot, with further work required to refine this exploration. We have demonstrated the ability to measure the carrier-envelope phase (CEP) of the FEL pulses shot-by-shot, an important achievement for studies requiring stable CEP. A study versus detuning was also performed and reveal potential for a FEL with a better stability.

In Chapter 5, we have developed a novel experimental setup, analogous to the previous one but operating at a different wavelength, the 1550 nm telecommunication wavelength to enhance the limit of photonic time-stretch and reduce the cost of the digitizer. In comparison with the previous setup at 1030 nm where signals were stretched up to $\sim$6 ns necessitating an oscilloscope of tens of GHz, the 1550 nm setup enabled stretching up to $\sim$35 ns reducing the detection bandwidth by a factor 10. This setup was tested at the storage ring SOLEIL enabling the first complete single-shot CSR THz pulses and this by using a 1 GHz oscilloscope and a 3 GHz ADC board. By doing so, this experiment showed promising avenues for THz oscilloscopes with a relatively low cost where the most expensive component is the laser making it accessible and suitable for table-top experiments. Additionally,

this work involved investigating the relationship between CSR formation and beam current, particularly the emergence of microbunching instability above a threshold by performing series of measurements at and above the threshold and observing experimentally their evolution with the augmentation of the beam current. These observations are important as they allow comparing with simulations and ameliorate existing models. Despite these achievements, improvements of the temporal resolution are still needed, as the sensitivity was insufficient for accurate reconstruction of the THz signals.

To sum up, our thesis highlights three distinct experiments involving different THz sources: the CDR THz source from the linear accelerator at ELBE with an ultrashort single-cycle temporal profile and a broad spectrum, the FEL THz source with a multi-cycle long temporal profile and a narrowband spectrum and finally the CSR at SOLEIL storage ring with both a long temporal profile and a broadband spectrum. We can see how the combination of optics and photonic in one setup allowed to reach various THz radiations with different properties with few modifications. We have demonstrated the capacity to monitor THz signals in real time and reach high repetition rates up to 26 MHz. These setups are robust and compact and ready to be installed in storage rings and FELs and can be adapted according to desired THz properties. The setup at SOLEIL will be soon installed permanently to monitor the microbunching instability in real-time. These investigations validate the efficacy of our "THz oscilloscope" and its adaptability in different contexts, while also bringing up a novel territory for cost optimization.

Beyond particle accelerators, these setups reveal promising insights for THz spectroscopy experiments for measuring THz spectra of irreversible phenomena in single shot. At ELBE for example, the high time jitter presents an obstacle [132] for experiments requiring phase measurements. We saw that even with a high jitter we were able to measure spectra in single shot. At FELBE, achieving CEP stable FEL pulses opens the way for new avenues in THz experiments requiring phase information. Additionally, the photonic time-stretch at 1550 nm at a reduced digitizer cost is very promising for spectroscopists seeking to study ultrafast irreversible phenomena and convenient for table-top experiments.

In the area of perspective, there are avenues for further exploration, particularly in optimizing the temporal resolution and the sensitivity at the 1550 nm wavelength. Additional strategies can be explored to enhance the sensitivity needed for table-top experiments. Open problems are relevant for FELs with higher THz frequencies (up to 10 THz and more) at high repetition rates such as FELBE, PITZ, etc., or even to measure in single-shot multi-cycle THz signals. Another perspective involves the study of higher orders dispersion in the detection scheme at which MRC-based reconstruction algorithm could be problematic.

Appendix A

Choice of the EO crystal

In this section, we discuss briefly the choice of the EO crystal used in the experimental setups presented in this work, in particular the material of the crystal and its thickness. In order to choose the appropriate electro-optic (EO) crystal for THz detection, we proceeded to the following calculations. Two important parameters are selected: the EO coefficient and the crystal thickness. A compromise between these parameters should be considered when choosing the appropriate EO crystal. This discussion is based on studies performed in [7, 86].

A.0.1 Crystal material

The selection of an appropriate electro-optic (EO) crystal is crucial to achieve a good EO response. The choice of the EO crystal depends on the phase matching condition, which stipulates that the laser probe pulse and the THz pulse should travel in the crystal at the same velocity. This phase mismatch can be defined by:

$$\Delta k = \frac{f_{THz}}{c}(n_{THz}(f_{THz}) - n_g(f_{probe})) \tag{A.1}$$

where n_{THz} is the refractive index at the THz frequency f_{THz} and n_g the group refractive index of the laser probe pulse.
The refractive index of the THz in the EO crystal is frequency dependent and affects the coupling of the THz inside the crystal. Thus, a good coupling should be assured to maximize the EO effect, provide a good time resolution and avoid distortions of the signal.

Zinc telluride (ZnTe) crystal, gallium phosphide (GaP) and gallium arsenide (GaAs) are the most widely used crystal materials for THz detection.
According to [145], ZnTe crystal is found suitable for THz detection at 800 nm laser wavelength, GaP is suitable for 1030 nm Ytterbium laser pulses and GaAs is adapted for 1550 nm wavelength, all having the most stable phase matching in the THz region. GaP can achieve high THz signals compared to ZnTe and GaAs due to its highest transverse optical (TO) lattice oscillations ($\sim$ 11 THz), defining the shortest time structure that can be detected. But this crystal has a lower EO coefficient compared to ZnTe (5.3 THz) and GaAs ($\sim$ 8 THz), implying that, for low frequencies, it is better to use a crystal with a high EO coefficient than to use a thick GaP crystal.

As in Chapter 3 and 4 experiments are operated with Ytterbium-doped laser system at 1030 nm, a GaP is used to assure a satisfying EO effect whereas in Chapter 5, a GaAs crystal is utilized, at 1550 nm fulfilling the phase matching condition with the 1550 nm Erbium laser.

EO crystal	ϵ_{el}	S_0	f_0 (THz)	Γ_0	γ_{41} (THz)
GaAs	11.1	1.8	8.025	0.066	1.43
GaP	8.7	1.8	10.98	0.02	0.97

TABLE A.1: Crystal coefficients for GaAs and GaP EO crystals.

A.0.2 Thickness of the EO crystal

The electro-optic efficiency is determined by an EO response function which depends on the THz frequency f and the crystal thickness d of the crystal. It is defined by:

$$G(f,d) = \frac{2}{1+n(f)+i\kappa(f)} \frac{1}{d} \int_0^d \exp[i2\pi f z(\frac{1}{v_{ph}(f)} - \frac{1}{v_g})]dz \tag{A.2}$$

where $n(f)$ is the refractive index, $\kappa(f)$ the extinction coefficient in the THz regime, $v_{ph}(f)$ the phase velocity of the THz frequency and v_g the laser optical group velocity.
The complex index of the crystal $n(f) + i\kappa(f)$ is frequency dependent given by:

$$n(f) + i\kappa(f) = \sqrt{\epsilon(f)} \tag{A.3}$$

with $\epsilon(f)$ the complex dielectric function defined by:

$$\epsilon(f) = \epsilon_{el} + \frac{S_0 f_0^2}{f_0^2 - f^2 - i\Gamma_0 f} \tag{A.4}$$

ϵ_{el} is the optical dielectric constant, S_0 the oscillator strength, f_0 the eignefrequency and Γ_0 the damping constant of the lowest TO lattice oscillation.

For the effective response $G(f,d) * r_{41}(f)$, the EO coefficient r_{41} is frequency dependent and affected by lattice oscillations, expressed by:

$$r_{41}(f) = d_E(1 + \frac{C f_0^2}{f_0^2 - f^2 - i\Gamma_0 f}) \tag{A.5}$$

This EO efficiency shows the effect of the phase mismatch and absorption on detection. It can be optimized by reducing the thickness of the crystal.

We limited the study of the EO response for GaP crystal in Figure A.1 and GaAs crystal in Figure A.2 for different crystal thicknesses.

Having all parameters summarized in Table A.1, taken from [7, 86, 146], with $d_E = 1.10^{-12}$, $C = 0.53$ for GaP, we can represent the electro-optic response of GaP EO crystal for a 50 μm, 100μm, 200μm, 2 mm, 3 mm and 5 mm thickness.
It is obvious that higher THz frequencies can be reached with thinner crystals. Strong absorptions are observed around the TO lattice oscillations frequency limiting the detection bandwidth achieved by the crystal. The amplitude of detection response increases with the increase of the crystal thickness but on the cost of the detection bandwidth. Thus, a compromise between high EO response and detection bandwidth should be considered when choosing the EO crystal.

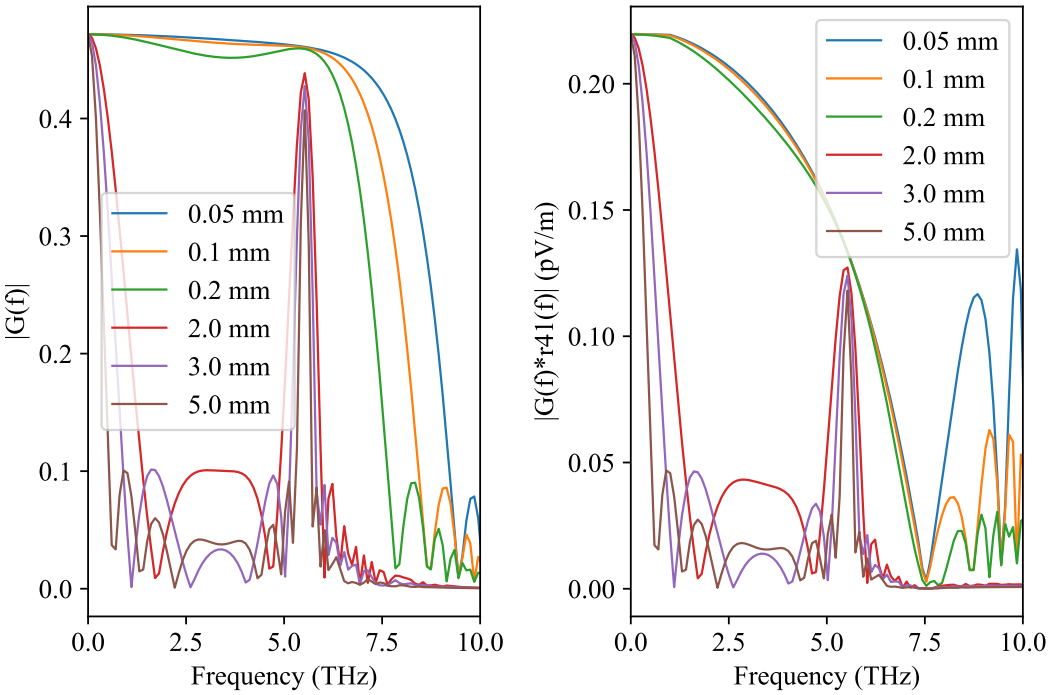

FIGURE A.1: (a) Electro-optic response and (b) effective electro-optic responses of GaP crystal at 1040 nm for different crystal thicknesses.

Another parameter should be considered when choosing the crystal thickness which is the coherence length which is given in the case of pulsed near-infrared laser radiation by:

$$L_c(\omega_{THz}) = \frac{\pi c}{w_{THz}|n_{opteff}(\omega_0) - n_{THz}(\omega_{THz})|} \tag{A.6}$$

with

$$n_{opteff} = n_{opt}(\omega) - \lambda_{opt}(\frac{\partial n_{opt}}{\partial \lambda})|_{\lambda opt} \tag{A.7}$$

The thickness of the crystal should be smaller than the coherence length, but should be large to have a better bandwidth.

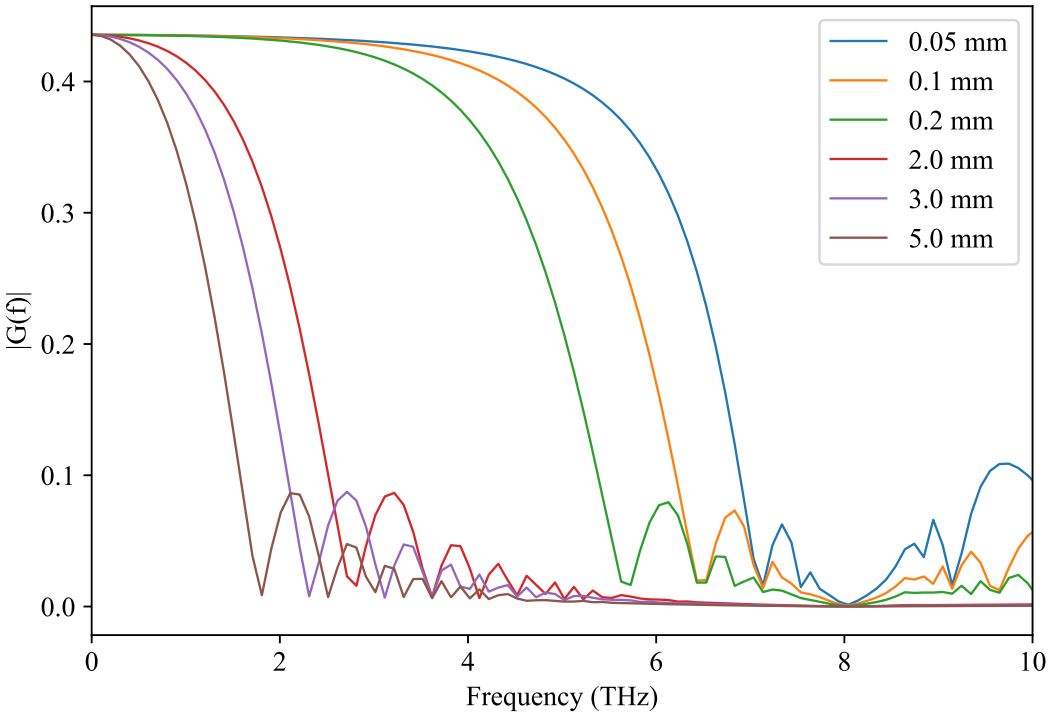

FIGURE A.2: EO responses function for a GaAs crystal for different crystal thicknesses.

Appendix B

Data analysis

This Appendix summarizes the computational data analysis adapted for the extraction of the THz signals in the presented experimental results.

B.1 Balanced detection configuration

In classical balanced detection configuration, the same laser pulse on both arms of the polarizing beam splitter is subtracted at the input of the balanced detector resulting in a suppression of the common laser shot-to-shot fluctuations, as described in section 2.4 (Figure 2.8).

Pulses are cut and interpolated at the laser repetition rate and then sorted between pulses with THz and without THz (used as zero field background). Reference laser pulses are also recorded by measuring the signal on only one of the detection arms. The electro-optic phase shift at each shot n recorded at the output of the balanced detector is obtained after suppression and normalization according to :

$$S_{nTHz}(\text{or } \Delta\Phi) = \frac{V_{nbdTHz} - V_{bdnoTHz}}{G(V_1^{ref} + V_2^{ref})} \tag{B.1}$$

where V_{nbdTHz} is the amplitude of the single-shot balanced detected signal containing the THz signal, $V_{bdnoTHz}$ is the amplitude of the zero-field background without THz signal, V_1^{ref} and V_2^{ref} ($V_1^{ref} \approx V_2^{ref}$) are the references laser signals on each balanced detector input recorded at minimal gain respectively with G the ratio gain factor of the balanced detector between the maximal 2800 V/W and minimal 30 V/W gain. Note that the laser pulses references are not the same pulses on which the THz was imprinted.

The THz electric field was thereby deduced using:

$$E_{THz} = \frac{\lambda}{2\pi d n_0^3 r_{41}} \Delta\Phi \tag{B.2}$$

B.2 Phase diversity configuration

In the phase diversity configuration, each polarization state is measured separately as shown in Figure B.1. And to do so, pulses on one of the arms are delayed by a period corresponding to one laser repetition rate as explained in section 2.4, Figure 2.8. However, this prevents the cancellation of shot-to-shot laser fluctuations.

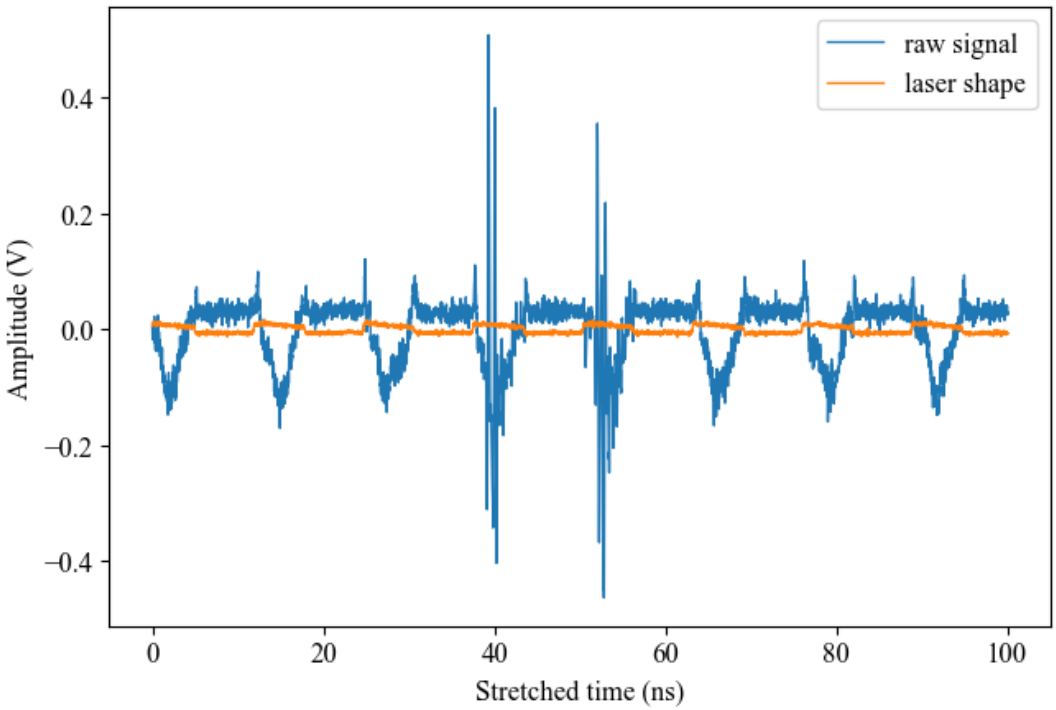

FIGURE B.1: Raw data (blue) recorded by the oscilloscope, showing the two electro-optic output polarization states recorded separately after balanced detection. Reference laser pulses (in orange) recorded on one of the detection arms.

Each shot of the EO signals polarization is obtained after suppression from the background noises and normalized by the laser shape before MRC reconstruction algorithm according to :

$$Y_{1n} = \frac{V_{1n} - \beta_1 V_{0n}}{\beta_1 V_{0n}} \tag{B.3}$$

$$Y_{2n} = \frac{V_{2n} - \beta_2 V_{0n}}{\beta_2 V_{0n}} \tag{B.4}$$

with

$$\beta_1 = \frac{V_{1n}^{ref}}{V_{0n}^{ref}} \text{ and } \beta_2 = \frac{V_{2n}^{ref}}{V_{0n}^{ref}} \tag{B.5}$$

where V_0 is the unmodulated laser pulse with the sign ^{ref} refers to the measured signals in the absence of THz electric field.

The THz electric field is deduced from the phase shift of the reconstructed MRC THz signal using:

$$E_{THz} = \frac{\lambda}{\pi d n_0^3 r_{41}} \Delta\Phi \tag{B.6}$$

Appendix C

Coherent diffraction radiation (CDR) pulses recordings with an 8 GHz bandwidth oscilloscope

C.0.1 Recordings with an 8 GHz oscilloscope

As seen in the spectra of the recovered THz in Figure 3.9, no information appears after $\sim$8 GHz. Using an oscilloscope with a smaller bandwidth can help in reducing noise and improve the signal-to-noise-ratio, as it excludes high-frequency noises, irrelevant to the THz signal of interest. Given the broad THz bandwidth (up to 1 THz) of the CDR source and the laser pulse duration of 6 ns, the 20 GHz oscilloscope used is quite oversized for our experiment and may have introduced unnecessary noise. Therefore, we performed additional EO measurements with an 8 GHz oscilloscope with 40 Gs/s according to the availability, that should be sufficient and efficient to capture the THz signals, with minimal noise and cost.

Figure C.1(a) shows the phase shift induced by CDR THz signals in radians as recorded by the 8 GHz oscilloscope shot to shot over more than 16000 electron bunches after processing and reconstruction with MRC algorithm. These measurements are accompanied by their corresponding THz spectra in single shot, as depicted in Figure C.1(b). Signals were recorded in sequence mode to reach more electron bunches seen the relatively low THz repetition rate. The observed discrepancy in time jitter between the measurements obtained with the 8 GHz (in Figure C.2) and 20 GHz oscilloscopes can be attributed to several factors. As the measurements were not done at the same time, these observations show a smaller time jitter compared to the ones measured with the 20 GHz oscilloscope according to the perfomance of the accelerator. Additionally, one possible explanation is the introduction of extra noise at higher frequencies and the broader bandwidth of the 20 GHz oscilloscope, which can impact the accuracy and precision of the recorded signal. The higher response to high-frequency noise can lead to a larger jitter measurement. Another factor that may contribute to the observed difference is the variation in the internal clock jitter between the two oscilloscopes.

C.0.2 Fluctuations of the experimental setup using the 8 GHz oscilloscope

In Figure C.3, it is evident that the observed fluctuations are lower when using the 8 GHz oscilloscope compared to the 20 GHz oscilloscope. Specifically, the fluctuations amount to 0.005 rad when employing the 8 GHz oscilloscope, while they reach 0.015

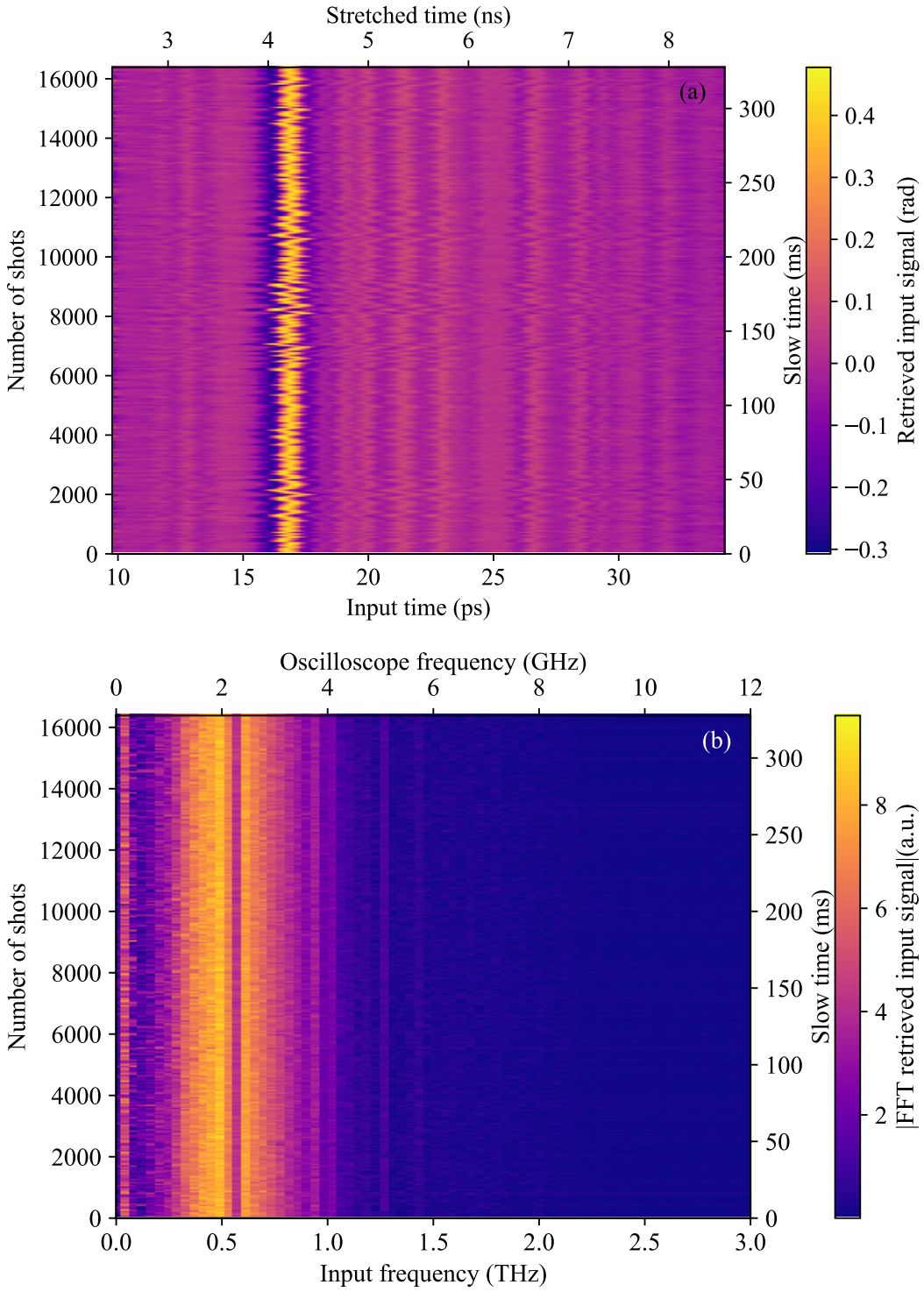

FIGURE C.1: Color maps of the retrieved single shot THz signals (a) and their spectra (b) recorded by the 8 GHz oscilloscope.

rad when utilizing the 20 GHz oscilloscope. This discrepancy can be attributed to the square root relationship between the fluctuations and the bandwidth frequency difference between both acquisition systems. Moreover, the system is still subject to more optimization work and suppressing noises, as a remarkable difference is seen

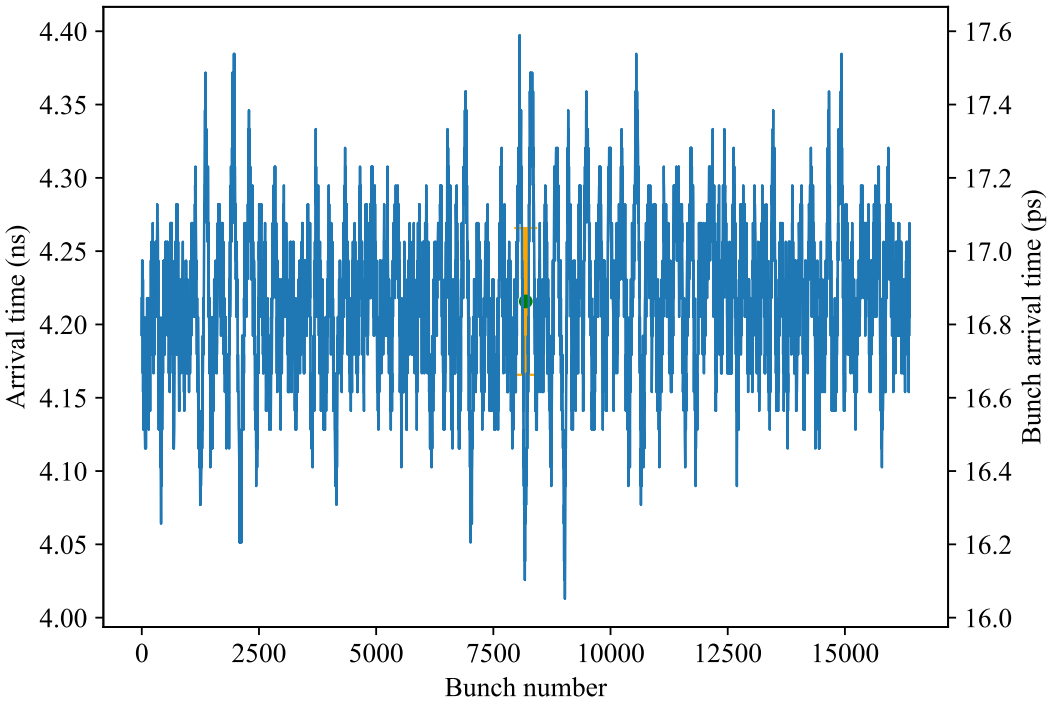

FIGURE C.2: Electron bunch arrival time over more than 16000 shots corresponding to signals in Figure C.1 recorded by the 8 GHz oscilloscope. A time jitter is observed varying between 16 ps and 17.6 ps with an average arrival time of 16.8 ps and a standard deviation of 0.2 ps. The jitter observed in this set of data is smaller than the jitter recorded with the 20 GHz oscilloscope.

between the fluctuations of the system with and without laser.

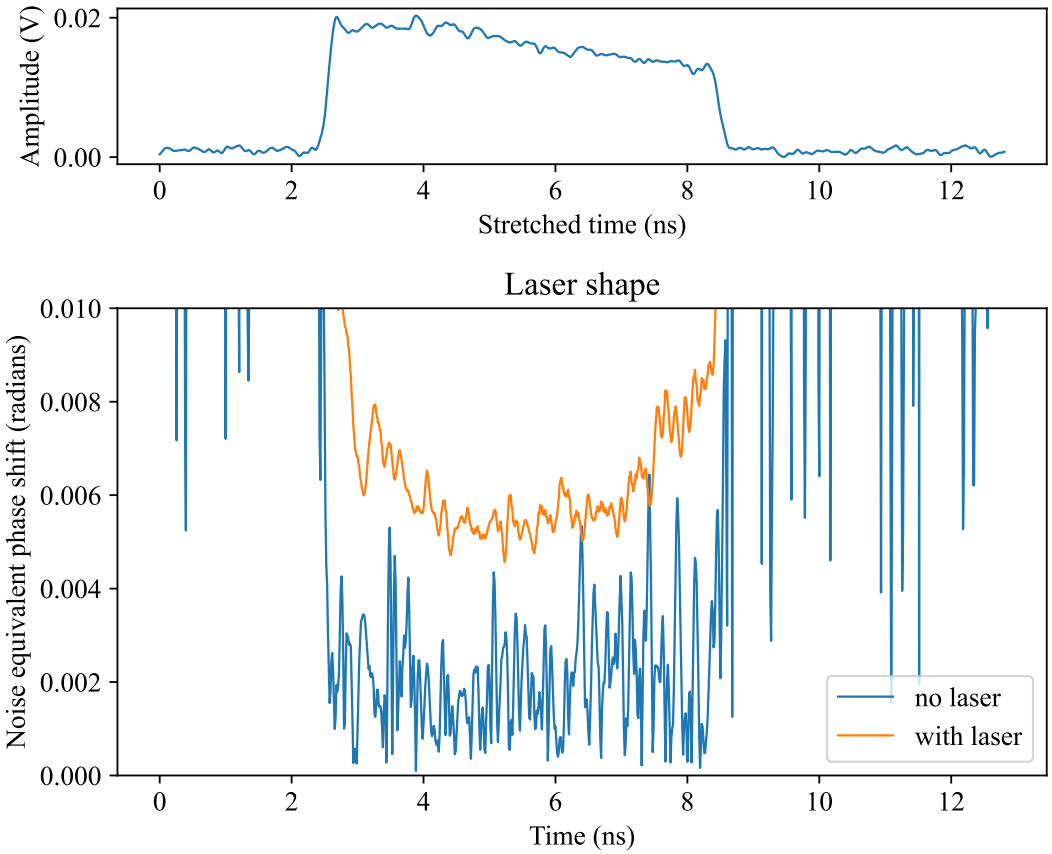

FIGURE C.3: (a) Laser pulse stretched and measured by the 8 GHz oscilloscope, with the (b) resulting fluctuations of the experimental scheme measured by the same oscilloscope with laser signal (in orange) and without laser signal (in blue).

Appendix D

DEOS transfer functions: sensitivity to the crystal and THz orientations

D.1 Polarization, crystal and waveplates orientations

The birefringence induced in the Pockels crystal depends on the THz electric field orientation. The configuration used for the DEOS strategy requires the THz polarization being perpendicular to the [-110]-axis and the laser polarization set at 45 degrees with respect to the [-110]-axis, as shown in Figure D.1. In this configuration, the laser polarization is also at 45 degrees with respect to the slow and fast axis of the induced-birefringence.

Experimentally, the main error in the geometry is likely to come from the crystal orientation (and thus the induced-birefringence orientation by the THz signal), while the laser polarization and waveplates orientations can be precisely aligned by adjusting the extinction on the output ports in absence of THz signal.

D.2 General form of the transfer functions

From [119], we know that the transfer function of a system where an input signal modulates in phase and amplitude a chirped probe laser, has the following form:

$$H(\Omega) = 2m\cos\left(\psi + B\Omega^2\right), \tag{D.1}$$

with $B = \frac{1}{2C}$ where $C = \frac{\partial\omega_{opt}}{\partial t}$ is the laser chirp rate, and m and ψ the amplitude and phase modulations (see supplementary material of [119] for details).

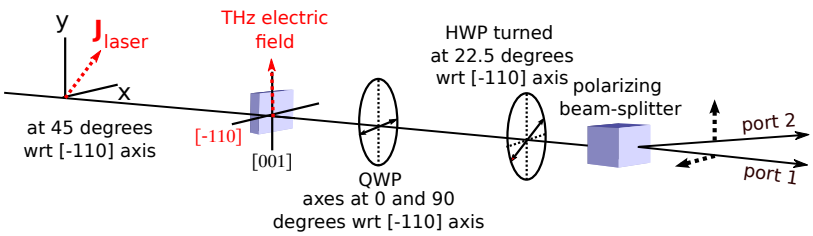

FIGURE D.1: Axes orientations for the phase-diversity-based EO configuration.

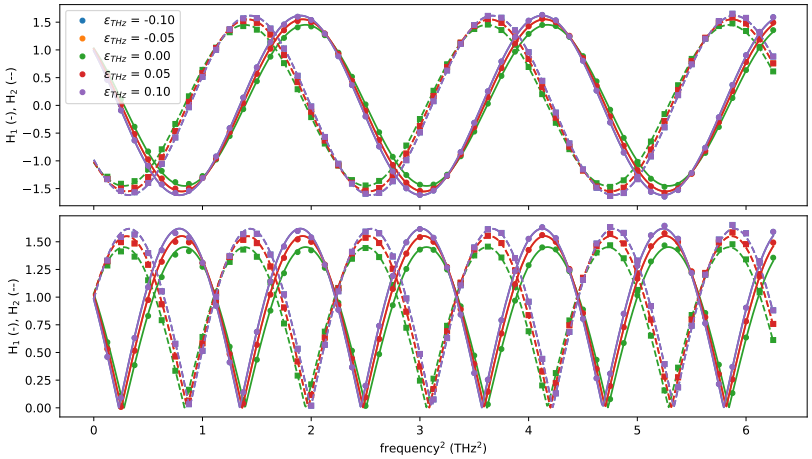

FIGURE D.2: Transfer functions (top) and its norms (bottom) as function of the THz polarization angle error ε_{THz}. Dots: numerical results, lines: numerical fit using Eq. (D.1).

In the case of the DEOS configuration, the transfer functions of the two output ports are written as:

$$H_i(\Omega) = \pm\sqrt{2}\cos\left(\frac{\Omega^2}{2C} \pm \frac{\pi}{4}\right), \tag{D.2}$$

with $m_i = \pm\sqrt{2}/2$ and $\psi_i = \pm\pi/4$.

In the next section, we will numerically investigate the variation of m_i and ψ_i with respect to small perturbation on the THz and crystal orientations.

D.3 Numerical simulations of DEOS configuration

D.3.1 Error on THz polarization angle

The THz polarization is set perpendicular to the [-110]-axis. We consider a small perturbation ε_{THz} to the THz orientation angle

$$\theta_{THz} = (1 + \varepsilon_{THz}) \times \frac{\pi}{2} \qquad \text{with} \quad \varepsilon_{THz} \ll 1. \tag{D.3}$$

Figure D.2 shows the numerical transfer functions and its numerical fit using the analytical expression Eq. (D.1). The amplitude m_i and phase ψ_i of the analytical formula presents a clear symmetry between the two output ports, such that $m_1 = -m_2$ and $\psi_1 = -\psi_2$ (Figure D.3).

D.3.2 Error on crystal orientation

The [-110]-axis of the EO crystal is usually set horizontally. We consider a small perturbation ε_{Xtal} to the [-110]-axis horizontality such that:

$$\theta_{Xtal} = \varepsilon_{Xtal} \times 2\pi \qquad \text{with} \quad \varepsilon_{Xtal} \ll 1, \tag{D.4}$$

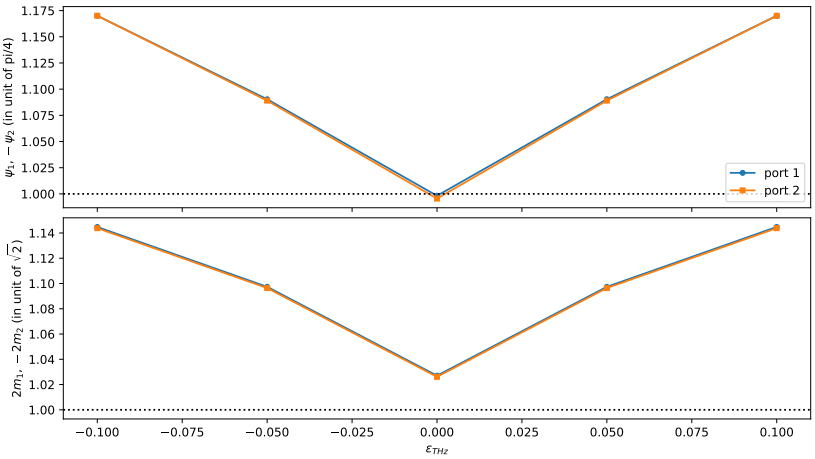

FIGURE D.3: Results of the numerical fit of the transfer function using Eq. (D.1): phase ψ (top) and amplitude $2m$ (bottom), for the two output ports.

while keeping the THz polarization angle perpendicular to the [-110]-axis.

Figure D.4 shows the numerical transfer functions and its numerical fit using the analytical expression Eq. (D.1). The amplitude m_i and phase ψ_i of the analytical formula presents a clear symmetry between the two output ports, such that $m_1 = -m_2$ and $\psi_1 = -\psi_2$ (Figure D.5).

D.4 Generalization of the DEOS transfer functions

As seen in the previous section, the two transfer functions of the two output ports presents a symmetry with the amplitude coefficient $m_1 = -m_2$ and the phase $\psi_1 = -\psi_2$. One can thus generalize the transfer functions of the DEOS configuration by:

$$H_{1,2}(\Omega) = \pm 2m \cos\left(B\Omega^2 \pm \psi\right). \tag{D.5}$$

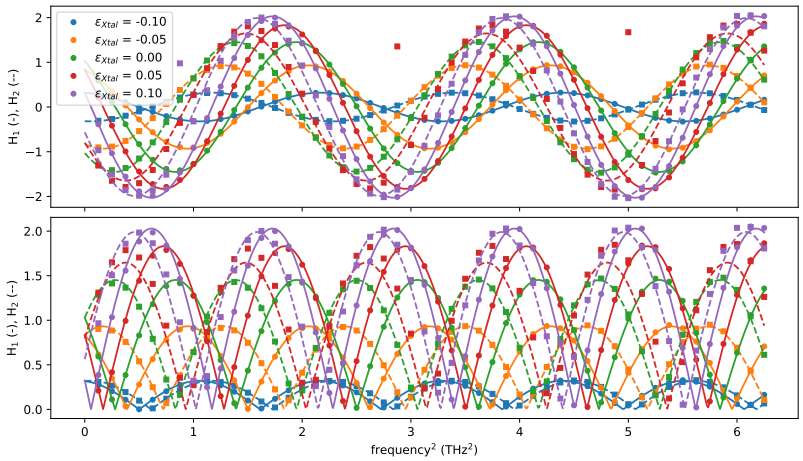

FIGURE D.4: Transfer functions (top) and its norms (bottom) as function of the [-110]-axis orientation error ε_{Xtal}. Dots: numerical results, lines: numerical fit using Eq. (D.1).

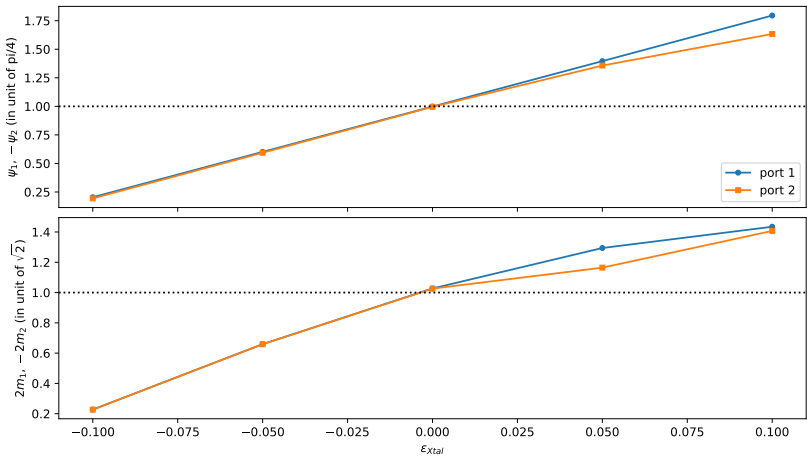

FIGURE D.5: Results of the numerical fit of the transfer function using Eq. (D.1): phase ψ (top) and amplitude $2m$ (bottom), for the two output ports.

Bibliography

1. Sun, Q. *et al.* Recent advances in terahertz technology for biomedical applications. *Quantitative imaging in medicine and surgery* **7,** 345 (2017).
2. McIntosh, A. I., Yang, B., Goldup, S. M., Watkinson, M. & Donnan, R. S. Terahertz spectroscopy: a powerful new tool for the chemical sciences? *Chemical Society Reviews* **41,** 2072–2082 (2012).
3. Tonouchi, M. Cutting-edge terahertz technology. *Nature photonics* **1,** 97–105 (2007).
4. Hoffmann, M. C. & Fülöp, J. A. Intense ultrashort terahertz pulses: generation and applications. *Journal of Physics D: Applied Physics* **44,** 083001 (2011).
5. Dhillon, S. *et al.* The 2017 terahertz science and technology roadmap. *Journal of Physics D: Applied Physics* **50,** 043001 (2017).
6. Wilke, I *et al.* Single-shot electron-beam bunch length measurements. *Physical review letters* **88,** 124801 (2002).
7. Steffen, B. R. Electro-optic methods for longitudinal bunch diagnostics at FLASH (2007).
8. Müller, F. *et al.* Electro-optical measurement of sub-ps structures in low charge electron bunches. *Physical Review Special Topics-Accelerators and Beams* **15,** 070701 (2012).
9. Roussel, E. *et al.* Observing microscopic structures of a relativistic object using a time-stretch strategy. *Scientific reports* **5,** 1–8 (2015).
10. Steffen, B. *et al.* Compact single-shot electro-optic detection system for THz pulses with femtosecond time resolution at MHz repetition rates. *Review of Scientific Instruments* **91,** 045123 (2020).
11. Lynch, D. W. Tantalus, a 240MeV Dedicated Source of Synchrotron Radiation, 1968–1986. *Journal of Synchrotron Radiation* **4,** 334–343 (1997).
12. Bathow, G., Freytag, E & Haensel, R. Measurement of Synchrotron Radiation in the X-Ray Region. *Journal of Applied Physics* **37,** 3449–3454 (1966).
13. Schwinger, J. On the classical radiation of accelerated electrons. *Physical review* **75,** 1912 (1949).
14. Tomboulian, D. H. & Hartman, P. Spectral and angular distribution of ultraviolet radiation from the 300-Mev Cornell synchrotron. *Physical Review* **102,** 1423 (1956).
15. Codling, K & Madden, R. Characteristics of the"Synchrotron Light"from the NBS 180-MeV Machine. *Journal of Applied Physics* **36,** 380–387 (1965).
16. Kamada, M, Hama, H, Kinoshita, T & Kosugi, N. Present Status of the UVSOR Facility–1997. *Journal of Synchrotron Radiation* **5,** 1166–1169 (1998).

17. Couprie, M. *et al.* Orsay free electron laser activities on the storage rings ACO and super-ACO. *Nuclear Instruments and Methods in Physics Research Section A: Accelerators, Spectrometers, Detectors and Associated Equipment* **282,** 455–476 (1989).
18. Filhol, J.-M. *et al. Overview of the status of the SOLEIL project* in *EPAC* **6** (2006), 249.
19. Gabriel, F *et al.* The Rossendorf radiation source ELBE and its FEL projects. *Nuclear Instruments and Methods in Physics Research Section B: Beam Interactions with Materials and Atoms* **161,** 1143–1147 (2000).
20. Ackermann, W. a. *et al.* Operation of a free-electron laser from the extreme ultraviolet to the water window. *Nature photonics* **1,** 336–342 (2007).
21. Allaria, E *et al.* Highly coherent and stable pulses from the FERMI seeded free-electron laser in the extreme ultraviolet. *Nature Photonics* **6,** 699–704 (2012).
22. Romaniuk, R. S. *Fifth generation light sources* in *Laser Technology 2016: Progress and Applications of Lasers* **10159** (2016), 15–27.
23. Tajima, T. & Dawson, J. M. Laser electron accelerator. *Physical review letters* **43,** 267 (1979).
24. Esarey, E., Sprangle, P., Krall, J. & Ting, A. Overview of plasma-based accelerator concepts. *IEEE Transactions on plasma science* **24,** 252–288 (1996).
25. Malka, V. *et al.* Principles and applications of compact laser–plasma accelerators. *Nature physics* **4,** 447–453 (2008).
26. Bellisola, G. & Sorio, C. Infrared spectroscopy and microscopy in cancer research and diagnosis. *American journal of cancer research* **2,** 1 (2012).
27. Spence, J. C. & Chapman, H. N. *The birth of a new field* 2014.
28. Kaertner, F. X. *et al.* AXSIS: Exploring the frontiers in attosecond X-ray science, imaging and spectroscopy. *Nuclear Instruments and Methods in Physics Research Section A: Accelerators, Spectrometers, Detectors and Associated Equipment* **829,** 24–29 (2016).
29. Barros, J *et al.* Coherent synchrotron radiation for broadband terahertz spectroscopy. *Review of Scientific Instruments* **84,** 033102 (2013).
30. Ginzburg, V. in *The lesson of quantum theory* (1986).
31. Elder, F., Gurewitsch, A., Langmuir, R. & Pollock, H. Radiation from electrons in a synchrotron. *Physical Review* **71,** 829 (1947).
32. Elder, F., Gurewitsch, A., Langmuir, R. & Pollock, H. A 70-Mev Synchrotron. *Journal of Applied Physics* **18,** 810–818 (1947).
33. Hiller, N. *et al.* Electro-optical bunch length measurements at the ANKA storage ring-First lessons learned. *Verhandlungen der Deutschen Physikalischen Gesellschaft* (2013).
34. Brown, G., Halbach, K, Harris, J. & Winick, H. Wiggler and undulator magnets—A review. *Nuclear Instruments and Methods in Physics Research* **208,** 65–77 (1983).
35. Nodvick, J. S. & Saxon, D. S. Suppression of coherent radiation by electrons in a synchrotron. *Physical Review* **96,** 180 (1954).
36. Warnock, R. L. & Morton, P. Fields Excited By A Beam In A Smooth Toroidal Chamber: pt. 1. Longitudinal coupling Impedance. *Part. Accel.* **25,** 113 (1988).

37. Andersson, A., Johnson, M. S. & Nelander, B. Coherent synchrotron radiation in the far-infrared from a 1 mm electron bunch. *Optical Engineering* **39,** 3099–3105 (2000).

38. Abo-Bakr, M, Feikes, J, Holldack, K, Wüstefeld, G & Hübers, H.-W. Steady-state far-infrared coherent synchrotron radiation detected at BESSY II. *Physical review letters* **88,** 254801 (2002).

39. Katayama, I. *et al. Coherent synchrotron terahertz radiation using electron bunch slicing* in *35th International Conference on Infrared, Millimeter, and Terahertz Waves* (2010), 1–2.

40. Nakazato, T *et al.* Observation of coherent synchrotron radiation. *Physical review letters* **63,** 1245 (1989).

41. Carr, G. *et al. Investigation of coherent emission from the NSLS VUV ring* in *Proceedings of the 1999 Particle Accelerator Conference (Cat. No. 99CH36366)* **1** (1999), 134–136.

42. Carr, G., Kramer, S., Murphy, J., Lobo, R. & Tanner, D. Observation of coherent synchrotron radiation from the NSLS VUV ring. *Nuclear Instruments and Methods in Physics Research Section A: Accelerators, Spectrometers, Detectors and Associated Equipment* **463,** 387–392 (2001).

43. Müller, A.-S. *et al.* Far infrared coherent synchrotron edge radiation at ANKA. *Synchrotron Radiation News* **19,** 18–24 (2006).

44. Byrd, J. *et al.* Observation of broadband self-amplified spontaneous coherent terahertz synchrotron radiation in a storage ring. *Physical review letters* **89,** 224801 (2002).

45. Abo-Bakr, M, Feikes, J, Holldack, K, Kuske, P & Wustefeld, G. *Coherent emission of synchrotron radiation and longitudinal instabilities* in *Proceedings of the 2003 Particle Accelerator Conference* **5** (2003), 3023–3025.

46. Takashima, Y. *et al.* Observation of intense bursts of terahertz synchrotron radiation at UVSOR-II. *Japanese journal of applied physics* **44,** L1131 (2005).

47. Karantzoulis, E, Penco, G, Perucchi, A & Lupi, S. Characterization of coherent THz radiation bursting regime at Elettra. *Infrared physics & technology* **53,** 300–303 (2010).

48. Bartel, T, Gaal, P, Reimann, K, Woerner, M. & Elsaesser, T. Generation of single-cycle THz transients with high electric-field amplitudes. *Optics letters* **30,** 2805–2807 (2005).

49. Wüstefeld, G *et al. Coherent THz measurements at the metrology light source* in *International Particle Accelerator Conference, Kyoto, Japan. Place of publication: Joint Accelerator Conferences Website (JACoW). Paper WEPEA015 (2010, June)* (2010).

50. Evain, C *et al.* Spatio-temporal dynamics of relativistic electron bunches during the micro-bunching instability in storage rings. *Europhysics Letters* **98,** 40006 (2012).

51. Shields, W *et al. Microbunch instability observations from a THz detector at diamond light source* in *Journal of Physics: Conference Series* **357** (2012), 012037.

52. Katayama, I *et al.* Electric field detection of coherent synchrotron radiation in a storage ring generated using laser bunch slicing. *Applied Physics Letters* **100** (2012).

53. Feikes, J *et al.* Metrology Light Source: The first electron storage ring optimized for generating coherent THz radiation. *Physical Review Special Topics-Accelerators and Beams* **14,** 030705 (2011).
54. Judin, V *et al.* Spectral and temporal observations of CSR at ANKA. *TUPPP010, Proc. IPAC* **12** (2012).
55. Kuske, P. *Investigation of the Temporal Structure of CSR-Bursts at BESSY II* in *Proc. of PAC* **9** (2009).
56. Ries, M, Feikes, J, Schmid, P, Wüstefeld, G & Hoehl, A. *THz bursting thresholds measured at the metrology light source* in *Proceedings of the 3rd International Particle Accelerator Conference, New Orleans, LA* (2012), 3030.
57. Arp, U. *et al.* Spontaneous coherent microwave emission and the sawtooth instability in a compact storage ring. *Physical Review Special Topics-Accelerators and Beams* **4,** 054401 (2001).
58. Chao, A. W. Physics of collective beam instabilities in high energy accelerators. *Wiley series in beam physics and accelerator technology* (1993).
59. Stupakov, G & Heifets, S. Beam instability and microbunching due to coherent synchrotron radiation. *Physical Review Special Topics-Accelerators and Beams* **5,** 054402 (2002).
60. Venturini, M. & Warnock, R. Bursts of coherent synchrotron radiation in electron storage rings: a dynamical model. *Physical review letters* **89,** 224802 (2002).
61. Cai, Y. *et al.* Theory of microwave instability and coherent synchrotron radiation in electron storage rings. *Proceedings of IPAC,* 3774–3778 (2011).
62. Bane, K. L., Cai, Y & Stupakov, G. Threshold studies of the microwave instability in electron storage rings. *Physical Review Special Topics-Accelerators and Beams* **13,** 104402 (2010).
63. Kerr, R. P. Gravitational field of a spinning mass as an example of algebraically special metrics. *Physical review letters* **11,** 237 (1963).
64. Warnock, R. L. & Ellison, J. A. in *The Physics of High Brightness Beams* 322–348 (World Scientific, 2000).
65. Roussel, E *et al.* Microbunching instability in relativistic electron bunches: Direct observations of the microstructures using ultrafast YBCO detectors. *Physical review letters* **113,** 094801 (2014).
66. Evain, C *et al.* Stable coherent terahertz synchrotron radiation from controlled relativistic electron bunches. *Nature Physics* **15,** 635–639 (2019).
67. Chu, A., Piestrup, M., Barbee Jr, T. & Pantell, R. Transition radiation as a source of x rays. *Journal of Applied Physics* **51,** 1290–1293 (1980).
68. Shibata, Y. *et al.* Coherent transition radiation in the far-infrared region. *Physical Review E* **49,** 785 (1994).
69. Shibata, Y. *et al.* Diagnostics of an electron beam of a linear accelerator using coherent transition radiation. *Physical Review E* **50,** 1479 (1994).
70. Bolotovskiĭ. Diffraction and diffraction radiation.
71. Lekomtsev, K *et al.* Coherent diffraction radiation as a tool for longitudinal beam profile diagnostics at CTF3 (2010).
72. Castellano, M *et al.* Measurements of coherent diffraction radiation and its application for bunch length diagnostics in particle accelerators. *Physical Review E* **63,** 056501 (2001).

73. Deacon, D. A. *et al.* First operation of a free-electron laser. *Physical Review Letters* **38,** 892 (1977).
74. Happek, U, Sievers, A. & Blum, E. Observation of coherent transition radiation. *Physical review letters* **67,** 2962 (1991).
75. Valdmanis, J., Mourou, G & Gabel, C. Picosecond electro-optic sampling system. *Applied Physics Letters* **41,** 211–212 (1982).
76. Valdmanis, J., Mourou, G & Gabel, C. Subpicosecond electrical sampling. *IEEE Journal of Quantum Electronics* **19,** 664–667 (1983).
77. Jiang, Z. & Zhang, X.-C. Electro-optic measurement of THz field pulses with a chirped optical beam. *Applied Physics Letters* **72,** 1945–1947 (1998).
78. Yan, X *et al.* Subpicosecond electro-optic measurement of relativistic electron pulses. *Physical Review Letters* **85,** 3404 (2000).
79. Tsang, T *et al.* Electro-optical measurements of picosecond bunch length of a 45 MeV electron beam. *Journal of Applied Physics* **89,** 4921–4926 (2001).
80. Fitch, M. *et al.* Electro-optic measurement of the wake fields of a relativistic electron beam. *Physical Review Letters* **87,** 034801 (2001).
81. Loos, H *et al. Electro-optic longitudinal electron beam diagnostic at SDL* in *Proceedings of the 2003 Particle Accelerator Conference* **4** (2003), 2455–2457.
82. Winter, A. *et al. Bunch length measurements at the SLS linac using electro-optical techniques* in *Proceedings of the EPAC'04* (2004).
83. Katayama, I. *et al. THz field detection of the coherent synchrotron radiation produced by laser bunch slicing* in *Conference on Lasers and Electro-Optics* (2010), CMF6.
84. Bielawski, S. *et al.* From self-organization in relativistic electron bunches to coherent synchrotron light: observation using a photonic time-stretch digitizer. *Scientific reports* **9,** 10391 (2019).
85. Van der Valk, N. C., Wenckebach, T. & Planken, P. C. Full mathematical description of electro-optic detection in optically isotropic crystals. *JOSA B* **21,** 622–631 (2004).
86. Casalbuoni, S *et al.* Numerical studies on the electro-optic detection of femtosecond electron bunches. *Physical review special topics-Accelerators and beams* **11,** 072802 (2008).
87. Wu, Q. & Zhang, X.-C. Free-space electro-optic sampling of terahertz beams. *Applied Physics Letters* **67,** 3523–3525 (1995).
88. Wu, Q & Zhang, X.-C. 7 terahertz broadband GaP electro-optic sensor. *Applied Physics Letters* **70,** 1784–1786 (1997).
89. Mourou, G. & Valdmanis, J. A. *Measurement of electrical signals with subpicosecond resolution* US Patent 4,618,819. 1986.
90. Nahata, A., Weling, A. S. & Heinz, T. F. A wideband coherent terahertz spectroscopy system using optical rectification and electro-optic sampling. *Applied physics letters* **69,** 2321–2323 (1996).
91. Ferguson, B., Wang, S., Gray, D., Abbot, D. & Zhang, X.-C. T-ray computed tomography. *Optics Letters* **27,** 1312–1314 (2002).
92. Wynne, K. & Jaroszynski, D. A. Superluminal terahertz pulses. *Optics Letters* **24,** 25–27 (1999).

93. Teo, S. M., Ofori-Okai, B. K., Werley, C. A. & Nelson, K. A. Invited Article: Single-shot THz detection techniques optimized for multidimensional THz spectroscopy. *Review of scientific instruments* **86,** 051301 (2015).
94. Matlis, N., Plateau, G., van Tilborg, J. & Leemans, W. Single-shot spatiotemporal measurements of ultrashort THz waveforms using temporal electric-field cross correlation. *JOSA B* **28,** 23–27 (2011).
95. Wakeham, G. P. & Nelson, K. A. Dual-echelon single-shot femtosecond spectroscopy. *Optics Letters* **25,** 505–507 (2000).
96. Han, P. Y., Jiang, Z., Riordan, J. A., Wang, L. & Zhang, X.-C. *Ultrafast electro-optic sensors and magneto-optic sensors for THz beams* in *Ultrafast Phenomena in Semiconductors II* **3277** (1998), 198–207.
97. Rota, L *et al.* KALYPSO: Linear array detector for high-repetition rate and real-time beam diagnostics. *Nuclear Instruments and Methods in Physics Research Section A: Accelerators, Spectrometers, Detectors and Associated Equipment* **936,** 10–13 (2019).
98. Sun, F., Jiang, Z. & Zhang, X.-C. Analysis of terahertz pulse measurement with a chirped probe beam. *Applied Physics Letters* **73,** 2233–2235 (1998).
99. Jamison, S. *et al.* Electro-optic techniques for temporal profile characterisation of relativistic Coulomb fields and coherent synchrotron radiation. *Nuclear Instruments and Methods in Physics Research Section A: Accelerators, Spectrometers, Detectors and Associated Equipment* **557,** 305–308 (2006).
100. Steffen, B., Schlott, V. & Muller, F. A compact single shot electro-optical bunch length monitor for the SwissFEL. *Proceedings DIPAC09* (2009).
101. Plech, A *et al. Electro-optical sampling of terahertz radiation emitted by short bunches in the ANKA synchrotron* in *Proceedings of PAC* **9** (2009).
102. Peng, X.-Y., Willi, O., Chen, M. & Pukhov, A. Optimal chirped probe pulse length for terahertz pulse measurement. *Optics express* **16,** 12342–12349 (2008).
103. Caselle, M *et al.* A PICOSECOND SAMPLING ELECTRONIC ^{3}KAPTURE FOR TERAHERTZ SYNCHROTRON RADIATION (2014).
104. Patil, M. *et al. An ultra-fast and wide-spectrum linear array detector for high repetition rate and pulsed experiments* in *10th International Particle Accelerator Conf.(IPAC'19), Melbourne, Australia* (2019).
105. Funkner, S. *et al.* High throughput data streaming of individual longitudinal electron bunch profiles. *Physical Review Accelerators and Beams* **22,** 022801 (2019).
106. Patil, M. *et al.* Ultra-Fast Line-Camera KALYPSO for fs-Laser-Based Electron Beam Diagnostics. *Proc. IBIC'21,* 1–6 (2021).
107. Gerth, C. *et al.* KALYPSO: Linear Array Detector with Continuous Read-Out at MHz Frame Rates. *JACoW IBIC2019, TUPP001* (2019).
108. Goda, K. & Jalali, B. Dispersive Fourier transformation for fast continuous single-shot measurements. *Nature Photonics* **7,** 102–112 (2013).
109. Kobayashi, M. *et al.* Fast-frame single-shot pump-probe spectroscopy with chirped-fiber Bragg gratings. *Optics letters* **44,** 163–166 (2019).
110. Coppinger, F, Bhushan, A. & Jalali, B. Photonic time stretch and its application to analog-to-digital conversion. *IEEE Transactions on microwave theory and techniques* **47,** 1309–1314 (1999).

111. Bhushan, A. S., Coppinger, F & Jalali, B. Time-stretched analogue-to-digital conversion. *Electronics Letters* **34,** 1081–1083 (1998).

112. Han, Y. & Jalali, B. Photonic time-stretched analog-to-digital converter: Fundamental concepts and practical considerations. *Journal of Lightwave Technology* **21,** 3085 (2003).

113. Coppinger, F, Bhushan, A. & Jalali, B. Time magnification of electrical signals using chirped optical pulses. *Electronics Letters* **34,** 399–399 (1998).

114. Szwaj, C. *et al.* High sensitivity photonic time-stretch electro-optic sampling of terahertz pulses. *Review of Scientific Instruments* **87,** 103111 (2016).

115. Evain, C *et al.* High Repetition-Rate Electro-optic Sampling: Recent Studies Using Photonic Time-Stretch. *JACoW Pub,* 121–124 (2017).

116. Kobayashi, M. *et al.* High-acquisition-rate single-shot pump-probe measurements using time-stretching method. *Scientific reports* **6,** 37614 (2016).

117. Couture, N. *et al.* Single-pulse terahertz spectroscopy monitoring submillisecond time dynamics at a rate of 50 kHz. *Nature Communications* **14,** 2595 (2023).

118. Couture, N. *et al.* Performance analysis of table-top single-pulse terahertz detection up to 1.1 MHz. *arXiv preprint arXiv:2309.09803* (2023).

119. Roussel, E. *et al.* Phase Diversity Electro-optic Sampling: A new approach to single-shot terahertz waveform recording. *Light: Science & Applications* **11,** 14 (2022).

120. Roussel, E. *Spatio-temporal dynamics of relativistic electron bunches during the microbunching instability: study of the Synchrotron SOLEIL and UVSOR storage rings* PhD thesis (Université Lille1-Sciences et Technologies, 2014).

121. Szwaj, C. *et al. Unveiling relativistic electron bunch microstructures and their dynamical evolutions, using photonic time-stretch* in *Real-time Measurements, Rogue Phenomena, and Single-Shot Applications II* **10089** (2017), 9–14.

122. Wong, J. H. *et al.* Photonic time-stretched analog-to-digital converter amenable to continuous-time operation based on polarization modulation with balanced detection scheme. *Journal of lightwave technology* **29,** 3099–3106 (2011).

123. Han, Y., Boyraz, O. & Jalali, B. Ultrawide-band photonic time-stretch A/D converter employing phase diversity. *IEEE Transactions on Microwave Theory and Techniques* **53,** 1404–1408 (2005).

124. Han, Y. & Jalali, B. Time-bandwidth product of the photonic time-stretched analog-to-digital converter. *IEEE Transactions on Microwave Theory and Techniques* **51,** 1886–1892 (2003).

125. Kahn, L. R. Ratio Squarer. *Proc. IRE* **42,** 1704 (1954).

126. Shah, A. & Haimovich, A. M. Performance analysis of maximal ratio combining and comparison with optimum combining for mobile radio communications with cochannel interference. *IEEE Transactions on Vehicular Technology* **49,** 1454–1463 (2000).

127. Angerer, C., Langwieser, R., Maier, G. & Rupp, M. *Maximal ratio combining receivers for dual antenna RFID readers* in *2009 IEEE MTT-S International Microwave Workshop on Wireless Sensing, Local Positioning, and RFID* (2009), 1–4.

128. Roussel, E. *et al.* Single-shot terahertz time-domain spectrometer using 1550 nm probe pulses and diversity electro-optic sampling. *Optics Express* **31,** 31072–31081 (2023).

129. Yang, Y., Shutler, A. & Grischkowsky, D. Measurement of the transmission of the atmosphere from 0.2 to 2 THz. *Optics express* **19,** 8830–8838 (2011).

130. Slocum, D. M., Slingerland, E. J., Giles, R. H. & Goyette, T. M. Atmospheric absorption of terahertz radiation and water vapor continuum effects. *Journal of Quantitative Spectroscopy and Radiative Transfer* **127,** 49–63 (2013).

131. Teichert, J *et al.* Successful user operation of a superconducting radio-frequency photoelectron gun with Mg cathodes. *Physical Review Accelerators and Beams* **24,** 033401 (2021).

132. Ilyakov, I *et al.* Field-resolved THz-pump laser-probe measurements with CEP-unstable THz light sources. *Optics Express* **30,** 42141–42154 (2022).

133. Lehnert, U *et al.* First experiences with the FIR-FEL at ELBE. *Proceeding of FEL, Novosibirsk* (2007).

134. Michel, P *et al. The rossendorf ir-fel elbe* in *Proc. FEL* (2006), 488.

135. Regensburger, S. *et al.* Broadband Terahertz Detection With Zero-Bias Field-Effect Transistors Between 100 GHz and 11.8 THz With a Noise Equivalent Power of 250 pW/$\sqrt{Hz}$ at 0.6 THz. *IEEE Transactions on Terahertz Science and Technology* **8,** 465–471 (2018).

136. Steffen, B. *et al. Electro-Optical Bunch Length Detection at the European XFEL* in *39th Free Electron Laser Conference (FEL'19), Hamburg, Germany, 26-30 August 2019* (2019), 360–363.

137. Couture, N. *et al.* Single-pulse time-resolved terahertz spectroscopy of sub-millisecond time dynamics. *arXiv preprint arXiv:2207.11766* (2022).

138. Roussel, E *et al.* SINGLE-SHOT ELECTRO-OPTIC SAMPLING COMBINED WITH PHOTONIC TIME-STRETCH: DETAILED RESULTS AT SOLEIL. *Spectrum (au)* **6,** 10.

139. SOLEIL. *SOLEIL* `https://fr.wikipedia.org/wiki/SOLEIL`. Accessed on June 20, 2023.

140. Nadji, A *et al. Operation and performance upgrade of the soleil storage ring* in *this conference* (2011).

141. Roy, P., Rouzières, M., Qi, Z. & Chubar, O. The AILES infrared beamline on the third generation synchrotron radiation facility SOLEIL. *Infrared Physics & Technology* **49,** 139–146 (2006).

142. Nelson, D. & Turner, E. Electro-optic and piezoelectric coefficients and refractive index of Gallium Phosphide. *Journal of Applied Physics* **39,** 3337–3343 (1968).

143. Gupta, S., Jalali, B., Stigwall, J. & Galt, S. *Demonstration of distortion suppression in photonic time-stretch ADC using back propagation method* in *Microwave Photonics, 2007 Interntional Topical Meeting on* (2007), 141–144.

144. Stigwall, J. & Galt, S. Signal reconstruction by phase retrieval and optical back-propagation in phase-diverse photonic time-stretch systems. *Journal of Lightwave Technology* **25,** 3017–3027 (2007).

145. Wu, B., Cao, L., Fu, Q., Tan, P., Xiong, Y., *et al. Comparison of the detection performance of three nonlinear crystals for the electro-optic sampling of a FEL-THz source* in *Proceedings of the 5th International Particle Accelerator Conference* (2014), 2891–2893.

146. Pradarutti, B *et al.* Highly efficient terahertz electro-optic sampling by material optimization at 1060 nm. *Optics communications* **281,** 5031–5035 (2008).